A Boiling Water Reactor Simulator for Stability Analysis

by

Chi Kao

M.S., National Tsing-Hua University (1984)

B.S., National Tsing-Hua University (1982)

Submitted to the Department of Nuclear Engineering
in partial fulfillment of the requirements for the degree of

Doctor of Philosophy

at the

MASSACHUSETTS INSTITUTE OF TECHNOLOGY

February 1996

Author .....
Department of Nuclear Engineering
January 12, 1996

Certified by .....
John E. Meyer
Professor of Nuclear Engineering
Thesis Supervisor

Certified by .....
David D. Lanning
Professor of Nuclear Engineering, Emeritus
Thesis Reader

Accepted by .....
Jeffrey P. Freidberg
Chairman, Departmental Committee on Graduate Students

A Boiling Water Reactor Simulator for Stability Analysis

by

Chi Kao

Submitted to the Department of Nuclear Engineering
on January 12, 1996, in partial fulfillment of the
requirements for the degree of
Doctor of Philosophy

Abstract

The objectives of this research are: (1) to develop a fast-running Boiling Water Reactor (BWR) simulator, and (2) to develop a stability analysis procedure using this simulator. Recent BWR power oscillation events have prompted the need for a new tool to describe the stability margin of BWRs. Currently acceptable approaches to deal with this issue are Prevention and Detection/Suppression. However, both approaches have drawbacks. The BWR simulator developed in this research, which can both monitor and predict the stability margin, is a valuable tool in supplementing the above two approaches.

This BWR simulator is applicable to normal and operational transient conditions. It is capable of simulating core-wide (in-phase) power oscillations. The thermal-hydraulic model used in this simulator is a three-equation model with a linear enthalpy profile assumption. A drift-flux model is used to treat the two-phase flow. Subcooled boiling is modeled by a profile-fit. The momentum equation is decoupled from the mass and energy equations by a single pressure assumption (the Momentum Integral Model). The steam dome region of the reactor vessel is modeled using a two-region thermally nonequilibrium basis. The reactor dynamics is described by the point kinetics model and distributed reactivity feedback. A two-node fuel rod model is adopted. The recirculation system model consists of two separate recirculation loops. The jet pumps are treated with a momentum mixing approach. The assumptions of ideal gas and adiabatic flow are used in the steam line model. The simulator also includes models of controllers for reactor pressure, recirculation flow, and level. Many of the models used in the simulator have been validated individually.

The BWR simulator has been benchmarked against actual plant transient data. The data include results from Kuosheng recirculation pump trip test and Peach Bottom-2 turbine trip tests. The results calculated by the simulator are in good agreement with the measured data. One simulator discrepancy is a too slow pressure response, which is due to the single pressure assumption. Using this simulator, the procedures for analyzing BWR stability in both time and frequency domains have been developed.

The results of thirteen Peach Bottom-2 stability tests were used to validate the stability analysis capability of the BWR simulator. The comparison of the decay

ratios and oscillation periods from simulations and tests shows that (1) the simulated results show the same trend as test results, and (2) the simulated decay ratios and oscillation periods are higher than test results. However, for the less stable cases with decay ratios obtained form test data greater than 0.4, the simulated decay ratios agree well with test data. The BWR simulator is faster than real time when applied to mild transients. As for stability analysis, the calculation of one case in the time domain takes about two minutes. This simulator/stability analyzer can be used in the control room as a stability margin indicator/predictor. It can also be used for training and planning purposes.

Thesis Supervisor: John E. Meyer
Title: Professor of Nuclear Engineering

Thesis Reader: David D. Lanning
Title: Professor of Nuclear Engineering, Emeritus

Acknowledgments

The author would like to express his sincere gratitude to Professor John E. Meyer for his guidance, encouragement, and support. Special thanks are due to Professor David D. Lanning for reviewing this thesis, and for his valuable advice. It is truly a privilege to work with them, and benefit from their invaluable expertise.

The author would like to thank Professor Allan F. Henry for his suggestions on the neutronics model. Thanks are also due to Dr. Shih-Ping Kao for his helpful discussion with the author. Help with computer software and hardware from Rachel Morton is appreciated.

The author acknowledges the contributions of the followings for providing useful information:

- Dr. Lin-Wen Hu,
- Tsu-Mu Kao,
- Wen-Ching Tsai of Taiwan Power Company,
- Janson Post of GE Nuclear Energy,
- Professor M. Z. Podowski of RPI,
- Dr. Cherng-Shing Lin,
- Professor W. E. Kastenberg of UCLA,
- Professor Chun-Kuan Shih of National Tsing-Hua University, Taiwan, and
- Dr. Horngshyang Lein of GPI.

Financial support from the Taiwan Power Company is gratefully acknowledged.

Contents

List of Figures

List of Tables

Chapter 1

Introduction

1.1 Background and Motivation

Safe and reliable operation of nuclear power reactors is the basic requirement for the utilization of nuclear energy. The stability of a nuclear power reactor with respect to internal and external disturbances must be ensured. Boiling Water Reactors (BWRs) use water both as a coolant and a neutron moderator. Bulk boiling takes place in the reactor core of a BWR. Due to the nuclear feedback and two-phase flow instability mechanisms, the possibility of BWR power oscillation exists. During the early stage of BWR development, oscillatory behaviors were observed in the BORAX reactors and the Experimental Boiling Water Reactor [1]. These reactors use natural circulation and metal fuel with low system pressure. The stability of commercial BWRs is greatly enhanced by adopting high system pressure, ceramic fuel, and core inlet orificing. Thus modern BWRs are stable at most conditions.

Nevertheless, several BWR power oscillation events have been reported in the past two decades. Following the instability event of the LaSalle County Unit 2 in 1988 [2], the search for long-term solutions to resolve the BWR stability issue began. At the same time, a set of Interim Corrective Actions was adopted by the BWR owners to minimize the possibility of instability [3]. These Interim Corrective Actions prohibit reactor operations in the regions most susceptible to power oscillations based on the past experience. However, another BWR instability event occurred in Washington

Nuclear Power Unit 2 in 1992 [4], which was operated outside the exclusion regions defined in the Interim Corrective Actions. This event shows that the unstable region depends on many factor, and is difficult to define.

After several years of research, some long-term solution options that have been proposed are approved by the U.S. Nuclear Regulatory Commission [5]. Two basic approaches are used in these long-term solution options. They are Prevention and Detection/Suppression. Automatic protection systems are required for all long-term solutions. The Prevention approach designates exclusion regions as in the Interim Corrective Actions. Operation in these exclusion regions is prevented by automatic protection systems. This approach reduces the available operation domain. Moreover, because of the complexity of the BWR instability, it is difficult to establish exclusion regions that can cover all possible operation conditions. The detection/Suppression approach uses stability monitors to detect unstable occurrences. Once detected, power oscillations are suppressed by automatic protection systems. This approach relies on the stability monitors to identify system conditions. These stability monitors must be highly reliable so that no unstable condition will be undetected, and also there shall be no false alarm.

Even if the above approaches work perfectly, they can not provide information about system stability in advance. This information will be valuable to the operators for steering the reactor out of undesirable conditions. Currently available stability monitors cannot provide stability predictions. A tool that can both detect and predict system stability margins is needed to avert unstable situations and to minimize the impact of this BWR stability issue.

1.2 Research Goals

In order to have the ability to both monitor and predict stability margins, a tool based on the deterministic approach is required. Because many system parameters affect the stability of a BWR, dynamic simulations of system parameters are necessary for accurate stability predictions [6]. Also, for a stability monitor/predictor to be useful,

its computation time must be faster or near real time.

The goals of this research are

1. To develop a BWR simulator that can accurately simulate the phenomenon of power oscillations. This simulator shall be capable to simulate normal and operational transient conditions. The computation speed of this BWR simulator shall be faster than real time.

2. To develop a stability analysis procedure using this BWR simulator.

These BWR simulator and stability analysis procedure can be used for

- Stability margin monitoring and prediction,
- Operational transient analysis,
- Operator support, and
- Training.

1.3 Thesis Organization

This thesis is divided into eight chapters. Chapter 1 presents the background, motivation, and goals of this research. Chapter 2 gives an overview of the BWR stability issue. This chapter describes the safety concerns of BWR power oscillations, the mechanisms and modes of BWR instability, the effects of changes in system parameters on the stability margin, the analysis methods, and the approaches to resolve this issue.

Chapter 3 gives a brief description of modern BWRs and defines the scope of the simulation. Chapter 4 describes the physical models used in the BWR simulator. Validation results of individual models are also presented. Chapter 5 discussed the numerical solution methods for steady-state and transient calculations. Chapter 6 presents the validation results of the BWR simulator. The simulator is benchmarked

against data from the Kuosheng recirculation pump trip test and the Peach Bottom-2 turbine trip tests.

Chapter 7 describes the procedures for stability analysis in both time and frequency domains using this BWR simulator. The results of stability analyses of the Peach Bottom-2 stability tests using these procedures are compared to test data and the analysis results by other researchers. Chapter 8 summaries the conclusions obtained from this research and lists the recommendations for future research.

Chapter 2

Overview of the Boiling Water Reactor Stability Issue

2.1 Introduction

The potential for Boiling Water Reactor (BWR) instabilities has been recognized since the beginning of BWR development. Government regulations require that a nuclear reactor be designed such that power oscillations "are not possible or can be reliably and readily detected and suppressed" [7]. For BWRs, analyses in the design stage were used to show compliance with the regulations in the past.

BWR power oscillation experience outside the United States include the Coarso in Italy [8], the Ringhals-1 in Sweden [9], and the Confrentes in Spain [10]. In the United States, two BWR power oscillation events have occurred recently. On March 9, 1988, a power oscillation event occurred at LaSalle Unit 2 (LaSalle-2) reactor [2]. This event raised concerns about the adequacy of the past analyses and the impact on plant safety; research was initiated to resolve this issue. On August 15, 1992, another power oscillation event was experienced by Washington Nuclear Power Unit 2 (WNP-2) [4]. This event again confirms the need for new approaches to ensure BWR stability.

This chapter reviews the issue of BWR stability. First, the safety concerns of BWR power oscillation are described. Then, the oscillation mechanism and the sensitivity

of stability to system parameters are discussed. Next, the methods to study BWR stability are summarized. Finally, the approaches to resolve this issue are presented.

2.2 Safety Concerns of BWR Power Oscillations

Power and flow oscillations in a nuclear reactor are very undesirable. One of the major concerns is the fuel integrity during power oscillations. If the oscillation amplitude is large, the fuel rods may experience periodic dryout and rewetting [11]. The safety limit of the Minimum Critical Power Ratio (MCPR) may be violated during an extended period of dryout.

Another safety concern is the consequences of an Anticipated Transient Without Scram (ATWS) event. By procedure, if an ATWS event occurs the recirculation flow is reduced to reduce the reactor power. But this will drive the reactor into a high power, low flow condition which is most susceptible to power oscillations. If an ATWS event is followed by power oscillations, the heat capacity of the suppression pool may not be large enough to accommodate the possible heat load. Several analyses have shown that the mean fission power increases as the amplitude of power oscillation increases [6, 12]. The steam that is discharged into the suppression pool during the ATWS and power oscillation event may cause the temperature of the suppression pool to exceed its limit.

Because of these safety concerns, it is necessary to demonstrate the stability margin of a BWR in the design stage and identify the stability boundary in the operation stage. If a power oscillation event occurs, it has to be suppressed immediately.

2.3 Mechanism of BWR Power Oscillations

The basic mechanism of BWR power oscillations has been identified as nuclear-coupled density-wave oscillations [13]. Two types of power oscillations have been observed: core-wide (or in-phase) and regional (or out-of-phase) oscillations.

2.3.1 Density-wave instability

A BWR core contains a two-phase coolant and is susceptible to two-phase flow instabilities. Various types of two-phase flow instabilities have been studied. At reasonably high pressures, the density-wave instability is the most commonly encountered type [14, 15, 16].

Density-wave oscillations are usually observed in systems with a two-phase mixture. It may also occur in a system with a single-phase fluid if the density change is large enough. The essential ingredients to produce density-wave oscillations are [17]

1. A density distribution throughout the system which depends on the flow rate of the system,

2. A time delay between the flow rate changes and the density responses,

3. A cause/effect relationship between flow rate and density changes, and pressure loss/buoyancy changes.

Density-wave instabilities can be explained by the phenomenon of kinematic wave propagation. They are caused by the finite time necessary for the enthalpy and void fraction waves to propagate in the channel. These finite propagation times induce time-lag effects and phase-angle shifts between the channel pressure drop and flow rate, which under certain conditions can result in self-sustained oscillations [14].

Consider a heated channel containing a two-phase fluid initially at steady- state. An incremental decrease in the inlet flow rate produces an increase of the void fraction along the channel. This void fraction perturbation (or density wave) travels in a speed near the vapor velocity, and produces a channel pressure drop fluctuation with a time delay with respect to the initial flow rate change. If the flow rate and pressure drop fluctuations satisfy certain relations, self-sustained oscillations may occur. The period of density-wave oscillations is usually close to twice that of the vapor transit time through the channel and is on the order of seconds [16].

Two types of density-wave instabilities have been observed: loop instabilities and parallel-channel instabilities [18]. For loop instabilities, the boundary conditions of

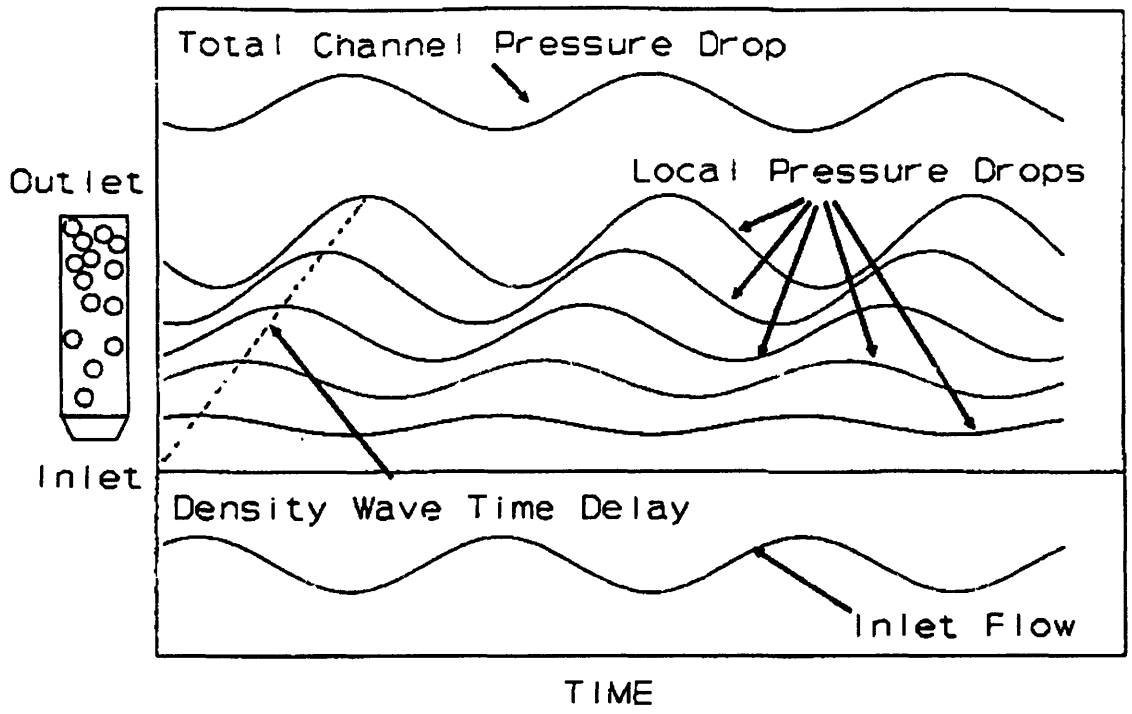

Figure 2-1: Local pressure drop variations due to inlet flow fluctuation (from [19]).

the channel are determined by the flow rate versus pressure drop characteristics of the external loop. Figure 2-1 shows the variations of the local pressure gradients of a boiling channel with sinusoidal inlet flow rate fluctuations [19]. The time delay of local pressure drops introduced by the traveling density wave is shown. The resulting total channel pressure drop variation is sinusoidal but with a phase lag with respect to the inlet flow rate. If this phase lag reaches 180 degrees, then the effective channel pressure drop versus flow rate characteristic curve will have a negative slope, and loop instabilities may occur.

For parallel-channel instabilities, a constant pressure drop boundary condition is imposed by either a large number of parallel channels or a large bypass flow path. Figure 2-2 illustrates the variations of pressure drop components for parallel-channel instabilities [20]. The total pressure drop is broken down into frictional, elevation (gravity), spatial acceleration, and temporal acceleration (inertia) terms. Each term has a different dependency on velocity and void fraction profiles and, thus, has a

different phase shift with respect to the inlet mass velocity variation. Under certain conditions, the phase relationships between pressure drop components may result in a total cancellation on the pressure drop variation. Then the flow oscillations can be sustained.

Several modes of parallel-channel oscillations can occur [19]. It can be that only the flow of one channel is oscillating, while the flow of the rest of the channels stays nearly constant; or it can be that the flow of half of the channels oscillates out-of-phase with the flow of the other half of the channels; or it can be three groups of channels oscillate 120 degrees out-of-phase with respect to each other.

2.3.2 Nuclear feedback

The power generation from a BWR core is coupled to the coolant thermal-hydraulic conditions through a reactivity feedback mechanism. The water in a BWR acts both as a coolant and a neutron moderator. The density of the water affects the efficiency of neutron moderation. A BWR usually has a negative void reactivity feedback coefficient. If the void fraction in a BWR core increases, it produces a negative reactivity change and the power decreases.

This coupling between the void fraction and power, combined with the dynamics of fuel rods, forms a feedback loop that can lead to power oscillations. Figure 2-3 illustrates the nuclear feedback loop in a BWR [21]. Starting from the upper left corner of Figure 2-3, an increase in voids in the core reduces reactivity and the power. The heat transfer from the fuel rods to the coolant is reduced, but with a time delay due to the thermal inertia of the fuel rods. With less heat transferred to the coolant, the void in the core is reduced, and the power is increased through the void reactivity feedback. Then, after the time delay due to fuel rod dynamics, the void is increased again. This completes a cycle of power oscillations. This mechanism when acting alone is also called reactivity instability [19].

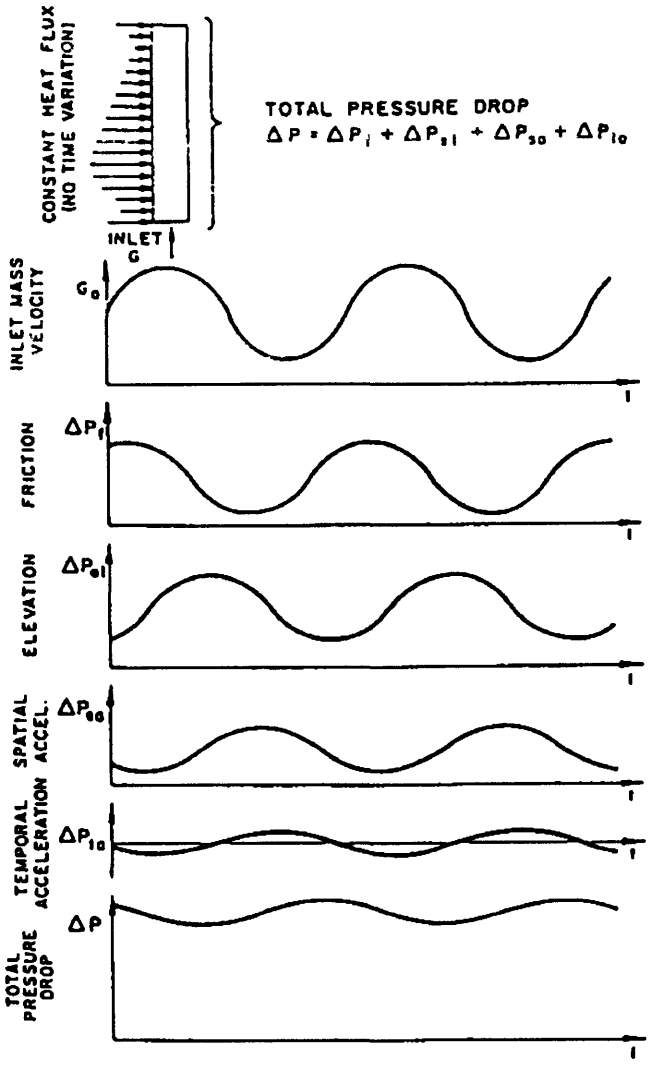

Figure 2-2: Variations of pressure drop components for parallel-channel type oscillations (from [20]).

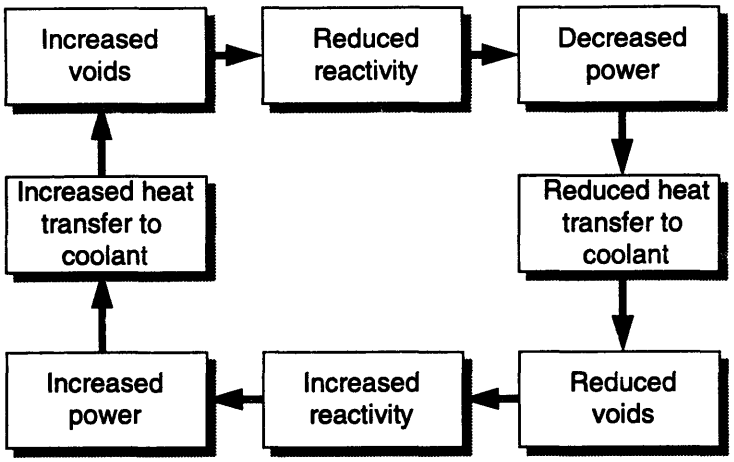

Figure 2-3: Nuclear feedback loop in a BWR (adapted from [21]).

2.3.3 Modes of BWR instabilities

Three spatial modes of BWR instabilities have been observed: single channel, core-wide (in-phase), and regional (out-of-phase) oscillations [19].

Single channel oscillations were observed during special tests when a coolant channel was partially blocked by a failed flowmeter. The flow of this channel then oscillated following the density-wave mechanism while all other channels remained stable. This type of instability has been reported only once, but it can be very dangerous because it is hard to detect [19].

Core-wide oscillations are caused by loop type density-wave instabilities coupled with reactivity instabilities. In this type of instability, all the channels in the core oscillate in phase with each other. The spatial power shape during oscillations corresponds to the fundamental mode of neutron flux shape (steady-state distribution). Axial power shape changes have also been observed during core-wide power oscillations. Because the whole core responds in phase, this type of oscillation can be detected by Average Power Range Monitors (APRMs).

Regional oscillations are parallel-channel type density-wave instabilities coupled

with neutronic oscillations. During regional oscillations, part of the channels oscillate out of phase with the other channels: the power or flow of the channels in one region increases while that of the channels in the other region decreases. The power shape in regional oscillations relates to a higher harmonic mode of the neutron flux shape (subcritical modes). Normally, these subcritical modes would be damped out because the eigenvalues of these modes are less than one. However, when these subcritical flux modes are coupled with parallel-channel oscillations, sustained power oscillations can be realized [22].

The variations in the total power and flow rate during regional power oscillations are smaller than the local variations due to spatial cancellations. Multiple Local Power Range Monitors (LPRMs) are needed for early detection of out-of-phase oscillations.

2.4 Dependence of Stability on Changes in Operating Variables

Many parameters affect the stability of a BWR. Because BWR power oscillations involve complex processes, the effect of a physical parameter on BWR stability sometimes depends on other parameters. So it is not always possible to find a set of system parameters that can ensure stability.

In general, the following changes of individual parameter decrease stability [15, 16, 19, 21, 23, 24, 25, 26, 27]:

1. Increasing power: This increases the void content of the core, which increases feedback from the density-wave mechanism. It also increases reactivity feedback because the magnitude of the void reactivity coefficient is increased [19].

2. Decreasing core flow: This also increases the core void content.

3. Increasing two-phase pressure drop in the core: This enhances the density-wave mechanism.

4. Decreasing single-phase pressure drop in the core: This also enhances the density-wave mechanism.

5. Increasing void reactivity feedback: This enhances the reactivity feedback mechanism.

6. Reducing the fuel rod thermal time constant: This increases the variation of heat flux on the fuel surface during power oscillations, which then increases the void fraction variations and enhances power and flow oscillations. Decreasing the fuel rod thermal time constant also reduces the phase shift between the flow rate and power responses which tends to stabilize the system. For the current BWR fuel designs, the stabilizing effect is usually out-weighed by the destabilizing effect [19, 24, 27].

7. Increasing radial peaking factor: The channel with the highest power usually has more voids and has a higher weighting for reactivity feedback. This hot channel is less stable. The stability of high power channels dominates over lower power channels. So a high radial peaking factor is destabilizing.

The effects of system pressure, axial power shape and inlet subcooling on stability are more complicated.

- System pressure: Decreasing system pressure increases the density difference between water and steam, which is destabilizing. However, Blakeman and March-Leuba observed the opposite effect for extremely bottom-peaked power shapes [23].

- Axial power shape: Bottom-peaked power shapes have a longer two-phase region and larger voids, so they are more unstable. However, extremely bottom-peaked shapes have been shown to be more stable than intermediate shapes because the reactivity weighting in the upper part is reduced [23].

- Core inlet subcooling: For the density-wave mechanism, the effect of changing inlet subcooling depends on the original inlet subcooling level [15]. At medium

or high subcoolings, an increase in subcooling increases non-boiling length and stabilizes the flow. However, at small subcoolings, the non-boiling length is very short. An increase in subcooling reduces voids near the inlet region, so the pressure drop that is in phase with the inlet flow rate is reduced, and the flow is destabilized. For nuclear feedback, increasing the core inlet subcooling reduces the void contents in the core and increases core power. The net effect of increasing inlet subcooling is stabilizing when at high subcoolings and destabilizing when at low subcoolings.

Core-wide and regional oscillations have different sensitivities to system parameters. Regional oscillations have a large gain from parallel-channel instabilities because they do not have damping of the external loop, but they have a damped feedback from subcritical neutronic modes. The damping of subcritical neutronic modes depends on the eigenvalue of each mode, and a larger eigenvalue corresponds to a less damped mode. From the one-group diffusion theory, the eigenvalue of a harmonic mode can be expressed as [28]

$$\lambda_i = \frac{\nu\Sigma_f}{DB_i^2 + \Sigma_a} ,$$

where

λ_i is the eigenvalue of the ith neutronic mode,

$\nu\Sigma_f$ is the fission neutron yield times the fission cross section,

D is the diffusion coefficient,

B_i^2 is the geometric buckling of the ith mode, and

Σ_a is the absorption cross section.

These eigenvalues are less than one except for the fundamental mode which is equal to one for steady-state conditions. The reactivity separation between fundamental and subcritical modes can be expressed as [22]

$$\Delta\rho_{subcritical,i} = \frac{1}{\lambda_i} - \frac{1}{\lambda_0} = \frac{D\Delta B_i^2}{\nu\Sigma_f} ,$$

where $\Delta B_i^2 = B_i^2 - B_0^2$. A small subcritical reactivity means less damping of the subcritical mode. In that case, the reactor is more prone to the out-of-phase type instability.

So, the conditions that favor out-of-phase oscillations over the in-phase type are [19]

- low geometric buckling,
- high fission cross section,
- high pressure drop across the core,
- high core flow rate,
- high pressure loss in the external loop,
- highly bottom-peaked axial power shapes, and
- low single-phase friction.

Another important factor that greatly affects stability is the uniformity of channel hydrodynamics characteristics. If a core contains two types of channels with different pressure drop characteristics, then this core will be less stable than the cores with channels of only one type [4, 29]. Therefore, when doing reload designs, the compatibility between different fuel designs must be examined.

2.5 Analysis Methods for BWR Stability

Various methods have been used to analyze BWR stability. These methods have different applications, and they are complimentary to each other in understanding and controlling BWR stability.

BWR stability is traditionally described in terms of Decay Ratios (DRs). The decay ratio is defined as the ratio of the peak amplitude of an oscillation to that of the previous oscillation following an impulse disturbance (see Figure 2-4 [21]). A system is stable with a DR less than one, and unstable with a DR greater than one.

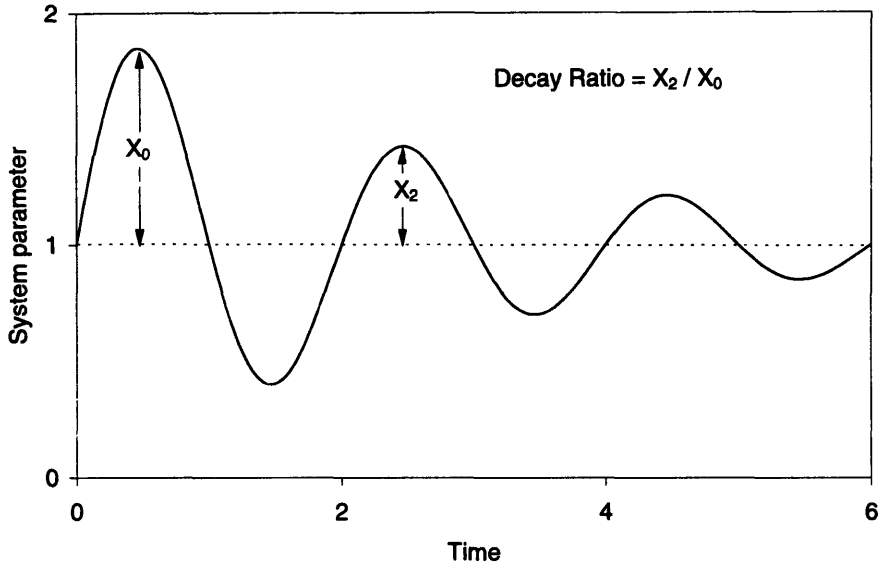

Figure 2-4: Definition of the Decay Ratio (adapted from [21]).

The DR relates to the poles of a system's closed loop transfer function [30]. For a second order linear dynamic system, the DR is the same for any two consecutive oscillation peaks. For higher order system, the DR is not a constant, and the appropriate stability indicator is the asymptotic DR corresponding to the least stable poles of the system.

The decay ratio is the stability indicator for single-input, single-output systems (SISO). BWRs, however, are multiple-input, multiple-output systems (MIMO). A single DR cannot be expected to represent the whole picture of the stability of a BWR [31].

2.5.1 Experimental methods

Several BWRs have performed special stability tests [32, 33]. These tests not only determined the stability of the particular plant but also formed a data base for the qualification of analytical methods.

These tests were done by perturbing one input parameter and measuring the output responses of reactor power. The two input parameters that have been used are

pressure and reactivity. Control rod oscillations were used to generate reactivity perturbations. Pressure perturbations were produced by disturbing the system pressure controller.

Two time variations have been used for input perturbations. The first type is sinusoidal oscillations. Several frequencies of sinusoidal signals were used to cover the frequency range of interest. The other type of perturbation is Pseudo Random Binary Sequence (PRBS), which simulate white noise.

Collected test data were reduced by frequency domain analysis. A transfer function was fitted to the test data, and the decay ratio was calculated from this transfer function.

2.5.2 Stochastic methods

Stochastic methods are based on neutron noise analysis to deduce stability information. Random processes such as the collapse of a steam bubble in the core produce noise in neutron flux signals. This noise contains information about the system.

The stability of BWRs can be estimated by methods such as an autocorrelation function, autoregressive modeling, or a power spectral density fit [30]. To have an accurate estimation, a long history of neutron noise data is needed. The required data length also depends on the system conditions: the more stable the system is, the longer data length is needed.

On-line stability monitors based on neutron noise analysis have been developed [34]. This type of stability monitor can only provide the current status. It can not predict stability that would result from changes in conditions.

2.5.3 Analytical methods

Analytical calculations of BWR stability are very complicated and require computer simulations. Many computer codes have been used to study BWR stability. They fall in two categories: frequency-domain and time-domain codes [13].

Frequency domain codes

Frequency-domain codes are developed particularly for BWR stability analysis. The procedure of stability analysis in the frequency domain is

1. Select a set of governing equations and constitutive relations,
2. Linearize these equations by using a first order perturbation approximation,
3. Laplace transform the linearized equations into frequency domain, and
4. Determine the stability by using linear control theories.

The advantages of using frequency domain codes are less computer time and fewer numerical problems [29]. Some examples of frequency domain codes are FABLE, LAPUR and NUFREQ [13]. Note, however, that non-linear phenomena such as limit-cycle oscillations cannot be modeled.

Time domain codes

Time domain codes integrate the system governing equations directly, and calculate the state variables at each time step. These codes are usually general purpose codes, not developed specifically for stability analysis. They are useful in calculating system parameters, such as the peak clad temperature and MCPR during power oscillations. They can also predict the peak amplitude of non-linear limit cycle oscillations.

When using time domain codes to study BWR stability, special caution should be paid to the numerical damping problem [6]. Many time domain codes incorporate special numerical methods for avoiding numerical instability and reducing computer time. Numerical schemes such as up-wind differencing and multi-step methods will produce a numerical damping effect that may mask the oscillatory behavior.

Examples of time domain codes used for BWR stability analysis are RAMONA-3B, TRAC-BF1, TRACG, RETRAN, BNL EPA, SABRE, TRAB, TOSDYN-2, STANDY, and SPDA [13].

2.6 Approaches for Resolution of the BWR Stability Issue

2.6.1 Interim Corrective Actions

After the LaSalle-2 event, a set of Interim Corrective Actions were adopted by the BWR owners while the research for long term solutions was ongoing [3]. The Interim Corrective Actions define exclusion regions on the power-flow map (see Figure 2-5). These high power, low flow regions are most susceptible to instability. In these regions, the natural circulation flow contributes to a large portion of the total core flow. So the core flow is very sensitive to the void contents in the core. This situation enhances the density-wave instability.

Region A in Figure 2-5 is the area above 100% rod line and on the left of the 40% flow line; Region B is the area between 100% and 80% rod lines, and on the left of the 40% flow line; Region C is the area above 80% rod line and on the left of the 45% flow line. Operation within Regions A and B are prohibited, and if entered, the operators should bring the reactor out of these regions immediately by inserting control rods or scram. Operation in Region C is allowed only for control rod withdrawals during startup requiring Preconditioned Interim Operational Management Recommendations (PCIOMR). Operators are also required to scram the reactor if power oscillations occur, or if all the recirculation pumps are tripped.

The operating point of the WNP-2 when power oscillations occurred is outside the exclusion regions. This event proves again that the approaches used in the past are insufficient in dealing with BWR stability problem. It also shows that these exclusion regions do not cover all the unstable conditions.

2.6.2 Long Term Solutions

Before the LaSalle-2 event occurred, it was believed that an analysis is sufficient to ensure compliance with regulatory requirements on BWR stability. Now, an automatic protection system is required for resolving the stability issue. The Boiling

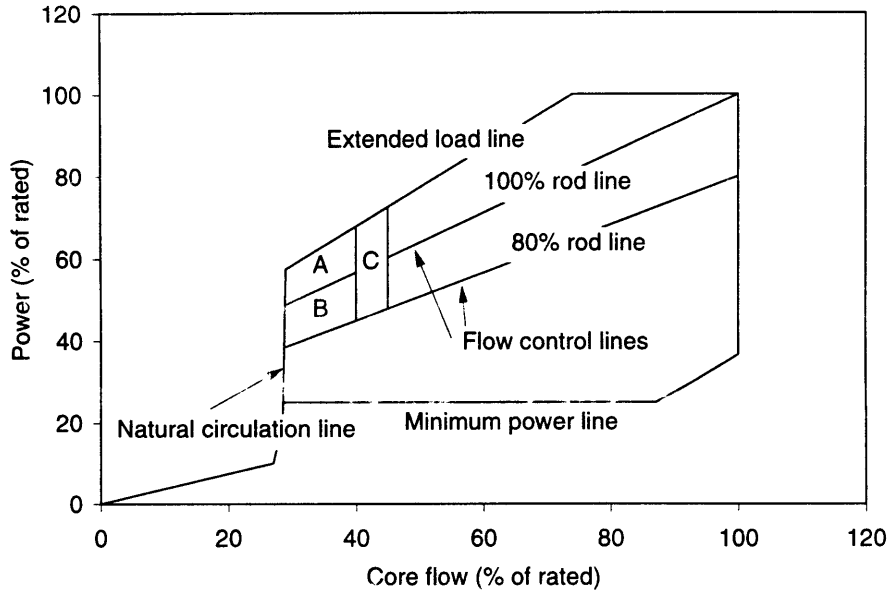

Figure 2-5: Exclusion regions defined by the Interim Corrective Actions (adapted from [3]).

Water Reactor Owners' Group (BWROG) has developed several options for the long term solution, and the U.S. Nuclear Regulatory Commission (NRC) has accepted some of the options [2, 5]. The proposed Long Term Solutions are based on two basic approaches:

1. Prevention—regional exclusion with automatic protection actions, and

2. Detection and Suppression.

The automatic protection actions being considered are reactor scram and selected rod insertion (SRI). The prevention approach is basically the same as the Interim Corrective Action except that operation in the exclusion regions is prevented by an automatic protection system instead of administrative control. This approach requires minimum plant modifications, but reduces the available operation domain. To define a conservative exclusion region for a wide range of operating conditions is the biggest challenge for adopting this approach.

The second approach uses LPRM based stability monitors such as Oscillation Power Range Monitors (OPRMs) to detect power oscillations. This approach does not

impose any restriction on the operation domain. The reliability of stability monitors is the main concern for this approach.

2.6.3 Stability control

Controlling BWR stability during normal operation is not straightforward because many factors affect stability. An operational strategy has been proposed for maintaining large stability margins [35]. This control strategy is to maintain the average bulk boiling boundary above a predetermined elevation. With a sufficient length of the single-phase region, density-wave oscillations are suppressed, and the stability can be ensured.

The location of the average bulk boiling boundary depends on many parameters that are also important to stability, such as pressure, power, core flow rate, inlet subcooling and core power distribution. Changes in these parameters will be reflected in the change in the location of the boiling boundary. It has been shown that the stability margin of the system is insensitive to changes in operating parameters as long as the average bulk boiling boundary is above a predetermined height.

The desired boiling boundary height is not always achievable, however. The achievable power shapes are limited by fuel loading, burnup, and other safety limits. The boiling boundary control strategy may be in conflict with other operating recommendations.

2.7 Chapter Summary

Recent BWR power oscillation events have prompted the need for new approaches to ensure BWR stability. Two major concerns are the thermal margin of the fuel during power oscillations, and the possible consequences of an ATWS plus power oscillation event .

The mechanism of BWR power oscillations is nuclear-coupled density-wave instability. Many parameters affect BWR stability, and their effects on stability are sometimes counter intuitive. BWR stability can be analyzed by experimental, stochastic,

or analytical methods. However, because of the complexity of the processes, it is difficult to establish a stability boundary that could cover all the operation conditions.

Two basic approaches have been proposed for the long term solution: Prevention, and Detection/Suppression. An operational strategy that controls the core average boiling boundary elevation has also been proposed for maintaining a large stability margin. These approaches either restrict the operation domain or impose risk from inadvertent actuation of the safety system.

A simulator-based stability monitor/predictor can alleviate the side effects of the long term solutions. The capability of both monitoring and predicting stability margin makes the simulator-based stability monitor more useful than a stochastic-based stability monitor. With a simulator-based stability monitor/predictor, the operators can keep track of the current stability margin as well as the stability conditions at future operating points. Thus unnecessary challenge to the automatic stability protection system can be avoided.

Chapter 3

BWR Simulator – Overview

3.1 Description of a BWR

Modern BWR power plants employ a direct steam cycle as shown in Figure 3-1 [36]. This system consists of a BWR Nuclear Steam Supply System (NSSS) and a conventional Balance-of-Plant (BOP). The steam generated in the reactor vessel goes directly into the main turbine. After expansion through turbine stages, the exhaust steam is condensed into water in the main condenser. The condensed water is purified, heated up, and pressurized by the condensate and feedwater systems, and is fed into the reactor vessel as the feedwater.

The reactor vessel of a BWR is an integrated steam generating unit. It encloses the nuclear reactor core, steam separators, and steam dryers. Figure 3-2 [37] shows the steam and recirculation water flow paths in a BWR of General Electric (GE) design. The single-phase coolant flows up into the reactor core by forced circulation. In the reactor core, the coolant is heated up by the nuclear fission power, and is turned into a two-phase mixture. The coolant then exits the reactor core, flows through the upper plenum and stand pipes, and enters the steam separators. The steam in the two-phase mixture is separated out and dried by the steam separators and dryers, and exits the reactor vessel to the main steam lines.

The water separated from the steam goes down to a water pool surrounding the separators, and flows into the downcomer between the reactor vessel and core shroud.

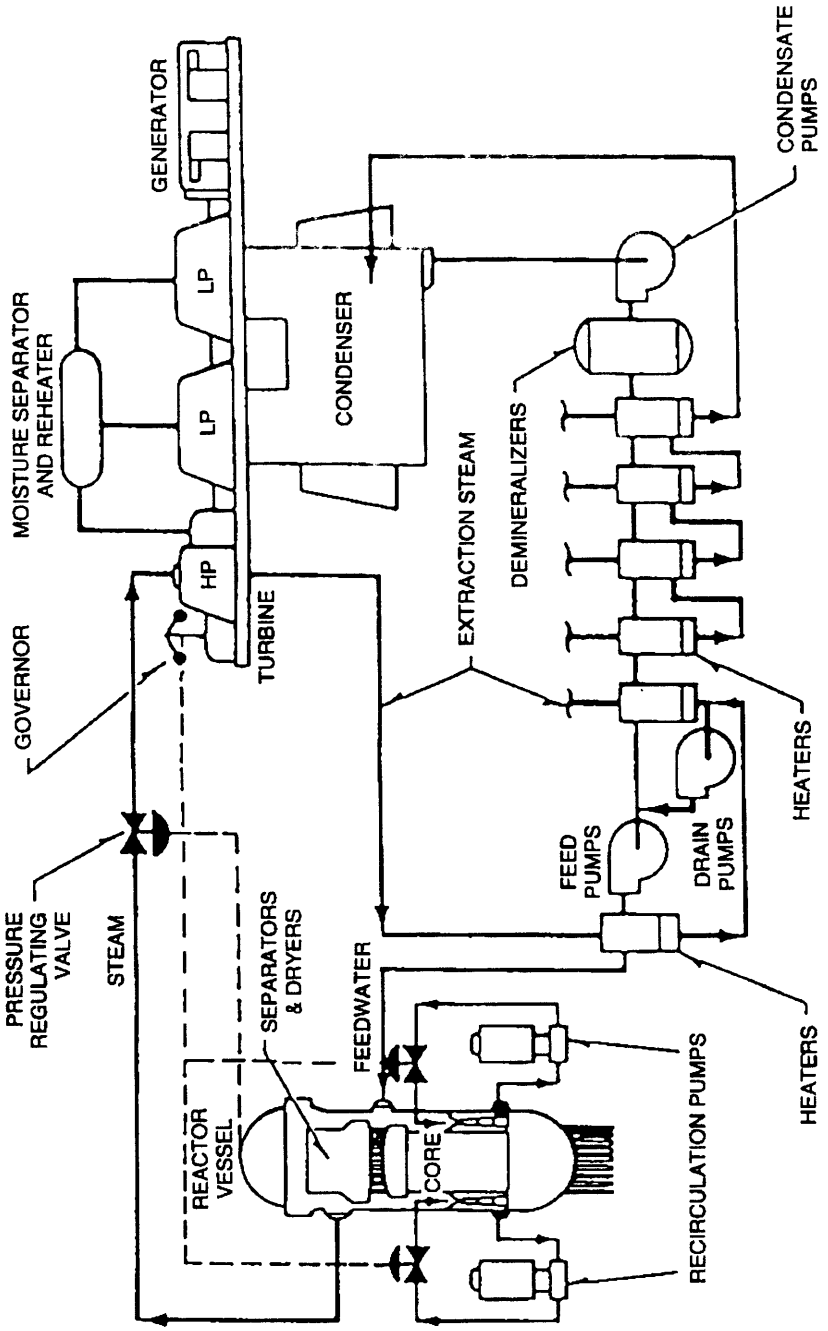

Figure 3-1: Direct cycle reactor system (from [36]).

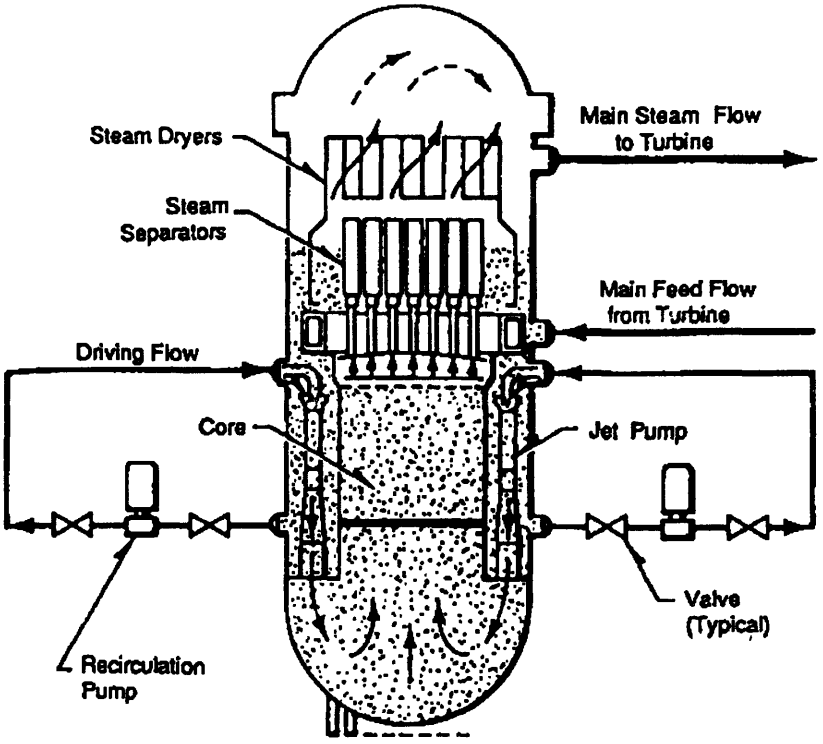

Figure 3-2: Steam and recirculation flow paths (from [37]).

The feedwater flow is sprayed down through the feedwater spargers into the downcomer and mixes with the returning liquid flow from the separators and dryers. Part of this mixed flow of water leaves the reactor vessel to the recirculation system, is pressurized by the recirculation pumps, re-enters the reactor vessel and is injected into the jet pumps with high velocity through the jet pump nozzles. The rest of the mixed flow is sucked into the jet pumps by the low pressure created by the high speed jet stream. The combined flow is discharged into the lower plenum through the jet pump diffusers. This recirculation and jet pump system provides the pressure head for the forced circulation of the coolant through the core. An alternative to the jet pump system for driving core flow is the use of internal recirculation pumps.

The reactor power level is controlled mainly by two systems. The first one is the control rod system. BWRs employ bottom entry control rods. The control rods are used for three purposes:

1. To compensate for the fuel depletion;

2. To adjust the power distribution shape;

3. To provide a large amount of negative reactivity for reactor scram.

The second system that controls the power is the recirculation system. Changes in the recirculation flow affect the flow through the core and the amount of vapor in the core. Because of the negative void reactivity coefficient, the reactor power is changed in the opposite direction as the core vapor content. By changing the recirculation flow, the reactor power can be adjusted fast and uniformly.

The 100% and 80% rod lines shown in Figure 2-5 (page 35) are typical BWR flow control lines. Operation along these forced convection flow control lines can be achieved without control rod movement. Power changes of up to 25% of rated power can be accomplished automatically by the recirculation flow control system [38]. The changes in the recirculation flow are controlled by using either variable-speed recirculation pumps or flow control valves.

3.2 Scope of the Simulation

The main focus of this BWR simulator is to simulate the phenomenon of BWR power oscillations accurately. Thus the scope of the simulation is limited to the portion of a BWR that is related to the processes of power oscillations. The simulator developed here covers the major components inside the reactor vessel, the external recirculation system, and the main steam system including the turbine bypass lines.

The nodalization of this BWR simulator is shown in Figure 3-3. Except for the steam dome node, all the nodes have constant cross sectional areas. The steam dome node represents the vapor space and the water pool outside the steam dryers and separators. The feedwater mixing node is used to model the part of downcomer that contains the feedwater spargers. The upper downcomer node is the part of downcomer below the feedwater mixing node and above the jet pumps. The lower downcomer node covers the jet pumps and the external recirculation lines. Two separate recirculation loop models are used to calculate the pressure difference and

flow rate across the lower downcomer node. Each recirculation loop model consists of one recirculation pump, one flow control valve, and one jet pump. The lower plenum, upper plenum, and the dryer/separator are each represented by one node. The standpipes are included in the dryer/separator node.

The reactor core region is the only region with flexibility in nodalization. The core can be modeled by either a single channel or two parallel channels connected only at plena. The core channels are formed by axial stacks of fuel nodes. The total number of core nodes is limited to 40. Within each fuel node, the radial temperature distribution of the fuel rods and the heat flux to the coolant are calculated by a fuel conduction and convection model. This flexible scheme of modeling the core allows for many simulation choices. The reactor core can be represented by a single channel, or one core channel with one bypass channel, or two core channels with each representing a half of the core.

The main steam lines are modeled by a single string of nodes. Two nodes are used to represent the steam lines inside the containment upstream of the Main Steam Isolation Valves (MSIVs). Four nodes are used for the steam line between the MSIVs and the turbine stop/control valves. The turbine bypass lines are modeled by one node. The safety/relief valves, the MSIVs, the turbine stop/control valves, and the turbine bypass valves are each simulated by one valve.

The boundary points of the simulator are upstream of the feedwater nozzle, and downstream of the safety valve, turbine control valve, and turbine bypass valve. The flow rate of the feedwater is calculated by the feedwater controller. The feedwater enthalpy is specified as an input parameter, and can be varied with time. The pressure at the downstream of the safety valve is fixed at the suppression pool pressure. The pressure at the turbine bypass valve outlet is at the main condenser pressure. The pressure after the turbine control valve is also fixed and is specified as an input parameter.

The BWR simulator developed here is simple when compared to other system codes. However, it is versatile and has enough details for simulations of many operational transient events.

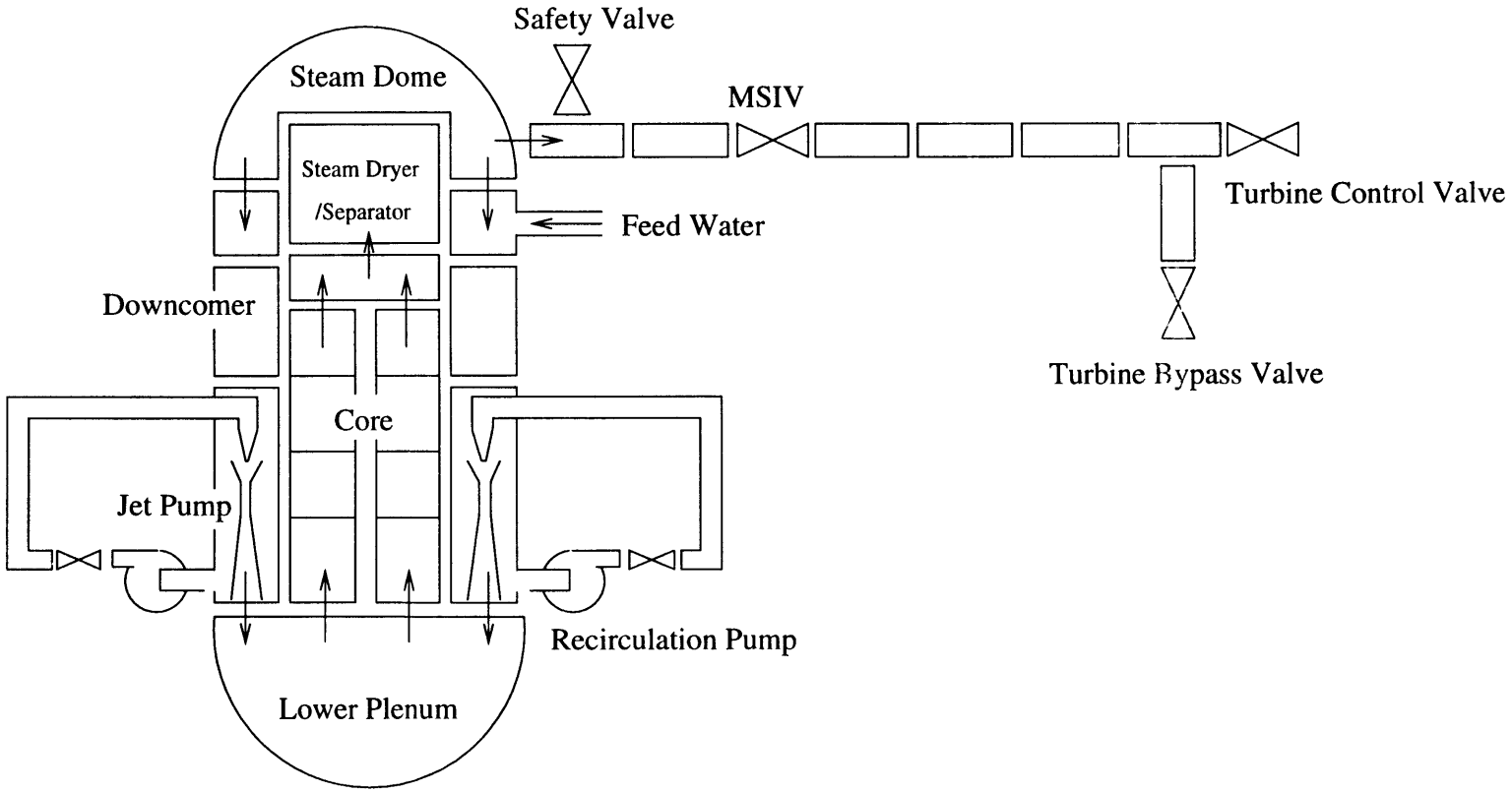

Figure 3-3: Nodalization of the BWR simulator.

3.3 Chapter Summary

Modern BWR power plants use a direct steam cycle consisting of a BWR nuclear reactor and a conventional steam plant. The power level of a BWR is controlled by control rods and the recirculation flow rate. In this research, the major components in the reactor vessel, the recirculation system, and the main steam lines are covered in the BWR simulator. The BWR is modeled by nodes of constant cross sectional area, except for the steam dome node. The core region can be modeled flexibly to accommodate different simulation needs. This BWR simulator is simple, yet it also has enough details to simulate operational transient conditions.

Chapter 4

Development of Models of Physical Processes

The physical processes involved in a BWR include single- and two-phase fluid flows, conductive and convective heat transfer, nuclear fission and decay power generation, and control actions. Because the aim of this research is to develop a fast-running BWR simulator, the physical processes are modeled with simplifications. Nevertheless, these models are capable of simulating BWR power oscillations accurately.

The BWR simulator consists of six main modules:

1. Thermal-hydraulic model;
2. Core neutronics model;
3. Fuel conduction and convection model;
4. Recirculation system and jet pump model;
5. Steam line model;
6. Control system model.

The details of these models are discussed below. The results of validation calculations for individual models are also presented.

4.1 Thermal-Hydraulic Model

Various two-phase flow models have been used to model boiling channels. These models range from three-equation models to two-fluid, six-equation models. The dimension in space also varies from one-dimensional to three-dimensional.

In this study, a one-dimensional three-equation model is used. The reactor vessel is assumed to be at a single pressure. A drift flux model is used to represent the non-homogeneous velocity distribution in vapor and liquid phases. A linear enthalpy profile assumption is adopted. A two-region non-equilibrium model is used for the steam dome. Subcooled boiling is described by a profile-fit model. The momentum integral method is applied.

This thermal-hydraulic model has been used to simulate an Argonne National Laboratory (ANL) two-phase test loop. The stability boundary calculated by this model is in good agreement with the measured stability boundary.

4.1.1 One dimensional conservation equations for mixtures

The one-dimensional conservation equations for mixtures used here are [37, 39]

Mass:

$$\frac{\partial \rho_m}{\partial t} + \frac{\partial}{\partial z}\frac{W}{A} = 0 \; ; \tag{4.1}$$

Energy (neglecting kinetic, compressibility, dissipation, and gravity terms):

$$\frac{\partial}{\partial t}\left(\rho_m h_m - P\right) + \frac{\partial}{\partial z}\frac{W h'}{A} = q''' \; ; \tag{4.2}$$

Momentum:

$$\frac{\partial}{\partial t}\frac{W}{A} + \frac{1}{A}\frac{\partial}{\partial z}\frac{W^2}{\rho' A} = -\frac{\partial P}{\partial z} - \frac{f}{2D_h}\frac{|W|W}{\rho' A^2} - \rho_m g \sin\theta \; ; \tag{4.3}$$

where

ρ_m is the mixture density, $\rho_m = \alpha\rho_v + (1-\alpha)\,\rho_l$,

W is the mass flow rate,

A is the flow area,

h_m is the mixture enthalpy, $h_m = \dfrac{\alpha\rho_v h_v + (1-\alpha)\,\rho_l h_l}{\rho_m}$,

P is the pressure,

h' is the flow enthalpy, $h' = xh_v + (1-x)\,h_l$,

q''' is the volumetric heat addition rate,

ρ' is the dynamic density, $\dfrac{1}{\rho'} = \dfrac{x^2}{\alpha\rho_v} + \dfrac{(1-x)^2}{(1-\alpha)\,\rho_l}$,

f is the friction factor,

D_h is the hydraulic diameter,

g is the acceleration of gravity,

θ is the angle from horizontal to the flow direction,

α is the vapor fraction,

x is the flow quality,

subscript v denotes vapor,

subscript l denotes liquid, and

subscript m denotes mixture.

The space derivative terms in these conservation equations are treated with a nodal (or finite volume) approach [40, 41]. The system is divided into nodes with constant cross-sectional area, and the conservation equations are integrated over the nodes. The mass and energy equations become

$$\frac{dM_i}{dt} = \sum_k W_k \ , \tag{4.4}$$

$$\frac{dE_i}{dt} = q_i + \sum_k W_k h'_k \ , \tag{4.5}$$

where

M_i is the total mass in node i , $M_i = \int_{V_i} \rho_m \, dV$;

E_i is the total energy content in node i , $E_i = \int_{V_i} (\rho_m h_m - P) \, dV$;

V_i is the volume of node i ;

q_i is the heat addition rate in node i ;

the summations are over all flow paths entering or leaving node i , and the flow entering the node has a positive flow rate.

The momentum equation is integrated from the inside of the inlet to the outside of the outlet of each node (see Figure 4-1). The mass flow rate is assumed to vary linearly from the inlet to the outlet.

$$\begin{aligned} & \frac{\ell_i}{A_i}\frac{d\overline{W}_i}{dt} + \frac{1}{A_i^2}\left[\left(\frac{W^2}{\rho'}\right)_i - \left(\frac{W^2}{\rho'}\right)_{i-1}\right] + \frac{1}{2}\left(\frac{W^2}{\rho'}\right)_i \left(\frac{1}{A_{i+1}^2} - \frac{1}{A_i^2}\right) \\ = \; & \Delta P_i - \left(\frac{f\,\ell}{2D_h}\frac{|\overline{W}|\,\overline{W}}{\overline{\rho}A^2}\right)_i - \left(K\frac{|W|\,W}{2\rho' A^2}\right)_i - m_i g \Delta z_i \, , \end{aligned} \tag{4.6}$$

where

$\overline{W}_i$ is the average flow rate in node i , $\overline{W}_i = \dfrac{W_{i-1} + W_i}{2}$;

W_{i-1} is the flow rate from node $i-1$ to node i ;

W_i is the flow rate from node i to node $i+1$;

A is the cross-sectional area;

$\overline{\rho}$ is the appropriate density for frictional pressure drop calculations;

ℓ_i is the length of node i ;

ΔP_i is the pressure drop form the inlet to the outlet of node i ;

K_i is the form loss coefficient; the loss is assumed to occur at the outlet of a node;

m_i is the average density of node i;

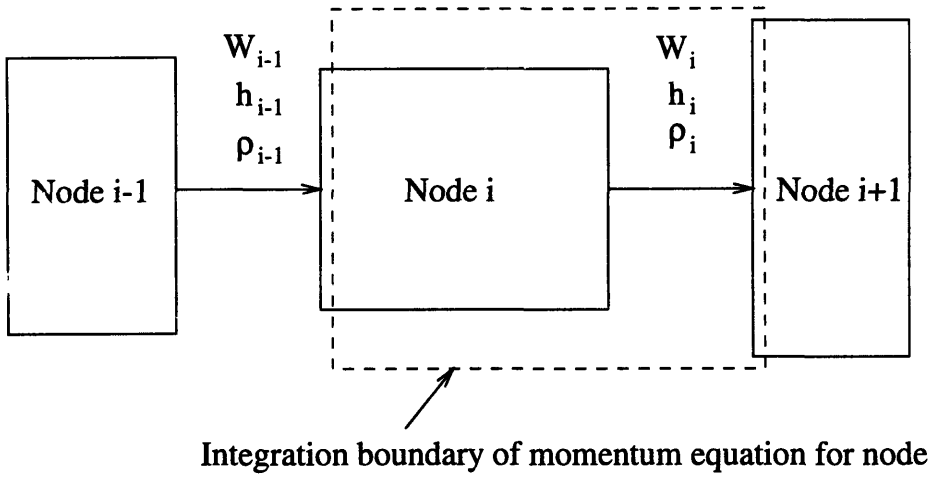

Figure 4-1: Control volume used in the governing equations.

Δz_i is the elevation difference of node i (outlet elevation minus inlet elevation).

The following assumptions are applied in the thermal-hydraulic model:

1. The system is in thermal equilibrium conditions, except for the steam dome node and heating nodes;

2. A single reference pressure is assumed for the reactor vessel. This pressure may vary with time.

4.1.2 Treatment of the mass and energy equations

Normal nodes

The normal nodes are the nodes with a well defined unidirectional flow. In these nodes, the following assumptions are applied:

1. A linear enthalpy profile exists within a node. This assumption eliminates the discontinuity of the derivative of density with respect to the enthalpy across the boiling boundary [42].

2. The local density is a function of the local enthalpy and the reference pressure. The density is assumed to be a linear function of the enthalpy for subcooled liquid, and the inverse of the density is assumed to be a linear function of the enthalpy for two-phase mixtures [41].

From these assumptions, the local density and enthalpy within a node can be expressed as functions of the system pressure, the inlet and outlet mixture enthalpies of the node (see Figure 4-1):

$$h_m(z) = h_m(h_{i-1}, h_i, P, z),$$

and

$$\rho_m(z) = \rho_m(h_m(z)).$$

Define the nodal-averaged density

$$m_i = \frac{\int_{V_i} \rho_m \, dV}{V_i} = \frac{\int_{z_{in}}^{z_{out}} \rho_m(z) \, dz}{\ell_i} = \frac{M_i}{V_i}, \tag{4.7}$$

and the nodal-averaged volumetric enthalpy

$$e_i = \frac{\int_{V_i} \rho_m h_m \, dV}{V_i} = \frac{\int_{z_{in}}^{z_{out}} \rho_m(z) \, h_m(z) \, dz}{\ell_i} = \frac{E_i + PV_i}{V_i}. \tag{4.8}$$

From the assumptions, the expressions for the averaged density and volumetric enthalpy have been derived [40, 41].

For $h_{i-1} < h_i < h_f$,

$$m_i = \frac{\rho_{i-1} + \rho_i}{2},$$

$$e_i = \frac{1}{6}\left[(2h_{i-1} + h_i)\,\rho_{i-1} + (h_{i-1} + 2h_i)\,\rho_i\right].$$

For $h_{i-1} < h_f < h_i$,

$$m_i = \beta \left(\frac{\rho_{i-1} + \rho_f}{2} \right) + (1 - \beta) \frac{\ln (v_i / v_f)}{(v_i - v_f)} ,$$

$$\begin{aligned} e_i &= \frac{\beta}{6} \left[(2h_{i-1} + h_f) \rho_{i-1} + (h_{i-1} + 2h_f) \rho_f \right] \\ &+ (1 - \beta) \left[\left(\frac{h_i - h_f}{v_i - v_f} \right) - \frac{(h_i v_f - h_f v_i) \ln (v_i / v_f)}{(v_i - v_f)^2} \right] , \end{aligned}$$

where

$\beta = \dfrac{h_f - h_{i-1}}{h_i - h_{i-1}}$, and

v is the specific volume.

For $h_f < h_{i-1} < h_i$,

$$m_i = \frac{\ln (v_i / v_{i-1})}{(v_i - v_{i-1})} ,$$

$$e_i = \left(\frac{h_i - h_{i-1}}{v_i - v_{i-1}} \right) - \frac{(h_i v_{i-1} - h_{i-1} v_i) \ln (v_i / v_{i-1})}{(v_i - v_{i-1})^2} .$$

Using Equations 4.7 and 4.8, the mass and energy equations become

$$V_i \frac{dm_i}{dt} = W_{i-1} - W_i , \tag{4.9}$$

and

$$V_i \left(\frac{de_i}{dt} - \frac{dP}{dt} \right) = q_i + W_{i-1} h'_{i-1} - W_i h'_i . \tag{4.10}$$

The time derivatives of m_i and e_i can be expanded in terms of h_{i-1} , h_i , and P :

$$\begin{aligned} \frac{dm_i}{dt} &= \left(\frac{\partial m_i}{\partial h_{i-1}} \right) \frac{dh_{i-1}}{dt} + \left(\frac{\partial m_i}{\partial h_i} \right) \frac{dh_i}{dt} + \left(\frac{\partial m_i}{\partial P} \right) \frac{dP}{dt} ; \\ \frac{de_i}{dt} &= \left(\frac{\partial e_i}{\partial h_{i-1}} \right) \frac{dh_{i-1}}{dt} + \left(\frac{\partial e_i}{\partial h_i} \right) \frac{dh_i}{dt} + \left(\frac{\partial e_i}{\partial P} \right) \frac{dP}{dt} . \end{aligned}$$

Substituting into Equations 4.9 and 4.10, we get

$$V_i \left[\left(\frac{\partial m_i}{\partial h_{i-1}} \right) \frac{dh_{i-1}}{dt} + \left(\frac{\partial m_i}{\partial h_i} \right) \frac{dh_i}{dt} + \left(\frac{\partial m_i}{\partial P} \right) \frac{dP}{dt} \right] = W_{i-1} - W_i , \tag{4.11}$$

and

$$V_i \left\{ \left(\frac{\partial e_i}{\partial h_{i-1}} \right) \frac{dh_{i-1}}{dt} + \left(\frac{\partial e_i}{\partial h_i} \right) \frac{dh_i}{dt} + \left[\left(\frac{\partial e_i}{\partial P} \right) - 1 \right] \frac{dP}{dt} \right\}$$

$$= \; q_i + W_{i-1} h'_{i-1} - W_i h'_i \; .$$

The partial derivatives $\left(\frac{\partial m_i}{\partial h_{i-1}} \right)$, $\left(\frac{\partial m_i}{\partial h_i} \right)$, $\left(\frac{\partial e_i}{\partial h_{i-1}} \right)$, and $\left(\frac{\partial e_i}{\partial h_i} \right)$ can be evaluated analytically. The partial derivatives $\left(\frac{\partial m_i}{\partial P} \right)$ and $\left(\frac{\partial e_i}{\partial P} \right)$ can be evaluated numerically [40, 41].

$$\frac{\partial m_i}{\partial h_{i-1}} = \frac{m_i - \rho_{i-1}}{h_i - h_{i-1}} \; ; \tag{4.12}$$

$$\frac{\partial m_i}{\partial h_i} = \frac{\rho_i - m_i}{h_i - h_{i-1}} \; ; \tag{4.13}$$

$$\frac{\partial e_i}{\partial h_{i-1}} = \frac{e_i - \rho_{i-1} h_{i-1}}{h_i - h_{i-1}} \; ; \tag{4.14}$$

$$\frac{\partial e_i}{\partial h_i} = \frac{\rho_i h_i - e_i}{h_i - h_{i-1}} \; ; \tag{4.15}$$

$$\frac{\partial m_i}{\partial P} = \frac{m\left(h_{i-1} \; , \; h_i\right)\big|_{P+\Delta P} - m\left(h_{i-1} \; , \; h_i\right)\big|_P}{\Delta P} \; ;$$

$$\frac{\partial e_i}{\partial P} = \frac{e\left(h_{i-1} \; , \; h_i\right)\big|_{P+\Delta P} - e\left(h_{i-1} \; , \; h_i\right)\big|_P}{\Delta P} \; .$$

Next, the energy equation is combined with the mass equation:

$$\text{(Energy equation)} - \overline{h}_i \times \text{(Mass equation)} \; ,$$

where

$\overline{h}_i$ is the average nodal enthalpy, $\overline{h}_i = \frac{e_i}{m_i}$.

The resulting equation is

$$
\begin{aligned}
& V_i \left\{ \left[\left(\frac{\partial e_i}{\partial h_{i-1}} \right) - \overline{h}_i \left(\frac{\partial m_i}{\partial h_{i-1}} \right) \right] \frac{dh_{i-1}}{dt} + \left[\left(\frac{\partial e_i}{\partial h_i} \right) - \overline{h}_i \left(\frac{\partial m_i}{\partial h_i} \right) \right] \frac{dh_i}{dt} \right. \\
+ & \left. \left[\left(\frac{\partial e_i}{\partial P} \right) - \overline{h}_i \left(\frac{\partial m_i}{\partial P} \right) - 1 \right] \frac{dP}{dt} \right\} \\
= & \; q_i + W_{i-1} \left(h'_{i-1} - \overline{h}_i \right) - W_i \left(h'_i - \overline{h}_i \right) \; .
\end{aligned}
\tag{4.16}
$$

The advantages of this form are that the equation is independent on the enthalpy reference point, and the error is minimized if the mass equation is not solved precisely [43]. This form of the energy equation is called a "coupled" form.

Strong coupling between nodes is one of the characteristics of this form. Because each equation involves both h_{i-1} and h_i , the disturbance at one node of the system will propagate instantaneously to all other nodes [44]. This numerical diffusion can be eliminated by a "donor-cell" approach. By assuming that

$$
\frac{dh_{i-1}}{dt} \approx \frac{dh_i}{dt} \text{ within node } i,
$$

the energy equation becomes

$$
\begin{aligned}
& V_i \left\{ \left[\left(\frac{\partial e_i}{\partial h_{i-1}} \right) - \overline{h}_i \left(\frac{\partial m_i}{\partial h_{i-1}} \right) + \left(\frac{\partial e_i}{\partial h_i} \right) - \overline{h}_i \left(\frac{\partial m_i}{\partial h_i} \right) \right] \frac{dh_i}{dt} \right. \\
+ & \left. \left[\left(\frac{\partial e_i}{\partial P} \right) - \overline{h}_i \left(\frac{\partial m_i}{\partial P} \right) - 1 \right] \frac{dP}{dt} \right\} \\
= & \; q_i + W_{i-1} \left(h'_{i-1} - \overline{h}_i \right) - W_i \left(h'_i - \overline{h}_i \right) \; .
\end{aligned}
\tag{4.17}
$$

this donor-cell form of the energy equation is called a "decoupled" form.

Although the donor-cell approach reduces numerical diffusion, it also introduces numerical dissipation. This numerical dissipation may mask the oscillatory behavior of the system. The differences of using the coupled form versus decoupled form in stability calculations have been studied with nuclear and non-nuclear experiments, as described in Sections 4.1.6 and 7.3.1. The results show that for nuclear-coupled oscil-

lations, the coupled form predictions are more unstable than the test results while the decoupled form predictions are close to the test results. For pure thermal-hydraulic oscillations without nuclear feedback, however, both forms give similar results which are close to the measurements. Thus the decoupled form was selected to be used in the BWR simulator.

Mixing nodes

Mixing nodes are the nodes that have more then one inlet or outlet flows, or the nodes for which the inlet and outlet flows are in different directions. The feedwater node, upper and lower plena, and the nodes of flow reversal are mixing nodes. In these nodes, the fluid is assumed to mix completely and instantaneously [41]. So,

$$m_i = \rho_{out} \ ,$$

$$e_i = \rho_{out} h_{out} \ , \text{ and}$$

$$\overline{h}_i = h_{out} \ .$$

The mass and energy equations become

$$V_i \left[\left(\frac{\partial m_i}{\partial \overline{h}_i} \right) \frac{d\overline{h}_i}{dt} + \left(\frac{\partial m_i}{\partial P} \right) \frac{dP}{dt} \right] = \sum W_{in} - \sum W_{out} \ , \tag{4.18}$$

and

$$\begin{aligned} & V_i \left\{ \left[\left(\frac{\partial e_i}{\partial \overline{h}_i} \right) - \overline{h}_i \left(\frac{\partial m_i}{\partial \overline{h}_i} \right) \right] \frac{d\overline{h}_i}{dt} + \left[\left(\frac{\partial e_i}{\partial P} \right) - \overline{h}_i \left(\frac{\partial m_i}{\partial P} \right) - 1 \right] \frac{dP}{dt} \right\} \\ = \ & q_i + \sum W_{in} \left(h'_{in} - \overline{h}_i \right) - \sum W_{out} \left(h'_{out} - \overline{h}_i \right) \ . \end{aligned} \tag{4.19}$$

The partial derivatives are evaluated using the thermodynamic relations of water

and steam.

$$\frac{\partial m_i}{\partial \overline{h}_i} = \begin{cases} \left.\dfrac{\partial \rho}{\partial h}\right|_{\overline{h}_i} & \text{for } \overline{h}_i \le h_f \text{ or } h_g \le \overline{h}_i \ , \\ \dfrac{(v_f - v_g)(h_g - h_f)}{\left[\left(\overline{h}_i (v_g - v_f) + v_f h_g - v_g h_f\right)\right]^2} & \text{for } h_f < \overline{h}_i < h_g \ ; \end{cases}$$

$$\frac{\partial m_i}{\partial P} = \frac{\rho\left(\overline{h}_i\right)\Big|_{P+\Delta P} - \rho\left(\overline{h}_i\right)\Big|_P}{\Delta P} \ ;$$

$$\frac{\partial e_i}{\partial \overline{h}_i} = \overline{h}_i \frac{\partial m_i}{\partial \overline{h}_i} + m_i \ ;$$

$$\frac{\partial e_i}{\partial P} = \overline{h}_i \frac{\partial m_i}{\partial P} \ .$$

Here $\overline{h}_i$ and P are assumed to be independent.

4.1.3 Steam dome model

The steam dome node is treated by a two-region thermally non-equilibrium model (see Figure 4-2) [37, 41]. The steam flow from the steam separator node enters the vapor region. The steam then exits the vapor region and goes to the steam line system. The liquid flow from the separator node enters the feedwater mixing node. The separation of steam and water is assumed to occur at the outlet of the separator node. The liquid carry-over by the steam flow is considered to be negligible, and the steam entering the vapor region is saturated steam. The vapor carry-under by the liquid flow is included by a carry-under fraction which is a function of the steam dome water level. The liquid region of the steam dome is connected to the feedwater node by a liquid surge flow.

Three interactions between the vapor and liquid regions are simulated in this model. They are: flashing, rain-out, and wall condensation. The assumptions used in the steam dome model are the followings:

1. Meta-stable conditions, i.e., superheated liquid or subcooled vapor, are prohibited, and result in flashing or rain out.

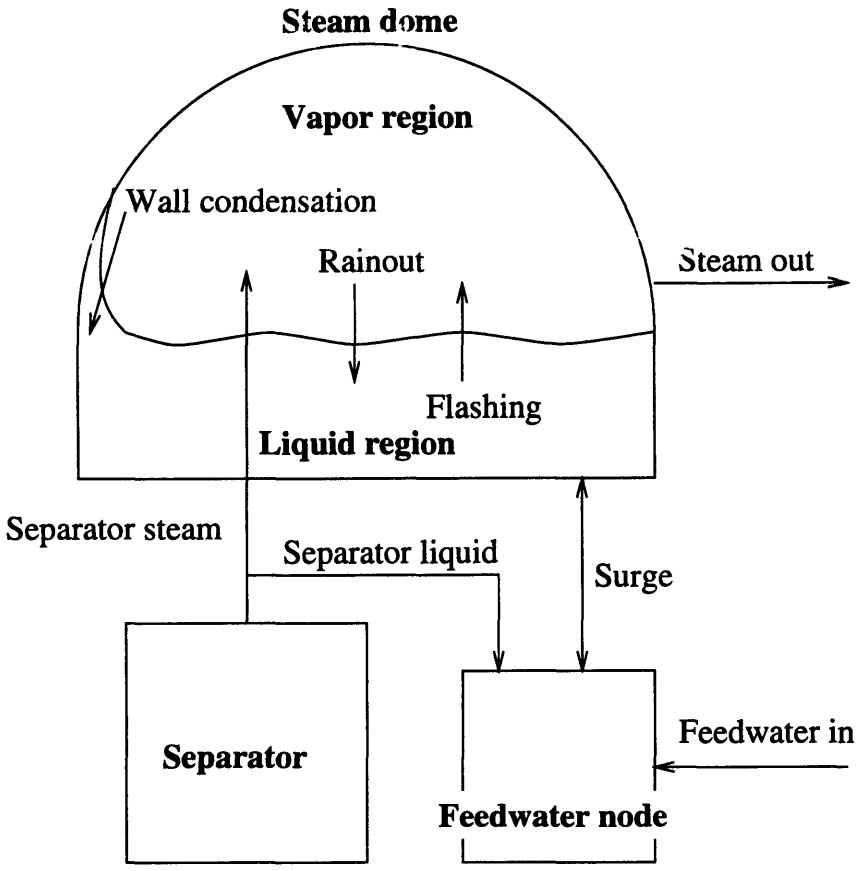

Figure 4-2: Schematic of the steam dome model.

2. The rain-out and condensed liquid, and vapor from flashing are at saturation conditions.

3. The total heat transfer coefficient of the steam dome wall is constant. This heat transfer coefficient is an input parameter supplied by the user.

4. The temperature of the steam dome wall is constant. This temperature is set as the initial saturation temperature. The heat capacity of the steam dome wall is assumed to be infinitive.

5. Heat transfer from the vapor region to the steam dome wall is permitted if conditions are appropriate. The heat transfer from the steam dome wall to the vapor region is prohibited.

Performing mass and energy balances to the vapor and liquid regions, we have:

vapor mass balance

$$\frac{d}{dt}\left(\rho_v V_v\right) = W_{sep,v} + W_{fl} - W_s - W_{ro} - W_{wc} \ ;$$

liquid mass balance

$$\frac{d}{dt}\left(\rho_l V_l\right) = W_{ro} + W_{wc} - W_{fl} - W_{su} \ ;$$

vapor energy balance

$$\frac{d}{dt}\left[V_v\left(\rho_v h_v - P\right)\right] = W_{sep,v} h_g + W_{fl} h_g - W_s h_v - W_{ro} h_f - W_{wc} h_v \ ;$$

liquid energy balance

$$\frac{d}{dt}\left[V_l\left(\rho_l h_l - P\right)\right] = W_{ro} h_f + W_{wc} h_f - W_{fl} h_g - W_{su} h_{su} \ ;$$

where the subscript v denotes vapor region, l denotes liquid region, sep, v denotes outflow of steam from the separator node to the steam dome vapor

region, fl denotes flashing, s denotes main steam, ro denotes rain-out, wc denotes wall condensation, and su denotes surge flow between the liquid region and the feedwater node.

The surge flow is positive when flowing out of the steam dome.

Expanding the time derivative terms, we get

$$\frac{d}{dt}(\rho_v V_v) = V_v\left[\left(\frac{\partial \rho_v}{\partial h_v}\right)\frac{dh_v}{dt} + \left(\frac{\partial \rho_v}{\partial P}\right)\frac{dP}{dt}\right] + \rho_v \frac{dV_v}{dt} ,$$

$$\frac{d}{dt}(\rho_l V_l) = V_l\left[\left(\frac{\partial \rho_l}{\partial h_l}\right)\frac{dh_l}{dt} + \left(\frac{\partial \rho_l}{\partial P}\right)\frac{dP}{dt}\right] - \rho_l \frac{dV_v}{dt} ,$$

$$\frac{d}{dt}\left[V_v\left(\rho_v h_v - P\right)\right] = V_v\left[h_v\left(\frac{\partial \rho_v}{\partial h_v}\right) + \rho_v\right]\frac{dh_v}{dt} + V_v h_v\left(\frac{\partial \rho_v}{\partial P}\right)\frac{dP}{dt} + \rho_v h_v \frac{dV_v}{dt} ,$$

and

$$\frac{d}{dt}\left[V_l\left(\rho_l h_l - P\right)\right] = V_l\left[h_l\left(\frac{\partial \rho_l}{\partial h_l}\right) + \rho_l\right]\frac{dh_l}{dt} + V_l h_l\left(\frac{\partial \rho_l}{\partial P}\right)\frac{dP}{dt} - \rho_l h_l \frac{dV_v}{dt} .$$

Notice that the total steam dome volume ($V_{SD} = V_v + V_l$) is constant.

Define the average steam dome enthalpy

$$\overline{h}_{SD} = \frac{V_v \rho_v h_v + V_l \rho_l h_l}{V_v \rho_v + V_l \rho_l} .$$

Substituting the time derivative terms and combining the mass and energy equations, we get:

vapor mass

$$V_v\left[\left(\frac{\partial \rho_v}{\partial h_v}\right)\frac{dh_v}{dt} + \left(\frac{\partial \rho_v}{\partial P}\right)\frac{dP}{dt}\right] + \rho_v \frac{dV_v}{dt} = W_{sep,v} + W_{fl} - W_s - W_{ro} - W_{wc} ;$$

liquid mass

$$V_l\left[\left(\frac{\partial \rho_l}{\partial h_l}\right)\frac{dh_l}{dt} + \left(\frac{\partial \rho_l}{\partial P}\right)\frac{dP}{dt}\right] - \rho_l \frac{dV_v}{dt} = W_{ro} + W_{wc} - W_{fl} - W_{su} ;$$

vapor energy

$$
\begin{aligned}
& V_v \left[\rho_v + \left(h_v - \overline{h}_{SD} \right) \left(\frac{\partial \rho_v}{\partial h_v} \right) \right] \frac{dh_v}{dt} + V_v \left[\left(h_v - \overline{h}_{SD} \right) \left(\frac{\partial \rho_v}{\partial P} \right) - 1 \right] \frac{dP}{dt} \\
+ \quad & \rho_v \left(h_v - \overline{h}_{SD} \right) \frac{dV_v}{dt} \\
= \quad & \left(h_g - \overline{h}_{SD} \right) \left(W_{sep,v} + W_{fl} \right) - \left(h_v - \overline{h}_{SD} \right) \left(W_s + W_{wc} \right) - \left(h_f - \overline{h}_{SD} \right) W_{ro} \ ;
\end{aligned}
$$

liquid energy

$$
\begin{aligned}
& V_l \left[\rho_l + \left(h_l - \overline{h}_{SD} \right) \left(\frac{\partial \rho_l}{\partial h_l} \right) \right] \frac{dh_l}{dt} + V_l \left[\left(h_l - \overline{h}_{SD} \right) \left(\frac{\partial \rho_l}{\partial P} \right) - 1 \right] \frac{dP}{dt} \\
- \quad & \rho_l \left(h_l - \overline{h}_{SD} \right) \frac{dV_v}{dt} \\
= \quad & \left(h_f - \overline{h}_{SD} \right) \left(W_{ro} + W_{wc} \right) - \left(h_g - \overline{h}_{SD} \right) W_{fl} - \left(h_{su} - \overline{h}_{SD} \right) W_{su} \ ;
\end{aligned}
$$

The steam flow rate from the separator node to the vapor region is

$$W_{sep,v} = \left(\frac{x_{sep} - cu}{1 - cu} \right) W_{sep} \ ,$$

and the total flow rate (liquid plus vapor) from the separator to the feedwater node is

$$W_{sep,l} = \left(\frac{1 - x_{sep}}{1 - cu} \right) W_{sep} \ ,$$

where

W_{sep} is the total outlet flow rate of the separator node,

x_{sep} is the flow quality at the separator outlet, and

cu is the vapor carry-under mass fraction, and is the steam quality of the flow from the separator to the feedwater node.

The surge flow between the liquid region and the feedwater node is defined to be positive when the flow is out from the liquid region. The enthalpy of the surge flow

depends on the flow direction:

$$h_{su} = \begin{cases} h_l & \text{if } W_{su} \geq 0 \ , \\ \overline{h}_{\text{FW node}} & \text{if } W_{su} < 0 \ . \end{cases}$$

The difference between the energy carry out of the vapor region and carry in to the liquid region by the wall condensation flow is the heat transfer to the steam dome wall. The heat transfer rate to the wall is

$$Q_{wall} = (UA)_{wc} (T_v - T_{wall}) = W_{wc} (h_v - h_f) \ ,$$

where

$(UA)_{wc}$ is the total heat transfer coefficient to the wall, $(UA)_{wc} = 0$ when $T_v < T_{wall}$,

T_v is the vapor temperature, and

T_{wall} is the steam dome wall temperature.

Thus the wall condensation flow rate is

$$W_{wc} = \frac{(UA)_{wc} (T_v - T_{wall})}{h_v - h_f} \ .$$

The surge flow rate W_{su} and the main steam flow rate W_s are boundary conditions of the steam dome model.

Now we have four mass and energy equations. The unknowns are h_v, h_l, P, V_v, W_{ro}, and W_{fl}. Two additional relations are needed to solve the equations. These relations are from the requirement that no meta-stable state exists. This requirement limits the vapor enthalpy to be no less than the saturation steam enthalpy. If the calculated vapor enthalpy is less than the saturated enthalpy, then rain-out must occurs to bring the vapor enthalpy up to the saturation value. Similarly, the liquid enthalpy can not be greater than the saturated water enthalpy. If it does, the liquid

Table 4.1: Additional relations for the steam dome model [41]

	Conditions	Additional relations	Unknowns
Case 1	$h_v \geq h_g$ $h_l \leq h_f$	$W_{ro} = 0$ $W_{fl} = 0$	h_v, h_l, P, V_v
Case 2	$h_v < h_g$ $h_l \leq h_f$	$h_v = h_g$ $W_{fl} = 0$	W_{ro}, h_l, P, V_v
Case 3	$h_v \geq h_g$ $h_l > h_f$	$W_{ro} = 0$ $h_l = h_f$	h_v, W_{fl}, P, V_v
Case 4	$h_v < h_g$ $h_l > h_f$	$h_v = h_g$ $h_l = h_f$	W_{ro}, W_{fl}, P, V_v

will flash and bring the liquid enthalpy down. If both constraints are not violated, then there will be no rain-out and flashing flows. Table 4.1 summarizes the additional relations for different combinations of vapor and liquid conditions [41].

4.1.4 Subcooled boiling model

For a heated node, subcooled boiling is a possible occurrence. A profile-fit model is used to calculate the flow quality under subcooled boiling conditions [36, 45]. Because the underlying assumption of a profile-fit subcooled boiling model is that the flow is predominantly in one direction, only the normal nodes are considered for subcooled boiling (see Section 4.1.2 for the definition of normal nodes).

The first step in the subcooled model calculation is to determine the point of onset of significant voiding (OSV). This point is also called the point of net vapor generation (NVG) or vapor departure. The correlation by Saha and Zuber is used to

calculate the liquid enthalpy at OSV [36, 37]:

$$h_d = \begin{cases} h_f - \dfrac{154\,q''}{G} & \text{for } Pe > 70000\ , \\ h_f - \dfrac{0.0022\,q''D_h\,c_{pf}}{k_f} & \text{for } Pe \leq 70000\ , \end{cases} \tag{4.20}$$

where

h_d is the liquid enthalpy at OSV,

Pe is the Peclet number, $Pe = \dfrac{GD_h\,c_{pf}}{k_f}$,

q'' is the heat flux, q'' is assumed to be uniformly distributed in a node,

G is the mass flux of the coolant,

c_{pf} is the constant pressure specific heat of the saturated water,

k_f is the thermal conductivity of the saturated water.

Because a linear enthalpy profile is assumed to exist in a normal node, the position of OSV can be calculated from the inlet, outlet, and OSV enthalpies. The flow quality before OSV is assumed to be zero. After OSV, the flow quality changes according to an exponential profile [45]:

$$x = \frac{x_e - x_d \exp\left(x_e/x_d - 1\right)}{1 - x_d \exp\left(x_e/x_d - 1\right)} \tag{4.21}$$

where

x_e is the equilibrium quality (thermodynamic quality), $x_e = \dfrac{h' - h_f}{h_{fg}}$, and

x_d is the equilibrium quality at OSV, $x_d = \dfrac{h_d - h_f}{h_{fg}}$.

The flow quality and the equilibrium quality coincide when the flow goes from the subcooled boiling regime to the saturated boiling regime. Because the exponential terms in Equation 4.21 will not actually equal zero, an arbitrarily selected point is set for the transition to the saturated boiling regime [45]:

$$x = x_e \text{ if } x_e \geq 3.36\,|x_d| \ .$$

4.1.5 Momentum Integral Model

Because of the single pressure assumption, the momentum equation must be solved in an integral sense [46]. The momentum equation is integrated around the flow paths in the reactor vessel. The integration path starts at the feedwater node, down through the upper and lower downcomer nodes to the lower plenum, up through the core, the upper plenum, the separator node, and follows the liquid flow path from the separator back to the feedwater node.

The momentum equations of each node, Equation 4.6, are summed to obtain the integral momentum equation for flow within the reactor vessel:

$$\begin{aligned} &\sum_i \frac{\ell_i}{A_i}\frac{d\overline{W}_i}{dt} \\ &= P_{jet} - \sum_i \left[\frac{1}{2}\left(\frac{W^2}{\rho'}\right)_i \left(\frac{1}{A_{i-1}^2} - \frac{1}{A_i^2}\right) + \left(\frac{f\,\ell}{2D_h}\frac{|\overline{W}|\,\overline{W}}{\overline{\rho}A^2}\right)_i + \left(K\frac{|W|\,W}{2\rho' A^2}\right)_i + m_i g \Delta z_i\right] ; \end{aligned}$$

or

$$\begin{aligned} &\sum_i \frac{1}{2}\left(\frac{\ell_i}{A_i} + \frac{\ell_{i+1}}{A_{i+1}}\right)\frac{dW_i}{dt} \\ &= P_{jet} - \sum_i \left[\frac{1}{2}\left(\frac{W^2}{\rho'}\right)_i \left(\frac{1}{A_{i-1}^2} - \frac{1}{A_i^2}\right)\right. \\ &+ \left.\left(\frac{f\,\ell}{8D_h}\right)_i \frac{|W_{i-1}+W_i|\,(W_{i-1}+W_i)}{\overline{\rho}_i A_i^2} + \left(K\frac{|W|\,W}{2\rho' A^2}\right)_i + m_i g \Delta z_i\right] ; \end{aligned} \tag{4.22}$$

where

P_{jet} is the pressure gain from the jet pump operations.

The effects of spiral paths in the cyclone steam separators are represented by a form loss coefficient, and a flow inertia which is a function of the separator outlet flow quality [47]. The gravity head of the liquid in the steam dome is also included.

4.1.6 Model validation–ANL test loop stability calculations

To demonstrate that the thermal-hydraulic model discussed above can accurately simulate boiling channel flow oscillations, the model is used to study the stability of a natural circulation test loop. The test loop being modeled was operated at the Argonne National Laboratory (ANL) [48]. The geometry of the test loop is shown in Figure 4-3. Various steady-state operating data were recorded. The heater power at the inception of flow oscillations was recorded for several operating pressures. The calculation results are compared to these data.

The ANL natural circulation test loop is modeled by a set of nodes with constant flow area as shown in Figure 4-4. The heater can be modeled by different number of nodes. The number and size of other nodes are fixed.

The loop is assumed to be in thermal equilibrium conditions. Subcooled boiling is not considered. All of the flow from the riser goes into the steam dome. Perfect steam-water separation is assumed to occur in the steam dome. The state variable for the steam dome is the vapor volume V_v . Thus,

$$\begin{aligned} m_{SD} &= \frac{[(\rho_g - \rho_f) V_v + \rho_f V_{SD}]}{V_{SD}} \text{ , and} \\ e_{SD} &= \frac{[(\rho_g h_g - \rho_f h_f) V_v + \rho_f h_f V_{SD}]}{V_{SD}} . \end{aligned}$$

The mass and energy equations for the steam dome become

$$V_{SD} \left[\left(\frac{\partial m_{SD}}{\partial V_v} \right) \frac{dV_v}{dt} + \left(\frac{\partial m_{SD}}{\partial P} \right) \frac{dP}{dt} \right] = W_{riser} - W_{SD} - W_s \text{ ,}$$

and

$$\begin{aligned} & V_{SD} \left\{ \left[\left(\frac{\partial e_{SD}}{\partial V_v} \right) - \overline{h}_{SD} \left(\frac{\partial m_{SD}}{\partial V_v} \right) \right] \frac{dV_v}{dt} + \left[\left(\frac{\partial e_{SD}}{\partial P} \right) - \overline{h}_{SD} \left(\frac{\partial m_{SD}}{\partial P} \right) - 1 \right] \frac{dP}{dt} \right\} \\ = \; & W_{riser} \left(h'_{riser} - \overline{h}_{SD} \right) - W_{SD} \left(h_f - \overline{h}_{SD} \right) - W_s \left(h_g - \overline{h}_{SD} \right) . \end{aligned}$$

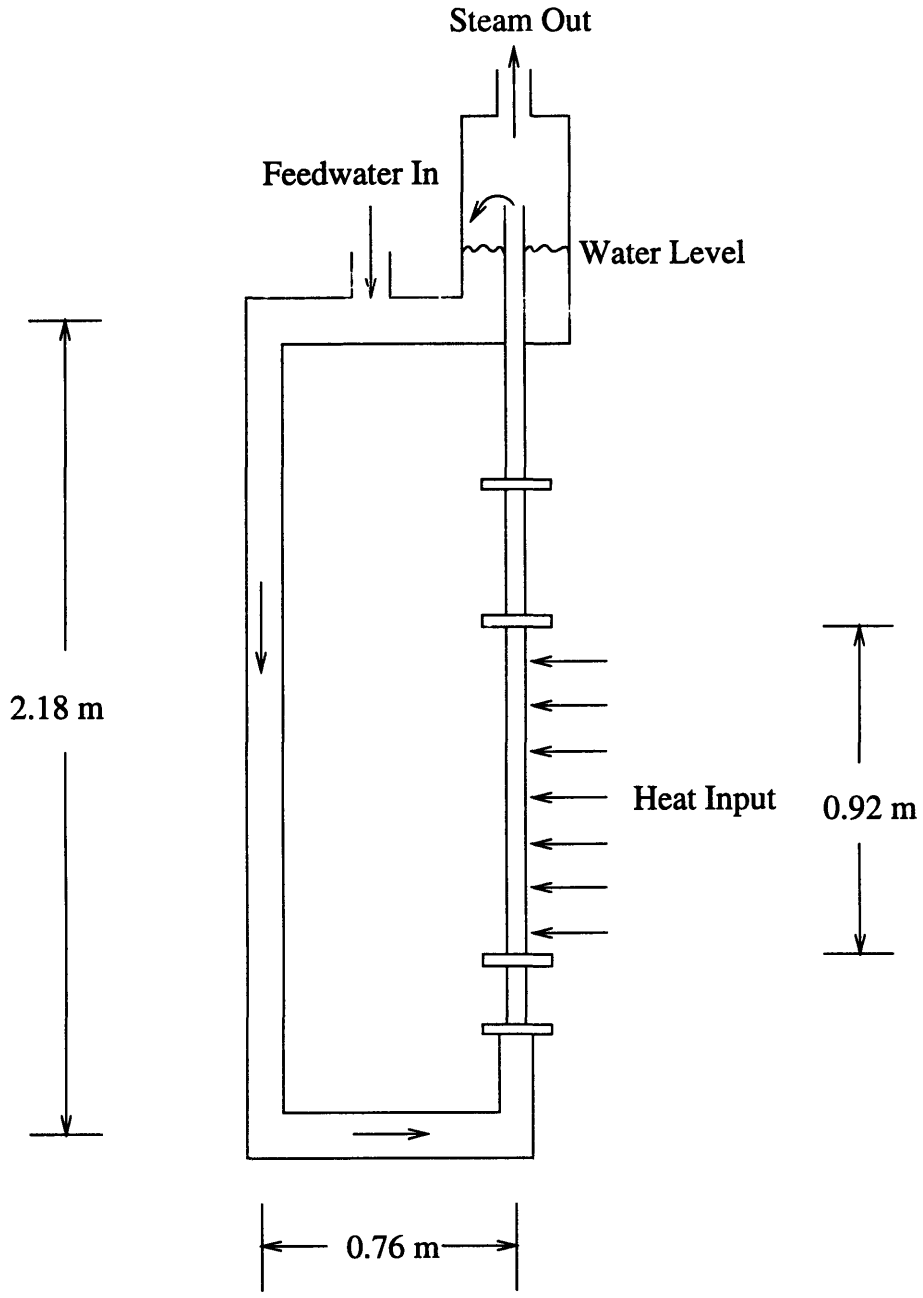

Figure 4-3: Schematic of the ANL natural circulation test loop.

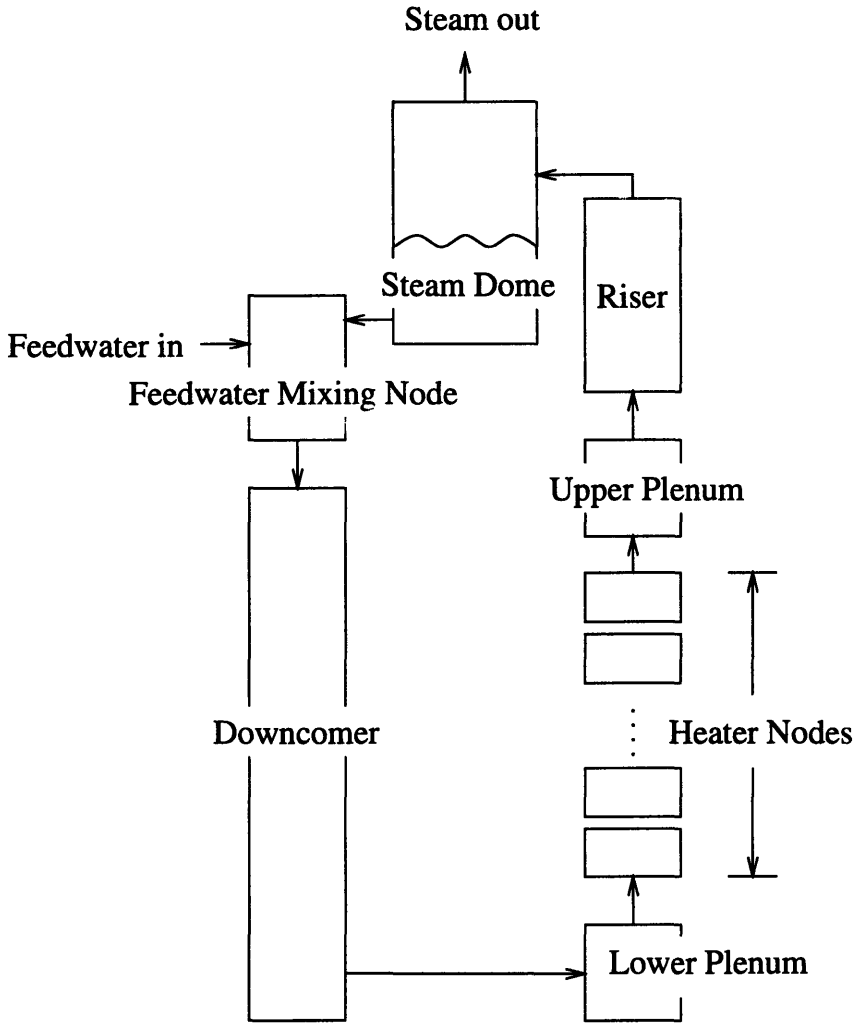

Figure 4-4: Nodalization of the ANL test loop.

Solution methods

The heater power is an input parameter and can be time dependent. A uniform heater power distribution is used for all calculations. The initial feedwater and steam flow rates are the same, and are calculated from a steady-state heat balance. During transient calculations, simple proportional plus integral (PI) controllers are used to maintain the pressure and water level at their set points. These controllers determine the steam and feedwater flow rates.

The steady-state natural circulation flow is calculated from the integral momentum equation by iterations. The temporal acceleration terms are dropped for steady-state calculations. The external pressure source term is zero for this natural circulation loop.

Because of the single pressure assumption, the energy and momentum equations are decoupled. The calculation of a transient step is performed in three sequential steps [41, 46]. The first step solves the energy equation for each node and the overall mass equation. The overall mass equation is the sum of mass equations of all the nodes. The second step solves the integral momentum equation and the mass equation for each node except for the steam dome node. The last step calculates the new vapor volume in the steam dome by an overall mass balance. The time derivatives in the equations are approximated by semi-implicit finite differencing. The resulting linear equation systems are solved using the Gaussian elimination and backward substitution.

Stability calculations

The stability of the system is determined by a direct simulation in the time domain. A disturbance of heater power is imposed on the system, and the time response of the heater flow rate is used to estimate the dominant eigenvalue of the system (the one with the largest real part). The stability of a system is determined by this dominant eigenvalue. If the real part of this dominant eigenvalue is greater than zero, then the system is unstable. On the stability boundary of the system, the real part of the

dominant eigenvalue is zero. If the dominant eigenvalue is a complex number, then the system exhibits an oscillatory behavior. The imaginary part of the dominant eigenvalue determines the system oscillation period.

Figure 4-5 shows the time response of a system parameter. Assuming that the oscillations are sinusoidal with varying amplitude, and all oscillation modes except for the dominant mode have died out, the time response can be described by

$$Y(t) = Y_a + Y_b \exp(\lambda_{real} t) \sin\left(\frac{2\pi}{T} t\right) ,$$

where

λ_{real} is the real part of the dominant eigenvalue,

T is the oscillation period, and

Y_a and Y_b are constants.

The real part of the dominant eigenvalue can be estimated from the peak and valley values of the time response:

$$\lambda_{real} \cong \frac{2}{T} \ln\left(\frac{Y_2 - Y_{\min}}{Y_1 - Y_{\min}}\right) ,$$

where

Y_1 and Y_2 are values at two adjacent peaks, and

$Y_{\min}$ is the value of valley between these two peaks.

The oscillation period T is the time separation between the two peaks.

Results and discussions

Steady-state flow rate The steady-state natural circulation flow rates of the test loop at various operating pressure and power combinations are calculated. These flow rates are sensitive to the water level in the steam dome because it affects the driving head of the natural circulation flow. Because the actual water levels in the tests are

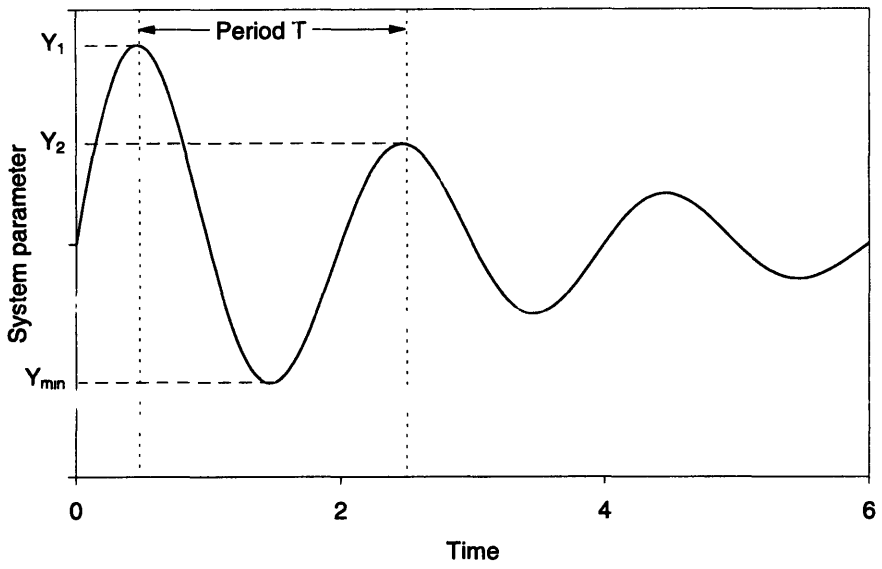

Figure 4-5: Time response of a system parameter.

not available, Pulick and Margolis have used a water level of 1.5 ft. in their study, for the calculated flow rates best fitted the measured data [48]. This water level is also used in the current work, and the sensitivity of flow rate to water level is studied.

Figures 4-6, 4-7, and 4-8 show the comparisons between measured and calculated natural circulation flow rates at three operating pressures. For the calculations with a water level of 1.5 ft., the average error is 5%, and the maximum error is 12.9%. For a water level of 1.28 ft., the average error is 3.3%, and the maximum error is 8.7%. From these results we can see that a change of 67 mm in water level gives flow rate differences of about 5 to 8%. These results also show that the model predicts the natural circulation flow rate accurately. The water level of 1.5 ft. is used in the stability calculations for the consistency with the work by Pulick and Margolis.

Stability analysis As mentioned in section 4.1.2, the treatment of space derivatives in normal nodes as in the coupled form may result in excess numerical diffusions, and a donor-cell technique as used in the decoupled form can eliminate this problem, but it may also introduce numerical dissipation. In this study, both coupled and decoupled forms are used to predict the stability boundary of the test loop. The

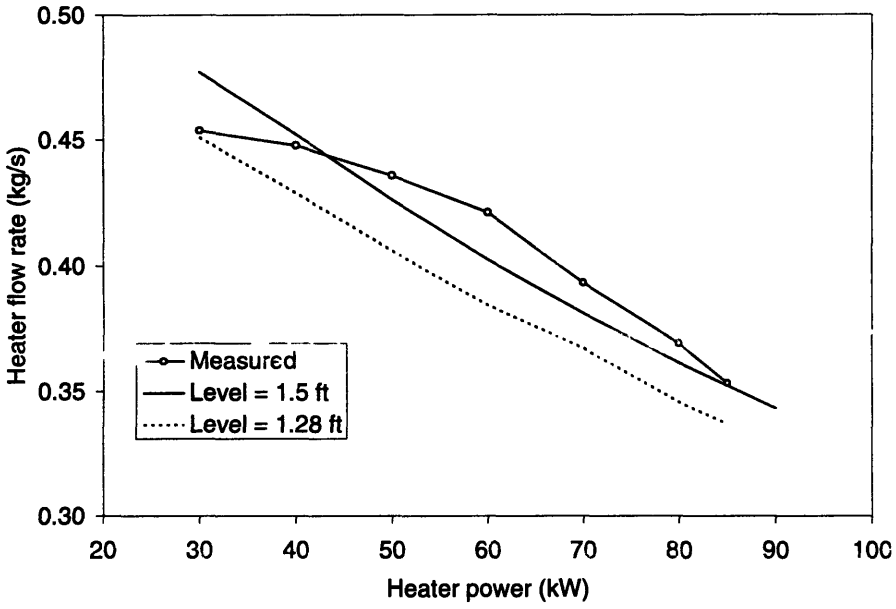

Figure 4-6: Steady-state natural circulation flow rates at 300 psig.

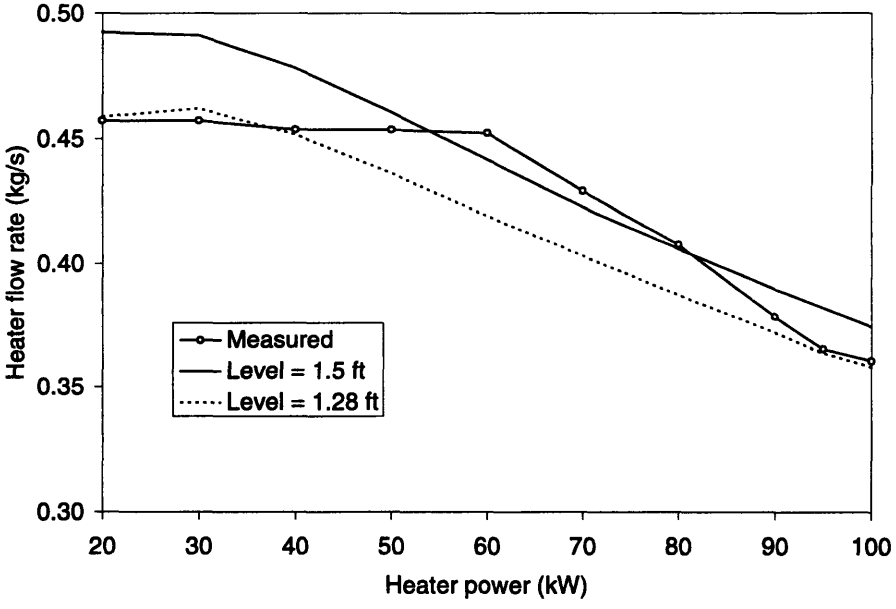

Figure 4-7: Steady-state natural circulation flow rates at 400 psig.

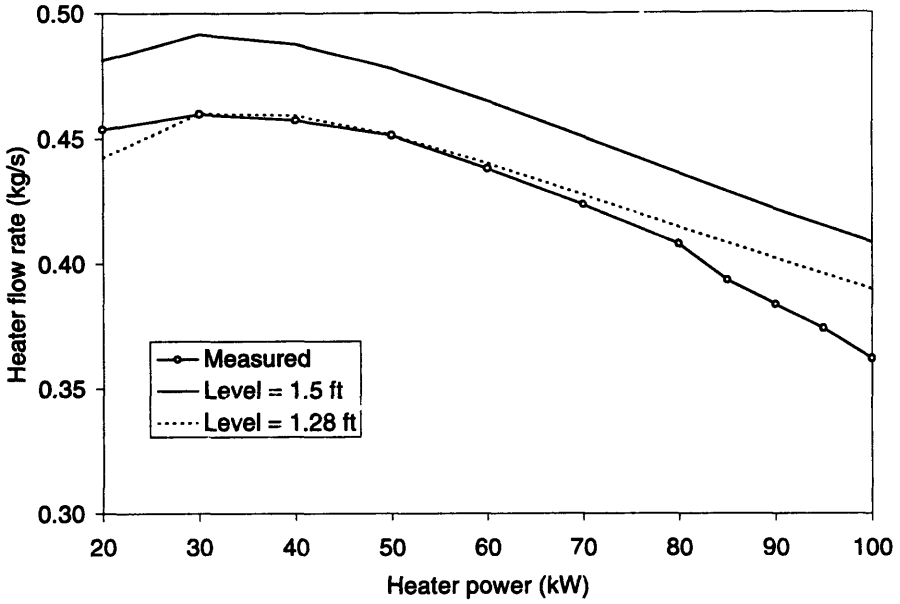

Figure 4-8: Steady-state natural circulation flow rates at 500 psig.

system is perturbed by a step change in heater power, and the dominant eigenvalue is calculated from the response of the heater flow rate.

The calculated eigenvalues are sensitive to the time step size and node size used in the calculation. Because both time and space derivatives are treated by first-order finite differencing, the truncation error associated with the numerical integration is in the order of the time step size (Δt) and node size (Δx). If the ratio $\frac{\Delta t}{\Delta x}$ is held constant, and Δx is reduced to zero, then the truncation error approaches zero, and the calculated eigenvalue will approach the true system eigenvalue. Thus the asymptotic eigenvalue obtained by extrapolating a series of calculated eigenvalues with the same $\frac{\Delta t}{\Delta x}$ ratio and successively larger number of nodes is a good estimation to the true system eigenvalue [42]. The combination of time step and node sizes that gives an eigenvalue similar to the asymptotic eigenvalue is then appropriate for stability calculations.

This procedure has been carried out using both forms of the energy equation, and the results are shown in Figures 4-9 and 4-10. In the plot of oscillation period in Figure 4-9, some of the data points of Dt/Dx =0.11, 0.055, and 0.0066 are overlapped.

So it may be hard to distinguish them. This is also the case for the plot of oscillation period in Figure 4-10. Notice that for the same number of heater nodes and same Δt , the results of decoupled form are more stable than that of coupled form. For fixed number of heater nodes, the effect of reducing Δt is larger for calculations using the coupled form than the decoupled one. Also, for the decoupled form, the effect of reducing Δx is larger than the effect of reducing Δt .

The combination of the time step size of 0.0012 second and the heater node size of 0.184 m (5 nodes in the heater section) gives the correct system eigenvalue for calculations using the coupled form. For the decoupled form, the calculation using the time step size of 0.0025 second and the heater node size of 0.023 m (40 nodes in the heater section) gives reasonable results. These sets of Δt and Δx were used to determine the stability boundary of the test loop.

It is worth noticing that the asymptotic oscillation periods are between 1.2 and 1.3 second, which is about twice of the fluid transport time through the heater section. This agrees with many experimental observations on density-wave oscillations in two-phase flow [15, 16].

Using the sets of time step and heater node sizes determined above, the power levels of the incipient of flow oscillations at different operating pressures are calculated. Figure 4-11 shows the calculated and measured stability boundaries. The average error of heater power is 7.5% and the maximum error is 11% for the coupled form. The average error is 9.1% and the maximum error is 18.3% for the decoupled form.

These results show that the model used here is able to simulate the two-phase flow oscillation events. The stability calculation using decoupled form requires more computation effort than the coupled form, since a much smaller Δx is needed for the decoupled form.

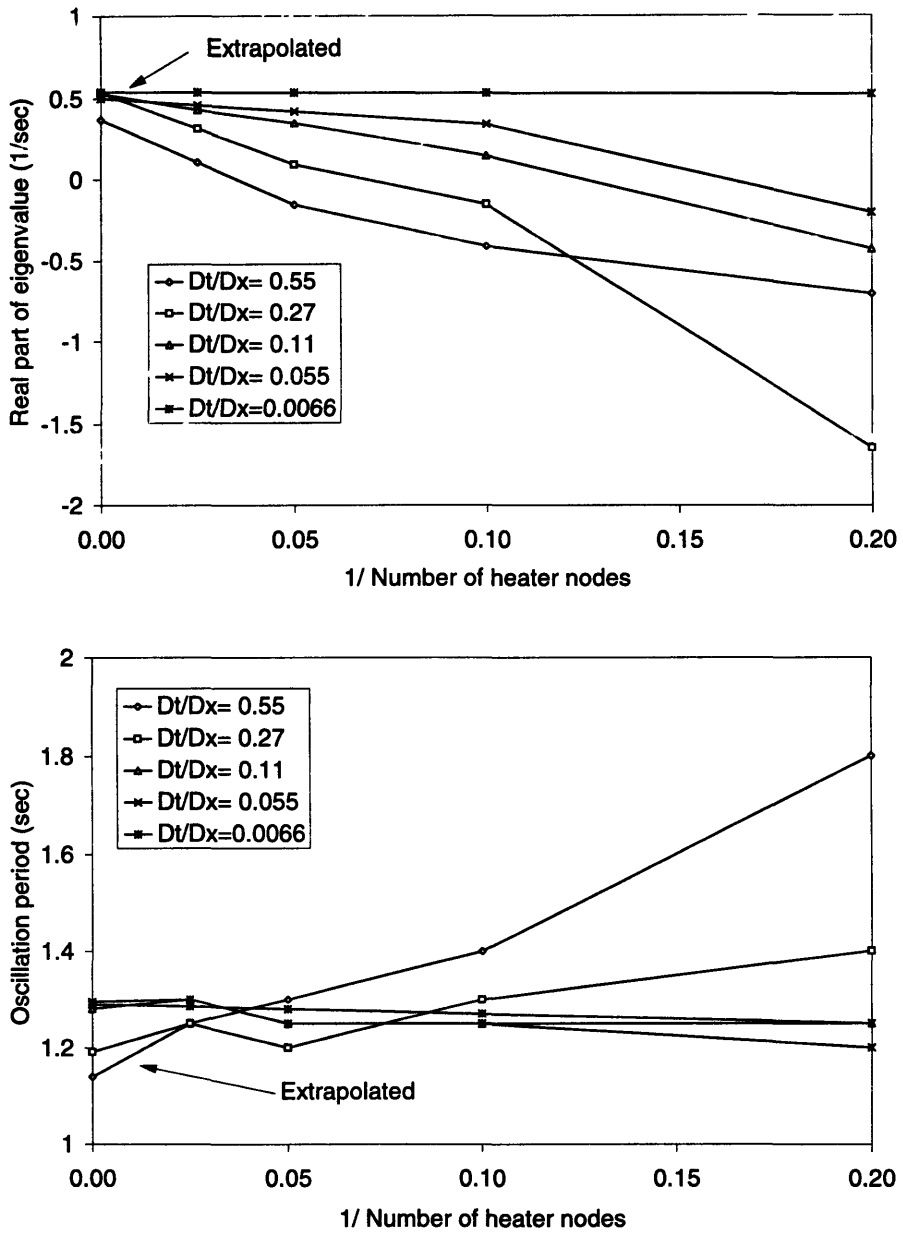

Figure 4-9: Determination of the asymptotic eigenvalue using the coupled form.

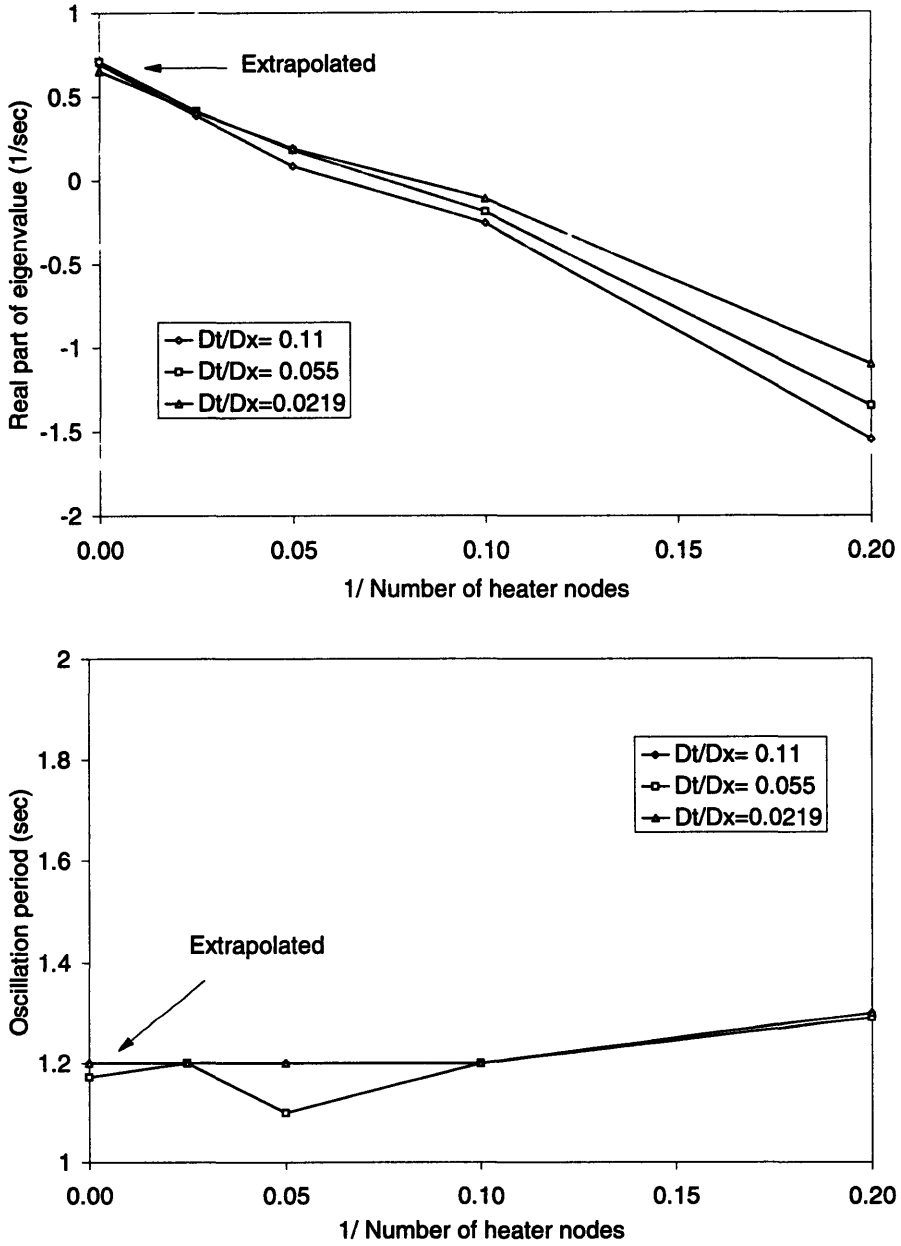

Figure 4-10: Determination of the asymptotic eigenvalue using the decoupled form.

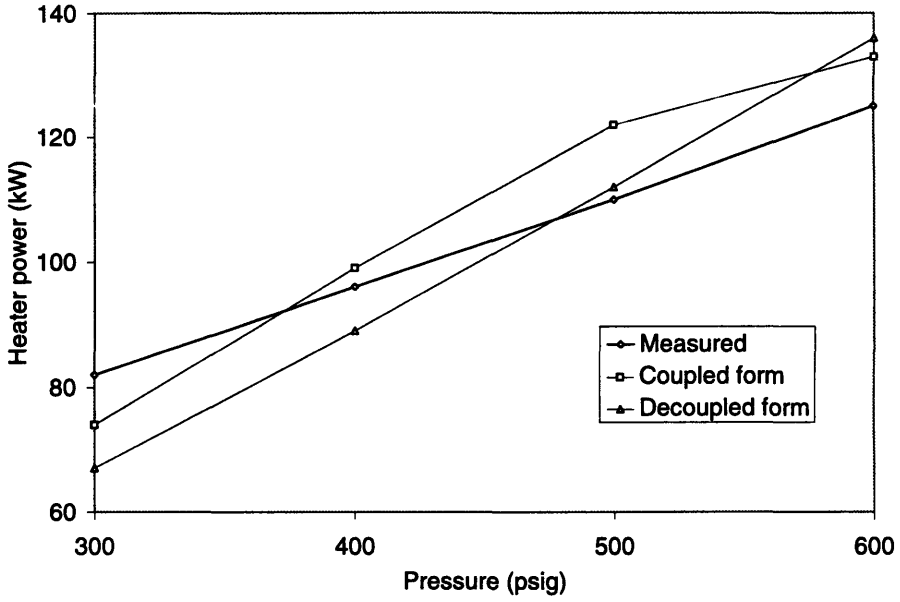

Figure 4-11: The measured and calculated stability boundaries.

4.2 Core Neutronics Model

The interaction between the nuclear fission process and core thermal-hydraulic states is a major factor affecting BWR power oscillations. Thus the modeling of the reactor dynamics is a crucial part of stability analysis. BWR power oscillations are multi-dimensional phenomena. This is true not only for the out-of-phase type instability which involves radial power oscillations, but also for the in-phase type oscillation. The in-phase power oscillations involve axial power fluctuations which are excited by the axial void distribution changes from density wave effects [19].

A three-dimensional reactor kinetics model can simulate both in- and out-of-phase instabilities, but is very time-consuming to use. A one-dimensional kinetics model may be sufficient for simulating the in-phase instability. Borkowski and others have studied the in-phase instability with both zero- and one-dimensional reactor models [49]. They found that the one-dimensional model tends to give less conservative results when compared to the results using the zero-dimensional model. The calculations using the point kinetics model show earlier oscillations and larger oscillation amplitudes than the one-dimensional results. They suggest that axial power fluctuations which are allowed in the one-dimensional model may have a stabilizing effect.

Because of the fast-running requirement for this BWR simulator, the point kinetics model is used in this study. Thus the stability analysis of this BWR simulator is applicable to the in-phase type instability only.

The reactor power generation rate is calculated as the sum of the instantaneous fission power and the decay heat from the fission products:

$$P = (1 - f_D)\, P_n + P_D$$

where

P is the total power,

P_n is the neutron power,

P_D is the decay power, and

f_D is the fraction of the neutron power that is released as the decay heat, $f_D = 0.0668$ [41].

4.2.1 Point kinetics model

The neutron power is proportional to the total neutron population in the core. In the point kinetics model, an amplitude function is defined as the weighted total neutron population. So the total fission power is proportional to this amplitude function. The point kinetics equations describe the relations between the amplitude function, the delay neutron precursor concentrations, and the reactivity [28]:

$$\frac{d}{dt}T = \frac{\rho - \beta}{\Lambda} + \sum_{i=1}^{6} \lambda_i C_i \ , \tag{4.23}$$

$$\frac{d}{dt}C_i = \frac{\beta_i}{\Lambda}T - \lambda_i C_i \ , \tag{4.24}$$

where

T is the amplitude function,

C_i is the weighted concentration of the i-th delay neutron precursor group; six groups of delay neutron precursors are used here,

λ_i is the decay constant of the i-th delay neutron precursor group,

β_i is the effective delay neutron fraction of the i-th delay neutron precursor group,

β is the total effective delay neutron fraction, $\beta = \sum_{i=1}^{6} \beta_i$,

ρ is the total reactivity, and

Λ is the prompt neutron life time.

The total reactivity ρ includes the thermal feedback reactivity and external reactivity. The thermal feedback reactivity is the reactivity contributions from fuel temperature changes (Doppler effect), moderator temperature changes, and moderator density changes (void fraction changes). The external reactivity represents the

effects of control rod movements. The total reactivity at time t is calculated as

$$\rho(t) = \rho_{FB}(t) - \rho_{FB}(0) + \rho_{ext}(t)$$

where

$\rho_{FB}(t)$ is the feedback reactivity at time t ,

$\rho_{FB}(0)$ is the feedback reactivity at time 0 , and

$\rho_{ext}(t)$ is the external reactivity at time t; the initial external reactivity is zero ($\rho_{ext}(0) = 0$).

4.2.2 Feedback reactivity

The thermal feedback reactivity is calculated as the weighted sum of the feedback reactivity of each core node [19]. Power-square weighting is used, which is an approximation to adjoint flux weighting. Each component of the thermal feedback reactivity in a core node is a function of a thermal-hydraulic state of that node.

$$\rho_{FB}(t) = \sum_{\text{core nodes}} w_i \left\{ \rho_{T_f}\left(T_f^i(t)\right) + \rho_{T_m}\left(T_m^i(t)\right) + \rho_{void}\left(\alpha^i(t)\right) \right\}$$

where

w_i is a weighting factor for node i , here $w_i \propto (\text{local power})^2$,

ρ_{T_f}, ρ_{T_m}, and ρ_{void} are the integral feedback reactivities, and are functions of the fuel temperature, moderator temperature, and void fraction,

T_f^i is the average fuel temperature of node i ,

T_m^i is the average moderator temperature of node i , and

α^i is the average void fraction of node i .

Table 4.2: Constants for decay heat calculations (from [41])

i	β_D^i	λ_D^i (sec^{-1})
1	0.097	1.28
2	0.22	0.152
3	0.237	1.93×10^{-2}
4	0.187	1.88×10^{-3}
5	0.132	1.43×10^{-4}
6	0.072	1.25×10^{-5}
7	0.055	2.20×10^{-7}

4.2.3 Decay power model

The decay power generated by the fission products is calculated by using seven groups of decay heat precursors [41]:

$$P_D = \sum_{i=1}^{7} \lambda_D^i C_D^i \ , \tag{4.25}$$

$$\frac{d}{dt} C_D^i = f_D \beta_D^i P_n - \lambda_D^i C_D^i \ , \tag{4.26}$$

where

C_D^i is the concentration of the i-th decay heat precursor group,

λ_D^i is the decay constant of the i-th decay heat precursor group, and

β_D^i is the fraction of the decay heat generated by the i-th decay heat precursor group.

Table 4.2 shows the constants of decay heat precursor groups.

4.3 Fuel Conduction and Convection Model

The fuel conduction and convection model is used to calculate the amount of energy transferred from the fuel to the coolant, and the average fuel temperature for reactivity calculations. All the power generated by nuclear fission is assumed to be deposited in the fuel. A two-node fuel conduction model is used, and single- and two-phase forced convection heat transfer regimes are considered.

4.3.1 Two-node fuel conduction model

The two-node fuel conduction model developed by Cabral is adopted here with modifications [45]. The basic assumptions of the fuel model are the following:

1. Only radial conduction is considered.
2. Material properties are determined from volume averaged temperatures.
3. The heat deposition is uniformly distributed in the fuel.
4. A temperature profile that holds for both steady-state and transient conditions exists. This temperature profile is parabolic in the fuel region, and linear in the gap and cladding regions.
5. The heat capacity of the gap is negligible.
6. A thermal jump distance is used to represent the temperature jumps at the fuel outer surface and the cladding inner surface.

Two radial nodes are used to represent a section of a fuel rod (see Figure 4-12). The boundary between them is located inside the fuel region, at radius r_b $\left(r_b = \frac{\sqrt{2}}{2} r_{fo}\right)$. Node 1 consists of the inner part of the fuel pellet, and node 2 consists of the outer part of the fuel pellet, the gap, and the cladding. From the assumptions, the energy balance of the two nodes are

$$V_{f1}\overline{(\rho c_p)}_f \frac{dT_1}{dt} = V_{f1}\, q'''_f - Q_{12} \ , \tag{4.27}$$

$$\left[V_{f2}\overline{(\rho c_p)}_f + V_c\overline{(\rho c_p)}_c\right]\frac{dT_2}{dt} = V_{f2}\,q'''_f + Q_{12} - Q_w\ , \tag{4.28}$$

where

T_1 and T_2 are heat capacity-weighted, volume-averaged temperatures of the nodes, $T_i = \dfrac{\int_{V_i}\rho c_p T\,dV}{\int_{V_i}\rho c_p\,dV}$,

$\overline{(\rho c_p)}_i$ is the volume-averaged heat capacity, $\overline{(\rho c_p)}_i = \dfrac{\int_{V_i}\rho c_p\,dV}{V_i}$,

q'''_f is the volumetric heat deposition rate in the fuel,

Q_{12} is the heat transfer rate from node 1 to node 2,

Q_w is the heat transfer rate from the cladding outer wall to the coolant,

the subscript f denotes fuel, c denotes cladding, $f1$ denotes fuel in node 1, $f2$ denotes fuel in node 2, and w denotes the outer wall of the cladding.

From the assumed temperature profile in both steady-state and transient conditions, the temperature in the fuel is

$$T_f(r) = T_{fo} + \frac{q'''_f}{4\overline{k}_f}\left(r_{fo}^2 - r^2\right) \tag{4.29}$$

where $\overline{k}_f$ is the fuel conductivity evaluated at the average fuel temperature, and the subscript fo denotes the fuel outer surface.

Then the volume-averaged fuel temperatures in node 1 and node 2 are

$$\overline{T}_{f1} = T_{fo} + \frac{q'''_f}{4\overline{k}_f}\left(r_{fo}^2 - \frac{r_b^2}{2}\right)\ ,$$

and

$$\overline{T}_{f2} = T_{fo} + \frac{q'''_f}{4\overline{k}_f}\left(\frac{r_{fo}^2 - r_b^2}{2}\right)\ .$$

Because node 1 consists of fuel only, and the heat capacity of the fuel is assumed to be independent of position, so $\overline{T}_{f1}$ is equal to T_1. The radius r_1 at which the fuel

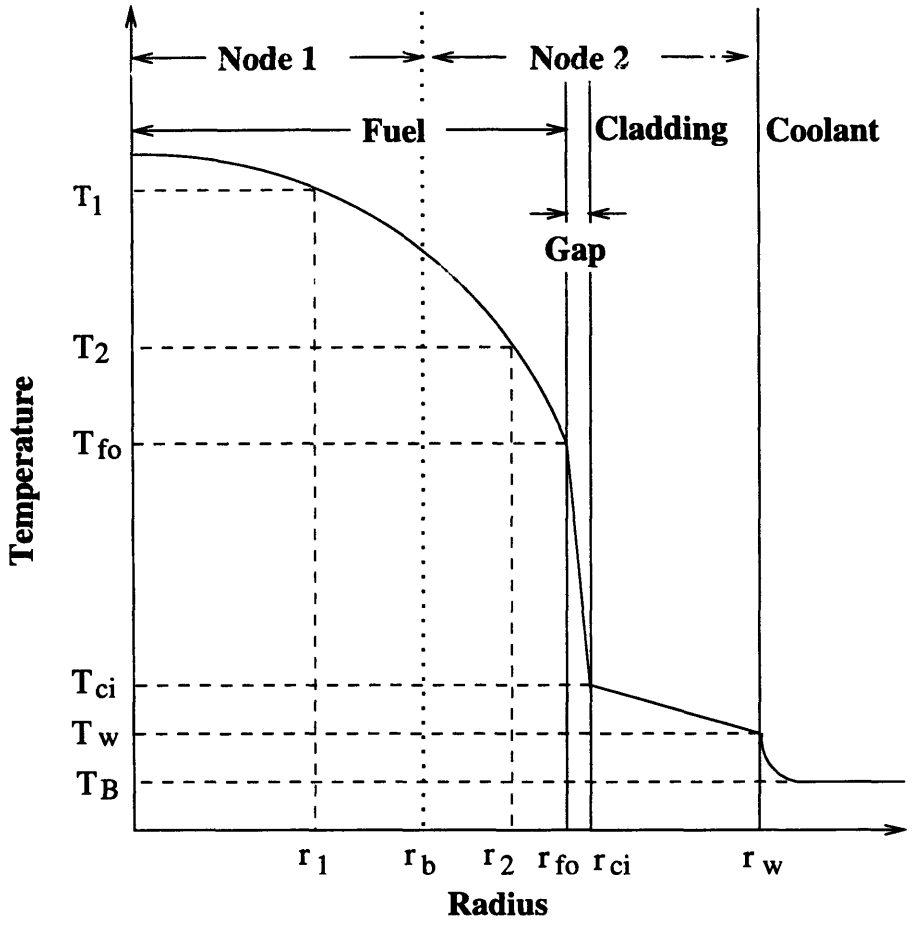

Figure 4-12: Schematic of fuel nodes.

temperature equals T_1 is given by

$$r_1 = \frac{\sqrt{2}}{2} r_b \ .$$

The heat capacity of the gap has been neglected. So,

$$T_2 = \frac{V_{f2}\overline{(\rho c_p)}_f \overline{T}_{f2} + V_c\overline{(\rho c_p)}_c \overline{T}_c}{V_{f2}\overline{(\rho c_p)}_f + V_c\overline{(\rho c_p)}_c} \ .$$

The volume-averaged cladding temperature is approximated as the average of the cladding inner and outer surface temperatures. The radius r_2 at which the fuel temperature equals T_2 is given by

$$r_2 = \sqrt{r_{fo}^2 - \frac{4\overline{k}_f}{q_f'''} (T_2 - T_{fo})} \ .$$

r_2 is not a constant, but Cabral has shown that with a fixed value of r_2 , the error in the average fuel temperature is small [45]. Thus r_2 determined at the initial state will be used in transient calculations.

The heat transfer rate from node 1 to node 2 can be expressed as

$$Q_{12} = -A_b \overline{k}_f \left.\frac{\partial T}{\partial r}\right|_{r_b} = (UA)_{12} (T_1 - T_2) \ , \tag{4.30}$$

where

$(UA)_{12}$ is the total heat transfer coefficient between node 1 and node 2.

A_b is the area of the fuel section at r_b , $A_b = 2\pi r_b \Delta z$, and

Δz is the length of the fuel section.

From Equation 4.29, and from the definitions of r_1 and r_2, we have

$$\left.\frac{\partial T}{\partial r}\right|_{r_b} = -\frac{q_f''' r_b}{2\overline{k}_f} \ ,$$

$$T_1 = T_{fo} + \frac{q'''_f}{4\bar{k}_f}\left(r_{fo}^2 - r_1^2\right) , \tag{4.31}$$

and

$$T_2 = T_{fo} + \frac{q'''_f}{4\bar{k}_f}\left(r_{fo}^2 - r_2^2\right) . \tag{4.32}$$

So,

$$(UA)_{12} = A_b \frac{2\,\bar{k}_f\, r_b}{(r_2^2 - r_1^2)} . \tag{4.33}$$

Similar temperature profiles are assumed to hold for both steady-state and transient conditions. Applying steady-state heat balance and linear temperature profiles in the gap and cladding, we get

$$Q_w = q'''_f\, \pi\, r_{fo}^2 \Delta z , \tag{4.34}$$

$$T_{ci} - T_w = Q_w \left(\frac{\delta_c}{2\pi r_w \Delta z \bar{k}_c}\right) , \tag{4.35}$$

and

$$T_{fo} - T_{ci} = Q_w \left(\frac{\delta_g + \delta_{jump}}{2\pi r_{fo} \Delta z \bar{k}_g}\right) , \tag{4.36}$$

where

δ_c is the cladding thickness,

δ_g is the gap thickness,

δ_{jump} is the thermal jump distance, $\delta_{jump} = 0.3\ \mu m$ [45], and

subscript *ci* denotes the cladding inner surface.

The heat transfer rate from node 2 to the wall can be expressed as

$$Q_w = (UA)_{2w}\,(T_2 - T_w) . \tag{4.37}$$

And the total heat transfer coefficient $(UA)_{2w}$ is obtained by combining Equations 4.32, and 4.34 to 4.37:

$$(UA)_{2w} = 2\pi\Delta z \left[\frac{\delta_c}{r_w \bar{k}_c} + \frac{\delta_g + \delta_{jump}}{r_{fo} \bar{k}_g} + \frac{\left(r_{fo}^2 - r_2^2\right)}{2\, r_{fo}^2 \bar{k}_f} \right]^{-1} . \tag{4.38}$$

Substituting Equations 4.30 and 4.37 into 4.27 and 4.28, we have

$$V_{f1} \overline{(\rho\, c_p)}_f \frac{dT_1}{dt} = V_{f1}\, q_f''' - (UA)_{12} (T_1 - T_2) , \tag{4.39}$$

and

$$\left[V_{f2} \overline{(\rho\, c_p)}_f + V_c \overline{(\rho\, c_p)}_c \right] \frac{dT_2}{dt} = V_{f2}\, q_f''' + (UA)_{12} (T_1 - T_2) - Q_w . \tag{4.40}$$

The material properties are determined using the average material temperatures. These temperatures can be expressed in terms of T_1, T_2, and T_w. The average cladding temperature is

$$\overline{T}_c \cong \frac{T_{ci} + T_w}{2} = a_1 T_w + a_2 T_2 ;$$

the average fuel temperature is

$$\overline{T}_f = b_1 T_1 + b_2 T_2 ;$$

the average gap temperature is

$$\overline{T}_g \cong \frac{T_{fo} + T_{ci}}{2} = c_1 T_w + c_2 T_2 ;$$

where

$$a_1 = 1 - \frac{\delta_c (UA)_{2w}}{4\pi r_w \Delta z\, \bar{k}_c} ,$$

$$a_2 = 1 - a_1 ,$$

$$b_1 = \frac{r_2^2 - r_{fo}^2/2}{r_2^2 - r_1^2} ,$$

$$b_2 = 1 - b_1 ,$$

$$c_1 = 1 - \frac{(UA)_{2w}}{2\pi\Delta z}\left(\frac{\delta_c}{r_w\bar{k}_c} + \frac{\delta_g + \delta_{jump}}{2\,r_{fo}\bar{k}_g}\right) \text{, and}$$

$$c_2 = 1 - c_1 \text{ .}$$

These coefficients are not constant. But they will be evaluated only at the initial state, and then used in transient calculations.

4.3.2 Convective heat transfer

Two heat transfer regimes are considered in this model: single-phase and two-phase forced convection. For the single-phase region, the Dittus-Boelter equation is used. The wall heat transfer rate is given by

$$Q_w = 2\pi r_w \Delta z\, h\, (T_w - T_B) \text{ ,} \tag{4.41}$$

where

h is the single-phase heat transfer coefficient from the Dittus-Boelter equation, and

T_B is the bulk coolant temperature.

For two-phase conditions, the Chen correlation is used. This correlation was originally developed for saturated boiling, but it can also be used in subcooled boiling conditions when temperature weighting is used [37]. The wall heat transfer rate for two-phase conditions is calculated as

$$Q_w = 2\pi\, r_w \Delta z\, [h_{FC}\,(T_w - T_B) + h_{NB}\,(T_w - T_{sat})] \text{ ,} \tag{4.42}$$

where

h_{FC} is the forced convection heat transfer coefficient,

h_{NB} is the nucleate boiling heat transfer coefficient, and

T_{sat} is the saturation temperature.

Table 4.3: Conditions of a fuel rod transient

Rod length	3.66 m
Rod outer radius	4.75 mm
Cladding thickness	0.572 mm
Gap thickness	0.0824 mm
Coolant pressure	15.5 MPa
Coolant inlet temperature	300 °C
Coolant flow area	8.79×10^{-5} m^2
Coolant flow rate	0.342 kg/s
Initial rod power	66.95 kW (100% power)
Final rod power	83.69 kW (125% power)
Axial power shape	uniform

Correlations for these heat transfer coefficients are listed in Appendix C.5.

The transition from the single-phase regime to two-phase regime is at the point of incipient nucleate boiling. The fuel wall temperature is higher than the saturation temperature at this point. But for BWR operating conditions, at the boiling inception, the difference between T_w and T_{sat} is small. So in this heat transfer model, the transition from single-phase to two-phase regimes is set at $T_w = T_{sat}$ [50].

4.3.3 Model validation against THERMIT-2 calculation

The fuel conduction and convection model described above has been named the "COND" model. This model has been validated with the calculation results of the THERMIT-2 code. THERMIT-2 is a two-fluid thermal-hydraulic code for light water reactor core transient analysis [51]. The fuel model in THERMIT-2 uses a finite difference scheme to solve the radial heat conduction equations.

The benchmark case is a step power increase transient of a typical pressurized water reactor (PWR) fuel rod. Table 4.3 shows the conditions of the transient.

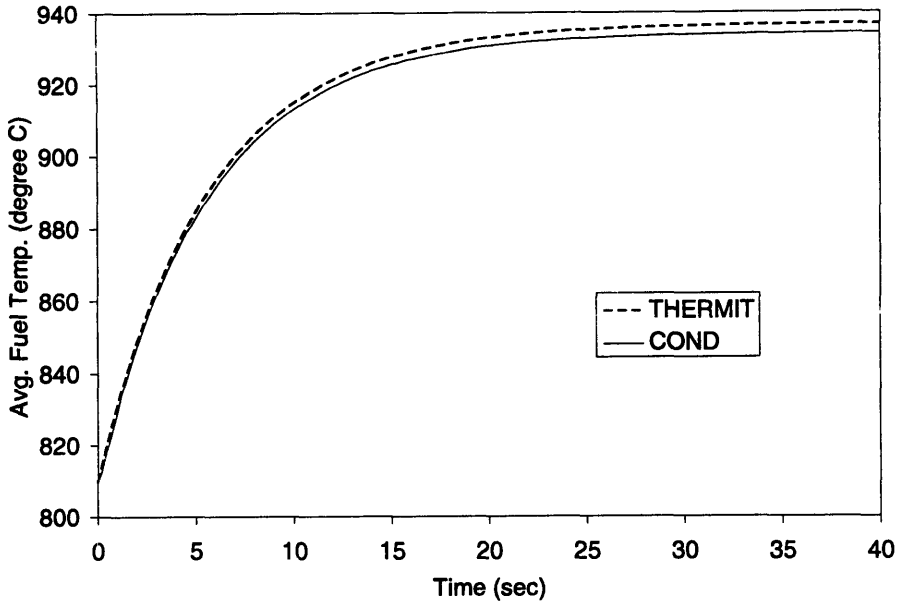

Figure 4-13: Comparison of fuel rod models.

In the THERMIT-2 calculation, the fuel rod is modeled by ten axial nodes. Each axial node is radially divided into eight fuel nodes, one gap node, and one cladding node. Constant fuel properties are used. In the COND calculation, only one axial node is calculated, which corresponds to the fifth axial node in the THERMIT-2 calculation. The fifth node coolant enthalpy from THERMIT-2 is used as a boundary condition in the COND calculation.

Figure 4-13 shows the average fuel temperatures calculated by the two models. The average fuel temperature calculated by the COND model is very close to the THERMIT-2 results. At the end of the transient, the temperature from the COND model is 2 °C lower than that from the THERMIT-2. The average fuel temperature is chosen for comparison because it dictates the Doppler reactivity feedback and the stored energy in the fuel rod, which are important factors in the power oscillation process.

This comparison shows that the COND model, though based on only two radial nodes, gives very good results when compared to the THERMIT-2 fuel rod model with ten radial nodes.

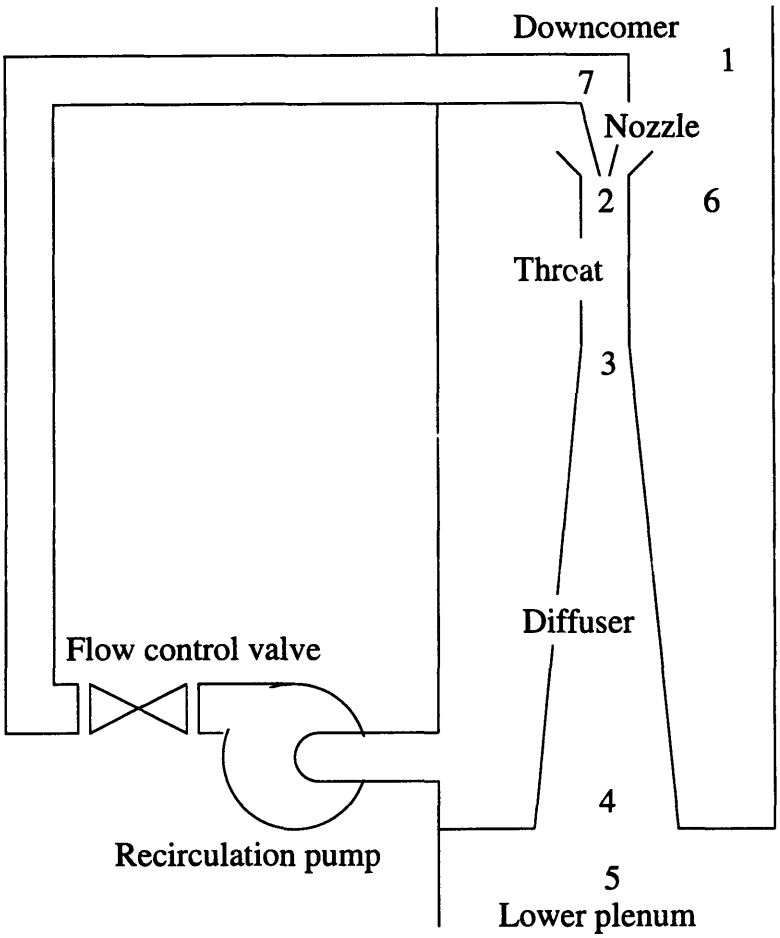

Figure 4-14: Schematic of a recirculation loop.

4.4 Recirculation System and Jet Pump Model

4.4.1 Recirculation system model

The recirculation system model calculates the pressure gain in the lower downcomer node from jet pump operations. Two separate recirculation loops are modeled. Each loop consists of one jet pump, one recirculation pump, one flow control valve, and one external recirculation line, as shown in Figure 4-14. Both recirculation loops are included in the lower downcomer node for the mass and energy calculations. The energy input from recirculation pumps is neglected.

A basic assumption in the recirculation system model is a single density assump-

tion. The entire recirculation system is assumed to have the same density and enthalpy as the outlet of the lower downcomer node. Thus only the mass and momentum balance is considered in the recirculation system model. Flow reversal is not allowed in the external recirculation line, but flow reversal in the jet pumps from the diffuser (point 4) to the upper downcomer (point 1) is allowed. The notations used in this section are listed in Table 4.4.

The annular space of the lower downcomer is divided into two parts, one for each recirculation loop. From the mass balance, we have

$$W_{dc}^{i} = W_{jet}^{i} ,$$

$$W_{lp} = W_{jet}^{1} + W_{jet}^{2} , \tag{4.43}$$

$$W_{jet}^{i} = W_{s}^{i} + W_{rc}^{i} ,$$

where the superscripts denote recirculation loops. From the momentum balance, we have

$$P_1 + \frac{W_{jet}^2}{2\rho A_{dc}^2} = P_2 + \frac{W_s^2}{2\rho A_s^2} + K_s \frac{|W_s| W_s}{2\rho A_s^2} , \tag{4.44}$$

$$P_1 + \frac{W_{jet}^2}{2\rho A_{dc}^2} = P_6 + \frac{W_{rc}^2}{2\rho A_{ldc}^2} , \tag{4.45}$$

$$\begin{aligned} \left(\frac{\ell}{A}\right)_{rc} \frac{dW_{rc}}{dt} &= P_{rcp} + P_6 - P_7 + \frac{W_{rc}^2}{2\rho A_{ldc}^2} - \frac{W_{rc}^2}{2\rho A_{rc}^2} \\ &- \left[\left(\frac{f\ell}{DA^2}\right)_{ldc} + \left(\frac{f\ell}{DA^2}\right)_{rc} + \left(\frac{K}{A^2}\right)_{rc} + \frac{c_v}{A_v^2}\right] \frac{|W_{rc}| W_{rc}}{2\rho} , \end{aligned} \tag{4.46}$$

$$P_7 + \frac{W_{rc}^2}{2\rho A_{rc}^2} = P_2 + \frac{W_{rc}^2}{2\rho A_n^2} + K_n \frac{|W_{rc}| W_{rc}}{2\rho A_n^2} , \tag{4.47}$$

where P_{rcp} is the pressure head of the recirculation pump, K is the loss coefficient, and c_v is the loss coefficient of the flow control valve. The pressure losses in the jet pump during flow reversal conditions are larger than that at positive flow conditions, so K_s and K_d are given different values for positive and reverse flow conditions [52].

Table 4.4: Notations used in the recirculation system model

Positions	
1	lower downcomer above the jet pumps
2	jet pump suction and nozzle discharge
3	jet pump throat
4	jet pump diffuser outlet
5	lower plenum
6	lower downcomer outside the jet pumps
7	recirculation line riser
Subscripts	
s	jet pump suction
n	jet pump nozzle
t	jet pump throat
d	jet pump diffuser
jet	jet pump
dc	lower downcomer above the jet pump
ldc	lower downcomer outside the jet pump
lp	lower plenum inlet
rc	recirculation line
v	flow control valve

From Equations 4.44 to 4.47, we get

$$\begin{aligned}\left(\frac{\ell}{A}\right)_{rc}\frac{dW_{rc}}{dt} &= P_{rcp}+\frac{W_s^2}{2\rho A_s^2}+K_s\frac{|W_s|\,W_s}{2\rho A_s^2}-\frac{W_{rc}^2}{2\rho A_n^2}-K_n\frac{|W_{rc}|\,W_{rc}}{2\rho A_n^2}\\ &- \left[\left(\frac{f\,\ell}{DA^2}\right)_{ldc}+\left(\frac{f\,\ell}{DA^2}\right)_{rc}+\left(\frac{K}{A^2}\right)_{rc}+\frac{c_v}{A_v^2}\right]\frac{|W_{rc}|\,W_{rc}}{2\rho}\,.\end{aligned} \tag{4.48}$$

4.4.2 Recirculation pump model

The pressure head of a recirculation pump is calculated by the recirculation pump model. The recirculation pumps are centrifugal pumps. The performance of the pump is described by the characteristics of the pump which involve four parameters: pressure head, pump speed, flow rate, and pump torque. Homologous curves of dimensionless parameters are used to represent the pump characteristics [53]. In this model, the homologous curves for positive rotation are given by third-order polynomials:

$$\frac{h}{\alpha}=a_0+a_1\left(\frac{\nu}{\alpha}\right)+a_2\left(\frac{\nu}{\alpha}\right)^2+a_3\left(\frac{\nu}{\alpha}\right)^3\;;$$

$$\frac{\beta}{\alpha}=b_0+b_1\left(\frac{\nu}{\alpha}\right)+b_2\left(\frac{\nu}{\alpha}\right)^2+b_3\left(\frac{\nu}{\alpha}\right)^3\;;$$

where

h is the dimensionless head, $h=\dfrac{H}{H_r}$,

H is the pump head, $H=\dfrac{P_{rcp}}{\rho g}$,

P_{rcp} is the pressure gain across the recirculation pump,

α is the dimensionless speed, $\alpha=\dfrac{\omega}{\omega_r}$,

ω is the pump speed,

ν is the dimensionless flow rate, $\nu=\dfrac{Q}{Q_r}$,

Q is the volumetric flow rate, $Q=\dfrac{W_{rc}}{\rho}$,

β is the dimensionless torque, $\beta=\dfrac{T_{rcp}}{T_r}$,

T_{rcp} is the pump torque, and

H_r , ω_r , Q_r , and T_r are the rated head, speed, flow rate, and pump torque, respectively.

The dynamic response of the pump is described by the torque equation [54]

$$I_{rcp}\frac{d\omega}{dt} = T_m - T_{rcp} - T_{loss} \ , \tag{4.49}$$

where

I_{rcp} is the moment of inertia of the pump, including the inertia of the motor-generator set,

T_m is the motor or electrical torque,

T_{loss} is the torque loss due to windage and frictions, $T_{loss} = r_{pump}\,\omega$, and

r_{pump} is a loss factor.

The pressure gain across the pump and the pump torque can be obtained from the homologous curves given the pump speed and flow rate:

$$P_{rcp} = \rho g \alpha^2 H_r \left[a_0 + a_1\left(\frac{\nu}{\alpha}\right) + a_2\left(\frac{\nu}{\alpha}\right)^2 + a_3\left(\frac{\nu}{\alpha}\right)^3\right] \ ; \tag{4.50}$$

$$T_{rcp} = \alpha^2 T_r \left[b_0 + b_1\left(\frac{\nu}{\alpha}\right) + b_2\left(\frac{\nu}{\alpha}\right)^2 + b_3\left(\frac{\nu}{\alpha}\right)^3\right] \ . \tag{4.51}$$

To avoid a singularity, the dimensionless flow ν is assumed to be equal to the dimensionless speed α for $\alpha < 0.001$. The partial derivatives of the pressure head and pump torque with respect to the speed and pump flow are needed during transient calculations. These partial derivatives are calculated from direct differentiations of Equations 4.50 and 4.51:

$$\frac{\partial P_{rcp}}{\partial W_{rc}} = \frac{gH_r}{Q_r}\left(a_1\alpha + 2\,a_2\alpha + 3\,a_3\frac{\nu^2}{\alpha}\right) \ ;$$

$$\frac{\partial P_{rcp}}{\partial \omega} = \frac{\rho g H_r}{\omega_r}\left(2\,a_o\alpha + a_1\nu - a_3\frac{\nu^3}{\alpha^2}\right) \ ;$$

$$\frac{\partial T_{rcp}}{\partial W_{rc}} = \frac{T_r}{\rho Q_r}\left(b_1\alpha + 2\,b_2\alpha + 3\,b_3\frac{\nu^2}{\alpha}\right) ;$$

$$\frac{\partial T_{rcp}}{\partial \omega} = \frac{T_r}{\omega_r}\left(2\,b_o\alpha + b_1\nu - b_3\frac{\nu^3}{\alpha^2}\right) .$$

4.4.3 Jet pump model

The pressure gain across the jet pump is the sum of four components. The first one is the pressure difference between point 1 and point 2 which is given by Equation 4.44. The second one is the pressure difference between point 2 and point 3. For forced circulation conditions, the momentum balance of the throat is given by [36, 55]

$$P_2A_t + \frac{W_s^2}{\rho A_s} + \frac{W_{rc}^2}{\rho A_n} = P_3A_t + \frac{W_{jet}^2}{\rho A_t} . \tag{4.52}$$

But for natural circulation conditions, $W_{rc} = 0$, and the momentum equation is

$$P_2 + \frac{W_s^2}{2\,\rho A_s^2} = P_3 + \frac{W_{jet}^2}{2\,\rho A_t^2} .$$

The transition from forced to natural circulation is calculated by a linear interpolation. An interpolation factor is defined as

$$crl = \begin{cases} 1 & \text{for } W_2 \le W_{rc} , \\ \left(\dfrac{W_{rc} - W_1}{W_2 - W_1}\right) & \text{for } W_1 < W_{rc} < W_2 , \\ 0 & \text{for } W_{rc} \le W_1 . \end{cases}$$

W_1 and W_2 are the limits of recirculation flow of pure natural and forced circulation. W_1 and W_2 have been arbitrarily set to 10 and 20 kg/s, respectively. The pressure difference across the throat is then

$$P_2 - P_3 = crl\left(\frac{W_{jet}^2}{\rho A_t^2} - \frac{W_s^2}{\rho A_s A_t} - \frac{W_{rc}^2}{\rho A_n A_t}\right) + (1 - crl)\left(\frac{W_{jet}^2}{2\,\rho A_t^2} - \frac{W_s^2}{2\,\rho A_s^2}\right) .$$

The rest of the pressure difference components are

$$\begin{aligned}\left(\frac{\ell}{A}\right)_{jet}\frac{dW_{jet}}{dt} &= P_3 - P_4 + \frac{W_{jet}^2}{2\rho A_t^2} - \frac{W_{jet}^2}{2\rho A_d^2} \\ &- \left(\frac{f\,\ell}{D\,A^2}\right)_{jet}\frac{|W_{jet}|\,W_{jet}}{2\rho} + \rho\,g\,\Delta z_{jet}\ ,\end{aligned} \tag{4.53}$$

and

$$P_4 + \frac{W_{jet}^2}{2\rho A_d^2} - K_d\frac{|W_{jet}|\,W_{jet}}{2\rho A_d^2} = P_5 + \frac{W_{lp}^2}{2\rho A_{lp}^2}\ .$$

Define the jet pump pressure gain $P_{jet} = P_5 - P_1 - \rho g \Delta z_{jet}$. Then,

$$\begin{aligned}\left(\frac{\ell}{A}\right)_{jet}\frac{dW_{jet}}{dt} &= -P_{jet} + \frac{W_{jet}^2}{2\rho A_{dc}^2} - \frac{W_{lp}^2}{2\rho A_{lp}^2} - \left(\frac{f\,\ell}{D\,A^2}\right)_{jet}\frac{|W_{jet}|\,W_{jet}}{2\rho} \\ &- K_s\frac{|W_s|\,W_s}{2\rho A_s^2} - K_d\frac{|W_{jet}|\,W_{jet}}{2\rho A_d^2} \\ &+ crl\left[\frac{W_s^2}{\rho A_s}\left(\frac{1}{A_t} - \frac{1}{A_s}\right) + \frac{W_{rc}^2}{\rho A_n A_t} - \frac{W_{jet}^2}{2\rho A_t^2}\right]\ .\end{aligned} \tag{4.54}$$

4.4.4 Validation of the jet pump model

The performance of a jet pump is governed by three parameters [55]:

1. The nozzle to throat area ratio, $R = \dfrac{A_n}{A_t}$;
2. The jet pump suction loss coefficient, K_s ;
3. The nozzle loss coefficient, K_n .

The steady-state characteristics curve of a jet pump is usually expressed in terms of the flow ratio M and head ratio N . The flow ratio is the ratio of jet pump suction flow to jet pump nozzle flow.

$$M = \frac{W_s}{W_{rc}}\ .$$

The head ratio is defined as

$$N = \frac{\text{(Diffuser outlet total head)} - \text{(Downcomer total head)}}{\text{(Riser total head)} - \text{(Diffuser outlet total head)}} = \frac{h_4 - h_1}{h_7 - h_4}\ ,$$

where the total head $h = \frac{P}{\rho} + \frac{W^2}{2\rho^2 A^2} + g z$.

At steady-state, neglecting friction losses, Equations 4.44, 4.52, and 4.53 give

$$h_4 - h_1 = \frac{W_s^2}{2\rho^2 A_s^2}\left(\frac{2A_s}{A_t} - K_s - 1\right) + \frac{W_{rc}^2}{\rho^2 A_n A_t} - \frac{W_{jet}^2}{\rho^2 A_t^2} .$$

Equations 4.47, 4.52, and 4.53 give

$$h_7 - h_4 = -\frac{W_s^2}{2\rho^2 A_s A_t} + \frac{W_{rc}^2}{2\rho^2 A_n^2}\left(1 + K_n - \frac{2A_n}{A_t}\right) + \frac{W_{jet}^2}{2\rho^2 A_t^2} .$$

Notice that $\frac{W_{jet}}{W_{rc}} = M + 1$, and $\frac{A_s}{A_t} = 1 - R$. Using these relations, the head ratio becomes

$$N = \frac{\frac{M^2}{(1-R)^2}(1 - K_s - 2R) + \frac{2}{R} - (M+1)^2}{\frac{(1 + K_n - 2R)}{R^2} + (M+1)^2 - \frac{2M^2}{(1-R)}} . \qquad (4.55)$$

This expression has also been derived by Liao [55]. From this expression, we can see that under steady-state, no friction conditions, the N–M curve is completely determined by R, K_s, and K_n .

Equation 4.55 has been used to calculate the N–M curve of a generalized General Electric (GE) first generation jet pump. The parameters used in the calculation are $R = 0.1589$, $K_s = 0.35$, and $K_n = 0.1$.

The calculated characteristics curve agrees very well with the measured curve, as shown in Figure 4-15 [55]. This result shows that the jet pump model discussed above can accurately predict the performance of the jet pumps.

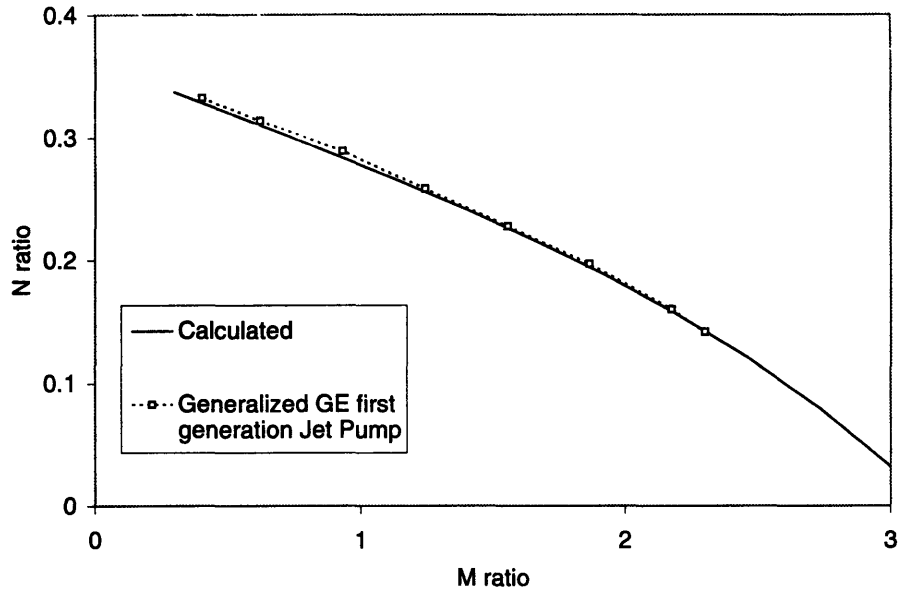

Figure 4-15: Jet pump characteristics curves. The generalized GE (measured) curve is from Liao [55].

4.5 Steam Line Model

4.5.1 Steam line dynamics

The steam line model developed by Wulff is adopted for calculating the dynamics of the steam lines [56]. This steam line model has also been used in the Brookhaven National Laboratory (BNL) Engineering Plant Analyzer (EPA) and the RAMONA-3B code [47]. The steam line model in this work uses seven constant cross-sectional nodes to represent the steam line system, as shown in Figure 4-16. The assumptions used in this model are as following:

1. Steam is an ideal gas;
2. Flow is adiabatic;
3. Gravity effects and spatial accelerations are negligible;
4. Viscous dissipation and axial conduction are negligible (isentropic flow).

From the assumptions of ideal gas and isentropic flow, the conservation of energy (expressed in terms of pressure P and density ρ) becomes

$$\gamma \frac{d\rho}{\rho} = \frac{dP}{P} , \tag{4.56}$$

where γ is the isentropic expansion coefficient , $\gamma = \frac{c_p}{c_v}$. Integrating Equation 4.56, we get

$$\left(\frac{\rho_1}{\rho_2}\right)^{\gamma} = \frac{P_1}{P_2} . \tag{4.57}$$

The isentropic expansion coefficient can be calculated with the help of the ideal gas and isentropic assumptions. For ideal gas,

$$du = c_v dT ,$$

and

$$dh = c_p dT .$$

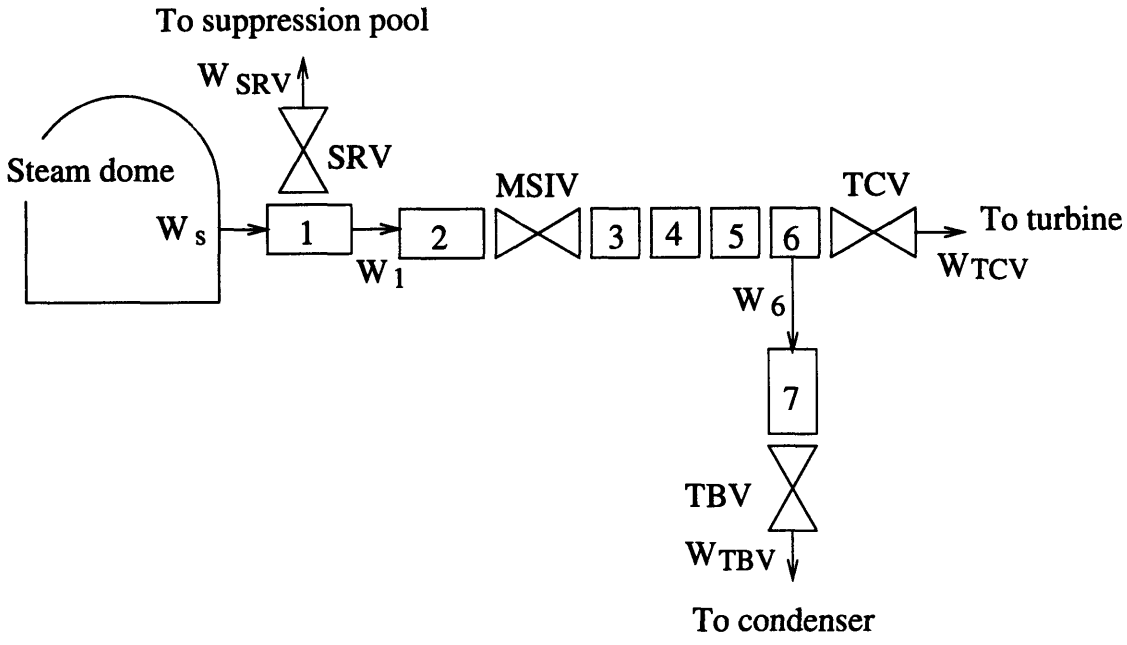

Figure 4-16: Nodalization of the steam line system. SRV: safety relief valve, MSIV: main steam isolation valve, TCV: turbine control valve, TBV: turbine bypass valve.

For an isentropic process,

$$du = -Pdv \ ,$$

and

$$dh = vdP = \frac{dP}{\rho} \ . \tag{4.58}$$

So,

$$\gamma = \frac{c_p}{c_v} = -\frac{dP/P}{dv/v} = \frac{dP/P}{d\rho/\rho} \ .$$

But

$$d\rho = \left(\frac{\partial \rho}{\partial P}\right)_h dP + \left(\frac{\partial \rho}{\partial h}\right)_P dh = dP\left[\left(\frac{\partial \rho}{\partial P}\right)_h + \frac{1}{\rho}\left(\frac{\partial \rho}{\partial h}\right)_P\right] \ .$$

So,

$$\gamma = \frac{\rho}{P\left[\left(\frac{\partial \rho}{\partial P}\right)_h + \frac{1}{\rho}\left(\frac{\partial \rho}{\partial h}\right)_P\right]} \ .$$

γ will only be evaluated once at the initial steam dome condition, and be used in all subsequent transient calculations.

The mass balance of a node is

$$V_i \frac{d\rho_i}{dt} = \sum_j W_j$$

where subscript j represents the flows in or out of node i. By applying Equations 4.56 and 4.57, we get

$$\frac{V_i}{\gamma}\left(\frac{\rho_0}{P_0}\right)\left(\frac{P_0}{P_i}\right)^{\left(\frac{\gamma-1}{\gamma}\right)} \frac{dP_i}{dt} = \sum_j W_j \ , \tag{4.59}$$

where P_0 and ρ_0 are the reference pressure and density which are evaluated at the initial steam dome condition.

The momentum balance for a flow path between node i and $i+1$ is

$$\begin{aligned}\frac{1}{2}\left[\left(\frac{\ell}{A}\right)_i+\left(\frac{\ell}{A}\right)_{i+1}\right]\frac{dW_i}{dt} &= P_i - P_{i+1} - \frac{1}{2}\left[\left(\frac{f\,\ell}{DA^2}\right)_i+\left(\frac{f\,\ell}{DA^2}\right)_{i+1}\right]\frac{|W_i|\,W_i}{2\,\rho_{i+\frac{1}{2}}} \\ &- K_i\frac{|W_i|\,W_i}{2\,\rho_{i+\frac{1}{2}}\,A_{i+\frac{1}{2}}^2} - c_v\frac{|W_i|\,W_i}{2\,\rho_{i+\frac{1}{2}}\,A_v^2}\,,\end{aligned} \tag{4.60}$$

where

$A_{i+\frac{1}{2}}$ is the flow area between node i and $i+1$,

$\rho_{i+\frac{1}{2}}$ is the density between the nodes, and is set as the density in the upwind node,

A_v and c_v are the flow area and loss coefficient of the valve between the nodes, such as the turbine control valve (TCV) or the main steam isolation valve (MSIV).

The state variables of the steam line system are the pressure of each node, the flow rates between nodes, and the steam flow rates from the steam dome and through the TCV. The boundary conditions for this system are the steam dome pressure, turbine inlet pressure, and the flow rates through the safety relief valve (SRV) and turbine bypass valve (TBV).

4.5.2 Valve model

The flow rates through the safety relief valve and turbine bypass valve are calculated from the pressure differences across the valves. Assuming the steam is an ideal gas, and the flow through the valve is isentropic, then the stagnation enthalpy of the steam is constant [36, 37]. Neglecting the kinetic energy upstream of the valve, the flow rate through the valve is

$$W_v = (\rho v A)_t = (\rho A)_t\sqrt{2\,(h_H - h_t)}\,,$$

where the subscript H denotes upstream, and t denotes valve throat. From Equations 4.57 and 4.58,

$$h_H - h_t = \left(\frac{\gamma}{\gamma-1}\right)\frac{P_H}{\rho_H}\left[1-\left(\frac{P_t}{P_H}\right)^{\left(\frac{\gamma-1}{\gamma}\right)}\right] .$$

Then,

$$\begin{aligned} W_v &= c_v A_v \left\{ 2\rho_H P_H \left(\frac{\gamma}{\gamma-1}\right)\left[\left(\frac{P_t}{P_H}\right)^{\frac{2}{\gamma}} - \left(\frac{P_t}{P_H}\right)^{\left(\frac{\gamma+1}{\gamma}\right)}\right]\right\}^{\frac{1}{2}} \\ &= c_v A_v \left\{ 2\rho_0 P_H \left(\frac{P_H}{P_0}\right)^{\frac{1}{\gamma}}\left(\frac{\gamma}{\gamma-1}\right)\left[\left(\frac{P_L}{P_H}\right)^{\frac{2}{\gamma}} - \left(\frac{P_L}{P_H}\right)^{\left(\frac{\gamma+1}{\gamma}\right)}\right]\right\}^{\frac{1}{2}} , \end{aligned} \tag{4.61}$$

here the subscript L denotes downstream, and c_v is the valve coefficient which accounts for flow contraction and losses [47]. For subsonic flows, the downstream pressure is equal to the throat pressure.

For choked flow, the flow rate is independent on the downstream pressure:

$$\frac{dW_v}{dP_L} = 0.$$

This leads to

$$\left(\frac{P_L}{P_H}\right)_{critical} = \left(\frac{2}{\gamma+1}\right)^{\left(\frac{\gamma}{\gamma-1}\right)} .$$

Thus for $\left(\frac{P_L}{P_H}\right) \le \left(\frac{P_L}{P_H}\right)_{critical}$, the valve flow is given by [36, 47]

$$(W_v)_{critical} = c_v A_v \left[\gamma\,\rho_0 P_H \left(\frac{P_H}{P_0}\right)^{\frac{1}{\gamma}}\left(\frac{2}{\gamma+1}\right)^{\left(\frac{\gamma+1}{\gamma-1}\right)}\right]^{\frac{1}{2}} . \tag{4.62}$$

4.5.3 Model validation

The steam line model discussed above has been named the "STMLN" model. This model is used to calculate fast valve closure transients and the results are compared to analytical and test results.

Two validation cases are studied. The first case is a theoretical one. The analytical solution of the transient is obtained with the following assumptions:

Table 4.5: Conditions for theoretical steam line transient case

Steam line flow area	0.1542 m^2
Steam line length	65.985 m
Initial steam dome pressure	6.88 MPa
Initial steam dome density	35.783 kg/m^3
Initial mass flow rate	268.3 kg/s
Fraction parameter β	3.1826 sec^{-1}

1. The isentropic expansion coefficient $\gamma = 1$.

2. The steam flow is laminar and with no form losses. The frictional pressure gradient is

$$\left(\frac{\partial P}{\partial z}\right)_{friction} = \beta\left(\frac{W}{A}\right) ,$$

where β is a constant friction parameter.

The analytical solution for this transient has been derived by Wulff [56]. The boundary conditions are constant steam dome pressure, and no SRV and TBV flows. The transient is initiated by fast turbine control valve closure (in 0.1 second). Table 4.5 lists the conditions for the calculation.

Figure 4-17 compares the turbine stop valve pressures calculated by the analytical solution and STMLN model [56]. The results from the STMLN model are in good agreement with the analytical solution.

The second case being studied is a turbine trip test conducted at the Peach Bottom unit 2 [32]. The turbine trip test 3 (TT3) of the Peach Bottom-2 transient tests is calculated. The calculation uses the measured steam dome pressure and TBV flow rate as the boundary conditions, as shown in Figure 4-18 [56]. The test conditions and steam line geometry are given in reference [56]. This test was also initiated by turbine control valve fast closure (also in 0.1 second). Figure 4-19 shows the measured and calculated stop valve pressures [56]. The results from STMLN model follow the measured data very well, except for the high frequency components in the

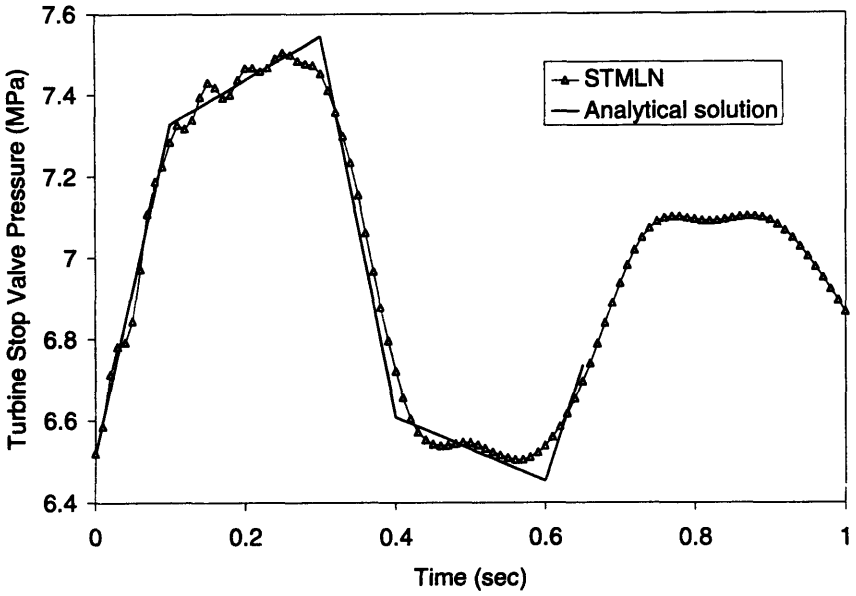

Figure 4-17: Turbine stop valve pressure variations in the theoretical transient. The analytical solution is from Wulff [56].

data which were caused by the pressure wave reflections in the pressure sensing lines [56].

From these two cases, we judge that the STMLN model is adequate for simulating the dynamic responses of the steam line system.

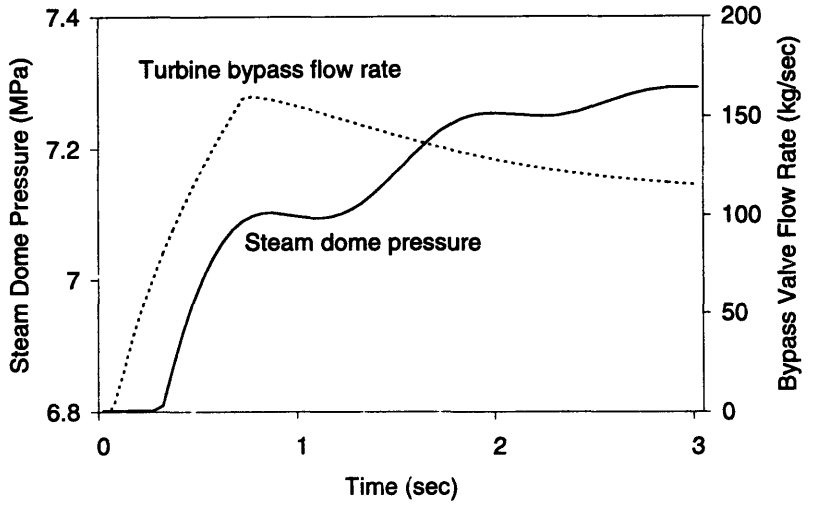

Figure 4-18: Boundary conditions for TT3 calculation (from [56]).

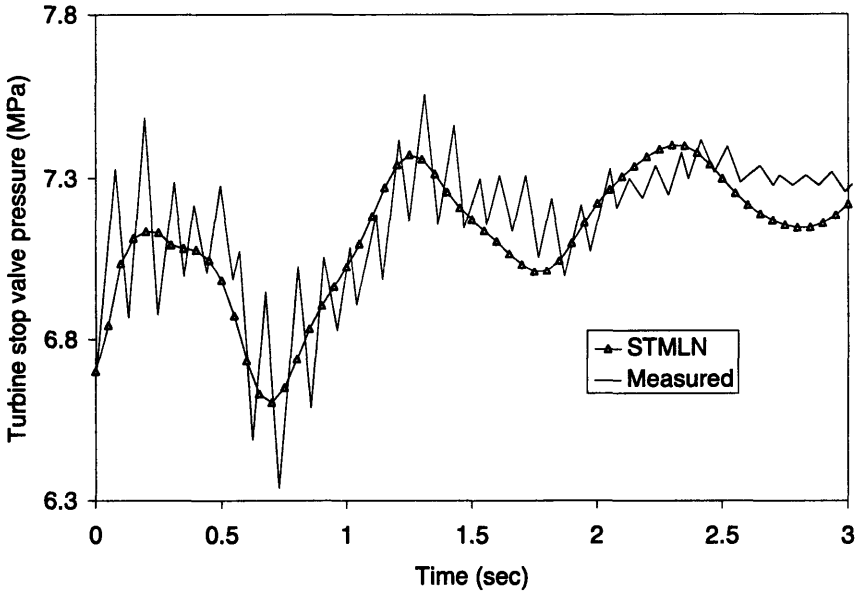

Figure 4-19: Turbine stop valve pressures of TT3 test. The measured data are from reference [56].

4.6 Control System Model

The control system model is used to determine the boundary conditions of the BWR simulator. The required boundary conditions are

1. turbine control valve open fraction,
2. turbine bypass valve open fraction,
3. safety relief valve open fraction,
4. recirculation flow control valve (FCV) open fraction or recirculation pump speed for each recirculation loop, and
5. feedwater flow rate.

Four control systems are needed. They are

1. reactor pressure controller, which determines the TCV and TBV openings;
2. recirculation flow controller,
3. feedwater controller, and
4. safety relief valve controller.

In addition to these controllers, the actions of MSIV and TCV fast closure are also modeled.

The major building blocks of the controllers are lead/lag compensators, and proportional-integral-differential (PID) controllers. The dynamics of these components are simulated by numerical integrations [57]. The transfer function of a lead/lag compensator is

$$\frac{Y(s)}{X(s)} = G\left(\frac{1+\tau_1 s}{1+\tau_2 s}\right)$$

where

$X(s)$ and $Y(s)$ are the Laplace transforms of the input and output signals $x(t)$ and $y(t)$,

τ_1 and τ_2 are lead and lag time constants,

G is the gain,

s is the Laplace variable, and

t denotes time.

The time domain equivalence to the above transfer function is

$$y(t) + \tau_2 \frac{d}{dt} y(t) = G\left[x(t) + \tau_1 \frac{d}{dt} x(t)\right] .$$

Using backward finite differencing, we get

$$y_i = \frac{G\left[x_i + \tau_1\left(\frac{x_i - x_{i-1}}{\Delta t}\right)\right] + \tau_2\left(\frac{y_{i-1}}{\Delta t}\right)}{1 + \frac{\tau_2}{\Delta t}}$$

where Δt is the time step size, $\Delta t = t_i - t_{i-1}$, and subscripts i and $i-1$ denote time steps. A lag compensator can be modeled by setting τ_1 to zero.

The transfer function of a PID controller is

$$\frac{Y(s)}{X(s)} = K_P + \frac{K_D}{s} + K_I s$$

where K_P, K_I , and K_D are the proportional, integral, and differential gains. The time domain equivalence is

$$\frac{d}{dt} y(t) = K_P \frac{d}{dt} x(t) + K_D \frac{d^2}{dt^2} x(t) + K_I x(t) .$$

A numerical solution is

$$y_i = \left(K_P + \frac{K_D}{\Delta t_i} + \Delta t_i K_I\right) x_i - \left[K_P + K_D\left(\frac{1}{\Delta t_i} + \frac{1}{\Delta t_{i-1}}\right)\right] x_{i-1} + \left(\frac{K_D}{\Delta t_{i-1}}\right) x_{i-2} + y_{i-1} ,$$

where $\Delta t_{i-1} = t_{i-1} - t_{i-2}$, and $\Delta t_i = t_i - t_{i-1}$. The proportional (P) and proportional-integral (PI) controllers can be modeled by setting the appropriate gains to zero.

The output of a controller is sent to the actuating system and causes the controlled device to respond. The dynamic behavior of the actuating system is modeled by a second order dynamic system:

$$\frac{Y(s)}{X(s)} = \frac{c_f}{s^2 + c_d\, s + c_f}$$

where

c_f is a constant related to the undamped natural frequency of the system, $c_f = \omega_n^2$,

c_d is a constant related to both the undamped natural frequency and damping factor, $c_d = 2\,\zeta\,\omega_n$,

ω_n is the undamped natural frequency, and

ζ is the damping ratio.

The numerical solution for this dynamic system is

$$y_i = \frac{c_f\,\Delta t_i^2\, x_i + \left(1 + \dfrac{\Delta t_i}{\Delta t_{i-1}} + c_d\,\Delta t_i\right) y_{i-1} - \left(\dfrac{\Delta t_i}{\Delta t_{i-1}}\right) y_{i-2}}{1 + c_d\,\Delta t_i + c_f\,\Delta t_i^2} \; .$$

The response speed of the actuator is also limited to a maximum rate given by the user.

The following sections describe the signal paths in the controllers. These controllers are simplified versions of controllers used in the BNL Engineering Plant Analyzer (EPA) [47].

4.6.1 Reactor pressure controller

Figure 4-20 shows the reactor pressure controller. The input signals are the load demand, turbine load, reactor pressure set point, and steam dome pressure. The

outputs are the TCV and TBV positions, and the demand error signal which goes to the recirculation flow controller. The flow rate though TCV is used to indicate the turbine load.

The difference between the load demand and actual turbine load is the demand error signal. This error signal goes through a lag compensator and gives the transient set point adjustment. This adjustment gives the correct TCV response to a load demand change.

The pressure error signal is the difference between the adjusted set point and the steam dome pressure. This pressure error goes though a proportional controller and a lead/lag compensator and gives the steam flow demand signal. The TCV flow demand is the smaller of the steam flow demand and load demand plus a load bias. This arrangement makes sure that the steam flow will not exceed by too much the flow required to meet the load demand.

The bypass flow demand is the difference of the steam flow demand and the TCV flow demand plus a bypass bias. So the TBV will open only when the TCV can not meet the steam flow demand.

Two function generators (lookup tables) are used to translate the flow demands of TCV and TBV into the position demands. The non-linearity of the characteristics of the valves can be modeled by these function generators. The final valve positions are calculated by the second order actuator models.

4.6.2 Recirculation flow and feedwater flow controllers

The recirculation flow controller is shown in Figure 4-21. The demand error signal from the pressure controller enters a PI controller (master controller) and produces a power demand signal. This power demand is compared to the filtered reactor power signal which is the amplitude function in the point kinetics model. The power error goes to a PI controller (flow controller) and gives the recirculation flow demand. This flow demand is translated to the flow control valve position demand or the recirculation pump speed demand by a function generator. An actuator model calculates the FCV position or pump speed.

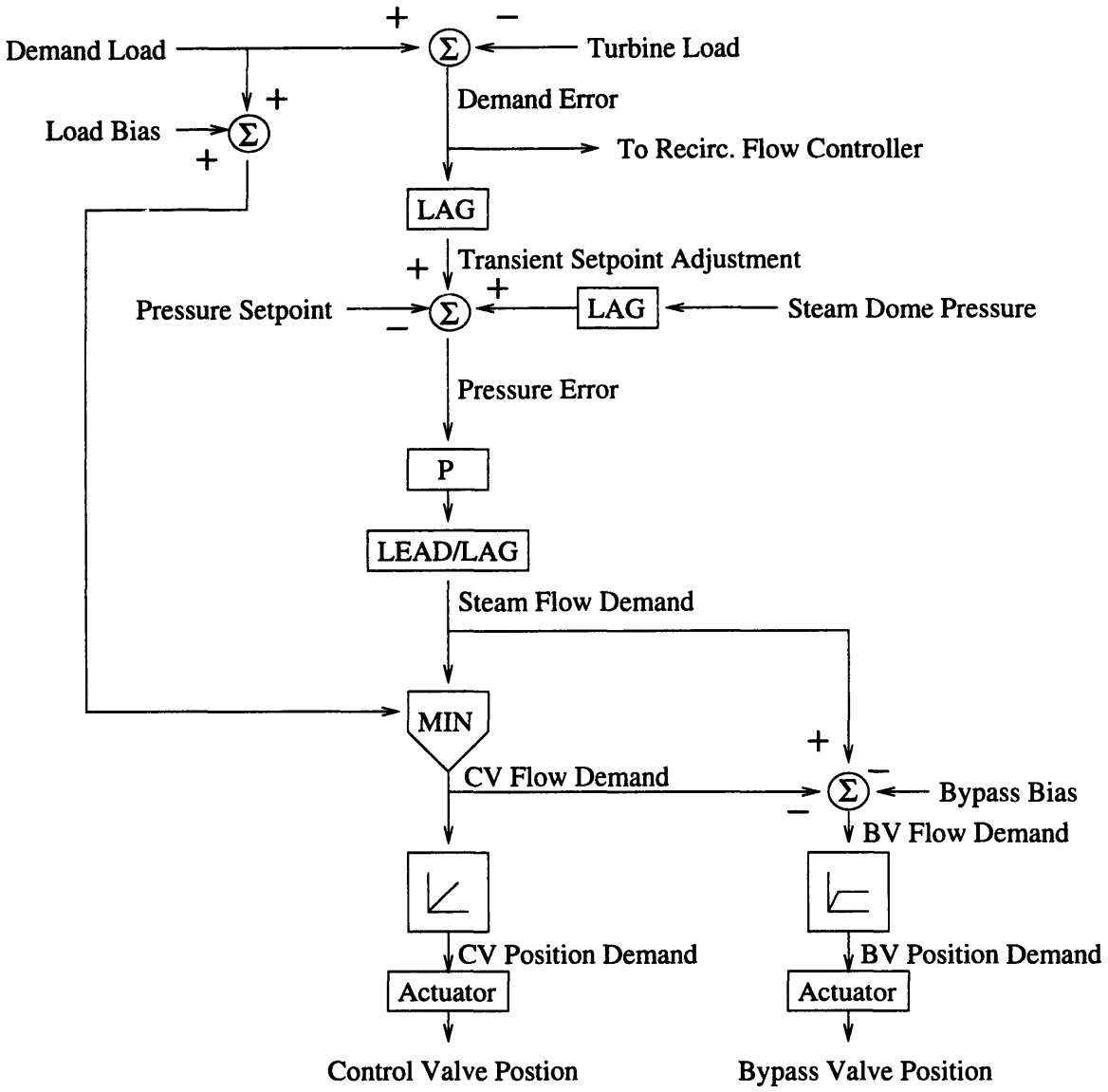

Figure 4-20: Reactor pressure controller.

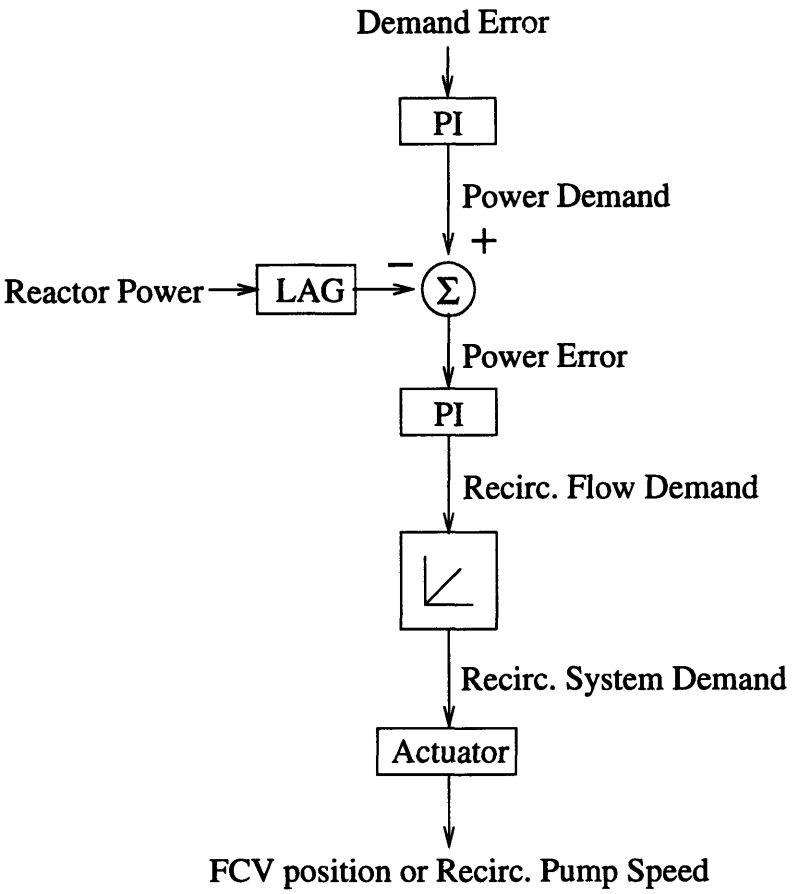

Figure 4-21: Recirculation flow controller.

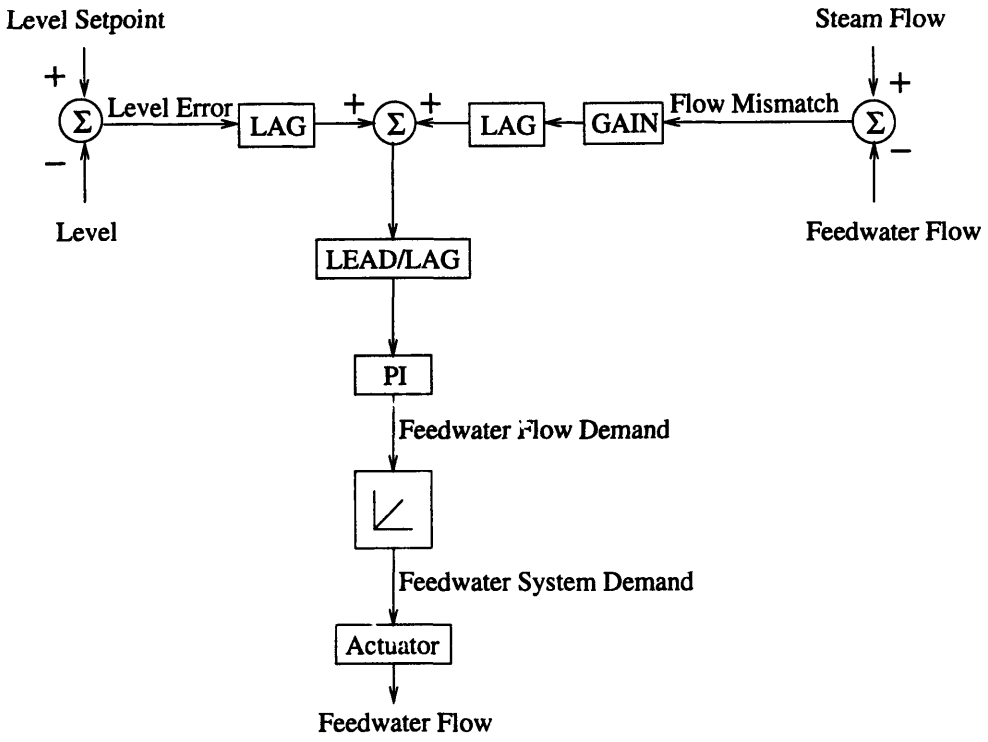

Figure 4-22: Feedwater controller.

The feedwater controller uses three-element control. The level error and the steam and feedwater flow mismatch are filtered and summed. The combined level error then passes through a lead/lag compensator, a PI controller, and gives the feedwater flow demand signal. The feedwater flow demand goes through a function generator and an actuator, and gives the feedwater flow rate. Figure 4-22 shows a schematic of the feedwater controller.

4.6.3 Safety relief valve control

The safety and relief valves are modeled as a single valve. This safety relief valve is opened in steps to simulate the operations of the safety and relief valve banks. The operation of this SRV is governed by the pressure at the first steam line node with an SRV connected. A maximum of ten valve banks can be simulated. For each valve bank, the required inputs are the open and reset pressure set points, P_{soi} and P_{sci}, and the cumulative open fraction when the bank is actuated, f_{srvi} . The speed of

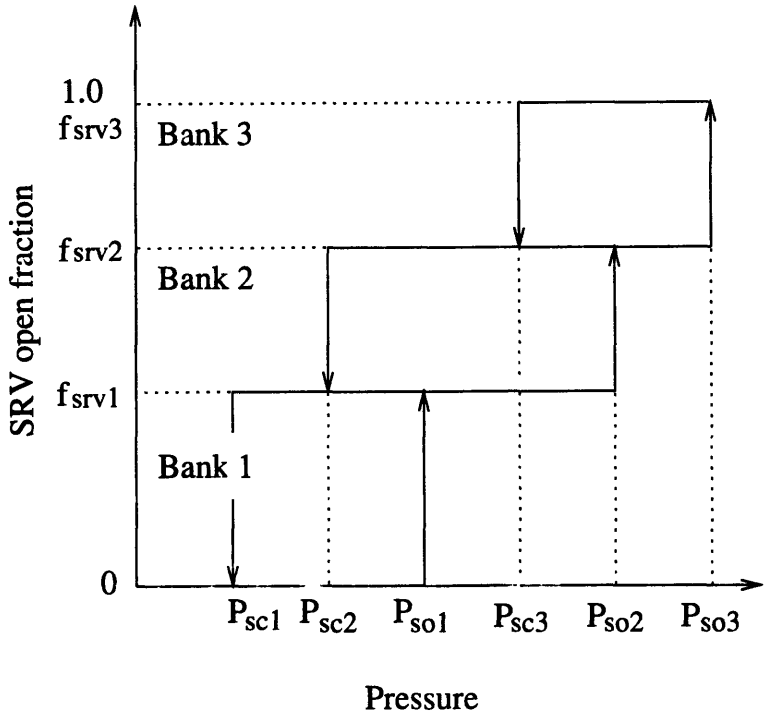

Figure 4-23: The pressure settings of the safety relief valve.

each SRV bank is limited by a maximum valve travel rate. Figure 4-23 shows the SRV settings of a three-bank case.

4.7 Chapter Summary

The models of physical processes simulated in the BWR simulator are presented in this chapter. The features of these models are summarized here.

The thermal-hydraulic model uses a three-equation model. The two-phase separation effects are represented by a drift-flux model. Subcooled boiling is model by a profile-fit. A single pressure assumption is applied. The steam dome is treated with a two-region non-equilibrium model. This thermal hydraulic model has been used to simulate the ANL natural circulation test loop. The calculated stability boundary of the test loop is in good agreement with measured data.

A point kinetics model is used to simulate reactor dynamics. The thermal feedback reactivity is calculated as the weighted sum of local reactivity changes. The decay power is modeled by seven groups of decay heat precursors. This core model is suited for in-phase type instability.

The fuel model uses a two-node fuel conduction model, and considers single-phase and boiling heat transfer regimes. This fuel model gives almost identical results as the THERMIT-2 finite difference fuel model.

Two separate recirculation loop are simulated in the recirculation system model. The system is assumed to have a single density. The pressure gain across the jet pump throat is calculated by momentum mixing. The steady-state characteristics calculated by this jet pump model agree well with the measured data.

The steam line model is based on the assumptions of ideal gas and isentropic flow. Two fast valve closure transients have been studied using this steam line model. One case is a theoretical case with analytical solution. The other is the Peach Bottom-2 turbine trip test TT3. The results calculated by this steam line model are in good agreement with the benchmark results.

Four model controllers are used to provide the necessary boundary conditions to the simulator. These are the reactor pressure controller, recirculation flow controller, feedwater flow controller, and safety relief valve model. Numerical integrations are used to simulate the lead/lag compensators, PID controllers, and second order models of the actuating devices.

The models discussed in this chapter have been integrated into the BWR simulator. The methods used to solve this integrated system of equations in the time domain are described in the next chapter.

Chapter 5

Numerical Solution Method

5.1 Equation Systems and Solution Methods

The models described in Chapter 4 are solved numerically to simulate the response of a BWR. The main equation systems to be solved are

1. core neutronics equations,
2. fuel conduction and convection equations,
3. reactor vessel energy equations,
4. steam dome equations,
5. steam line equations,
6. reactor vessel mass and momentum equations, and
7. recirculation system equations.

The procedures to solve these equation systems are described in this section.

5.1.1 Core neutronics equations

The point kinetics equations (Equations 4.23 and 4.24) and the decay heat equations (Equations 4.25 and 4.26) are solved to give the core heat generation rate. The point

kinetics equations are solved by direct integration of the delay neutron precursor equations, and θ-differencing of the amplitude function equation [58]. Integrating Equation 4.24 from t_n to t_{n+1} , we get

$$C_i^{n+1} = C_i^n \, e^{-\lambda_i \Delta t} + \frac{\beta_i}{\Lambda} e^{-\lambda_i \Delta t} \int_{t_n}^{t_{n+1}} T \, e^{-\lambda_i (t - t_n)} \, dt \, ,$$

where $\Delta t = t_{n+1} - t_n$. Assuming that the amplitude function T varies linearly from t_n to t_{n+1} , then the integral in the above equation can be evaluated analytically to give

$$C_i^{n+1} = k_{1,i} C_i^n + k_{2,i} \frac{\beta_i}{\lambda_i \Lambda} T^{n+1} - k_{3,i} \frac{\beta_i}{\lambda_i \Lambda} T^n,$$

where

$$k_{1,i} = e^{-\lambda_i \Delta t},$$
$$k_{2,i} = 1 - \frac{1 - e^{-\lambda_i \Delta t}}{\lambda_i \Delta t}, \text{ and}$$
$$k_{3,i} = e^{-\lambda_i \Delta t} - \frac{1 - e^{-\lambda_i \Delta t}}{\lambda_i \Delta t}.$$

Define $pc_i = \lambda_i C_i$. Then

$$pc_i^{n+1} = k_{1,i} \, pc_i^n + k_{2,i} \frac{\beta_i}{\Lambda} T^{n+1} - k_{3,i} \frac{\beta_i}{\Lambda} T^n. \tag{5.1}$$

The equation of the amplitude function (Equation 4.23) is discretized in time by the θ-method:

$$\frac{T^{n+1} - T^n}{\Delta t} = \theta \left(\frac{\rho - \beta}{\Lambda} T + \sum_{i=1}^{6} \lambda_i C_i \right)^{n+1} + (1 - \theta) \left(\frac{\rho - \beta}{\Lambda} T + \sum_{i=1}^{6} \lambda_i C_i \right)^{n} , \tag{5.2}$$

where θ is a parameter that determines the degree of implicitness of the finite difference scheme. $\theta = 1$ gives a fully implicit scheme, and $\theta = 0.5$ gives a semi-implicit scheme.

Substituting Equation 5.1 into Equation 5.2 and rearranging terms, we get

$$\begin{aligned}
&\left[1-\frac{\theta\Delta t}{\Lambda}\left(\rho^{n+1}-\beta+\sum_{i=1}^{6}\beta_i\,k_{2,i}\right)\right]T^{n+1} \\
&= \left\{1+\frac{\Delta t}{\Lambda}\left[(1-\theta)\,(\rho^n-\beta)-\theta\sum_{i=1}^{6}\beta_i\,k_{3,i}\right]\right\}T^n \\
&+ \theta\,\Delta t\sum_{i=1}^{6}\left[1+\theta\,(k_{1,i}-1)\right]pc_i^n\ .
\end{aligned} \tag{5.3}$$

The parameter θ is selected according to the magnitude of the reactivity ρ . The fully implicit scheme is used when $\rho < \beta$, and the semi-implicit scheme is used when $\rho \geq \beta$.

An adaptive procedure is used when calculating the amplitude function. An amplitude function T_0^{n+1} is first calculated using a time step size of Δt. Another amplitude function T_1^{n+1} is calculated using a time step size of $\frac{\Delta t}{2}$. If $\left|\frac{T_1^{n+1}-T_0^{n+1}}{T_0^{n+1}}\right| \leq 5\times10^{-4}$, then the procedure stops. Otherwise, the time step size is reduced in half again, and another amplitude function is calculated. This procedure continues until the amplitude function is converged, or until the time step size is smaller than 0.1 ms.

The decay heat precursor equations (Equation 4.26) are also solved by direct integration with the assumption that the total fission power, which is proportional to the amplitude function, varies linearly with time. Define $cd^i = \lambda_D^i C_D^i$. We get

$$\left(cd^i\right)^{n+1} = kd_{1,i}\left(cd^i\right)^n + f_D\beta_D^i\left[kd_{2,i}\left(P_n\right)^{n+1} - kd_{3,i}\left(P_n\right)^n\right]\ ,$$

where

$$kd_{1,i} = e^{-\lambda_D^i\Delta t},$$

$$kd_{2,i} = 1-\frac{1-e^{-\lambda_D^i\Delta t}}{\lambda_D^i\Delta t}, \text{ and}$$

$$k_{3,i} = e^{-\lambda_D^i\Delta t}-\frac{1-e^{-\lambda_D^i\Delta t}}{\lambda_D^i\Delta t}.$$

The decay power at t_{n+1} is calculated from Equation 4.25:

$$(P_D)^{n+1} = \sum_{i=1}^{7} \left(cd^i\right)^{n+1}.$$

The total core power is then

$$(P)^{n+1} = (1 - f_D)\,(P_n)^{n+1} + (P_D)^{n+1}.$$

5.1.2 Fuel conduction and convection equations

The fuel conduction and convection equations for each fuel node are solved to give the average fuel temperature for Doppler reactivity calculation, and to give the heat transfer rate from the fuel rods to the coolant. The solution method described below follows the work by Cabral [45]. The volumetric heat deposition rate in the fuel region of each fuel node (q'''_f) is calculated from the total core power and a user-specified power distribution. Equations 4.39 and 4.40 are discretized in time by semi-implicit finite differencing:

$$V_{f1}\,(\overline{\rho c_p})_f^n \left(\frac{T_1^{n+1} - T_1^n}{\Delta t}\right) = V_{f1}\left(q'''_f\right)^{n+1} - (UA)_{12}\left(T_1^{n+1} - T_2^{n+1}\right); \tag{5.4}$$

$$\begin{aligned} &\left[V_{f2}\,(\overline{\rho c_p})_f^n + V_c\,(\overline{\rho c_p})_c^n\right]\left(\frac{T_2^{n+1} - T_2^n}{\Delta t}\right) \\ = \;& V_{f2}\left(q'''_f\right)^{n+1} + (UA)_{12}\left(T_1^{n+1} - T_2^{n+1}\right) - Q_w^{n+1}\,. \end{aligned} \tag{5.5}$$

Linearizing the wall heat transfer rate with respect to the wall temperature, we have

$$Q_w^{n+1} = Q_w^n + \left(\frac{\partial Q_w}{\partial T_w}\right)^n \left(T_w^{n+1} - T_w^n\right). \tag{5.6}$$

From Equation 4.37 and using the old heat transfer coefficient, we get

$$Q_w^{n+1} = (UA)_{2w}^n \left(T_2^{n+1} - T_w^{n+1}\right). \tag{5.7}$$

Eliminating T_w^{n+1} by combining Equations 5.6 and 5.7, we arrive at

$$Q_w^{n+1} = \left[1 + \frac{(\partial Q_w / \partial T_w)^n}{(UA)_{2w}^n}\right]^{-1} \left[Q_w^n + \left(\frac{\partial Q_w}{\partial T_w}\right)^n \left(T_2^{n+1} - T_w^n\right)\right] . \qquad (5.8)$$

A two-step procedure is used to solve these equations. First, Equations 5.4, 5.5, 5.7, and 5.8 are solved to get predicted values $T_1^{n+\frac{1}{2}}$, $T_2^{n+\frac{1}{2}}$, $T_w^{n+\frac{1}{2}}$, and $Q_w^{n+\frac{1}{2}}$. The average temperatures and properties of fuel, gap, and cladding are updated by using these predicted values. The new heat transfer coefficients $(UA)_{12}^{n+1}$, and $(UA)_{2w}^{n+1}$ are calculated from Equations 4.33 and 4.38. Then $\left(\frac{\partial Q_w}{\partial T_w}\right)^{n+\frac{1}{2}}$ is calculated from Equations 4.41 or 4.42 using $T_w^{n+\frac{1}{2}}$. So,

$$\left(\frac{\partial Q_w}{\partial T_w}\right)^{n+\frac{1}{2}} = \begin{cases} 2\pi r_w \Delta z\, h & \text{if } T_w^{n+\frac{1}{2}} \le T_{sat}^n , \\ 2\pi r_w \Delta z\, h \left[h_{FC} + h_{NB} + \left(T_w^{n+\frac{1}{2}} - T_{sat}^n\right)\left(\frac{\partial h_{NB}}{\partial T_w}\right)\right] & \text{if } T_w^{n+\frac{1}{2}} > T_{sat}^n . \end{cases}$$

The second step solves Equations 5.4, 5.5, 5.7, and 5.8 again using $\left(\frac{\partial Q_w}{\partial T_w}\right)^{n+\frac{1}{2}}$ and updated material properties to get the corrected values T_1^{n+1}, T_2^{n+1}, T_w^{n+1}, and Q_w^{n+1}. T_w^{n+1} is then used to calculate $\left(\frac{\partial Q_w}{\partial T_w}\right)^{n+1}$, which is used in the calculations for t_{n+2} . The average fuel temperature is recalculated using T_1^{n+1} and T_2^{n+1}.

5.1.3 Reactor vessel energy equation system

The energy equations of reactor vessel nodes have been decoupled from the momentum equations by the single pressure assumption. These energy equations are combined with the overall vessel mass equation to form the vessel energy equation system. The nodalization of the reactor vessel is described by three indices:

1. NCH, which is the number of core channels, $NCH = 1$ or 2;

2. $NC1$, which is the number of axial nodes in channel 1;

3. $NC2$, which is the number of axial nodes in channel 2, $NC2 = 0$ for $NCH = 1$.

The total number of nodes in the reactor vessel, excluding the steam dome, is

$$NT = NC1 + NC2 + 6.$$

NT is limited to be less than 50. $NT = NC1 + 6$ for one channel cases. The total number of flow paths connecting the nodes is

$$NJ = NT + NCH - 1,$$

and

$$NJ = \begin{cases} NT & \text{when } NCH = 1, \\ NT + 1 & \text{when } NCH = 2. \end{cases}$$

The assignment of the indices of nodes and flow paths is illustrated in Figure 5-1. The outlet flow path of a node has the same index as the node. The flow path NJ exists only when two core channels are used.

For normal nodes, Equation 4.17 is discretized to give

$$\begin{aligned} & V_i \left\{ \left[\left(\frac{\partial e_i}{\partial h_{i-1}} \right) - \overline{h}_i \left(\frac{\partial m_i}{\partial h_{i-1}} \right) + \left(\frac{\partial e_i}{\partial h_i} \right) - \overline{h}_i \left(\frac{\partial m_i}{\partial h_i} \right) \right]^n \frac{\Delta h_i}{\Delta t} \right. \\ + & \left. \left[\left(\frac{\partial e_i}{\partial P} \right) - \overline{h}_i \left(\frac{\partial m_i}{\partial P} \right) - 1 \right]^n \frac{\Delta P}{\Delta t} \right\} \\ = & \; q_i^{n+1} + W_{i-1}^n \left[\left(h'_{i-1} \right)^n + \left(\frac{\partial h'}{\partial h} \right)_{i-1}^n \Delta h_{i-1} - \overline{h}_i^n \right] \\ - & \; W_i^n \left[(h'_i)^n + \left(\frac{\partial h'}{\partial h} \right)_i^n \Delta h_i - \overline{h}_i^n \right] , \end{aligned} \tag{5.9}$$

where Δ stands for the difference between new and old state variables, i.e., $\Delta P = P^{n+1} - P^n$. In the above equation, the flowing enthalpy are linearized with respect

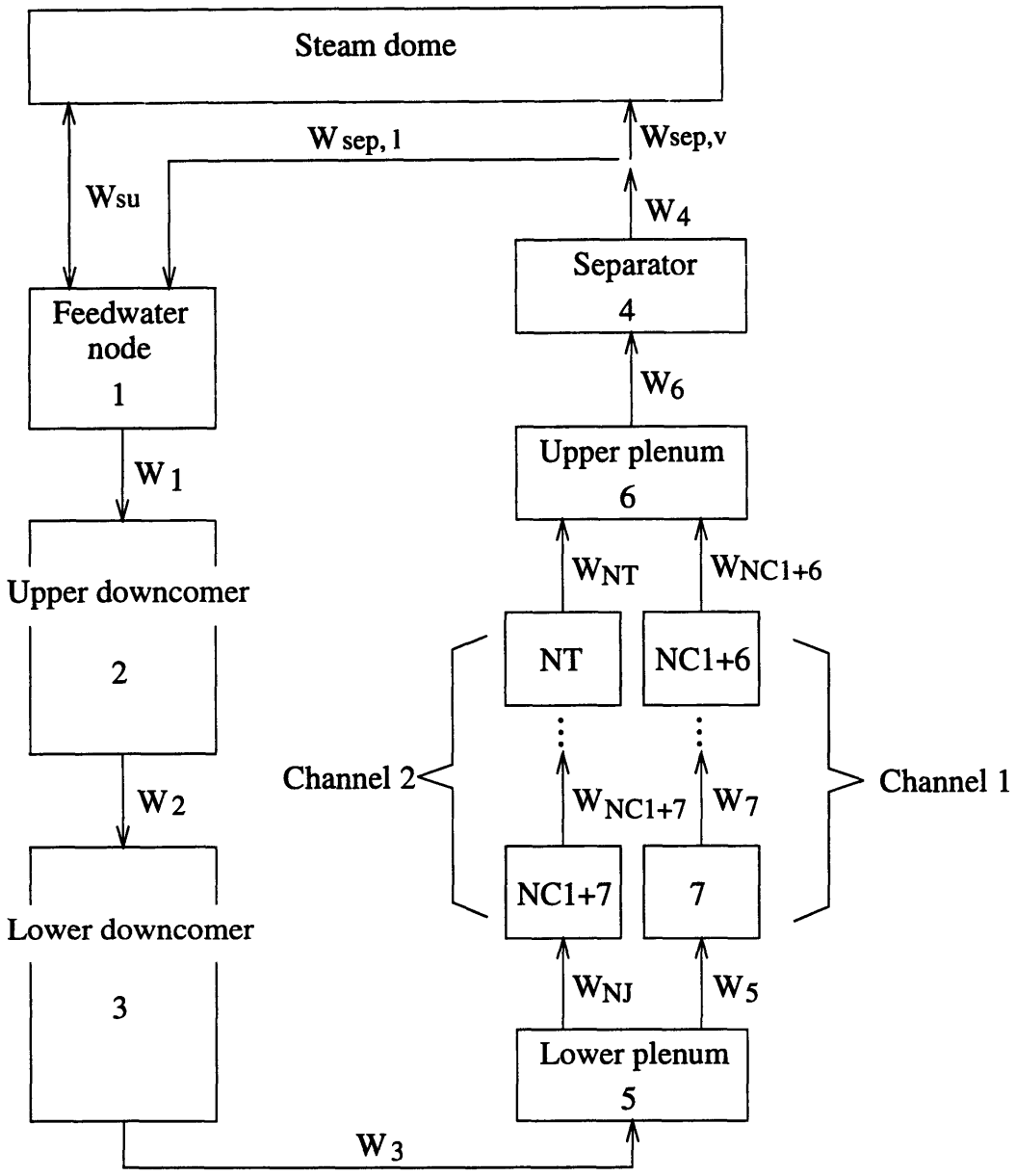

Figure 5-1: Designation of the indices of nodes and flow paths.

to the mixture enthalpy [41]. And

$$\frac{\partial h'}{\partial h} = \begin{cases} 1 & \text{for single-phase flows,} \\ \dfrac{C0 + \rho_f u_{gj} \left(\dfrac{A}{W}\right)}{\left[1 - (1 - C0)\left(1 - \dfrac{\rho_f}{\rho_g}\right)\left(\dfrac{h - h_f}{h_{fg}}\right)\right]^2} & \text{for two-phase flows,} \end{cases}$$

where $C0$ and u_{gj} are the distribution parameter and drift velocity contained in the drift-flux correlation.

Rearranging and collecting terms, we get

$$\begin{aligned} & - \left[W\left(\frac{\partial h'}{\partial h}\right)\right]_{i-1}^{n} \Delta h_{i-1} + \left\{\frac{(f0)_i^n + (f1)_i^n}{\Delta t} + \left[W\left(\frac{\partial h'}{\partial h}\right)\right]_i^n\right\} \Delta h_i + \frac{g_i^n}{\Delta t} \Delta P \\ & = q_i^{n+1} + W_{i-1}^n \left[\left(h'_{i-1}\right)^n - \overline{h}_i^n\right] - W_i^n \left[\left(h'_i\right)^n - \overline{h}_i^n\right] , \end{aligned} \tag{5.10}$$

where

$$\begin{aligned} (f0)_i^n &= V_i \left[\left(\frac{\partial e_i}{\partial h_{i-1}}\right) - \overline{h}_i \left(\frac{\partial m_i}{\partial h_{i-1}}\right)\right]^n , \\ (f1)_i^n &= V_i \left[\left(\frac{\partial e_i}{\partial h_i}\right) - \overline{h}_i \left(\frac{\partial m_i}{\partial h_i}\right)\right]^n , \text{ and} \\ g_i^n &= V_i \left[\left(\frac{\partial e_i}{\partial P}\right) - \overline{h}_i \left(\frac{\partial m_i}{\partial P}\right) - 1\right]^n . \end{aligned}$$

Notice that the discretized form of Equation 4.16 is very similar to the above equation. For the coupled form of the energy equation, the coefficient of the Δh_{i-1} term is

$$\frac{(f0)_i^n}{\Delta t} - \left[W\left(\frac{\partial h'}{\partial h}\right)\right]_{i-1}^n ,$$

and the coefficient of the Δh_i term is

$$\frac{(f1)_i^n}{\Delta t} + \left[W\left(\frac{\partial h'}{\partial h}\right)\right]_i^n .$$

The energy equation of mixing nodes, Equation 4.19, is discretized in time in the same manner:

$$
\begin{aligned}
&- \sum \left[W \left(\frac{\partial h'}{\partial h} \right) \right]_{in}^{n} \Delta h_{in} + \left\{ \frac{V_i m_i^n}{\Delta t} + \sum \left[W \left(\frac{\partial h'}{\partial h} \right) \right]_{out}^{n} \right\} \Delta \overline{h}_i - \frac{V_i}{\Delta t} \Delta P \\
&= q_i^{n+1} + \sum W_{in}^n \left[(h'_{in})^n - \overline{h}_i^n \right] - \sum W_{out}^n \left[(h'_{out})^n - \overline{h}_i^n \right] .
\end{aligned}
\tag{5.11}
$$

The discretized mass equation for normal nodes is

$$
\frac{\Delta M_i}{\Delta t} = a_i^n \frac{\Delta h_{i-1}}{\Delta t} + b_i^n \frac{\Delta h_i}{\Delta t} + c_i^n \frac{\Delta P}{\Delta t} = W_{i-1}^{n+1} - W_i^{n+1} , \tag{5.12}
$$

where

$$
a_i^n = V_i \left(\frac{\partial m_i}{\partial h_{i-1}} \right)^n ,
$$

$$
b_i^n = V_i \left(\frac{\partial m_i}{\partial h_i} \right)^n , \text{ and}
$$

$$
c_i^n = V_i \left(\frac{\partial m_i}{\partial P} \right)^n .
$$

For the mixing nodes, the mass equation becomes

$$
\frac{\Delta M_i}{\Delta t} = \frac{V_i}{\Delta t} \left(\frac{\partial m_i}{\partial \overline{h}_i} \right)^n \Delta \overline{h}_i + \frac{V_i}{\Delta t} \left(\frac{\partial m_i}{\partial P} \right)^n \Delta P = \sum W_{in}^{n+1} - \sum W_{out}^{n+1} . \tag{5.13}
$$

For the feedwater node, the surge flow from the steam dome is used as a state variable. So the mass equation of the feedwater node is

$$
\frac{V_1}{\Delta t} \left(\frac{\partial m}{\partial \overline{h}} \right)_1^n \Delta \overline{h}_1 + \frac{V_1}{\Delta t} \left(\frac{\partial m}{\partial P} \right)_1^n \Delta P - \Delta W_{su} = W_{su}^n + W_{sep.l}^{n+1} + W_{FW}^{n+1} - W_1^{n+1} .
$$

And the energy equation of the feedwater node becomes

$$
\begin{aligned}
&- \sum \left[W \left(\frac{\partial h'}{\partial h} \right) \right]_{in}^{n} \Delta h_{in} + \left\{ \frac{V_1 m_1^n}{\Delta t} + \sum \left[W \left(\frac{\partial h'}{\partial h} \right) \right]_{out}^{n} \right\} \Delta \overline{h}_1 \\
&- \frac{V_1}{\Delta t} \Delta P - \left(h_{su}^n - \overline{h}_1^n \right) \Delta W_{su} \\
&= W_{FW}^{n+1} \left[(h'_{FW})^{n+1} - \overline{h}_1^n \right] + W_{su}^n \left[h_{su}^n - \overline{h}_1^n \right] \\
&+ W_{sep,l}^n \left[\left(h'_{sep,l} \right)^n - \overline{h}_1^n \right] - W_1^n \left[(h'_1)^n - \overline{h}_1^n \right] ,
\end{aligned}
\tag{5.14}
$$

where $h'_{sep,l} = h_f + cu\, h_{fg}$.

The overall mass equation of the reactor vessel excluding the steam dome is the sum of the mass equations of all the nodes:

$$
\begin{aligned}
&\sum_{\text{mixing nodes}} \left[\frac{V_i}{\Delta t} \left(\frac{\partial m_i}{\partial \overline{h}_i} \right)^n \Delta \overline{h}_i + \frac{V_i}{\Delta t} \left(\frac{\partial m_i}{\partial P} \right)^n \Delta P \right] \\
&+ \sum_{\text{normal nodes}} \left(a_i^n \frac{\Delta h_{i-1}}{\Delta t} + b_i^n \frac{\Delta h_i}{\Delta t} + c_i^n \frac{\Delta P}{\Delta t} \right) - \Delta W_{su} \\
&= W_{FW}^{n+1} + W_{su}^n - W_{sep,v}^n .
\end{aligned}
\tag{5.15}
$$

Notice that the value of the vapor flow rate from the separator to the steam dome at t_n is used.

The partial derivatives of normal nodes $\frac{\partial m_i}{\partial h_{i-1}}$, $\frac{\partial m_i}{\partial h_i}$, $\frac{\partial e_i}{\partial h_{i-1}}$, and $\frac{\partial e_i}{\partial h_i}$ are singular when $h_{i-1} = h_i$. To circumvent this singularity, when h_{i-1} and h_i are close, these partial derivatives are evaluated with the expressions of the partial derivatives of mixing nodes:

For $|h_i - h_{i-1}| \geq 500$ J/kg , Equations 4.12 to 4.15 are used to evaluate $\frac{\partial m_i}{\partial h_{i-1}}$, $\frac{\partial m_i}{\partial h_i}$, $\frac{\partial e_i}{\partial h_{i-1}}$, and $\frac{\partial e_i}{\partial h_i}$.

For $|h_i - h_{i-1}| \leq 100$ J/kg ,

$$
\frac{\partial m_i}{\partial h_{i-1}} = \frac{\partial m_i}{\partial h_i} = \frac{1}{2} \frac{\partial \rho}{\partial h} \bigg|_{h_i} ,
$$

and

$$\frac{\partial e_i}{\partial h_{i-1}} = \frac{\partial e_i}{\partial h_i} = \frac{1}{2}\left[h_i\left(\frac{\partial \rho}{\partial h}\Big|_{h_i}\right) + \rho_i\right] .$$

For 100 J/kg $< |h_i - h_{i-1}| <$ 500 J/kg , a linear interpolation between the above two cases is used.

Equations 5.9, 5.11, and 5.15 form the reactor vessel energy equation system

$$[EM]^n \, \Delta [XE] = [EB]^n \ , \tag{5.16}$$

where

$\Delta [XE] = [\Delta XE(1), \Delta XE(2), \cdots, \Delta XE(NT), \Delta P, \Delta W_{su}]^T$,

$XE(i)$ is the state variable of the energy equation of node i ,

$[EM]$ is a $(NT+1) \times (NT+2)$ matrix, and

$[EB]$ is a $(NT+1) \times 1$ column vector.

The state variables $XE(i)$ and the structure of $[EM]$ depend on the flow pattern in the reactor vessel. Appendix B.1 gives the details of the reactor vessel energy equation system.

The discretized mass equations, Equations 5.12 and 5.13, give the change rates of mass in the nodes, $\frac{\Delta M_i}{\Delta t}$. These mass change rates are used in conjunction with the momentum integral equation to give the flow distribution in the reactor vessel.

5.1.4 Steam dome equation system

The mass and energy equations of the vapor and liquid regions described in section 4.1.3 are discretized in time. The steam and surge flow rates are also used as state variables. We have

vapor mass

$$\frac{V_v}{\Delta t}\left(\frac{\partial \rho_v}{\partial h_v}\right)^n \Delta h_v + \frac{V_v}{\Delta t}\left(\frac{\partial \rho_v}{\partial P}\right)^n \Delta P + \frac{\rho_v^n}{\Delta t}\Delta V_v$$
$$= W_{sep,v}^n + W_{fl}^{n+1} - (W_s^n + \Delta W_s) - W_{ro}^{n+1} - W_{wc}^{n+1} \ ;$$

liquid mass

$$\frac{V_l}{\Delta t}\left(\frac{\partial \rho_l}{\partial h_l}\right)^n \Delta h_l + \frac{V_l}{\Delta t}\left(\frac{\partial \rho_l}{\partial P}\right)^n \Delta P - \frac{\rho_l^n}{\Delta t}\Delta V_v$$
$$= W_{ro}^{n+1} + W_{wc}^{n+1} - W_{fl}^{n+1} - (W_{su}^n + \Delta W_{su}) \ ;$$

vapor energy

$$\frac{V_v}{\Delta t}\left[\rho_v + \left(h_v - \overline{h}_{SD}\right)\left(\frac{\partial \rho_v}{\partial h_v}\right)\right]^n \Delta h_v + \frac{V_v}{\Delta t}\left[\left(h_v - \overline{h}_{SD}\right)\left(\frac{\partial \rho_v}{\partial P}\right) - 1\right]^n \Delta P$$
$$+ \frac{\rho_v^n}{\Delta t}\left(h_v - \overline{h}_{SD}\right)^n \Delta V_v$$
$$= \left(W_{sep,v}^n + W_{fl}^{n+1}\right)\left[h_g^n + \left(\frac{\partial h_g}{\partial P}\right)^n \Delta P - \overline{h}_{SD}^n\right]$$
$$- \left[(W_s^n + \Delta W_s) + W_{wc}^{n+1}\right]\left(h_v^n + \Delta h_v - \overline{h}_{SD}^n\right)$$
$$- W_{ro}^{n+1}\left[h_f^n + \left(\frac{\partial h_f}{\partial P}\right)^n \Delta P - \overline{h}_{SD}^n\right] \ ;$$

liquid energy

$$
\begin{aligned}
& \frac{V_l}{\Delta t}\left[\rho_l + \left(h_l - \overline{h}_{SD}\right)\left(\frac{\partial \rho_l}{\partial h_l}\right)\right]^n \Delta h_l + \frac{V_l}{\Delta t}\left[\left(h_l - \overline{h}_{SD}\right)\left(\frac{\partial \rho_l}{\partial P}\right) - 1\right]^n \Delta P \\
- \; & \frac{\rho_l^n}{\Delta t}\left(h_l - \overline{h}_{SD}\right)^n \Delta V_v \\
= \; & \left(W_{ro}^{n+1} + W_{wc}^{n+1}\right)\left[h_f^n + \left(\frac{\partial h_f}{\partial P}\right)^n \Delta P - \overline{h}_{SD}^n\right] \\
- \; & \left(W_{su}^n + \Delta W_{su}\right)\left(h_{su}^n - \overline{h}_{SD}^n\right) \\
- \; & W_{fl}^{n+1}\left[h_g^n + \left(\frac{\partial h_g}{\partial P}\right)^n \Delta P - \overline{h}_{SD}^n\right].
\end{aligned}
$$

Additional relations for the steam dome model depending on the vapor and liquid enthalpies are listed in Table 4.1. These relations and the mass and energy equations form the steam dome equation system:

$$[A_{SD}]^n \, \Delta \left[X_{SD}\right] = [R_{SD}]^n , \tag{5.17}$$

where

$[A_{SD}]$ is a 4×6 matrix,

$\Delta[X_{SD}]$ is a 6×1 column vector, and

$[R_{SD}]$ is a 4×1 column vector.

The state variables and the elements in the steam dome equation system depend on the condition of the vapor and liquid enthalpies and are given in Appendix B.2.

5.1.5 Steam line equation system

Discretizing Equations 4.59 and 4.60, we get

$$\frac{V_i}{\gamma}\left(\frac{\rho_0}{P_0}\right)\left(\frac{P_0}{P_i^n}\right)^{\left(\frac{\gamma-1}{\gamma}\right)} \frac{\Delta P_i}{\Delta t} = \sum_j \left(W_j^n + \Delta W_j\right),$$

and

$$\frac{1}{2}\left[\left(\frac{\ell}{A}\right)_i + \left(\frac{\ell}{A}\right)_{i+1}\right]\frac{\Delta W_i}{\Delta t} = (P^n + \Delta P)_i - (P^n + \Delta P)_{i+1} - \frac{1}{2}\left[\left(\frac{f\,\ell}{D\,A^2}\right)_i + \left(\frac{f\,\ell}{D\,A^2}\right)_{i+1}\right]^n \frac{|W_i^n|\,(W_i^n + \Delta W_i)}{2\,\rho_{i+\frac{1}{2}}^n} - \left[\frac{K_i}{A_{i+\frac{1}{2}}^2} + \frac{c_{v,i}}{\left(A_{v,i}^{n+1}\right)^2}\right]\frac{|W_i^n|\,(W_i^n + \Delta W_i)}{2\,\rho_{i+\frac{1}{2}}^n}.$$

Taking the steam dome pressure as a state variable, the steam line equation system is

$$[STMA]^n\,\Delta\,[XS] = [STMR]^n\,, \tag{5.18}$$

where

$\Delta\,[XS] = [\Delta P_1, \cdots, \Delta P_7, \Delta W_1, \cdots, \Delta W_6, \Delta W_{TCV}, \Delta W_s, \Delta P]^T$, the indices of the state variables are indicated in Figure 4-16,

$[STMA]$ is a 15×16 matrix, and

$[STMR]$ is a 15×1 column vector.

The details of the steam line equation system are given in Appendix B.3

If the openings of MSIV or TCV are less than 1% of their full-open flow areas, $[STMA]$ and $[STMR]$ are modified to make the flow rate through the valve equals zero.

5.1.6 Reactor vessel mass and momentum equation system

The mass equations of reactor nodes and the momentum integral equation are solved together to get the flow rate for each individual flow path in the vessel. The mass equation of the feedwater node is not used. The mass equations used here are

$$\frac{\Delta M_i}{\Delta t} = \sum_j \left(W_j^n + \Delta W_j\right).$$

$\frac{\Delta M_i}{\Delta t}$ is calculated form Equations 5.12 or 5.13 after the vessel energy equation system is solved.

The integration of the momentum equation is done in two sections. The first section starts from inside the inlet of the upper plenum, up through the separator, follows the liquid path of the separator outlet to the feedwater node, down through the upper and lower downcomer nodes, and ends at the inside of the outlet of the lower plenum. The second section starts from the inside of the outlet of the lower plenum, follows one of the core channels, and ends at the inside of the inlet of the upper plenum. Let P_{core} be the pressure difference across the second section. If there are two core channels, then the integration of momentum equation along these two channels must give the same P_{core} . The discretized momentum integral equation along the first section, taking into account the gravity head of the steam dome water level, becomes

$$\begin{aligned}\sum_{i=1-4,6} I_i \frac{\Delta W_i}{\Delta t} &= -(P^n + \Delta P)_{core} + (P^n + \Delta P)_{jet} \\ &- \sum_{i=1-4,6} (F_{fr} + F_{loss} + F_{acc})^n (W^n + \Delta W)_i \\ &- \sum_{i=1}^{6} m_i^n g \Delta z_i + \rho_l^n g L_{SD}^n ,\end{aligned}$$

where

I_i is the flow inertia associated with flow path i,

F_{fr}, F_{loss}, F_{acc} are the pressure loss factors due to friction, form loss, and spatial acceleration,

ρ_l is the liquid density in the steam dome, and

L_{SD} is the water level in the steam dome.

The integration of the momentum equation along the second section and through

the first core channel gives

$$\begin{aligned}\sum_{i=5,7-(NC1+6)} I_i \frac{\Delta W_i}{\Delta t} &= (P^n + \Delta P)_{core} \\ &- \sum_{i=5,7-(NC1+6)} (F_{fr} + F_{loss} + F_{acc})^n (W^n + \Delta W)_i \\ &- \sum_{i=7}^{NC1+6} m_i^n g \Delta z_i \ .\end{aligned}$$

And the integration along the second core channel gives

$$\begin{aligned}\sum_{i=NC1+7}^{NJ} I_i \frac{\Delta W_i}{\Delta t} &= (P^n + \Delta P)_{core} \\ &- \sum_{i=NC1+7}^{NJ} (F_{fr} + F_{loss} + F_{acc})^n (W^n + \Delta W)_i \\ &- \sum_{i=NC1+7}^{NT} m_i^n g \Delta z_i \ .\end{aligned}$$

The flow rate inside a single-inlet, single-outlet node is assumed to vary linearly from the inlet to the outlet. The flow rate inside a multi-inlet/outlet node is assumed to be uniform. The flow rate inside the feedwater node is assumed to be W_1; and the flow rates inside the lower and upper plena are assumed to be W_3 and W_6, respectively. The temporal acceleration and friction terms are calculated using the average flow rate of a node. The expressions of I_i, $F_{fr,i}$, and $F_{acc,i}$ are listed in Tables 5.1, 5.2, and 5.3. The expression of $F_{loss,i}$ is

$$F_{loss,i} = \left(\frac{K\,|W|}{2\rho' A^2} \right)_i \ .$$

Combining the mass and momentum equations into matrix form, we get

$$[AM]^n \, \Delta \, [XM] = [AB]^n \, , \tag{5.19}$$

where

$$\Delta \, [XM] = [\Delta W_1, \, \Delta W_2, \, \Delta W_4, \cdots, \, \Delta W_{NJ}, \, \Delta P_{core}, \, \Delta P_{jet}, \, \Delta W_3]^T \, ,$$

Table 5.1: The expression of I_i

i	I_i
1	$\left(\frac{\ell}{A}\right)_1 + \frac{1}{2}\left(\frac{\ell}{A}\right)_2$
2	$\frac{1}{2}\left[\left(\frac{\ell}{A}\right)_2 + \left(\frac{\ell}{A}\right)_3\right]$
3	$\frac{1}{2}\left(\frac{\ell}{A}\right)_3 + \left(\frac{\ell}{A}\right)_5$
4	$\frac{1}{2}I_{sep}$
5	$\frac{1}{2}\left(\frac{\ell}{A}\right)_7$
6	$\frac{1}{2}I_{sep} + \left(\frac{\ell}{A}\right)_6$
$7\text{-}(NC1+5)$, $(NC1+7)\text{-}(NT-1)$	$\frac{1}{2}\left[\left(\frac{\ell}{A}\right)_i + \left(\frac{\ell}{A}\right)_{i+1}\right]$
$NC1+6$	$\frac{1}{2}\left(\frac{\ell}{A}\right)_{NC1+6}$
NT	$\frac{1}{2}\left(\frac{\ell}{A}\right)_{NT}$
NJ	$\frac{1}{2}\left(\frac{\ell}{A}\right)_{NC1+7}$

Note: I_{sep} is the separator inertia given by the empirical correlation.

Table 5.2: The expression of $F_{fr,i}$

i	$F_{fr,i}$
1	$\left(\frac{f\ell}{DA^2}\frac{\lvert W\rvert}{2\overline{\rho}}\right)_1 + \left(\frac{f\ell}{DA^2}\right)_2 \frac{\lvert W_1+W_2\rvert}{8\overline{\rho}_2}$
2	$\left(\frac{f\ell}{DA^2}\right)_2 \frac{\lvert W_1+W_2\rvert}{8\overline{\rho}_2} + \left(\frac{f\ell}{DA^2}\right)_3 \frac{\lvert W_2+W_3\rvert}{8\overline{\rho}_3}$
3	$\left(\frac{f\ell}{DA^2}\right)_3 \frac{\lvert W_2+W_3\rvert}{8\overline{\rho}_3} + \left(\frac{f\ell}{DA^2}\right)_5 \frac{\lvert W_3\rvert}{2\overline{\rho}_5}$
4	$\left(\frac{f\ell}{DA^2}\right)_4 \frac{\lvert W_4+W_6\rvert}{8\overline{\rho}_4}$
5	$\left(\frac{f\ell}{DA^2}\right)_7 \frac{\lvert W_5+W_7\rvert}{8\overline{\rho}_7}$
6	$\left(\frac{f\ell}{DA^2}\right)_4 \frac{\lvert W_4+W_6\rvert}{8\overline{\rho}_4} + \left(\frac{f\ell}{DA^2}\right)_6 \frac{\lvert W_6\rvert}{2\overline{\rho}_6}$
7	$\left(\frac{f\ell}{DA^2}\right)_7 \frac{\lvert W_5+W_7\rvert}{8\overline{\rho}_7} + \left(\frac{f\ell}{DA^2}\right)_8 \frac{\lvert W_7+W_8\rvert}{8\overline{\rho}_8}$
$8\text{–}(NC1+5)$, $(NC1+8)\text{–}(NT-1)$	$\left(\frac{f\ell}{DA^2}\right)_i \frac{\lvert W_{i-1}+W_i\rvert}{8\overline{\rho}_i} + \left(\frac{f\ell}{DA^2}\right)_{i+1} \frac{\lvert W_i+W_{i+1}\rvert}{8\overline{\rho}_{i+1}}$
$NC1+6$	$\left(\frac{f\ell}{DA^2}\right)_{i+1} \frac{\lvert W_i+W_{i+1}\rvert}{8\overline{\rho}_{i+1}}$
$NC1+7$	$\left(\frac{f\ell}{DA^2}\right)_{NC1+7} \frac{\lvert W_{NC1+7}+W_{NJ}\rvert}{8\overline{\rho}_{NC1+7}} + \left(\frac{f\ell}{DA^2}\right)_{NC1+8} \frac{\lvert W_{NC1+7}+W_{NC1+8}\rvert}{8\overline{\rho}_{NC1+8}}$
NT	$\left(\frac{f\ell}{DA^2}\right)_{NT} \frac{\lvert W_{NT-1}+W_{NT}\rvert}{8\overline{\rho}_{NT}}$
NJ	$\left(\frac{f\ell}{DA^2}\right)_{NC1+7} \frac{\lvert W_{NC1+7}+W_{NJ}\rvert}{8\overline{\rho}_{NC1+7}}$

Table 5.3: The expression of $F_{acc,i}$

i	$F_{acc,i}$
$1, 2, 7\text{–}(NC1+5)$, $(NC1+7)\text{–}(NT-1)$	$\frac{1}{2}\left(\frac{W}{\rho'}\right)_i\left(\frac{1}{A_i^2}-\frac{1}{A_{i+1}^2}\right)$
3	0
4	$\frac{1}{2}\left(\frac{W}{\rho'}\right)_4\left(\frac{1}{A_4^2}-\frac{1}{A_1^2}\right)$
5	$\frac{1}{2}\left(\frac{W}{\rho'}\right)_5\left(\frac{1}{A_5^2}-\frac{1}{A_7^2}\right)$
6	$\frac{1}{2}\left(\frac{W}{\rho'}\right)_6\left(\frac{1}{A_6^2}-\frac{1}{A_4^2}\right)$
$NC1+6$	$\frac{1}{2}\left(\frac{W}{\rho'}\right)_{NC1+6}\left(\frac{1}{A_{NC1+6}^2}-\frac{1}{A_6^2}\right)$
NT	$\frac{1}{2}\left(\frac{W}{\rho'}\right)_{NT}\left(\frac{1}{A_{NT}^2}-\frac{1}{A_6^2}\right)$
NJ	$\frac{1}{2}\left(\frac{W}{\rho'}\right)_{NJ}\left(\frac{1}{A_5^2}-\frac{1}{A_{NC1+7}^2}\right)$

Note: The spatial acceleration term associated with W_3 is included in P_{jet}.

$[AM]$ is a $(NJ+1) \times (NJ+2)$ matrix, and

$[AB]$ is a $(NJ+1) \times 1$ column vector.

Notice that ΔW_3 has been put in the last row of $\Delta\,[XM]$. This is to allow for the coupling with the recirculation system equations. The structure and elements of the reactor vessel mass and momentum equation system are given in Appendix B.4

5.1.7 Recirculation system

The equations needed for calculating the recirculation system parameters are the mass balance equation (Equation 4.43), momentum equations (Equations 4.48 and 4.54), and the pump torque equation (Equation 4.49) for each recirculation loop. Discretizing these equations, we get

$$(W^n + \Delta W)_3 = (W^n + \Delta W)_{jet,1} + (W^n + \Delta W)_{jet,2}\,,$$

$$\begin{aligned}\left(\frac{\ell}{A}\right)_{jet} \frac{\Delta W_{jet,i}}{\Delta t} &= -(P^n + \Delta P)_{jet} + r^n_{1,i}\,(W^n + \Delta W)_{jet,i} \\ &+ r^n_{2,i}\,(W^n + \Delta W)_{s,i} + r^n_{3,i}\,(W^n + \Delta W)_{rc,i} - r^n_4\,(W^n + \Delta W)_3\,,\end{aligned}$$

$$\begin{aligned}\left(\frac{\ell}{A}\right)_{rc} \frac{\Delta W_{rc,i}}{\Delta t} &= P^n_{rcp,i} + \left(\frac{\partial P_{rcp}}{\partial \omega}\right)^n_i \Delta\omega_i + \left(\frac{\partial P_{rcp}}{\partial W_{rc}}\right)^n_i \Delta W_{rc,i} \\ &- r^n_{5,i}\,(W^n + \Delta W)_{rc,i} + r^n_6\,(W^n + \Delta W)_{s,i}\,,\end{aligned}$$

and

$$\begin{aligned}I_{rcp}\frac{\Delta\omega_i}{\Delta t} &= T^{n+1}_m - \left[T^n_{rcp,i} + \left(\frac{\partial T_{rcp}}{\partial \omega}\right)^n_i \Delta\omega_i + \left(\frac{\partial T_{rcp}}{\partial W_{rc}}\right)^n_i \Delta W_{rc,i}\right] \\ &- r_{pump}\,(\omega^n_i + \Delta\omega_i)\,,\end{aligned}$$

where

$i = 1$ or 2, which denotes the recirculation loops,

$$r_{1,i} = \frac{1}{2\,\rho_3}\left\{W_{jet,i}\left(\frac{1}{A_{dc}^2} - \frac{crl_i}{A_t^2}\right) - |W_{jet,i}|\left[\left(\frac{f\,\ell}{D\,A^2}\right)_{jet,i} + \frac{K_{d,i}}{A_d^2}\right]\right\},$$

$$r_{2,i} = \frac{1}{2\,\rho_3 A_s}\left[crl_i\,W_{s,i}\left(\frac{2}{A_t} - \frac{1}{A_s}\right) - \frac{K_{s,i}\,|W_{s,i}|}{A_s}\right],$$

$$r_{3,i} = \frac{crl_i\,W_{rc,i}}{\rho_3 A_n A_t},$$

$$r_4 = \frac{W_3}{2\rho_3 A_5^2},$$

$$r_{5,i} = \frac{1}{2\,\rho_3}\left\{|W_{rc,i}|\left[\left(\frac{f\,\ell}{D\,A^2}\right)_{ldc} + \left(\frac{f\,\ell}{D\,A^2}\right)_{rc} + \left(\frac{K}{A^2}\right)_{rc} + \frac{c_v}{A_{v,i}^2} + \frac{K_{n,i}}{A_n^2}\right] + \frac{W_{rc,i}}{A_n^2}\right\}, \text{ and}$$

$$r_{6,i} = \frac{1}{2\,\rho_3 A_s^2}\left(W_{s,i} + K_{s\,i}\,|W_{s,i}|\right).$$

Notice that the jet pump pressure gain P_{jet} is the same for the two recirculation loops, and $\Delta W_{s,i} = \Delta W_{jet,i} - \Delta W_{rc,i}$. Using the matrix form, the recirculation system equations become

$$[AR]^n\,\Delta\,[XR]^n = [BR]^n\ , \tag{5.20}$$

where

$\Delta\,[XR] = [\Delta W_{jet,1},\ \Delta W_{jet,2},\ \Delta W_{rc,1},\ \Delta W_{rc,2},\ \Delta\omega_1,\ \Delta\omega_2,\ \Delta P_{jet},\ \Delta W_3]^T$,

$[AR]$ is a 7×8 matrix, and

$[BR]$ is a 7×1 column vector.

The structure and elements of the recirculation equation system are given in Appendix B.5.

Treatment of constant and variable speed pumps

Two types of recirculation pumps have been used: constant and variable speed pumps. The constant speed pumps can operate at two speed levels: the high speed mode (the rated speed) and the low speed mode (a quarter of the rated speed). The recirculation

flow control system controls the flow control valves in a system with constant speed pumps. It controls the electrical torque (by controlling the frequency of the motor-generator set) in a system with variable speed pumps.

The operation of the recirculation pumps is simulated by using three indices:

1. $IPTYPE$, which indicates the type of the pumps,

$$IPTYPE = \begin{cases} 0 & \text{for variable speed pumps,} \\ 1 & \text{for constant speed pumps;} \end{cases}$$

2. $IPST_i$, which indicates the status of a pump,

$$IPST_i = \begin{cases} 0 & \text{when the pump is tripped,} \\ 1 & \text{when the pump is at high speed mode,} \\ 2 & \text{when the pump is at low speed mode;} \end{cases}$$

for a variable speed pump, $IPST_i = 1$ if the pump is not tripped;

3. IP_i, which indicates whether the pump is changing speed or not,

$$IP_i = \begin{cases} 0 & \text{when the pump is changing speed,} \\ 1 & \text{when the pump has reached its required speed;} \end{cases}$$

$IP_i = 0$ for a variable speed pump at all conditions.

For a constant speed pump, if the pump speed is within $\pm 1\%$ of its required speed, then IP_i is set to 1, and the pump speed is set to the required speed. Otherwise, $IP_i = 0$. In this case, the electrical torque is set to the torque corresponding to the required speed if the pump speed is lower than the required speed, or the electrical torque is set to zero to allow the pump to coast down to the required speed.

For both types of pumps, if the pump is tripped ($IPST_i = 0$), then IP_i is set to zero, and the electrical torque is also set to zero. If the pump speed calculated in the previous time step is less than zero, then it is set to zero in the new time step.

5.1.8 Coupling between equation systems

The equation system developed in sections 5.1.3 to 5.1.7 have more unknowns than equations. Unique solutions are obtained by solving several equation systems simultaneously [41].

The reactor vessel energy, steam dome, and steam line equation systems are coupled by the state variables P, W_s, and W_{su}. Performing forward elimination on these systems, the last rows of these three systems become

$$EM(NT+1, NT+1)\Delta P + EM(NT+1, NT+2)\Delta W_{su} = EB(NT+1),$$

$$A_{SD}(4,4)\Delta P + A_{SD}(4,5)\Delta W_{su} + A_{SD}(4,6)\Delta W_s = R_{SD}(4),$$

and

$$STMA(15,15)\Delta W_s + STMA(15,16)\Delta P = STMR(15).$$

Solving the above equations simultaneously, ΔP, ΔW_s, and ΔW_{su} can be obtained. Then all other state variables of the three systems can be solved by backward substitution.

The reactor mass and momentum equation system and the recirculation system are coupled by P_{jet} and W_3. Using forward elimination, we get

$$AM(NJ+1, NJ+1)\Delta P_{jet} + AM(NJ+1, NJ+2)\Delta W_3 = AB(NJ+1),$$

and

$$AR(7,7)\Delta P_{jet} + AR(7,8)\Delta W_3 = BR(7).$$

ΔP_{jet} and ΔW_3 are obtained by solving the above two equations. Backward elimination is then performed to get the rest of the state variables.

5.2 Steady-State Initialization

The allowable initial conditions for this BWR simulator are that

1. the reactor is at power operation,
2. the recirculation loops are operated in symmetry with either forced circulation or natural circulation,
3. both SRV and TBV are closed,
4. the MSIV is fully opened.

The steady-state calculations are first used to find the system parameters at rated condition. The steam and feedwater flow rates are calculated from mass and energy balance. If the core is modeled by one core channel, the coolant flow rates and properties in the reactor vessel can be calculated directly from Equations 5.16 and 5.19:

$$[EB] = 0,$$

and

$$[AB] = 0.$$

If the core has two channels, then the above two equations must be solved by iteration. This iteration is converged when the flow split between the two channels gives the same core pressure drop P_{core}. From $AB(NT) = 0$, P_{jet} is also obtained. The total core flow is evenly divided into the two recirculation loops. The parameters of the recirculation system are calculated from Equation 5.18:

$$[BR] = 0.$$

The valve coefficient of the flow control valves is determined by matching the recirculation line pressure difference.

The rated steam line parameters are determined from the rated reactor pressure, steam flow, and by requiring that (from Equation 5.18)

$$[STMR] = 0.$$

The valve coefficient of the TCV is obtained from the rated steam flow rate, the turbine inlet pressure specified by the user, and the calculated steam line pressure distribution. The valve coefficients of the SRV and TBV are calculated from the given relief capacities at the rated condition.

If the initial condition is different than the rated condition, then the procedure described above is repeated to get the system parameters at the initial condition. But this time, the valve coefficients of TCV and the flow control valves are used to obtained the TCV position, and the flow control valve position or the electrical torque of the recirculation pump at the initial state.

If natural circulation is specified, then the initial core flow given in the input file is used as the first guess in calculating the natural circulation flow. In this case, the recirculation line flows and the electrical torque of the pumps are set to zero. The natural circulation flow is determined by iteration to solve $AB(NT) = 0$ (Equation 5.19) and $BR(7) = 0$ (Equation 5.20) simultaneously.

After the parameters of the reactor vessel, recirculation system, and system line are determined, the parameters of the fuel model are calculated by requiring the right hand sides of Equations 4.39 and 4.40 to vanish. Iterative procedures are used in the calculations of the wall heat transfer coefficients and average material temperatures. The initial delay neutron precursor concentrations and the decay heat precursor concentrations are obtained by assuming that the reactor is at the equilibrium condition of the initial power level, and setting the right hand sides of Equations 4.24 and 4.26 to zero. The initial thermal feedback reactivity is calculated from the initial fuel average temperatures, coolant temperatures, and average void fractions. The steam dome is initially set at a thermal equilibrium condition, and the vapor volume is determined from the initial steam dome water level.

5.3 Transient Calculations

The transient calculations start with the determination of the time step size. The time step size can either be a fixed value specified by the user, or be the minimum fluid transport time through the core nodes. The boundary conditions at the new time step are updated after the time step size is determined. The following time dependent parameters are given by input forcing functions:

1. Turbine load set;
2. Reactor pressure set point;
3. Steam dome water level set point;
4. Feedwater enthalpy;
5. External reactivity.

The controller models discussed in section 4.6 are used to calculate the TCV, TBV, SRV positions, feedwater flow rate, and FCV position or recirculation pump electrical torque. If the user specified time for MSIV or TCV fast closure is reached, the valve is closed in a pre-specified closing rate.

After the boundary conditions are set, the equation systems described in section 5.1 are solved in four sequential steps. The core neutronics equations are solved first, followed by the calculations of fuel parameters. Next, the vessel energy, steam dome, and steam line systems are solved. Because the steam dome condition is not known a priori, it is solved in two steps [41]. The steam dome is first assumed to be in case 1 condition, and the steam dome pressure, vapor enthalpy, and liquid enthalpy are calculated. The correct steam dome condition is identified using these parameters. If the correct condition is not case 1, then the calculations are repeated. After the vessel energy equations are solved, the mass change rates of each node $\frac{\Delta M_i}{\Delta t}$ are calculated to be used in the calculations of the vessel mass and momentum system.

The fourth step is the calculations of the vessel mass and momentum, and recirculation systems. Input forcing functions are used to specified the recirculation pump

statuses, and FCV position or pump electrical torque.

After all the equations are solved, the system parameters are updated. Then, the vapor volume in the steam dome is recalculated to ensure the overall mass balance of the reactor vessel. Let M_{total} be the total mass in the reactor vessel, including the steam dome and the recirculation system. Then,

$$M_{total}^{n+1} = \rho_v^{n+1} V_v^{n+1} + \rho_l^{n+1} \left(V_{SD} - V_v^{n+1} \right) + \sum_{i=1}^{NT} m_i^{n+1} V_i = M_{total}^{n} + \Delta t \left(W_{FW}^{n+1} - W_s^{n+1} \right).$$

So,

$$V_v^{n+1} = \frac{M_{total}^{n} + \Delta t \left(W_{FW}^{n+1} - W_s^{n+1} \right) - \rho_l^{n+1} V_{SD} - \sum_{i=1}^{NT} m_i^{n+1} V_i}{\left(\rho_v^{n+1} - \rho_l^{n+1} \right)}.$$

It $V_v < 0$ or $V_v > V_{SD}$, the simulation is terminated. This completes the calculations of a transient step.

5.4 Chapter Summary

The governing equations of the physical models developed in the previous chapter are solved numerically to simulate the transient response of a BWR. The point kinetics equations are solved by using the θ-method and direct integrations with an adaptive procedure. Direct integrations are also used to calculate the concentrations of the decay heat precursors. The fuel conduction and convection equation system is solved by a prediction-correction procedure.

The energy equations of the reactor vessel nodes and the sum of the mass equations of these nodes form the reactor vessel energy equation system. The state variables and the structure of this system depend on the flow pattern in the vessel. The steam dome equation system is formed by the mass and energy equations of the vapor and liquid regions. Depending on the status of the steam dome, the steam dome equation system has different state variables and structures. The mass and momentum equations of the steam line system form the steam line equation system. The vessel energy, steam dome, and steam line equation systems are coupled together

by the common state variables: the reactor pressure, steam flow rate, and liquid surge flow rate between the steam dome and feedwater node. These three equation systems are solved simultaneously.

The mass equations of the vessel nodes, except for the feedwater node, and the momentum integral equations form the vessel mass and momentum equation system. This system is coupled with the recirculation system by the lower downcomer outlet flow rate and jet pump pressure gain. The recirculation equation system is formed by the mass balance equation, momentum equations, and pump torque equations. These two equation systems are also solved together.

The initial condition of the BWR system is calculated by steady-state mass, momentum, and energy balances. Iterative procedures are used in steady-state initializations.

Transient calculations are done sequentially except for the coupled equation systems, which are solved simultaneously. The steam dome system is solved by two steps. First, a steam dome condition is guessed, and the parameters are calculated. These results permit determination of the correct steam dome condition and the calculations are repeated if the condition is different than the first guess. The overall mass balance of the reactor vessel is used to determined the new steam dome vapor volume after all system parameters have been updated.

Chapter 6

Validation of BWR Simulator

The BWR simulator developed in this work is used to simulate actual plant transients, and the calculated results are compared with measured data to assess the capability of the simulator. The transients being studied are the recirculation pump trip test of Kuosheng plant, and three turbine trip tests performed at Peach Bottom-2.

6.1 Kuosheng Recirculation Pump Trip Test

The Kuosheng nuclear power station is owned by the Taiwan Power Company, Taiwan, Republic of China. The station consists of two GE BWR/6 units. The specifications of the Kuosheng units are listed in Table 6.1 [59, 60, 61].

The recirculation pump trip test was performed as a part of the Kuosheng startup

Table 6.1: The specifications of Kuosheng plant [59, 60, 61]

Rated thermal power	2894 MW
Rated core flow rate	10647 kg/s
Rated steam flow rate	1569 kg/s
Rated steam dome pressure	7.2 MPa
No. of fuel assemblies	624

Table 6.2: The initial conditions of the Kuosheng recirculation pump trip test [60]

Reactor power	1920 MW
Core flow rate	10558 kg/s
Steam dome pressure	6.8 MPa
Steam flow rate	947 kg/s
Feedwater flow rate	997 kg/s

tests. Both recirculation pumps were tripped when the reactor was at 68% power, 99% flow. The initial condition of the recirculation pump trip test is listed in Table 6.2 [60].

The inputs to the BWR simulator are from a RETRAN model of the Kuosheng plant [61]. The parameters of the controllers are based on the values given in reference [47] with some modifications to achieve stable controller responses. The reactor core is modeled by two channels each with five axial nodes. A time step size of 0.1 sec. is used. A typical axial power shape is assumed. The separator form loss coefficient and the constants in the empirical separator inertia correlation are adjusted to have a good match between measured and calculated core flow rates. The input data of this case are listed in Appendix F.

Figures 6-1 through 6-6 compare the simulation results with test data. The test results are from reference [60]. Figure 6-1 shows the response of the core flow rate. The calculated trend matches the test data as expected. The calculated fission power follows closely the measured data as shown in Figure 6-2. In Figure 6-3, the calculated steam dome pressure also follows the test results, but the calculated trend is slower than the measured one. This is due to the single pressure assumption used in the thermal hydraulic model, which tends to dampen out the pressure fluctuation.

Figure 6-4 shows the changes in the downcomer water level. The measured responses of the narrow range and wide range level sensors are different because their calibration settings are different. The calculated water level follows the narrow range water level. The calculated steam flow rate is higher than the tests data, and the

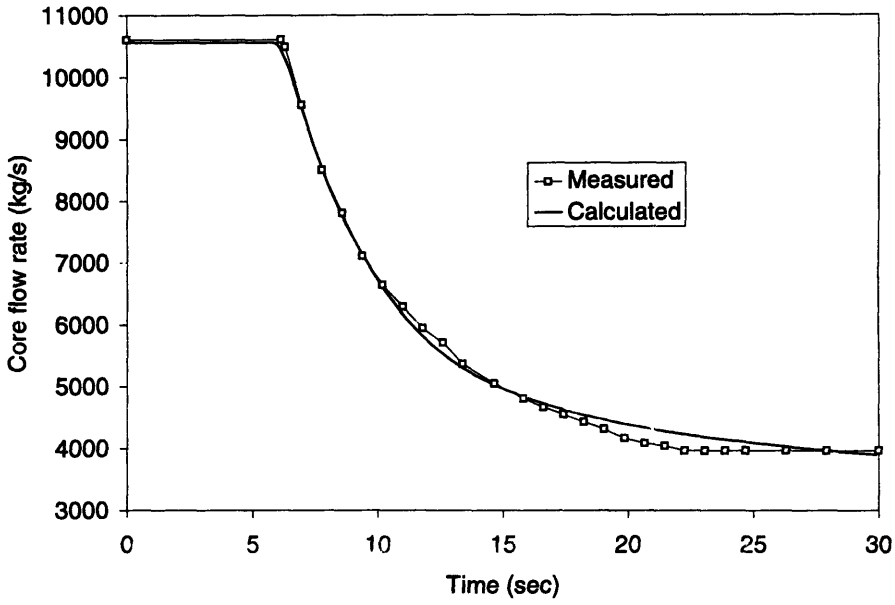

Figure 6-1: Core flow rate during Kuosheng recirculation pump trip transient.

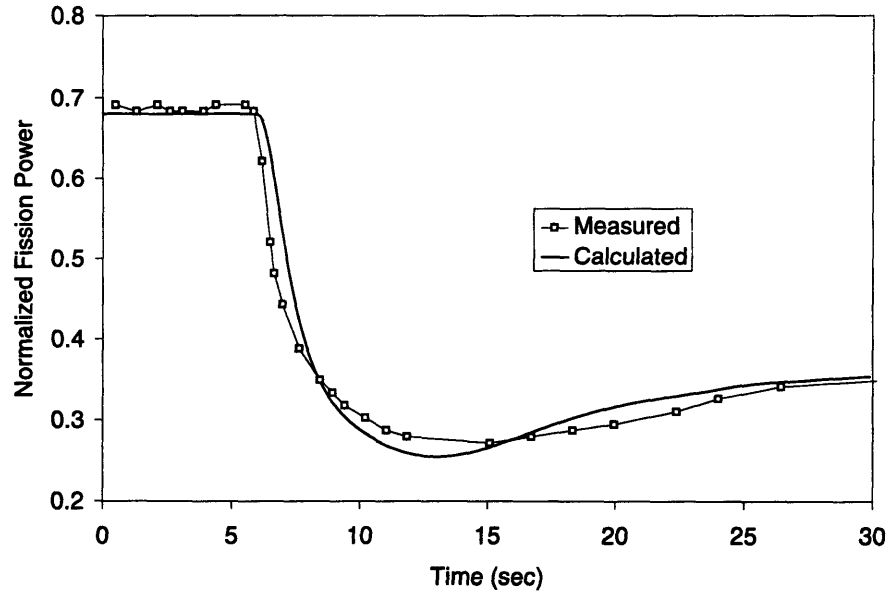

Figure 6-2: Fission power during Kuosheng recirculation pump trip transient.

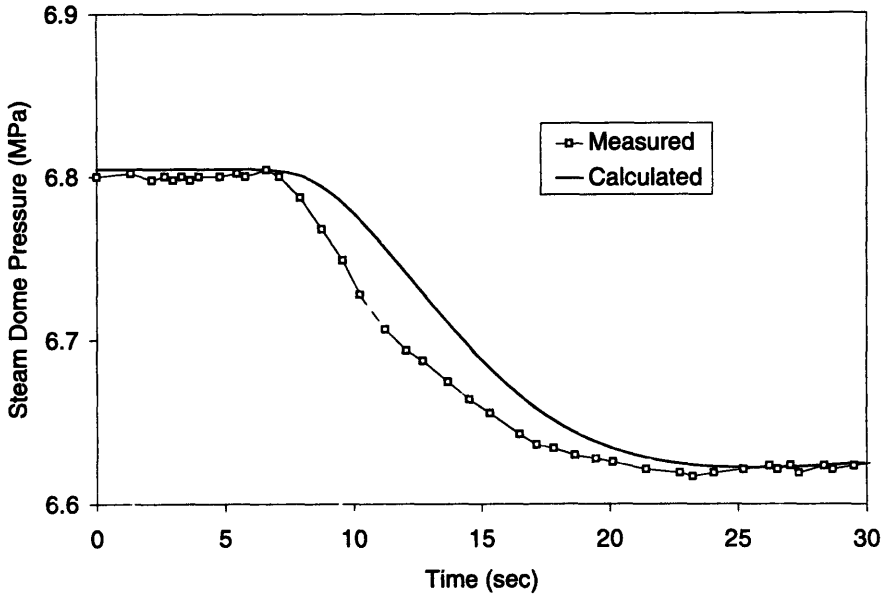

Figure 6-3: Steam dome pressure during Kuosheng recirculation pump trip transient.

calculated feedwater flow rate is lower than the measured one, as can be seen in Figures 6-5 and 6-6. These discrepancies may be due to the differences in the pressure and feedwater controller settings between the actual plant and simulation models. However, at the end of simulation (t = 30 sec.), the calculated steam and feedwater flow rates match very well. Whereas the measured steam and feedwater flow rate differ by 298 kg/s at that time, which is a mismatch of about 19% of rated steam flow rate. This magnitude of steam and feedwater flow mismatch seems to be unusually large. Notice that there is a 50 kg/s difference between the steam and feedwater flow rates at the initial condition.

From these results, we can see that the BWR simulator predicts the Kuosheng recirculation pump trip transient very well. The computation time for this case is faster than real time. A 30 sec. simulation takes 4.4 sec. of CPU time on a 90 MHz Pentium personal computer.

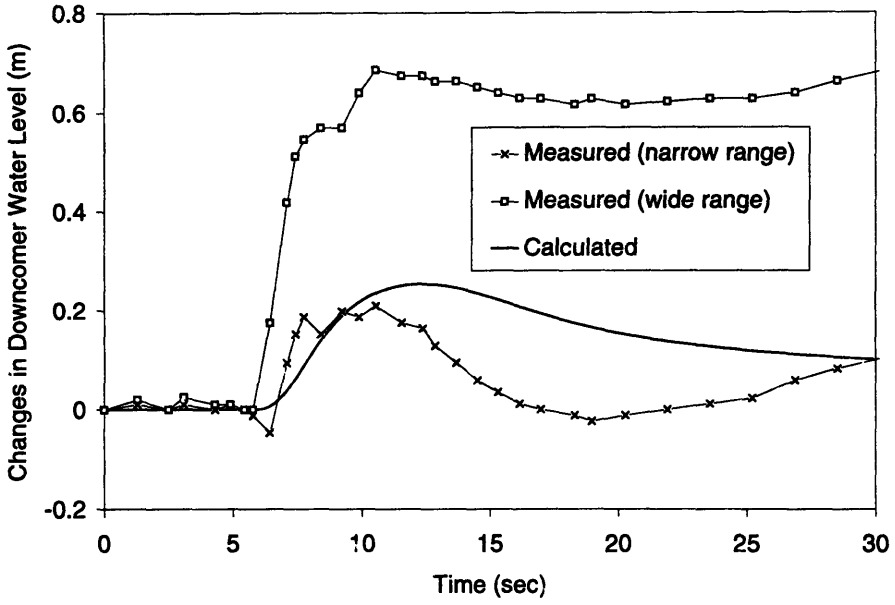

Figure 6-4: Changes in the downcomer water level during Kuosheng recirculation pump trip transient.

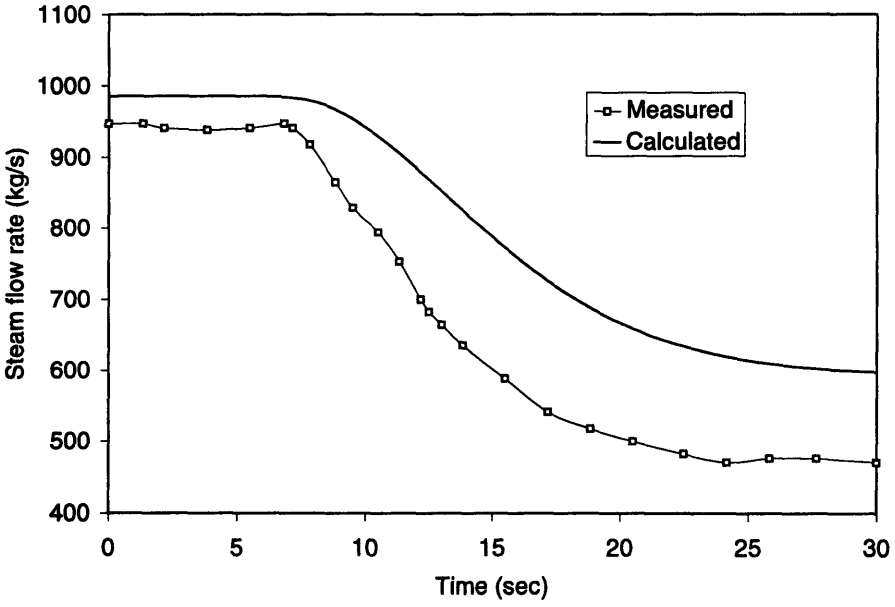

Figure 6-5: Steam flow rate during Kuosheng recirculation pump trip transient.

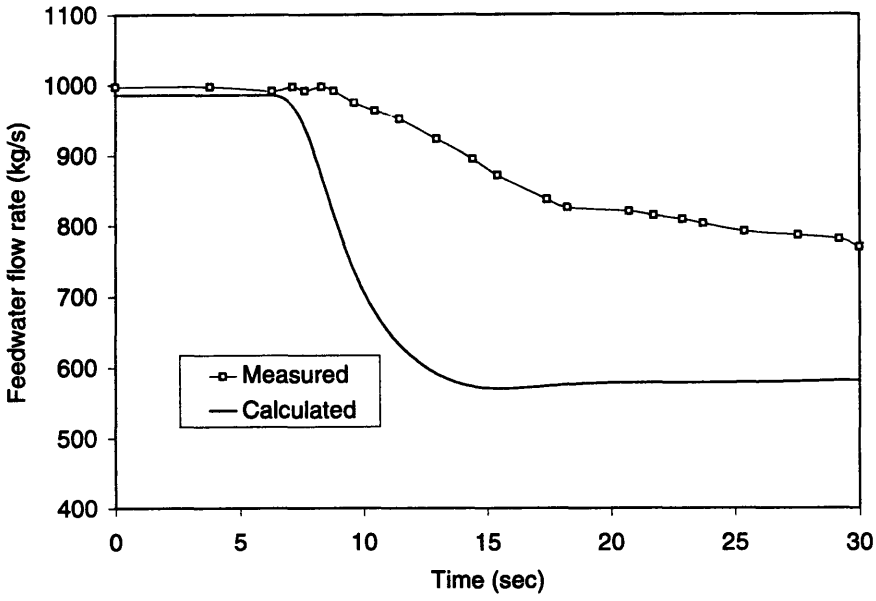

Figure 6-6: Feedwater flow rate during Kuosheng recirculation pump trip transient.

Table 6.3: The specifications of Peach Bottom-2 [62]

Rated thermal power	3293 MW
Rated core flow rate	12915 kg/s
Rated steam dome pressure	7.0 MPa
Rated steam flow rate	1686 kg/s
No. of fuel assemblies	764

6.2 Peach Bottom-2 Turbine Trip Tests

Peach Bottom-2 is a GE BWR/4 owned by the Philadelphia Electric Company. Table 6.3 lists the specifications of Peach Bottom-2 [62]. Three turbine trip tests were conducted at Peach Bottom-2 at the end of Cycle 2 to study the plant response during pressurization transients.

Because of its relative small steam bypass capacity (26.2% of rated steam flow), Peach Bottom-2 will have a more severe pressurization transient than other BWRs. To increase further the magnitude of the power excursion following a pressurization event, the direct reactor scram signal from the turbine stop valve closure was bypassed during the tests. The reactor scram was initiated by the APRM high neutron flux signal with a reduced set point. This arrangement resulted in about 0.6 sec. delay in reactor scram. The initial conditions, APRM high flux trip set points, and peak neutron flux levels for the three tests are listed in Table 6.4 [32].

Table 6.4: Peach Bottom-2 turbine trip test conditions [32]

Test number	TT1	TT2	TT3
Initial power (% rated)	47.4	61.6	69.1
Initial core flow (% rated)	98.8	80.9	99.4
APRM high flux trip set point (% rated)	85	95	77
Peak neutron flux (% rated)	239	280	339

The required plant characteristics for the simulation are from references [62] and [63]. Similar values of the controller parameters and separator inertia constants as used in the Kuosheng simulation are used here. The initial steam dome pressure, downcomer level, axial power shape, core inlet subcooling, and turbine stop valve closing rate for each test are given in reference [32]. A typical scram reactivity curve is used. The actual reactor kinetic parameters during the tests are not available. Instead, the values used in references [64] and [65] are used. The reactor core is modeled by one core channel with 12 axial nodes plus one bypass channel with one axial node. The form loss coefficients of the reactor nodes are adjusted to give the correct steady-state condition. The input data for test TT1 are listed in Appendix F.

The calculated peak fission power (neutron flux) depends on the void reactivity coefficient and time step size used. Because the power excursion occurs extremely fast, a time step size of 1 ms is required to give a converged peak fission power. The void reactivity coefficients are selected to give the correct peak fission powers. The void coefficients are -8.7, -5.8, -6.0 cents / % void for TT1, TT2, TT3, respectively.

The simulation results are shown in Figures 6-7 through 6-15. The measured data are from reference [32]. For test TT1, the steam dome pressure set point is reduced in the later part of the simulation. The water level set points for tests TT2 and TT3 are reduced in the later part of simulations. These are done to have a better agreement between the test and calculated results. These adjustments can be justified by comparing the measured trends of the three tests. As shown in Figure 6-8, the steam dome pressure is decreasing after t = 25 sec. for test TT1. But the trends of steam dome pressure are rising at that time for tests TT2 and TT3 (see Figures 6-11 and 6-14). As for the downcomer water level, Figure 6-9 shows a rising trend in the latter part for test TT1, while Figures 6-12 and 6-15 show flatter trends at that time.

Figures 6-7, 6-10, and 6-13 show the fission power during these three tests. The calculated curves agree well with test data. The slightly boarder peak may be due to the slower pressure responses of the simulator. The shape of the tail of the peak is determined by the scram reactivity curve, which may be different than the actual one.

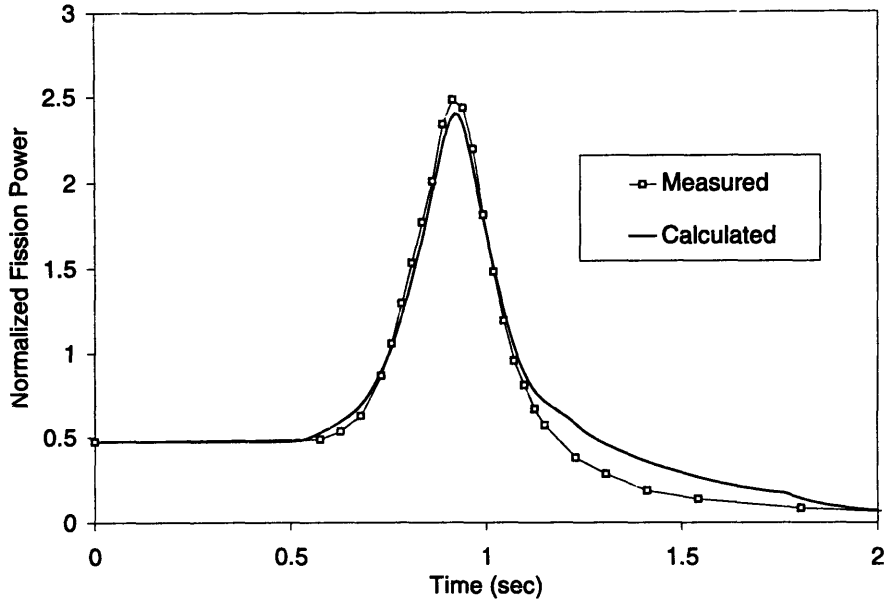

Figure 6-7: Fission power during Peach Bottom-2 turbine trip test TT1.

The calculated steam dome pressure shows a slower trend than the measured one in all three cases (see Figures 6-8, 6-11, and 6-14). This is due to the single pressure assumption. From Figures 6-9, 6-12, and 6-15, we can see that the calculated water level follows the measured narrow range and wide range water levels very well. Notice that the narrow range water levels in TT2 and TT3 have been lower than the lower tap of the sensor, as the flat portions suggested.

In general, the BWR simulator predicts the three turbine trip transients of Peach Bottom-2 satisfactorily, given that the actual nuclear data are not available. The simulation speed in these cases are slower than real time because a very small time step size is required. In these cases, a 50 sec. simulation takes 495 sec. of CPU time on a 90 MHz Pentium personal computer.

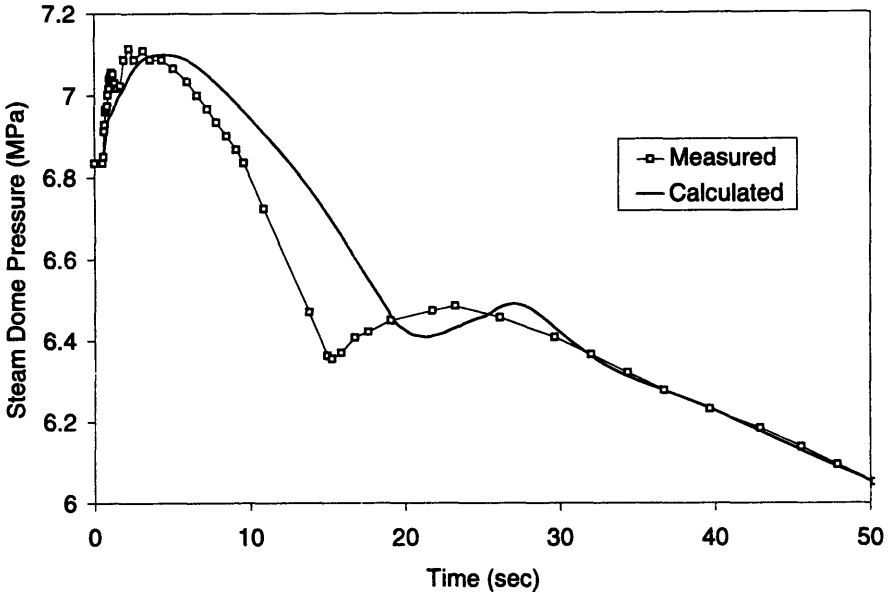

Figure 6-8: Steam dome pressure during Peach Bottom-2 turbine trip test TT1.

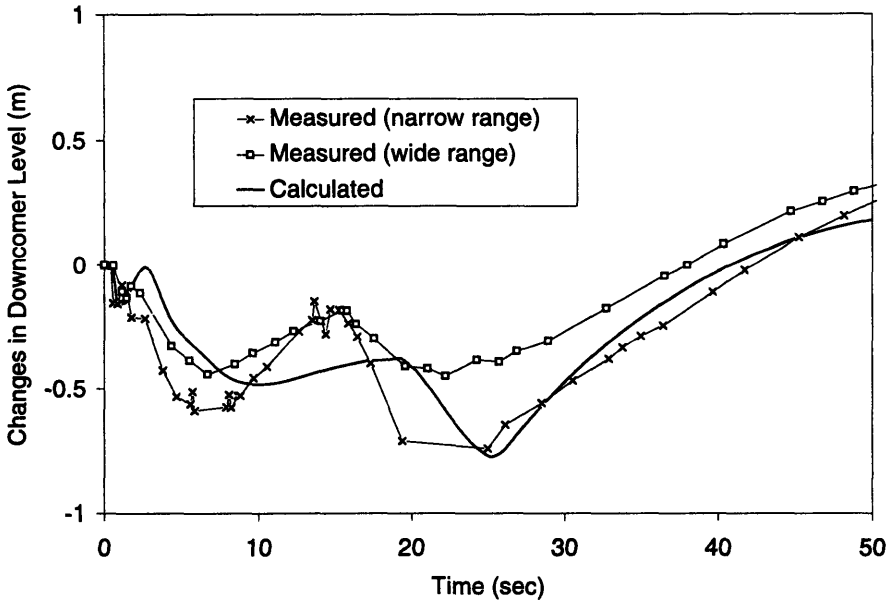

Figure 6-9: Changes in the downcomer level during Peach Bottom-2 turbine trip test TT1.

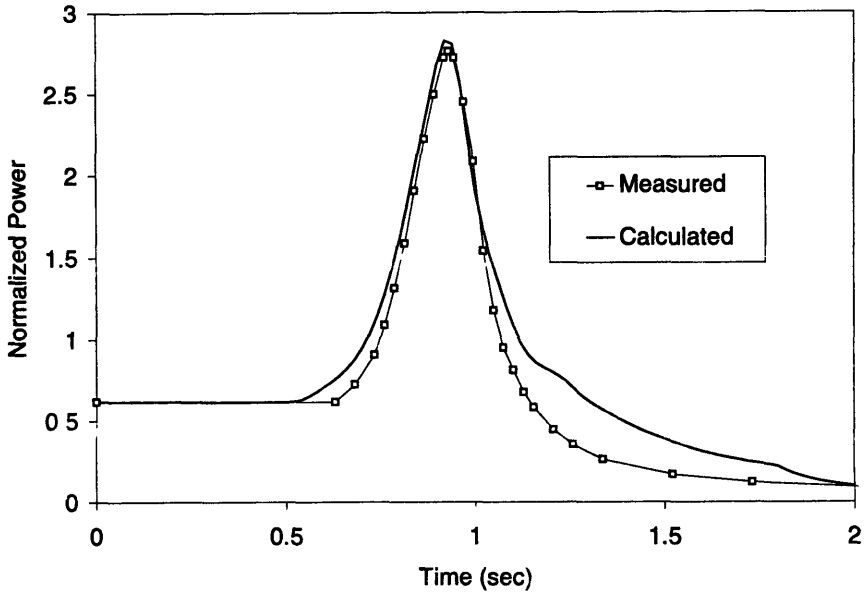

Figure 6-10: Fission power during Peach Bottom-2 turbine trip test TT2.

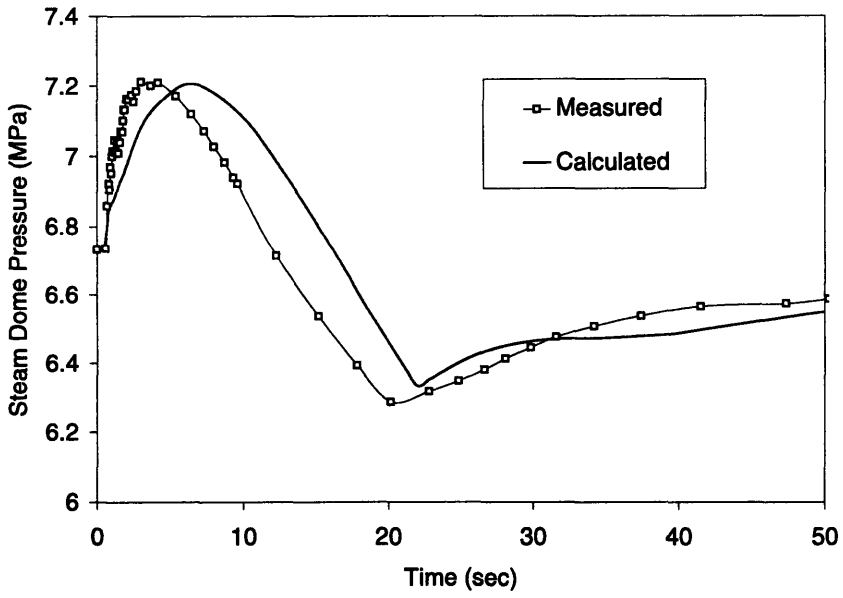

Figure 6-11: Steam dome pressure during Peach Bottom-2 turbine trip test TT2.

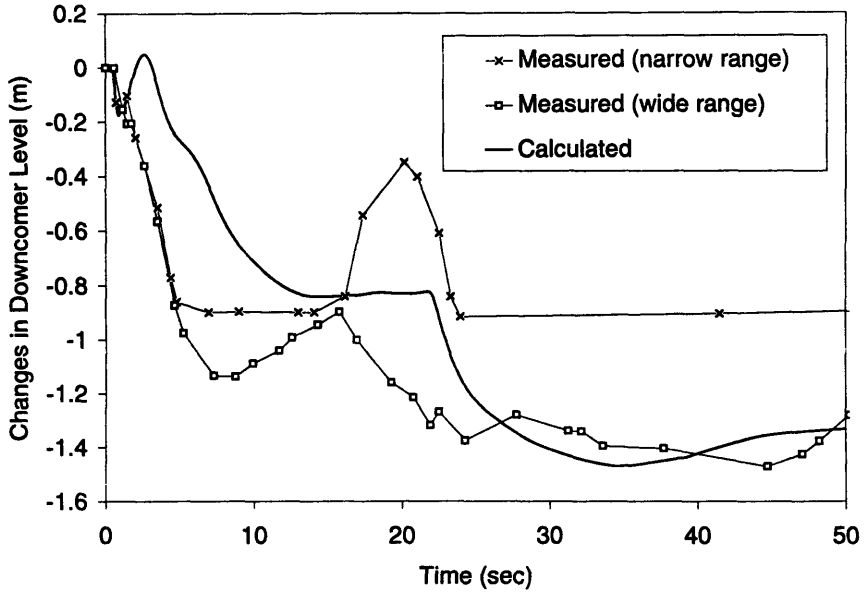

Figure 6-12: Changes in the downcomer level during Peach Bottom-2 turbine trip test TT2.

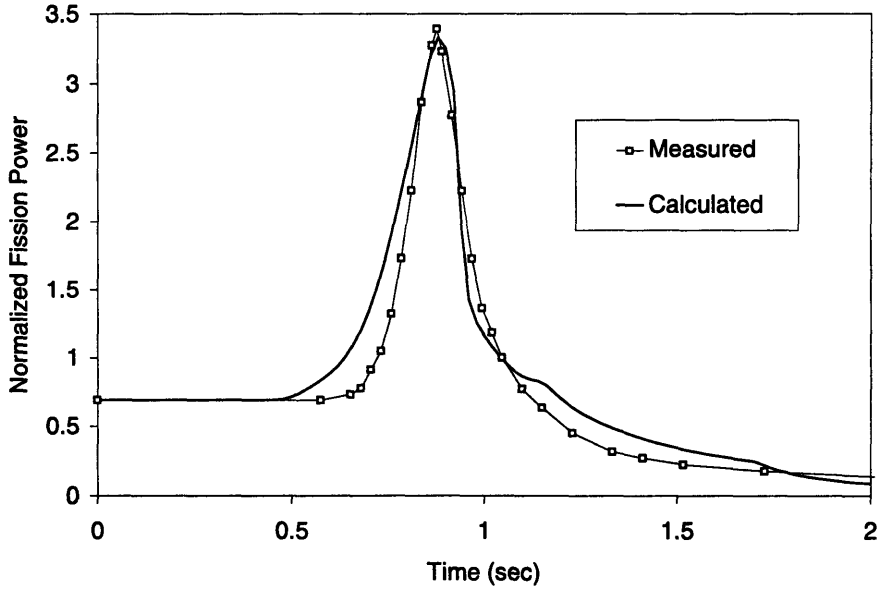

Figure 6-13: Fission power during Peach Bottom-2 turbine trip test TT3.

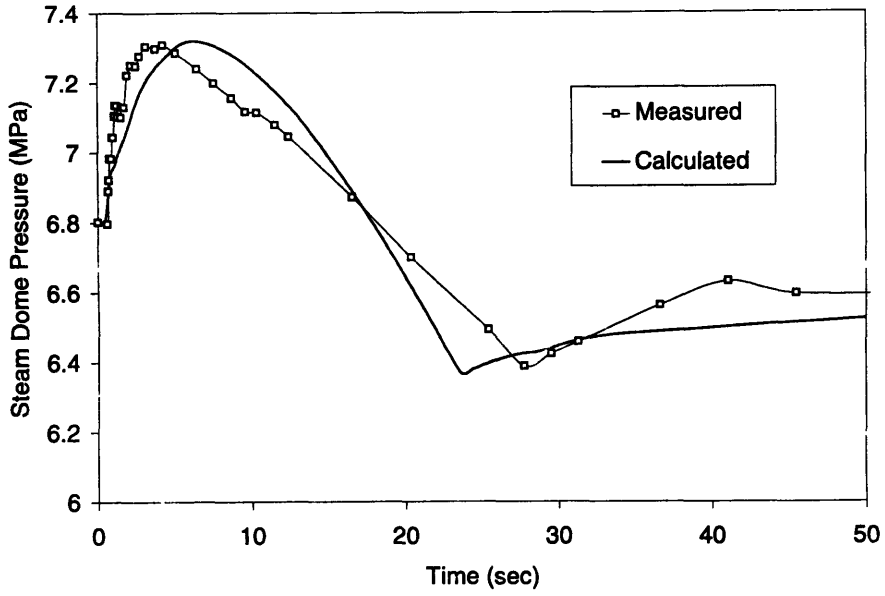

Figure 6-14: Steam dome pressure during Peach Bottom-2 turbine trip test TT3.

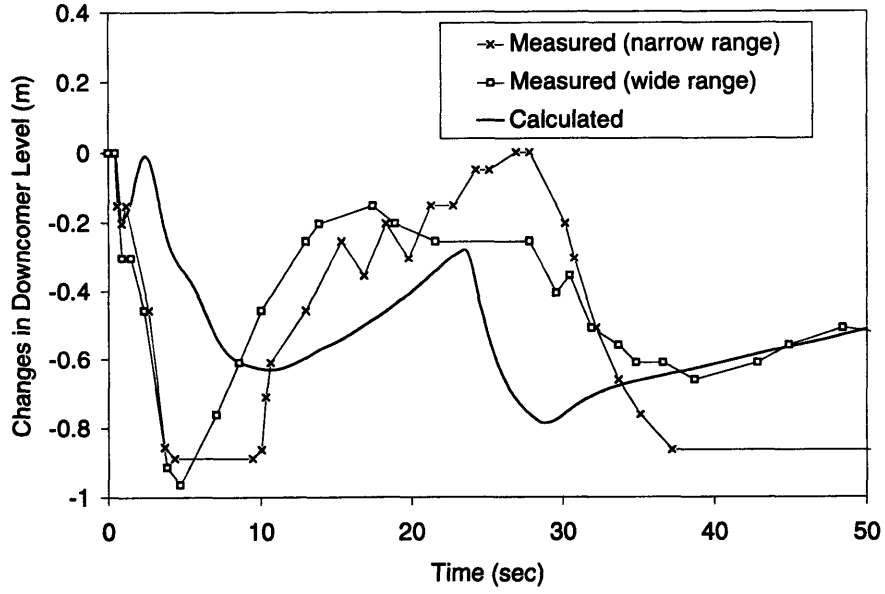

Figure 6-15: Changes in the downcomer level during Peach Bottom-2 turbine trip test TT3.

6.3 Chapter Summary

The BWR simulator is benchmarked against actual plant data to assess its simulation capability. The data from the Kuosheng recirculation pump trip test and three Peach Bottom-2 turbine trip tests are used. The simulation results are in good agreement with the test data.

One common discrepancy in all four cases simulated is that the calculated pressure responses are slower than the measured trends. This discrepancy is caused by the single pressure assumption used in the thermal hydraulic model. This assumption tends to dampen out pressure variations.

For the Kuosheng recirculation pump trip transient, the calculated and measured steam and feedwater flow rates have some differences. These differences may be due to the differences in controller settings between the actual plant and the simulator.

The calculation speed of the BWR simulator depends on the time step size and core nodalization. For a mild transient such as a recirculation pump trip transient, a time step size of 0.1 sec. is adequate, and the simulation speed is faster than real time.

Chapter 7

BWR Stability Analysis

The BWR simulator is used to perform BWR stability analyses in both time and frequency domains. The time domain analysis uses an external reactivity disturbance to perturb the system, and the decay ratio is estimated from the response of fission power. The frequency domain analysis simulates the stability test that imposes a Pseudo-Random Binary Sequence (PRBS) to the set point of the pressure controller. The stability margin of the system is then obtained by performing a spectral analysis on the system response. The results of thirteen Peach Bottom-2 stability tests are used to evaluate the accuracy of the stability analysis results using the BWR simulator.

7.1 Time Domain Analysis

7.1.1 Procedure of time domain analysis

The time domain analysis procedure is similar to the analysis procedure used to study the stability of the ANL test loop (see section 4.1.6):

1. The system response to an external reactivity disturbance is calculated. A simulation of 30 to 50 sec. will be adequate. The reactivity disturbance used here is a square wave with a magnitude of 5 cents, and a duration of 0.2 sec. The recirculation flow controller is disabled in the calculation to eliminate any contribution from its action. The pressure and feedwater controllers have only

minor effects on the time domain analysis.

2. The response of the fission power is used to estimate the stability margin of the system. Assuming that the response is sinusoidal with varying amplitude, and only one oscillation mode exists, the real part of the system eigenvalue can be estimated by

$$\lambda_{real} = \frac{2}{T} \ln \left(\frac{Y_2 - Y_{\min}}{Y_1 - Y_{\min}} \right),$$

where Y_1, Y_2, $Y_{\min}$ are adjacent peak and valley values of the fission power response, and T is the oscillation period (see Figure 4-5 in page 69). The decay ratio of the system is

$$DR = \left(\frac{Y_2 - Y_{\min}}{Y_1 - Y_{\min}} \right)^2 = \exp\left(\lambda_{real} T\right).$$

A post-processor is used to calculate DR, λ_{real}, and T from the output of the BWR simulator.

The post-processor gives a decay ratio for every pairs of two consecutive peaks in the fission power response. If the system is a second order system, which has only one pair of complex conjugate poles, the calculated decay ratios will all be the same. A BWR, however, is a very complex system of higher order. So the calculated decay ratios have different values. This series of decay ratios converges to an asymptotic value when the contributions from all poles except for the least stable pair diminish. This asymptotic decay ratio is directly related to the least stable pair of complex poles of the system, and is a good indicator of the stability margin of the system [30].

The time domain procedure is most effective when the system is less stable. For a stable system, the system parameters do not exhibit many oscillations following the disturbance. In this case, only few decay ratios can be calculated, and the asymptotic trend may not be observed. Engineering judgment is required in this case to select a decay ratio that is most representative to the system stability. Thus the results of this time domain analysis procedure are less accurate for very stable systems.

7.1.2 Sensitivity of time domain analysis

In this section, the sensitivity of time domain analysis results to the parameters used in the simulation is studied. Three parameters are considered: the time step size (Δt), the number of axial nodes in the core channel (N_{node}), and the void reactivity coefficient (α_v). The calculations of this section use the input data of the Kuosheng plant. Because parameters such as the feedwater inlet enthalpy, the axial power shape, and the reactor kinetic parameters are arbitrarily set, the results shown in this section do not represent the actual condition of that plant.

The effects of different Δt and N_{node} are shown in Figures 7-1 and 7-2. In these calculations, $\alpha_v = -12.8$ cents / % void. For Figure 7-1, the reactor is at 63% power, 40% flow. The reactor is at 123% power, 100% flow for Figure 7-2.

For both high and low flow conditions, λ_{real} for 20 nodes is smaller than that of 5 nodes, but the oscillation periods are similar. The effects of Δt on λ_{real} are different for high and low flow conditions. At low flow condition, λ_{real} decreases with decreasing Δt, but the trend is reversed at high flow condition. The oscillation period decreases with decreasing Δt for both high and low flow conditions.

Figures 7-3 and 7-4 show the time domain analysis results with different α_v's at different power and flow conditions. The calculations are done with five axial nodes in the core channel, and a time step size of 0.05 sec. Figure 7-3 is at 40 % flow condition, and Figure 7-4 is at 80% flow condition. As shown in these figures, λ_{real} increases at first with increasing power, then it decreases with increasing power. The oscillation period decreases with increasing power monotonically. At the low flow condition, the effect of α_v on λ_{real} is small for low power levels. For high power levels, larger $|\alpha_v|$ gives smaller λ_{real}. But at the high flow condition, larger $|\alpha_v|$ gives larger λ_{real}. The oscillation period decreases with increasing $|\alpha_v|$ for both high and low flow conditions.

The trends observed above can be explained by considering the feedback mechanisms responsible for BWR instabilities. With the power increases, the void contents in the core increases, and the fluid transport time through the core increases. This increases the gain of the nuclear feedback loop, which tends to increase λ_{real}. However,

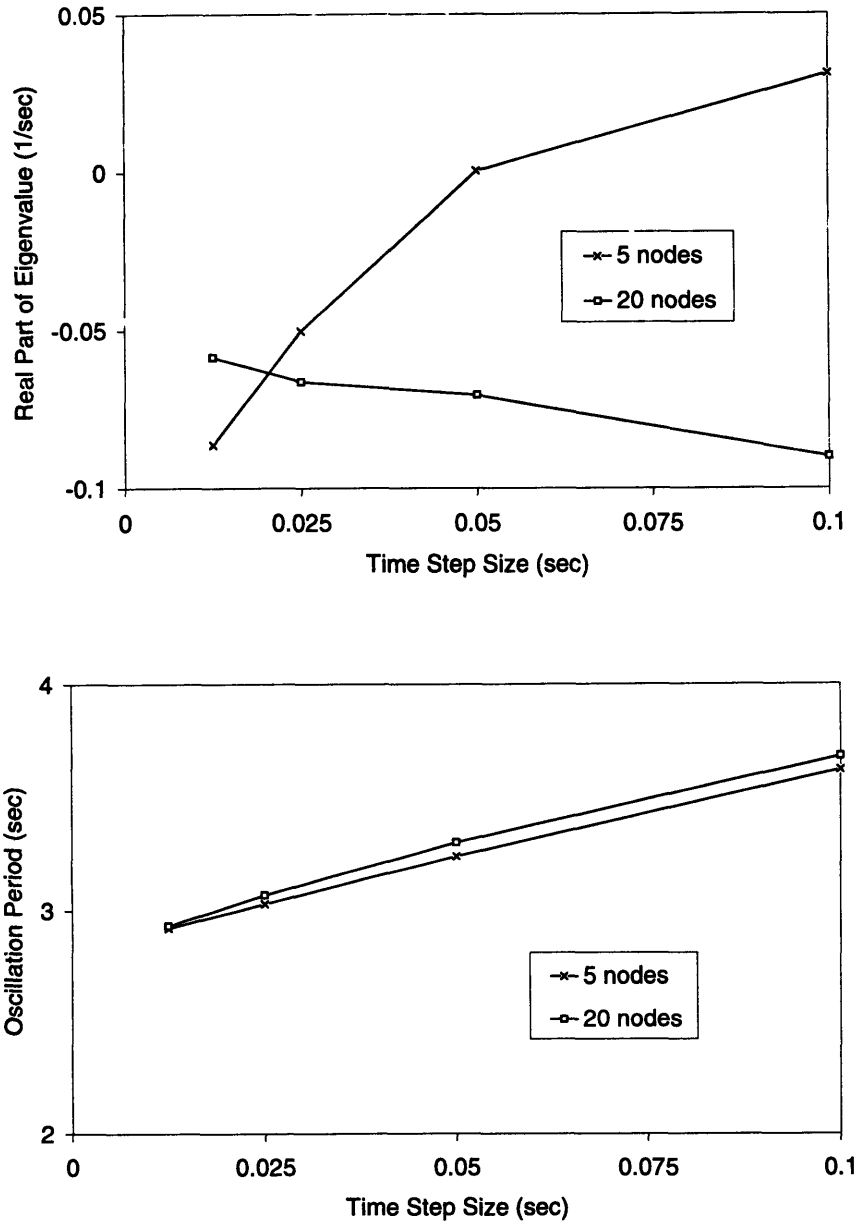

Figure 7-1: Sensitivity of time domain analysis results on the time step size and the number of axial nodes in the core channel at 63% power, 40% flow condition.

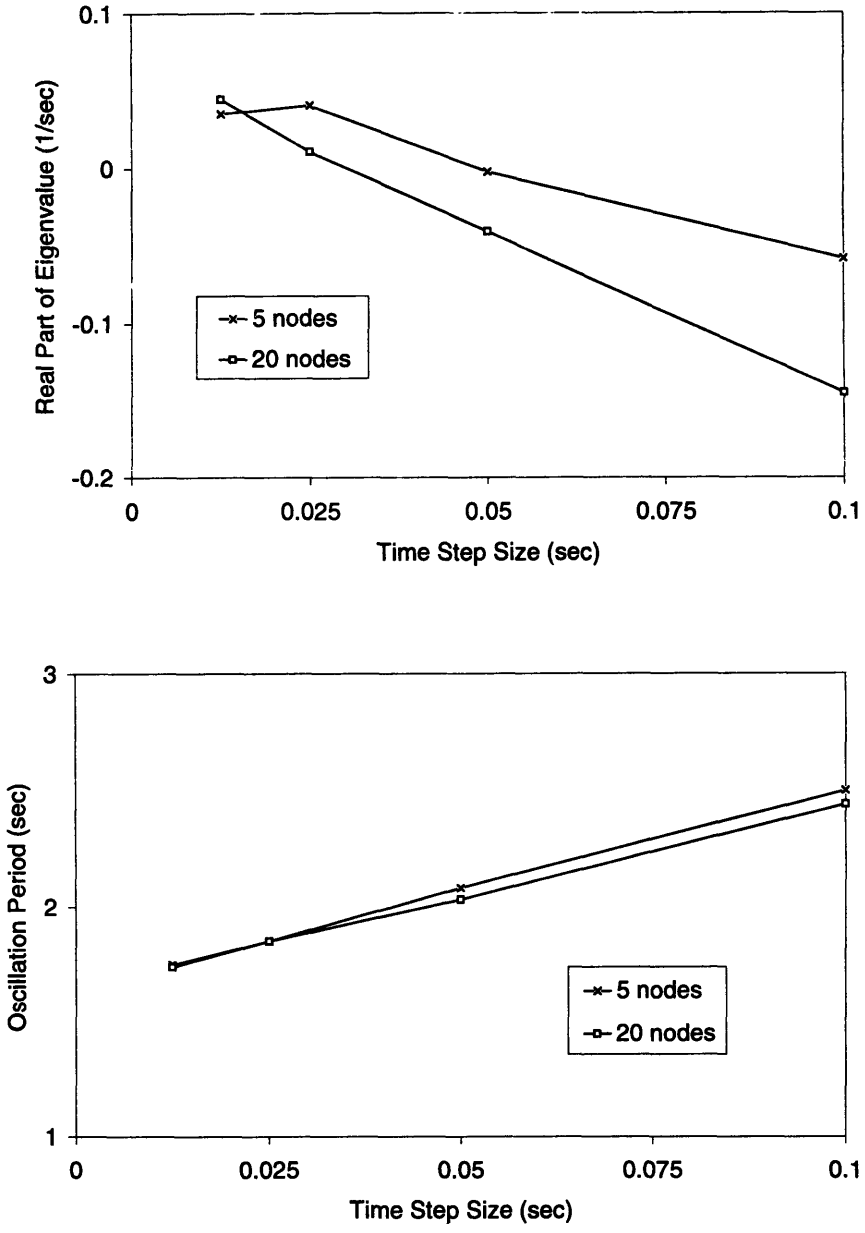

Figure 7-2: Sensitivity of time domain analysis results on the time step size and the number of axial nodes in the core channel at 123% power, 100% flow condition.

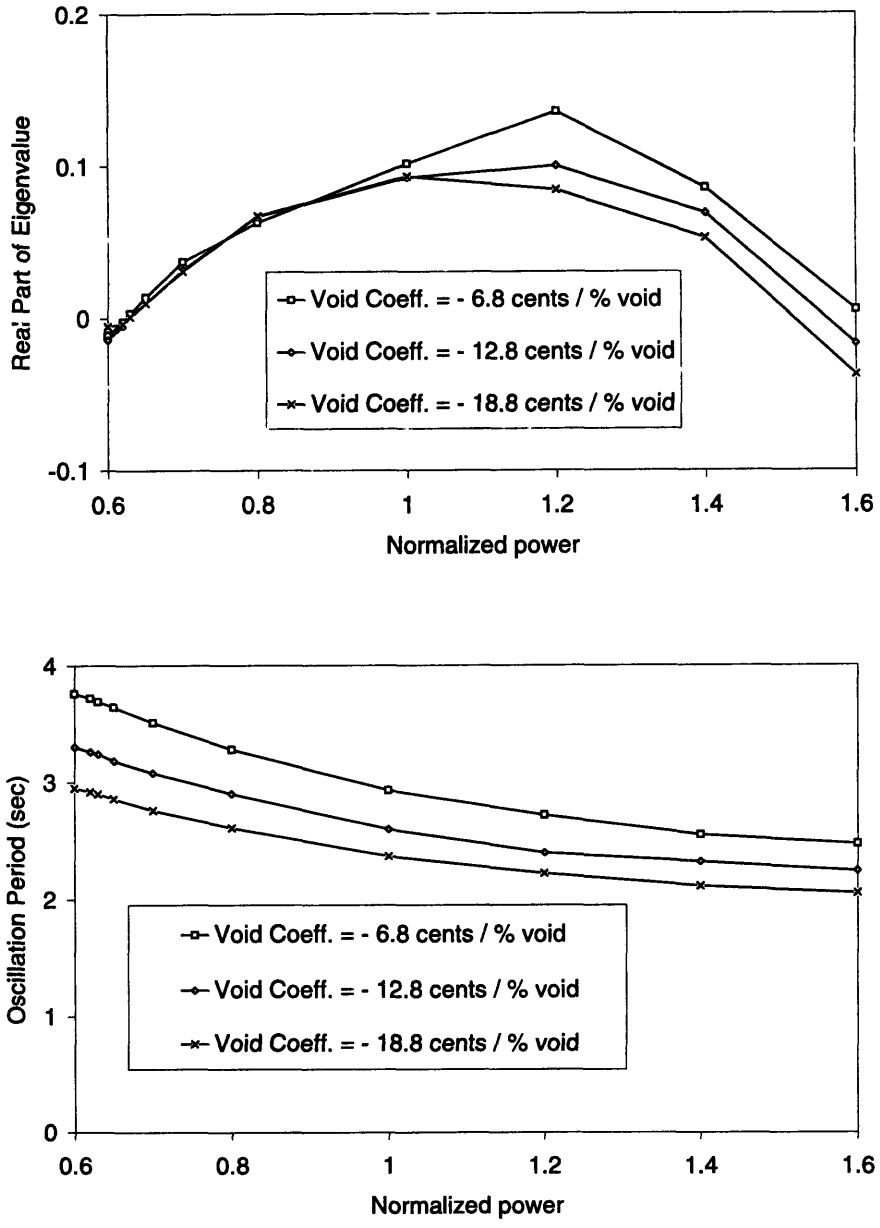

Figure 7-3: Sensitivity of time domain analysis results on the void reactivity coefficient at 40% flow condition.

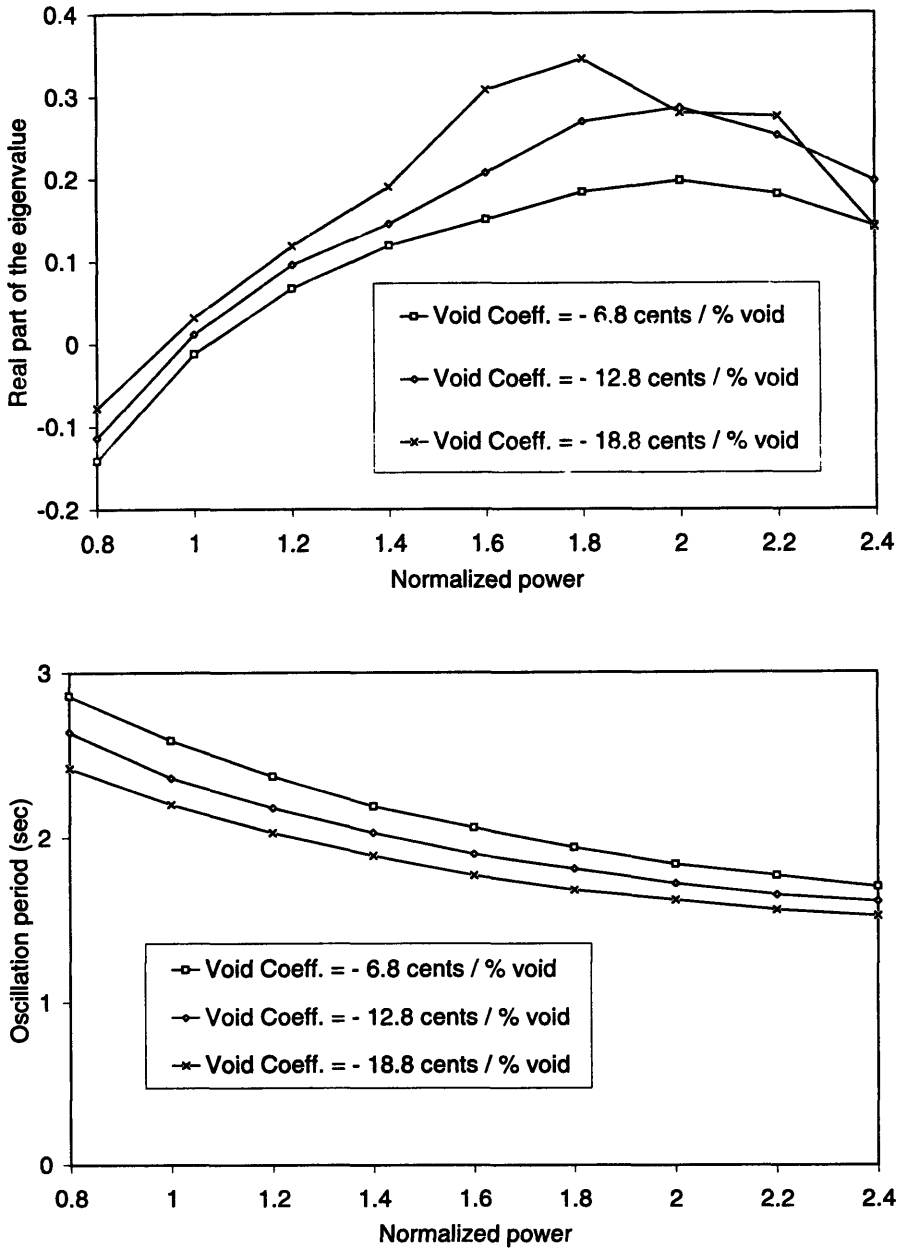

Figure 7-4: Sensitivity of time domain analysis results on the void reactivity coefficient at 80% flow condition.

the changes in the fluid transport time, which dominates the phase lag of the density-wave mechanism, also affect the phase angle difference between the thermohydraulic and nuclear feedback loops. (The phase lag of the nuclear feedback loop is dominated by the thermal time constant of the fuel rod, which is essentially fixed by the fuel design.) λ_{real} decreases when the phase shift between the two feedback processes changes from more favorable to less favorable conditions. If this phase shift is at a unfavorable condition, increasing void feedback gain may even reduces λ_{real}. At low power conditions, λ_{real} increases with power as the void feedback gain increases. But at high power conditions, the effect of changing the phase shift dominates over the effect of increasing the void feedback gain. So λ_{real} decreases with increasing power.

Increasing $|\alpha_v|$ also increases the void feedback gain. At the high flow condition, the nuclear feedback loop dominates. So λ_{real} increases with increasing $|\alpha_v|$. At the low flow condition, however, the density-wave mechanism becomes more important, and λ_{real} decreases with increasing $|\alpha_v|$.

The oscillation period corresponds to the frequency of the resonance peak of the system. Increasing power reduces the characteristic time of the density-wave mechanism, so the oscillation period increases. Increasing $|\alpha_v|$ increases the gain of the nuclear feedback loop, which also pushes the resonance peak to higher frequency and reduces oscillation period. This effect has also been reported in reference [65].

The stability boundary, at which $\lambda_{real} = 0$ ($DR = 1$), is of great interest to the operation of a BWR. Figure 7-5 shows the stability boundaries calculated by the time domain procedure for three sets of time step size and core channel nodes with constant $\left(\frac{\Delta t}{\Delta x}\right)$ ($\alpha_v = -12.8$ cents / % void). The stability boundary is higher for higher core flow as expected. The oscillation period decreases as core flow increases, and it also increases with decreasing Δt. At low flow conditions, small Δt and Δx give lower stability boundary. While at high flow conditions, large Δt and Δx give lower stability boundary.

The studies above show that the results of the time domain analysis are sensitive to the time step size and core nodalization. The void reactivity coefficient also greatly affects the stability analysis results. These parameters must be carefully selected for

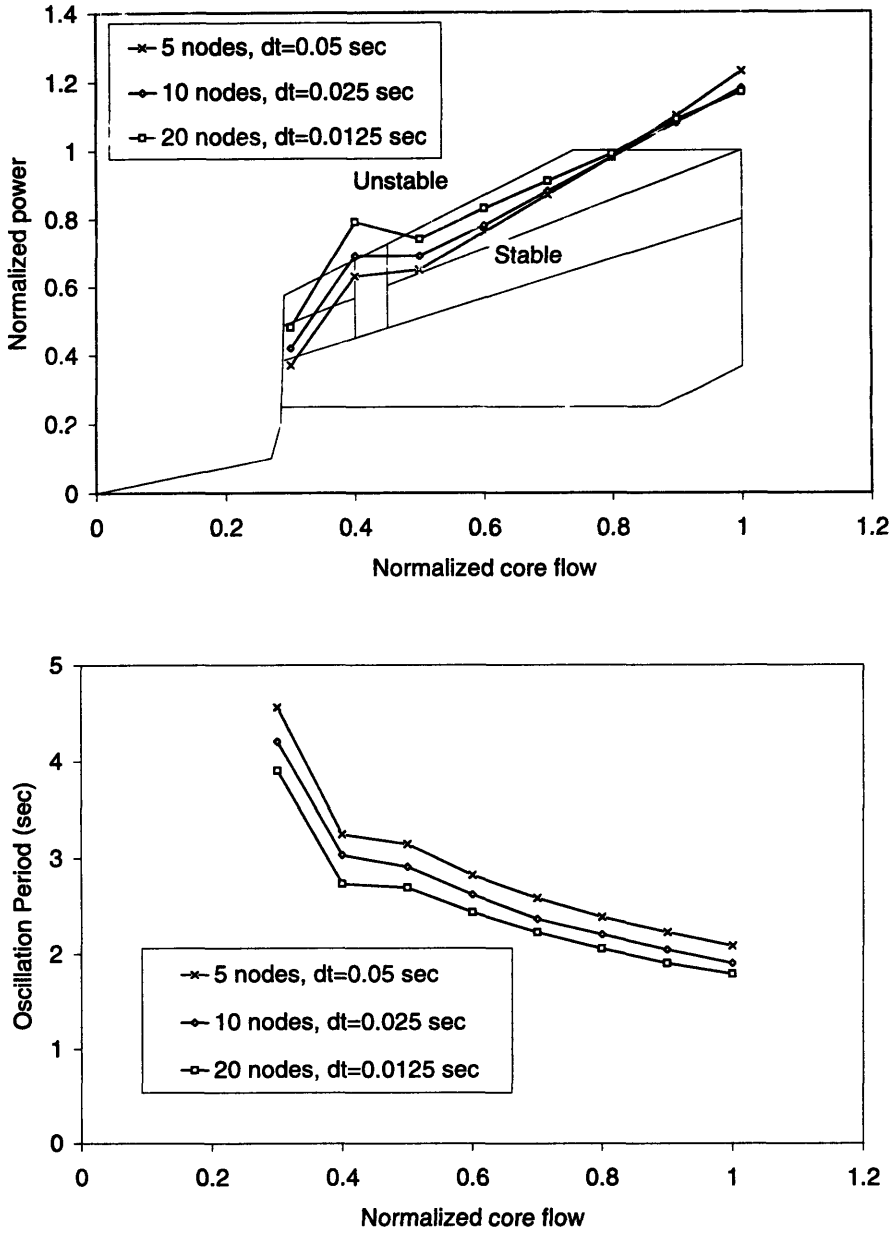

Figure 7-5: Stability boundaries calculated by the time domain analysis procedure.

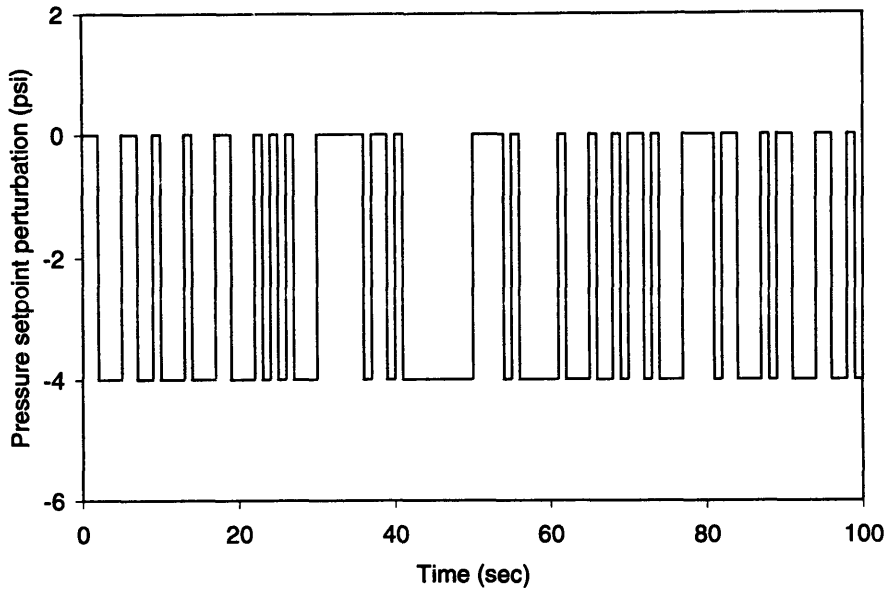

Figure 7-6: A segment of the Pseudo-Random Binary Sequence (PRBS).

accurate stability predictions.

7.2 Frequency Domain Analysis

Frequency domain analysis simulates the processes of the Peach Bottom-2 stability tests [32, 66]:

1. The system response of imposing a Pseudo-Random Binary Sequence (PRBS) to the set point of pressure controller is calculated. The simulation time determines the frequency resolution and errors associated with the frequency domain analysis results. Long simulation time in the order of ten minutes is required. Figure 7-6 shows a segment of the PRBS. The minimum step period is 1 sec., and the magnitude of the steps is 27.58 kPa (4 psi).

2. The time series of the fission power and reactor pressure from the first step are processed with spectral analysis to obtained an estimated pressure to power transfer function (G_E) [32, 67, 68].

(a) The data series are divided into overlapping segments. Each segment is detrended by subtracting their mean, and is multiplied by a Hanning window [69]

$$w(k) = 0.5\left[1 - \cos\left(\frac{2\pi k}{n+1}\right)\right], \; k = 1, \cdots, n,$$

where n is the number of data points in a segment, and k is the index of the point to be multiplied.

(b) The Fast Fourier Transforms (FFTs) of each data segment are calculated. The auto spectral density (ASD) functions of the input and output are the square of the magnitude of their FFTs. The cross spectral density (CSD) function are the product of the FFTs of the input and output. The smoothed ASD and CSD are obtained by averaging the ASDs and CSDs of all data segments. The estimated pressure (input) to power (output) transfer function is the ratio of the smoothed output ASD to the smoothed CSD.

(c) An estimated coherence function is also calculated. The coherence function indicates the dependence of the output on the input. The value of the coherence function is between 0 and 1. A coherence function of 1 indicates a perfect linear dependence between the input and output. The estimated coherence function is the ratio of the magnitude square of the smoothed CSD to the product of the smoothed input and output ASDs.

3. A second order model (G_M) is fitted to the estimated transfer function between the frequency range of 0.01 to 1 Hz. The second order model is

$$G_M(s) = \frac{K_p(\tau s + 1)}{\frac{s^2}{\omega_n^2} + \frac{2\zeta s}{\omega_n} + 1},$$

where K_p is the proportional gain, τ is a time constant, ω_n is the undamped natural frequency, and ζ is the damping ratio. The decay ratio and oscillation period are then calculated from the parameters of the second order model (for

$|\zeta| < 1$):

$$DR = \exp\left(-\frac{2\pi\zeta}{\sqrt{1-\zeta^2}}\right);$$

$$\text{oscillation period } T = \frac{2\pi}{\omega_n\sqrt{1-\zeta^2}}.$$

The fitting is done in two steps.

(a) A linear least square fitting is first performed. The objective is to minimize

$$\sum_{s=\ 0.01\text{Hz}}^{1\ \text{Hz}} \left[|G_E(s) - G_M(s)|^2 \times Wt(s)\right],$$

where Wt is a weighting function.

(b) A nonlinear least square fitting is performed. The result of the linear least square fitting is used as the initial guess in this step. The objective of this step is to minimize

$$\sum_{s=\ 0.01\text{Hz}}^{1\ \text{Hz}} \left\{[20\log_{10}|G_E(s)| - 20\log_{10}|G_M(s)|] \times Wt(s)\right\}.$$

The weighting function used in both steps is the estimated coherence function.

The spectral analysis and model fitting are performed using the MATLAB software [69]. The estimated transfer function and coherence function are calculated by functions TFE and COHERE in the Signal Processing Toolbox. The linear least square fitting is calculated by function INVFREQS also in the Signal Processing Toolbox. The nonlinear least square fitting is done by function LEASTSQ in the Optimization Toolbox. Function INVFREQS includes a denominator stabilizing step, so this fitting process is applicable to stable systems only.

The results of the frequency domain analysis are sensitive to the parameters used in each step of the analysis. These parameters include the time step size and node size used in the simulation, the length of data segments, the number of data segments, and the weighting function used in the fitting processes.

Table 7.1: Frequency domain analysis results given by different weighting functions

	Fit #1	Fit #2
Weighting function	coherence function	a constant
DR	0.482	0.087
T (sec)	2.55	2.28

Figure 7-7 shows an example of the results of frequency domain analysis. This example illustrates the sensitivity of the analysis results on the weighting function used in model fitting. The unit of the pressure to power transfer function is (% power / Pa). In this example, two weighting functions are used to calculate the second order model. They are the coherence function (Fit #1), and a constant (Fit #2). Table 7.1 lists the results obtained by using the two weighting functions. The decay ratios of these two cases differ by 0.39.

Similar spectral analysis performed on a time domain code has only been reported for the RAMONA-3B code [68].

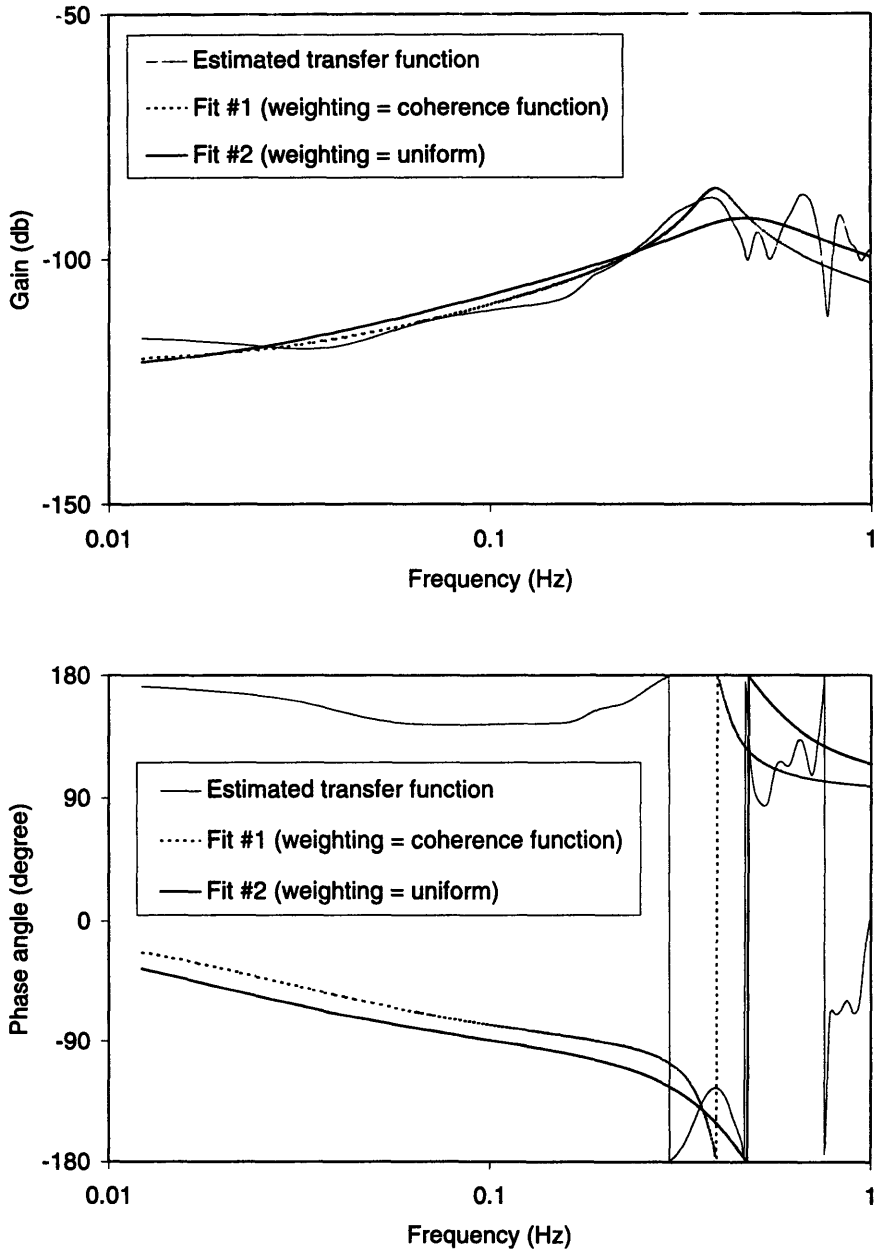

Figure 7-7: Example of the frequency domain analysis results.

Table 7.2: Test conditions and results of the Peach Bottom-2 stability tests [32, 66]

Test number	Fuel cycle	Power (%)	Flow (%)	DR	T (sec)
PT1	2	60.6	52.3	0.259	2.28
PT2	2	51.7	43.8	0.303	2.27
PT3	2	59.2	40.4	0.331	2.36
PT4	2	43.5	40.3	0.271	2.61
1PT1	3	39.7	47.8	0.236	2.34
1PT2	3	46.7	47.6	0.314	2.48
2PT2	3	52.0	45.5	0.435	2.31
2PT3	3	61.7	44.6	0.509	2.31
3PT2	3	52.1	47.1	0.391	2.45
3PT3	3	61.6	46.2	0.504	2.46
4PT1	3	50.7	47.5	0.355	2.55
4PT2	3	44.0	48.0	0.293	2.62
4PT3	3	38.4	48.1	0.210	2.66

7.3 Benchmark Against Peach Bottom-2 Stability Test Results

Thirteen special low flow stability tests have been performed at Peach Bottom-2. Four tests were performed at the end of Cycle 2, and another nine tests at the end of Cycle 3 [32, 66]. These tests use the procedure described in the previous section. Namely, the system is perturbed by a PRBS of pressure set point; a pressure to power transfer function is obtained by performing spectral analysis; a second order model is fitted to the transfer function, and the decay ratio is calculated from the parameters of the second order model. Table 7.2 lists the conditions and results of these stability tests [32, 66].

The test results show the expected trend that with similar core flow rates, the test

with higher power has a higher decay ratio. Detail test conditions such as reactor pressure, core inlet subcooling, and the axial power shape are given in references [32] and [66]. But the actual nuclear data for each test are not available.

Same input data as used in the simulations of Peach Bottom-2 turbine trip tests are used in the stability analysis. The void reactivity coefficient, time step size, and core nodalization are selected based on the sensitivity study. All thirteen tests are analyzed by the time domain procedure. Only tests 2PT3 and 3PT2 are analyzed by the frequency domain procedure. The analysis results are presented in the following sections.

7.3.1 Analysis using time domain procedure

Because the actual nuclear data during the Peach Bottom-2 stability tests are not available, and because the stability analysis results are sensitive to the time step size and core nodalization, a sensitivity study is performed to select a set of void coefficient (α_v), time step size (Δt), and number of core channel axial nodes (N_{node}) that gives the best result with respect to the test data.

Test 2PT3 is used as the basis of the sensitivity study. Figures 7-8 and 7-9 show the results of the sensitivity analysis with different parameters. The set of parameters that gives the best results is $\alpha_v = -12$ cents / % void, $N_{node} = 12$, and $\Delta t = 0.01$ sec. This set of parameters is used for all thirteen cases. Notice that the actual void coefficients of each test are not the same, since the tests are performed in two fuel cycles. And even in the same fuel cycle, the void coefficients are different because the test conditions and the power histories prior to the tests are different.

As discussed in section 4.1.2, two forms of the energy equation can be used in the thermal hydraulic model, and the decoupled form is used in the BWR simulator. In this section, both forms of the energy equation are used to analyze the Peach Bottom-2 stability tests, and the analysis results are listed in Table 7.3. Figure 7-10 compares the analysis results with the test data.

Both coupled and decoupled forms predict larger decay ratios and oscillation periods than test data, but the decay ratios calculated by the coupled form are much

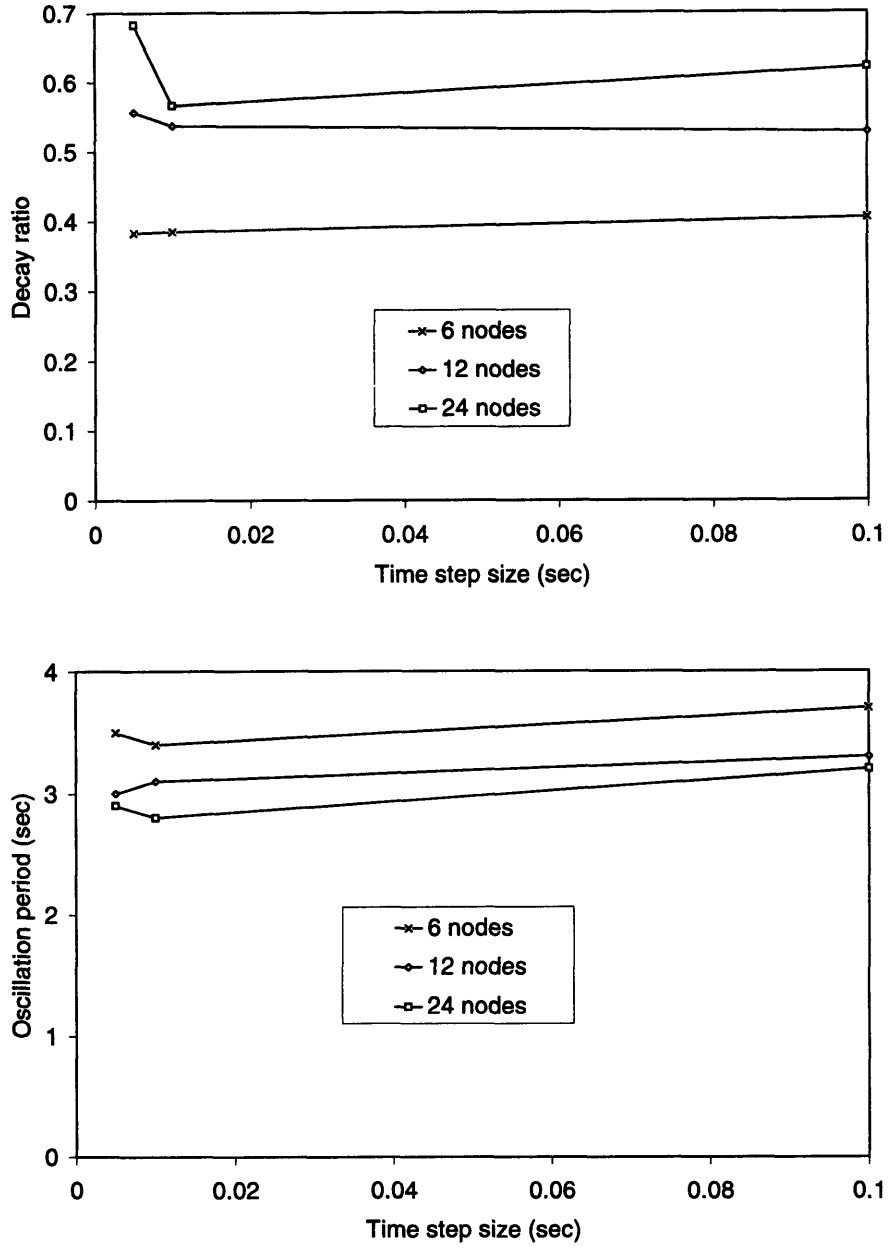

Figure 7-8: Stability analysis results of test 2PT3 with different time step sizes and core nodalization schemes. The void coefficient is -12 cents / % void.

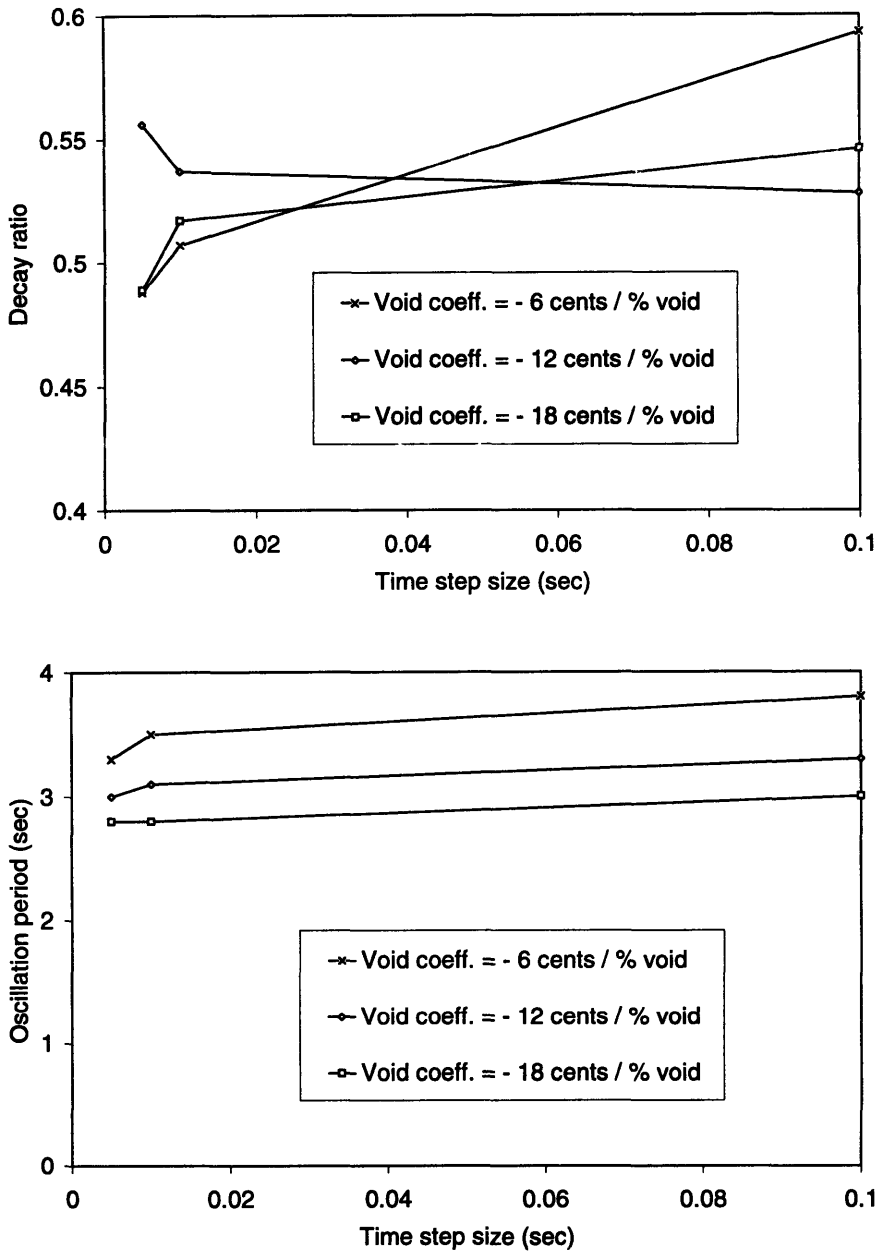

Figure 7-9: Stability analysis results of test 2PT3 with different void coefficients and time step sizes. The core channel has 12 axial nodes

Table 7.3: Time domain analysis results of the Peach Bottom-2 stability tests

Test number	De-coupled form		Coupled form	
	DR	T (sec)	DR	T (sec)
PT1	0.37	3.4	0.75	2.9
PT2	0.363	3.8	0.816	3.5
PT3	0.359	3.3	0.558	2.7
PT4	0.389	4.6	0.89	3.9
1PT1	0.352	3.6	0.551	3.5
1PT2	0.517	3.3	0.925	3.3
2PT2	0.488	3.3	1.054	3.2
2PT3	0.537	3.1	1.224	3.0
3PT2	0.514	3.3	1.145	3.3
3PT3	0.588	3.1	0.971	3.0
4PT1	0.582	3.3	0.962	3.3
4PT2	0.408	3.6	0.833	3.5
4PT3	0.345	3.9	0.617	3.7

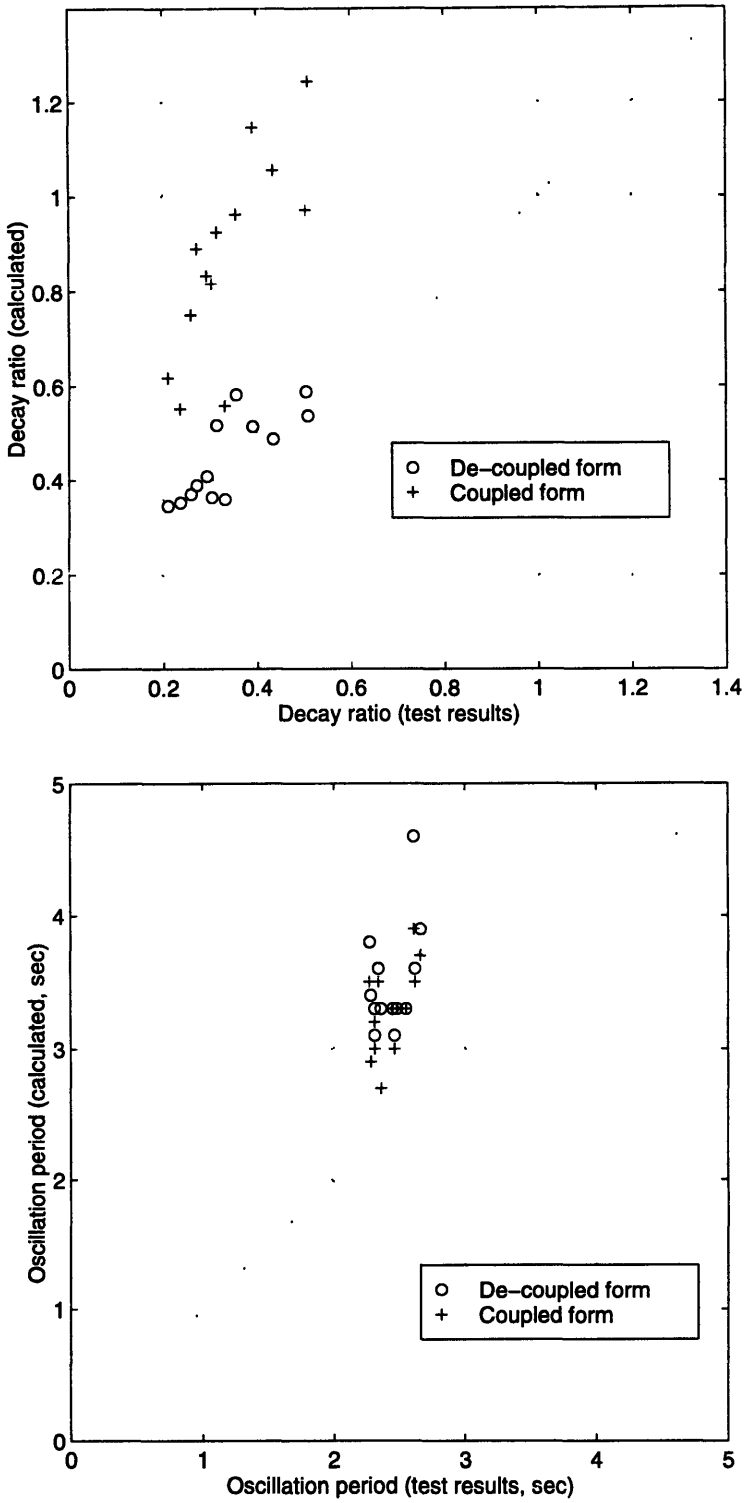

Figure 7-10: Comparison of time domain analysis results of Peach Bottom-2 stability tests with test data.

too high. The mean error of decay ratios calculated by the decoupled form is 0.108, and the maximum error is 0.227. The oscillation periods calculated by the decoupled form have a mean error of 1.07 sec., and the maximum error is 1.99 sec. These results show that the decoupled form of the energy equation is best suited for BWR stability analysis.

March-Leuba and Otaduy have analyzed the Peach Bottom-2 stability tests using the frequency domain code LAPUR-IV [65]. Their results underestimate the decay ratios and overestimate the oscillation periods. The mean error of decay ratios from LAPUR-IV is 0.133, and the mean error of the oscillation periods is 0.75 sec. Figure 7-11 compares the results of LAPUR-IV and the BWR simulator (de-coupled form) with the test data. The discrepancies of the LAPUR-IV results are probably due to lack of accurate nuclear data.

Figure 7-12 show the power and flow of each test along with the decay ratios and oscillation periods given by the test data, the BWR simulator (decoupled form), and LAPUR-IV. The BWR simulator predicts the correct trend as the test results have shown. Considering the uncertainty of the nuclear data, the stability analysis results of the BWR simulator agree well with test data.

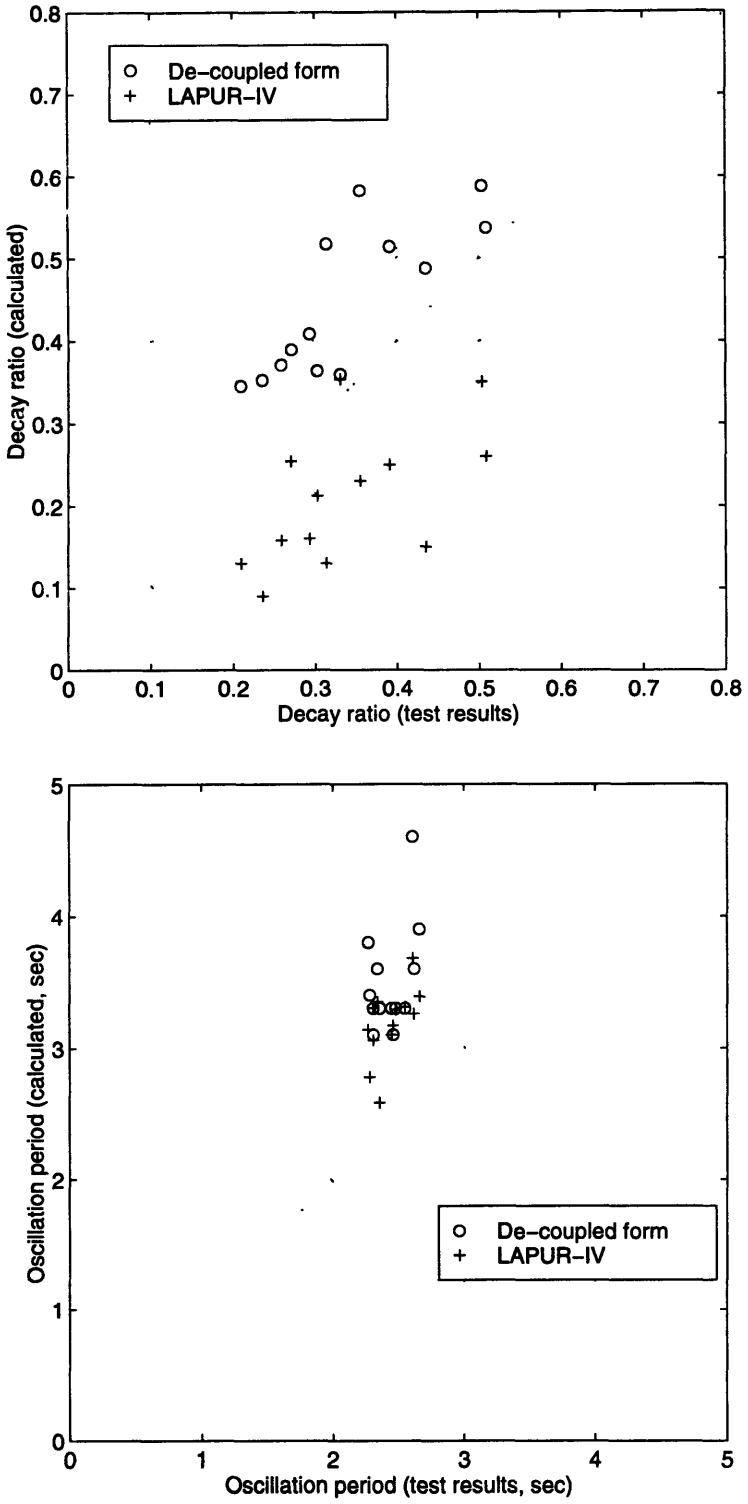

Figure 7-11: Comparison of stability analysis results from LAPUR-IV and the BWR simulator (decoupled form) with test data.

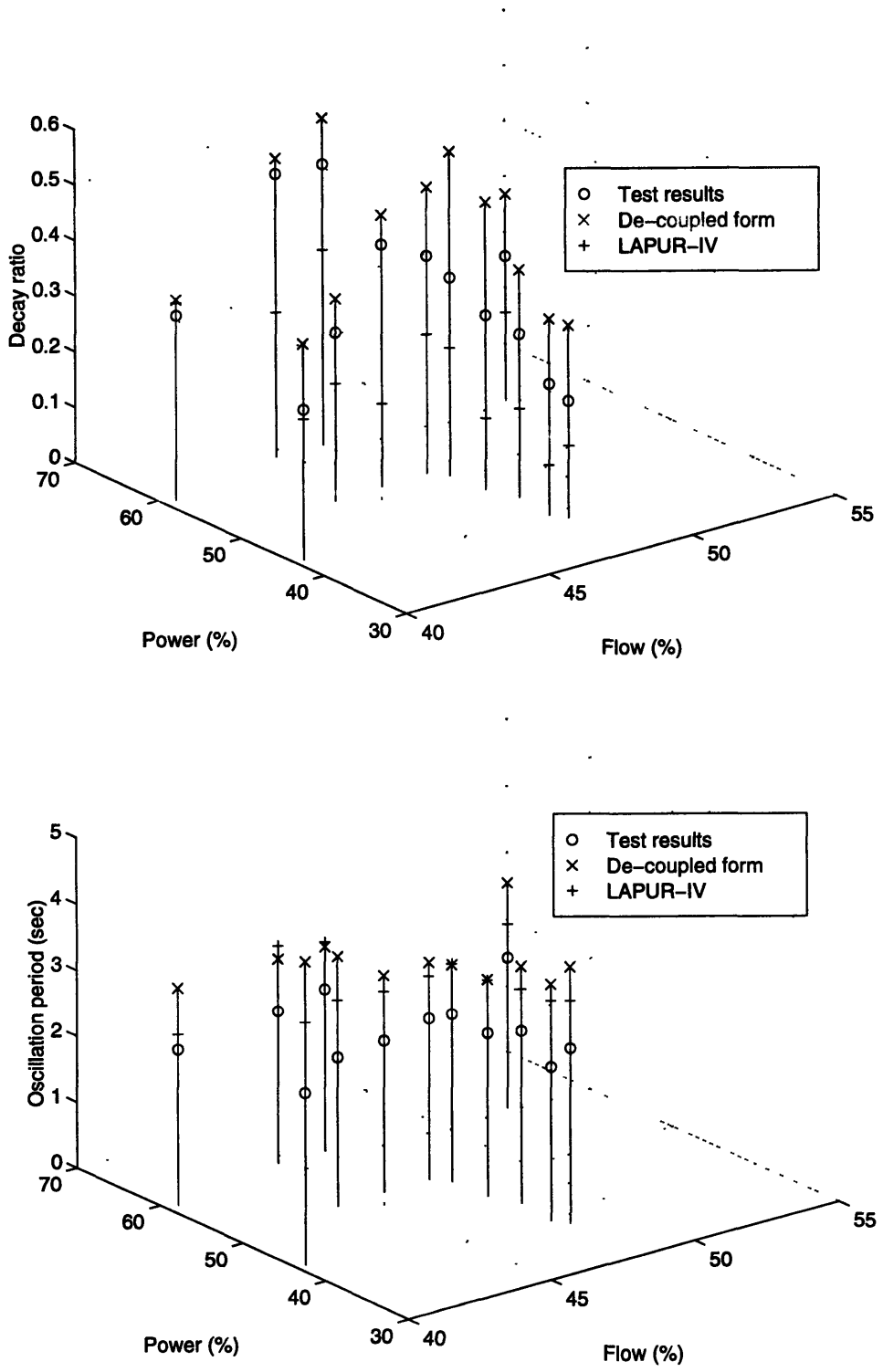

Figure 7-12: Test points and stability analysis results of the Peach Bottom-2 stability tests.

Table 7.4: Parameters used in the frequency domain analysis

Simulation time	512 sec.
Time step size	0.01 sec.
Data sampling rate	20 Hz
Data segment length	512
Length of data segment overlapping	256
Weighting function	estimated coherence function

Table 7.5: Void coefficients and core nodalization schemes used in the frequency domain analysis

	Case 1	Case 2	Case 3	Case 4
Void coeff. (cents / % void)	−12	−12	−6	−18
No. of core channel axial nodes	12	24	24	24

7.3.2 Analysis using frequency domain procedure

Tests 2PT3 and 3PT2 of Peach Bottom-2 stability tests are analyzed using the frequency domain procedure. The parameters used in the analysis are listed in Table 7.4. Four sets of void coefficient and core nodalization scheme are used for each test, as shown in Table 7.5.

The analysis results of test 2PT3 are listed in Table 7.6. The estimated transfer functions and their fitted models are compared with the second order model from the test data in Figures 7-13 through 7-16. The unit of the transfer function is (% power / Pa). The analysis results of test 3PT2 are shown in Table 7.7 and Figures 7-17 through 7-20.

The following observations can be drawn from the above results:

1. The calculated transfer functions have higher gains and different phase angles than the test results. These discrepancies may be due to the differences of the

Table 7.6: Frequency domain analysis results of test 2PT3

	Case 1	Case 2	Case 3	Case 4
K_p (% power / psi)	0.742	0.603	0.466	0.699
τ (sec)	3.56	5.55	5.23	5.9
ω_n (rad/s)	2.14	2.48	2.33	2.62
ζ	0.108	0.116	0.159	0.096
DR	0.506	0.482	0.363	0.545
T (sec)	2.95	2.55	2.73	2.41

Table 7.7: Frequency domain analysis results of test 3PT2

	Case 1	Case 2	Case 3	Case 4
K_p (% power / psi)	0.913	0.815	0.845	0.684
τ (sec)	2.17	2.78	1.21	4.55
ω_n (rad/s)	2.52	2.55	2.11	2.84
ζ	0.105	0.096	0.106	0.085
DR	0.514	0.545	0.512	0.584
T (sec)	2.51	2.48	3.0	2.22

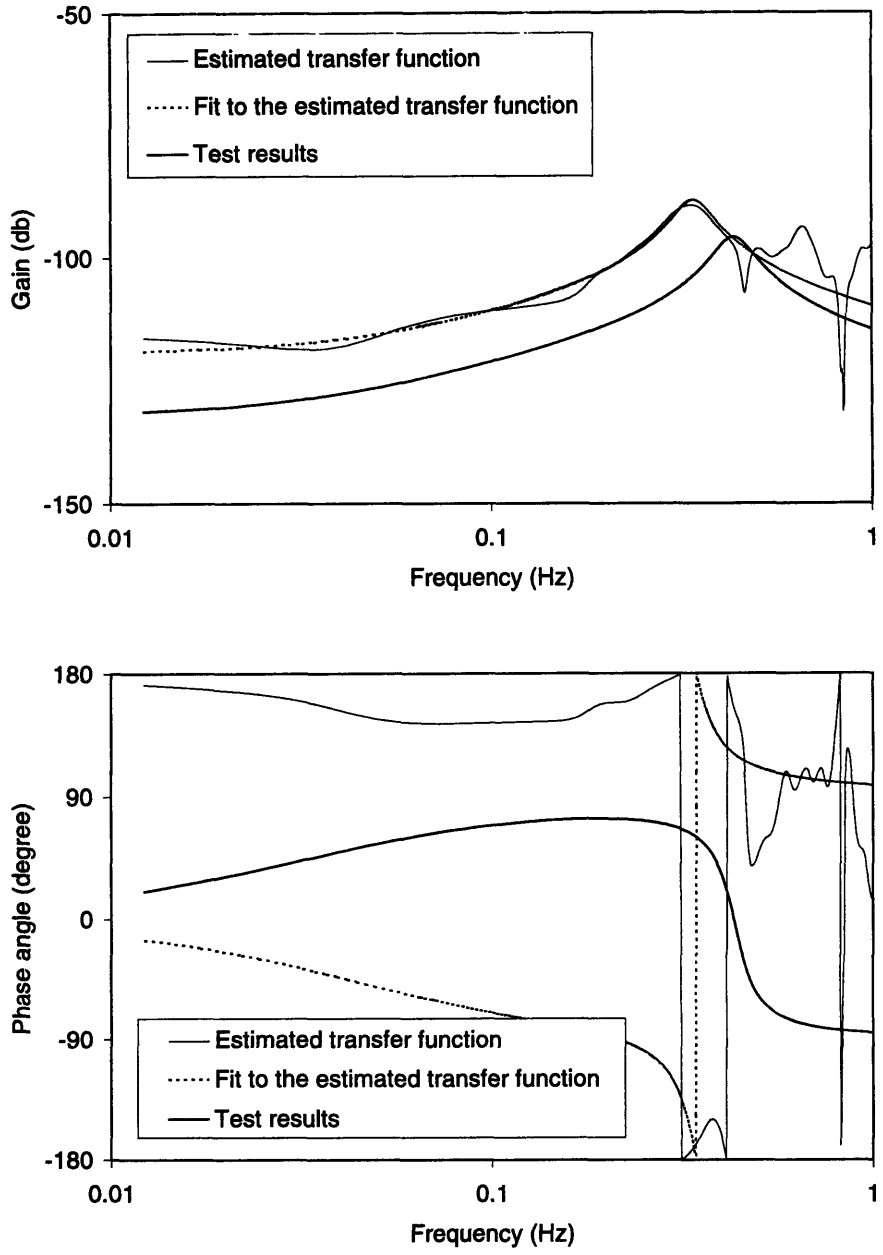

Figure 7-13: Comparison of calculated transfer function of test 2PT3 (case 1) with the model from test data.

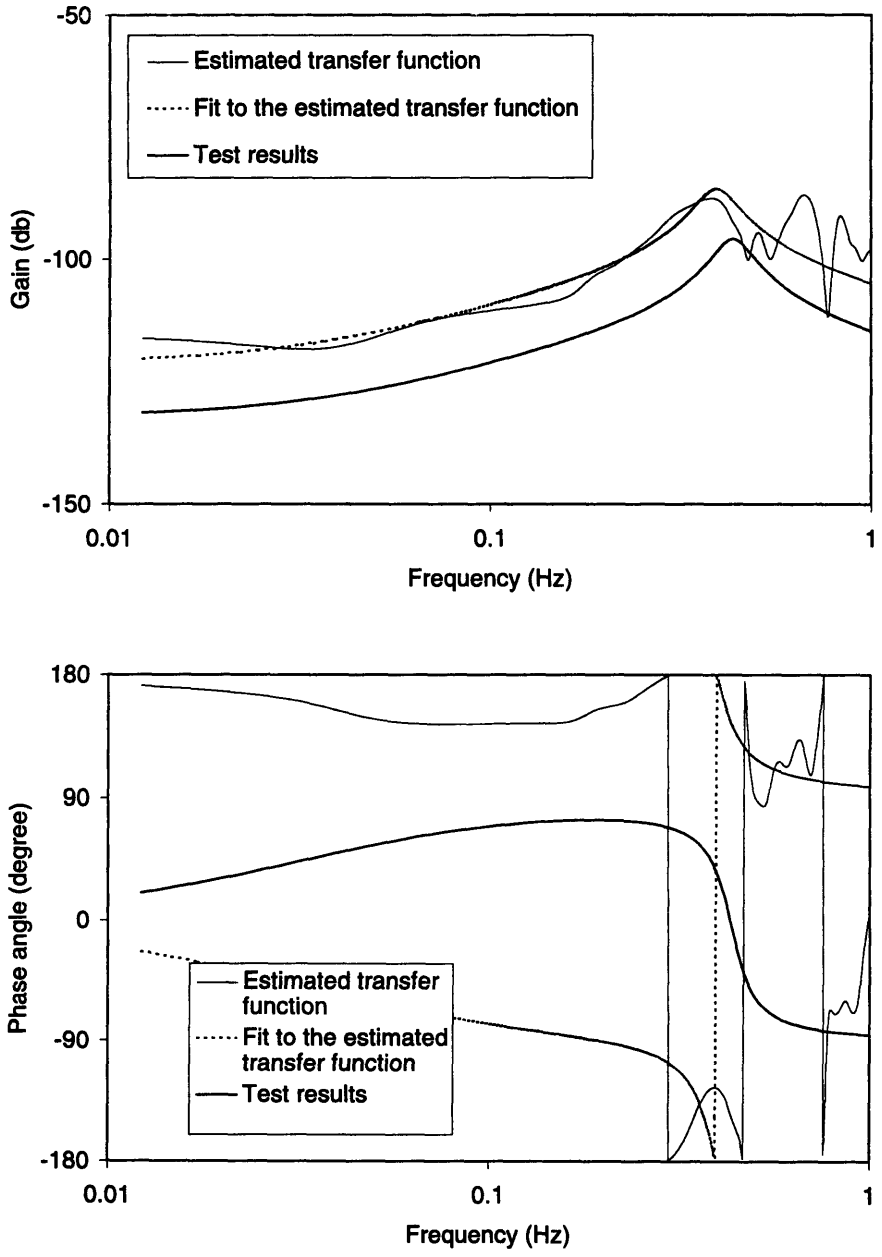

Figure 7-14: Comparison of calculated transfer function of test 2PT3 (case 2) with the model from test data.

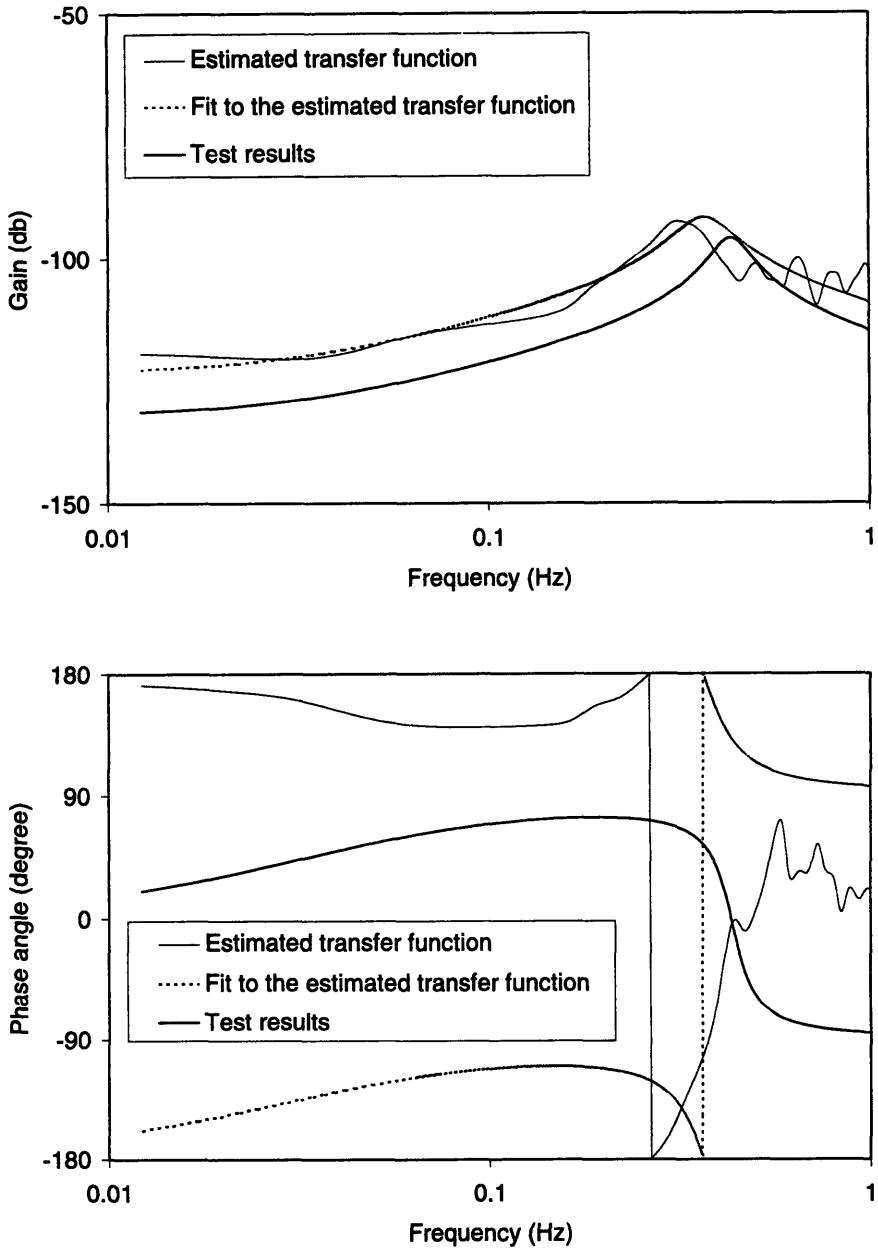

Figure 7-15: Comparison of calculated transfer function of test 2PT3 (case 3) with the model from test data.

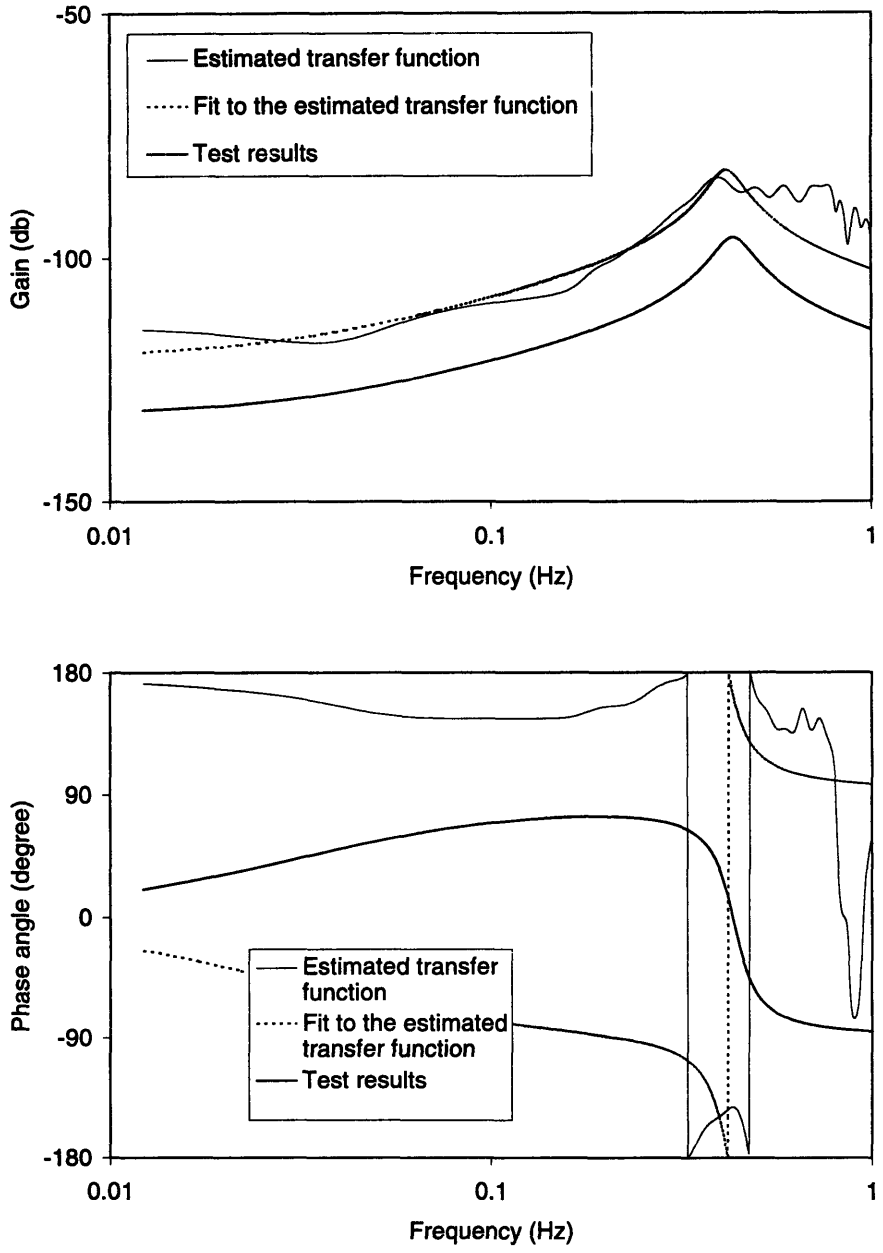

Figure 7-16: Comparison of calculated transfer function of test 2PT3 (case 4) with the model from test data.

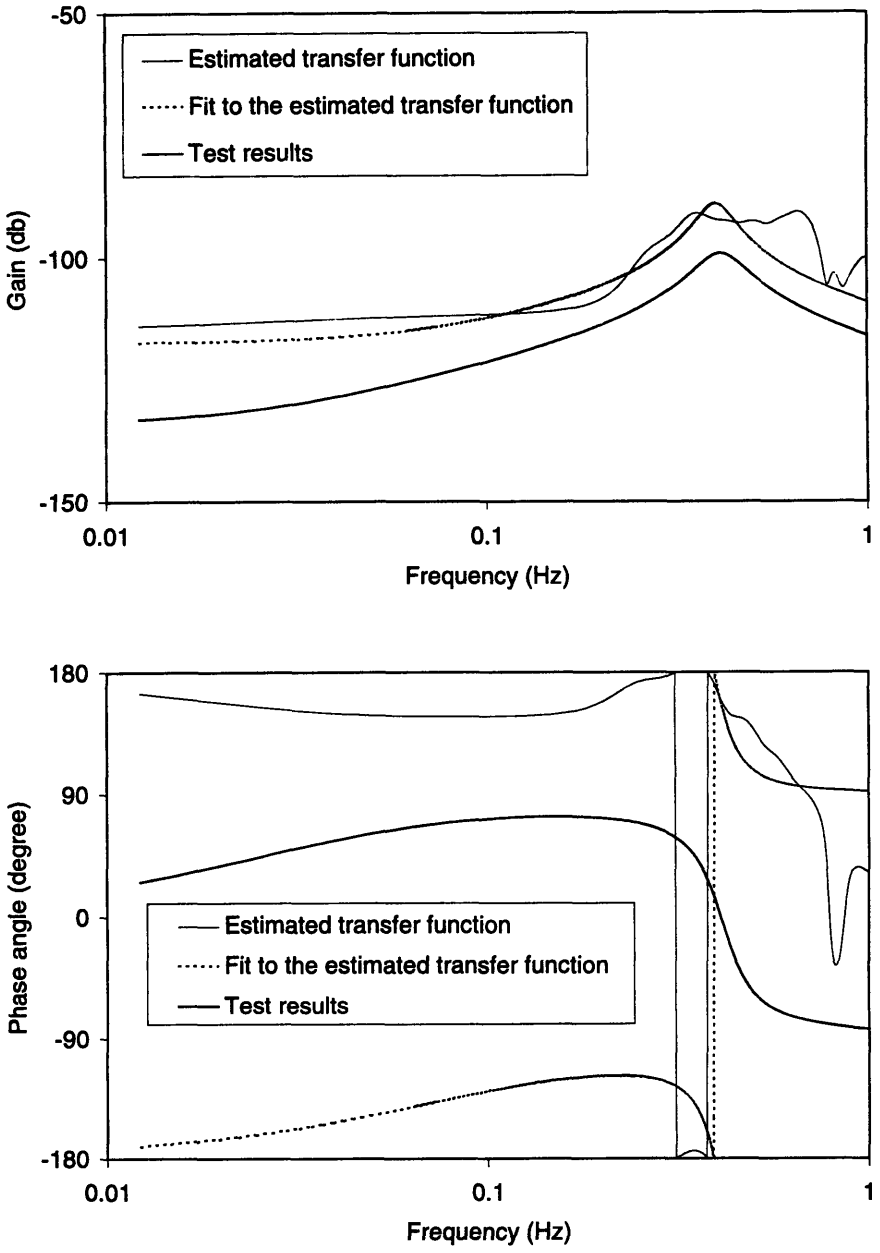

Figure 7-17: Comparison of calculated transfer function of test 3PT2 (case 1) with the model from test data.

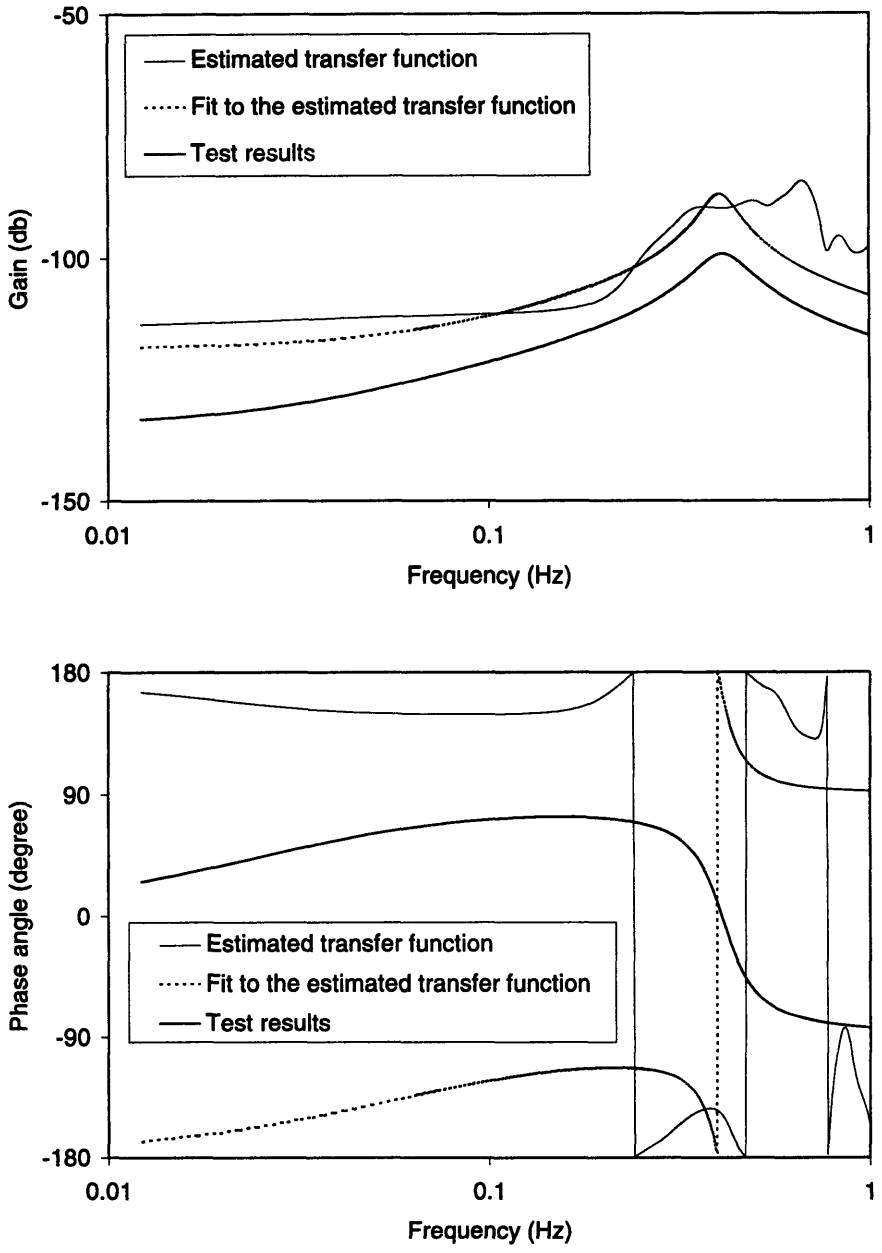

Figure 7-18: Comparison of calculated transfer function of test 3PT2 (case 2) with the model from test data.

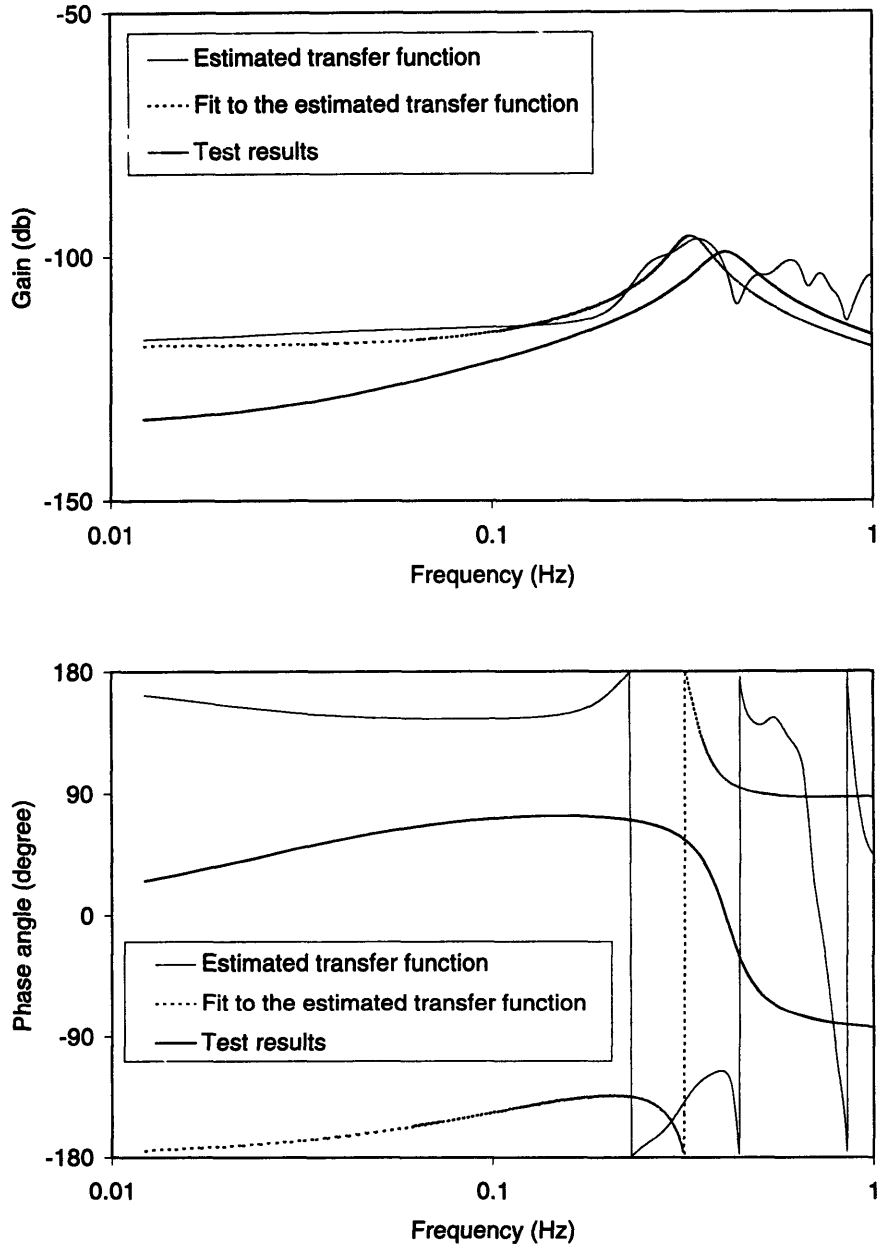

Figure 7-19: Comparison of calculated transfer function of test 3PT2 (case 3) with the model from test data.

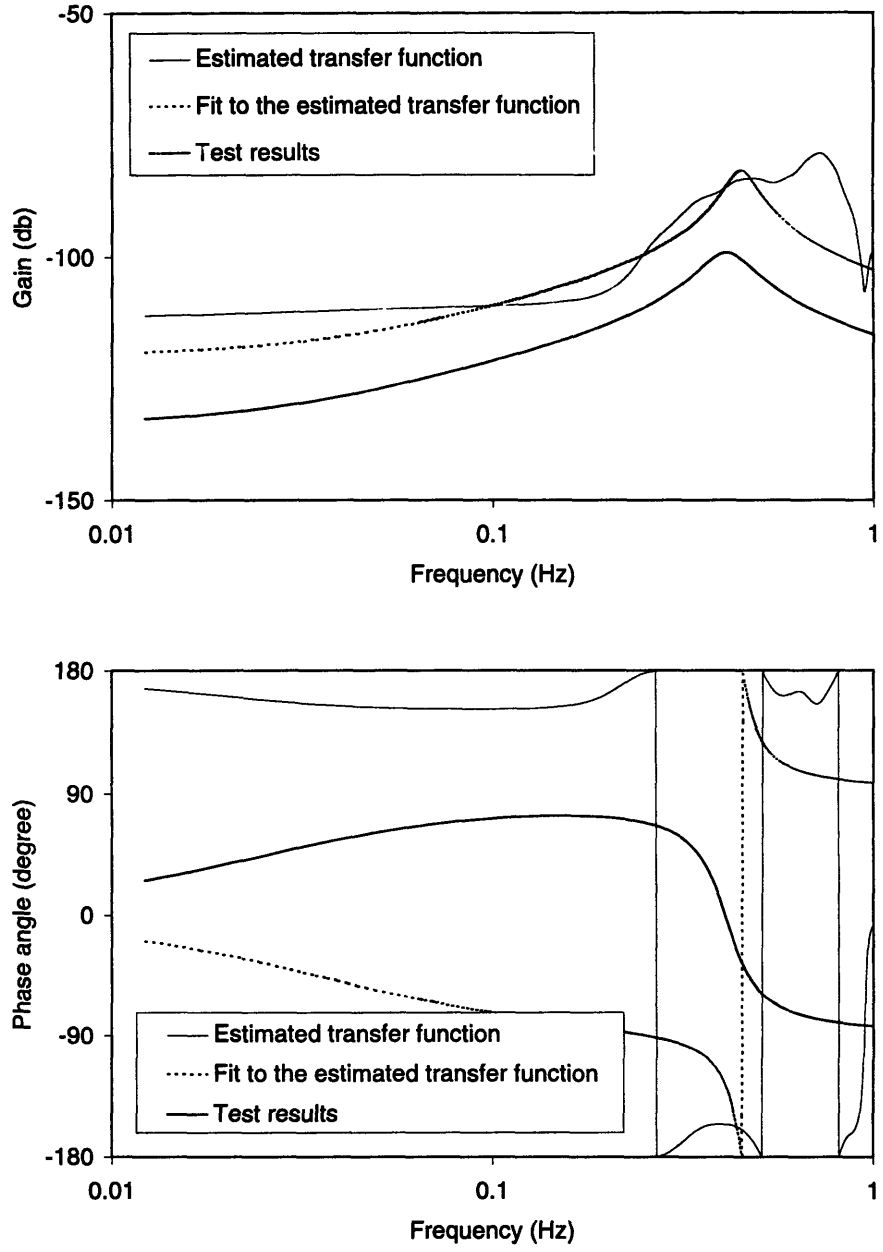

Figure 7-20: Comparison of calculated transfer function of test 3PT2 (case 4) with the model from test data.

Table 7.8: Comparison of time and frequency domain analysis results

	2PT3		3PT2	
	DR	T (sec)	DR	T (sec)
Test results	0.509	2.31	0.391	2.45
Time domain results	0.537	3.1	0.514	3.3
Frequency domain results	0.506	2.95	0.514	2.51

pressure controller characteristics between the actual plant and the simulator.

2. For cases with the same core nodalization scheme, a larger void coefficient gives a higher gain, a larger decay ratio, and a shorter oscillation period.

3. For cases with the same void coefficient, a larger number of core nodes gives a shorter oscillation period.

Table 7.8 compares the stability analysis results of the time and frequency domain procedures with the same parameters ($\alpha_v = -12$ cents / % void, 12 nodes in the core channel, $\Delta t = 0.01$ sec.). The frequency domain analysis results are similar to the time domain results.

7.4 Discussions

The time and frequency domain stability analysis procedures are sensitive to the parameters used in the calculation. Accurate nuclear data are necessary for an accurate prediction of the stability margin. The time step size and core nodalization scheme used in the calculation must be selected based on actual plant data.

The computation time of the time domain procedure is much shorter than that of the frequency domain procedure. A long simulation time is needed for the frequency domain procedure to have better resolution in the low frequency range of interest, and to have better smoothing of the estimated transfer function. The spectral analysis and model fitting also require intensive calculations.

The speed of time domain analysis depends on the time step size and number of core nodes. It also depends on the stability of the system. If the system is very stable, the disturbances of system parameters die out very fast, and a short simulation time (20 to 30 sec.) is sufficed. But the stability analysis results are less accurate. On the other hand, if the system is less stable, a longer simulation time is required to observe the asymptotic decay ratio, and the results are more accurate.

For the Peach Bottom-2 stability tests, a simulation of 30 sec. is adequate. Comparing the test data and calculated decay ratios by the time domain procedure, the calculated results are more accurate for the cases with decay ratio larger than 0.4. Using a time step size of 0.01 sec. and 12 axial nodes in the core channel, the analysis of one case by the time domain procedure takes about two minutes. A shorter analysis time can be achieved if the procedure is automated. An expert system to determine the simulation time and to select the representative decay ratio is required for the automation of the time domain procedure.

The oscillation periods predicted by the BWR simulator are longer than the test results. This discrepancy has also been reported for stability analyses using BNL-EPA [6], LAPUR-IV [65], RAMONA-3B [68], and TRAC/BF1 [49]. The possible causes of this discrepancy are as follow:

1. The nuclear data used in the analyses are inaccurate.

2. The non-boiling length in the core channel may be over-predicted [68]. This leads to a longer fluid transport time through the core.

3. The stability analyses using average core channels will give longer fluid transport time than that of the hot channel. The oscillation period of the system is influenced by the dynamics of the least stable channel (the hot channel). So using average channels may give a longer oscillation period.

Many researches have shown that the decay ratio may not be adequate to describe the stability margin of BWRs [31, 70]. A new index, the Stability Power Ratio (SPR), may be an alternative to the decay ratio. The stability power ratio is analogous to the Critical Power Ratio (CPR) used to indicate the thermal margin of a fuel channel, and is defined as

$$SPR = \frac{\text{Power level at the stability boundary}}{\text{Actual power level}}.$$

The stability boundary is calculated by increasing the reactor power with the feedwater temperature, core flow rate, and core power shape held constant. Despite the fact that the actual system parameters will not be the same as the power increases, this SPR can still provide a good picture about the stability margin of the system in terms of a meaningful parameter.

7.5 Chapter Summary

Two stability analysis procedures are developed in this chapter. The time domain procedure calculates the system response to a reactivity disturbance. The decay ratio and oscillation period are estimated from the response of the fission power. The frequency domain procedure simulates a stability test that imposes a Pseudo-Random Binary Sequence to the set point of the pressure controller. The pressure to power transfer function is estimated by spectral analysis, and the decay ratio and oscillation period are obtained by model fitting. Both time and frequency domain procedures are sensitive to the parameters used in the analysis.

Thirteen stability tests conducted at Peach Bottom-2 are analyzed by the time domain procedure. The calculated results show the same trend as the test results. Both the decay ratios and oscillation periods are slightly over predicted with respect to test data. The agreement between the calculated results and test data is fairly good even though accurate nuclear data are not available. Two stability tests are analyzed by the frequency domain procedure, and the results are similar to that of the time domain analysis.

The time domain procedure takes about two minutes to analyze one case. This analysis speed can be accelerated if the procedure is automated. The frequency domain procedure is very time consuming because of the long simulation time required and the intensive calculations in the data reduction processes.

The stability margin of a BWR may be described by a Stability Power Ratio (SPR). The SPR is the ratio of the power at the stability boundary to the actual power. This SPR can provide a more concrete ideal of the system stability in terms of a meaningful parameter—the reactor power.

Chapter 8

Conclusions and Recommendations

8.1 Conclusions

BWR power oscillation is a complex phenomenon caused by a nuclear-coupled density-wave instability. The stability of a BWR depends on many factors such as the reactor power, core flow, pressure, power shape, reactivity feedback coefficients, and the core inlet subcooling. The effects of changing these variables on the system stability may be counter intuitive.

Recent BWR power oscillation events, i.e., the LaSalle-2 and WNP-2 events, call for new approaches to ensure the stability of BWRs. After several years of research, two approaches have been accepted by the NRC. The first approach (Prevention) designates some exclusion regions. Operations inside the exclusion regions are prevented by automatic safety systems. The second approach (Detection/Suppression) uses stability monitors to detect unstable conditions. Automatic safety systems are used to suppress power oscillations once detected. These approaches either reduce the available operation domain or impose risks from inadvertent safety system actuation.

In this research, A BWR simulator targeted particularly at stability analysis is developed. It employs simplified physical models to describe the major processes in a BWR. However, the simulator is capable of simulating the power oscillation phe-

nomenon. The procedures for stability analysis using the simulator are also developed.

The BWR simulator that has been developed is applicable to normal and operational transient conditions, and has been shown to be suitable for analysis of the in-phase type of power oscillations. Therefore, the choice of incorporated physical representations is judged to be a correct one.

The computer time is also sufficiently close to real time on a personal computer (and probably will run much faster than real time for future advanced personal computers and/or for improved programming techniques). For example, the Peach Bottom-2 stability tests were studied using a core channel with 12 axial nodes plus a bypass channel with one axial node, using a time step size of 10 ms, and using a personal computer with a 90 MHz Pentium processer. The ratio of CPU time to simulated time was 1.2 (excluding the time required for finding the decay ratio).

The Brookhaven Laboratory Engineering Plant Analyzer runs even faster (CPU time to simulated time is one-sixth [60]); however, those speeds are achieved only by using special hardware that may be unavailable at many BWR plants that could be served by multiple simulators of the present study type. We understand that the other time domain codes that have been used for BWR stability analysis (such as RELAP, RETRAN, and TRAC) are all more time consuming for this problem scope or require the use of a super computer as special hardware.

Because of the fast computation speed of the BWR simulator, near real-time stability analysis can be achieved. The BWR simulator can be used to predict the stability margin of future operating conditions. With this monitor/prediction capability, the BWR simulator can be used to supplement the Prevention and Detection/Suppression approaches to achieve a higher degree of reliability. The simulator can also be used for transient analysis and training.

Many physical models used in the BWR simulator have been validated individually. Actual plant data and analysis results from others have been used to assess the transient simulation capability and the accuracy of the stability analysis results of this simulator. Several conclusions can be drawn from these studies:

1. The thermal hydraulic model can simulate the ANL test loop flow oscillation

accurately. Both coupled and decoupled forms of the energy equation give good predictions on the stability boundary of the ANL test loop. For nuclear-coupled instabilities, however, only the decoupled form of energy equation gives adequate results.

2. The two-node fuel model performs very well when compared with the fuel model in the THERMIT-2 code.

3. The jet pump characteristics calculated by the jet pump model agree well with test data.

4. The steam line model predicts turbine stop valve fast closure transients accurately when compared with both analytical solution and test data.

5. In general, the transient responses calculated by the BWR simulator agree well with test data. The slower pressure response calculated by the simulator is due to the single pressure assumption used in the thermal hydraulic model.

6. The decay ratios and oscillation periods calculated by the time domain stability analysis procedure are slightly over-predicted with respect to results of Peach Bottom-2 stability tests.

7. For the frequency domain analysis, the calculated gains are higher than test results, and the phase angles are different. Errors in simulating the pressure controller characteristics may be the cause of these discrepancies.

8. The decay ratios calculated by the frequency domain procedure are similar to those of the time domain procedure.

9. The results of the stability analysis are sensitive to the time step size and core nodalization scheme. These parameters should be selected based on actual plant data.

10. The nuclear data must be accurate in order to have accurate stability predictions.

8.2 Recommendations

This study developed the framework of a simulator-based stability indicator/predictor. Further work is needed to produce a practical tool for industry applications. The followings are the areas that can be explored .

1. More transient and stability data can be used for further assessment of the BWR simulator.

2. An interactive graphic user interface can be added to make the simulator more user friendly.

3. The models of protection systems and malfunctions can be added to improve the simulation capability.

4. An expert system can be developed to automate the input selections and engineering judgment required for time domain stability analysis.

5. A space-dependent reactor kinetics model can be incorporated to extend the stability analysis capability to out-of-phase type instability.

6. The scope of the simulation can be expanded by adding models of turbine plant components (the turbine, condenser, feedwater pumps, and feedwater heaters).

7. The feasibility of using the Stability Power Ratio as an index of stability margin should be explored.

Appendix A

Nomenclature

A	area
B^2	geometric buckling
C	decay neutron precursor concentration
C_0	distrbution parameter
C_D	decay heat precusor concentration
c_p	constant pressure specific heat
crl	jet pump interpolation factor
cu	vapor carryunder mass fraction
c_v	constant volume specific heat
	valve coefficient
D	diffusion coefficient
D_h	hydraulic diameter
E	total energy content in a node
e	average volumetric enthalpy of a node
f	Darcy friction factor
f_D	decay heat fraction
G	mass flux
g	acceleration of gravity
H	pump head
h	enthalpy
	heat transfer coefficient
	dimensionless pump head
h'	flow enthalpy
$\overline{h}$	average enthalpy of a node
I	flow inertia
	moment of inertia
K	loss coefficient
	controller gain
k	thermal conductivity

ℓ	length
M	total mass in a node
	jet pump flow ratio
m	average density in a node
N	jet pump head ratio
P	pressure
	total core power
P_{core}	reactor core pressure drop
P_D	decay power
Pe	Peclet number
P_{jet}	jet pump pressure gain
P_n	fission power
Pr	Prandtl number
P_{rcp}	recirculation pump pressure gain
Q	heat transfer rate
	volumetric flow rate
q	heat addition rate to a node
q''	heat flux
q'''	volumetric heat deposition rate
R	jet pump nozzle to throat area ratio
r	radius
Re	Reynolds number
s	Laplace variable
T	neutron amplitude function
	oscillation period
	temperature
	torque
t	time
UA	total heat transfer coefficient
u	internal energy
u_{gj}	drift velocity
V	volume
v	specific volume
W	mass flow rate
$X(s)$	Laplace transform of input signal
x	steam quality
$x(t)$	input signal
$Y(s)$	Laplace transform of output signal
$y(t)$	output signal
z	space coordinate
	elevation

Greek letters

α	void fraction

	dimensionless pump speed
α_v	void reactivity coefficient
β	effective delay neutron fraction
	dimensionless pump torque
β_D	normalized decay heat fraction
γ	isentropic expansion coefficient
δ	thickness
δ_{jump}	thermal jump distance
ζ	damping ratio
θ	angle from horizontal to flow direction
	implicit factor in the Theta method
λ	delay neutron precusor decay constant
	eigenvalue of neutronic mode
λ_D	decay heat precursor decay constant
λ_{real}	real part of system eigenvalue
μ	dynamic viscosity
ν	dimensionless flow rate
$\nu\Sigma_f$	fission neutron yield times fission cross section
ρ	density
	reactivity
ρ'	dynamic density
σ	surface tension
τ	time constant
ϕ_{lo}^2	two-phase friction multiplier
ω	pump speed
ω_n	undamped natural frequency
Δ	difference between values at new and old time step
Δt	time step size
Δx	node size
Δz	elevation difference
	length of fuel section
Λ	prompt neutron life time
Σ_a	absorption cross section

Subscripts

c	cladding
ci	cladding inner surface
D	decay heat precusor
	differential controller
d	jet pump diffuser
	point of OSV
dc	lower downcomer
ext	external
FB	feedback

FC	forced convection
FW	feedwater
f	saturated water
	fuel
fl	flashing
fo	fuel outer surface
g	saturated steam
	gap
I	integral controller
i	index of node
	index of neutronic mode
in	inlet
j	index of flow path
jet	jet pump
l	liquid
ldc	lower downcomer outside jet pumps
lp	lower plenum inlet
m	mixture
	moderator
	motor
NB	nucleate boiling
n	jet pump nozzle
out	outlet
P	proportional controller
r	rated condition
rc	recirculation line
rcp	recirculation pump
ro	rain out
SD	steam dome
s	main steam
	jet pump suction
sat	saturated condition
sep	separator
sep, l	separator to feedwater node
sep, v	separator to steam dome vapor region
su	surge between steam dome and feedwater node
t	jet pump throat
v	vapor
	valve
	flow control valve
$vent$	main steam line venturi tube
w	cladding outer wall
$wall$	steam dome wall
wc	steam dome wall condensation

Superscripts

-	average
i	time step
	index of node
n	time step

Acronyms

ANL	Argonne National Laboratory
APRM	Average Power Range Monitor
ASD	Auto Spectral Density
ATWS	Anticipated Transient Without Scram
BNL	Brookhaven National Laboratory
BOP	Balance Of Plant
BWR	Boiling Water Reactor
BWROG	Boiling Water Reactor Owners' Group
CPR	Critical Power Ratio
CSD	Cross Spectral Density
DR	Decay Ratio
EPA	Engineering Plant Analyzer
FCV	Flow Control Valve
FFT	Fast Fourier Transform
GE	General Electric Company
LPRM	Local Power Range Monitor
MCPR	Minimum Critical Power Ratio
MIMO	Multiple-Input, Multiple-Output system
MSIV	Main Steam Isolation Valve
NRC	Nuclear Regulatory Commission
NSSS	Nuclear Steam Supply System
NVG	Net Vapor Generation
OPRM	Oscillation Power Range Monitor
OSV	Onset of Significant Voiding
P(I)(D)	Proportional (-Integral) (-Differential) controller
PCIOMR	Pre-Conditioned Interim Operational Management Recommendations
PRBS	Pseudo Random Binary Sequence
PWR	Pressurized Water Reactor
SISO	Single-Input, Single-Output system
SPR	Stability Power Ratio
SRI	Selected Rod Insertion
SRV	Safety Relief Valve
TBV	Turbine Bypass Valve
TCV	Turbine Control Valve
WNP	Washington Nuclear Power Sataion

Appendix B

Details of the Equation Systems

B.1 Reactor Vessel Energy Equation System

The reactor vessel energy equation system (Equation 5.16) is

$$[EM]^n \Delta [XE] = [EB]^n \ ,$$

where

$\Delta [XE] = [\Delta XE(1), \Delta XE(2), \cdots, \Delta XE(NT), \Delta P, \Delta W_{su}]^T$,

$XE(i)$ is the state variable of the energy equation of node i ,

$[EM]$ is a $(NT+1) \times (NT+2)$ matrix, and

$[EB]$ is a $(NT+1) \times 1$ column vector.

The state variables $XE(i)$ and the structure of $[EM]$ depend on the flow pattern in the reactor vessel.

Feedwater node For the feedwater node, there are four possible flow patterns when considering the flow directions of W_1 and $W_{sep,l}$, as shown in Figure B-1.

Because the feedwater node is a mixing node, the state variable is $XE(1) = \overline{h}_1$ for all cases. Neglecting the terms accounted for the enthalpy changes of W_{su} and

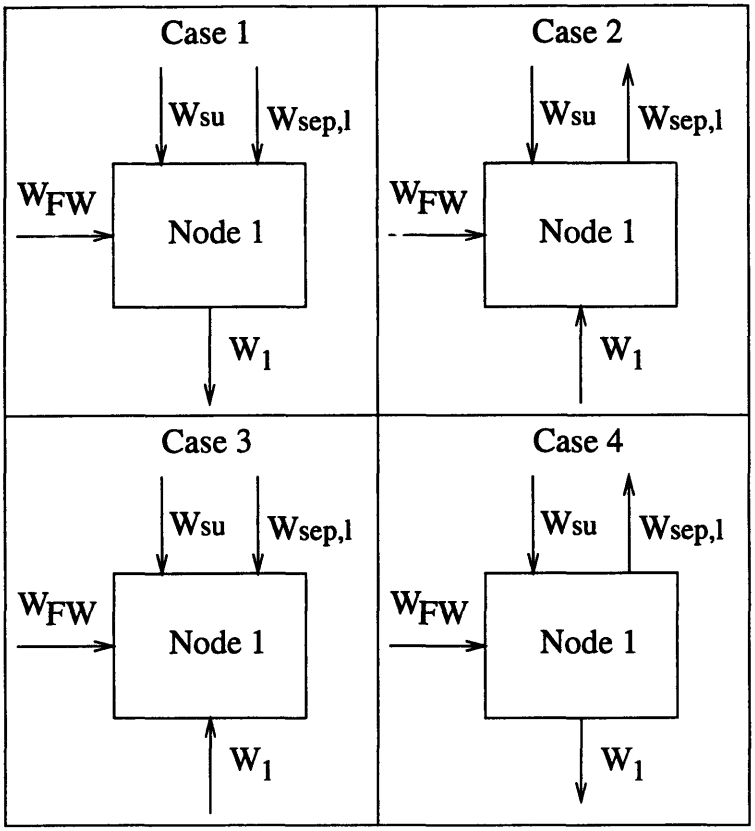

Figure B-1: Possible flow patterns of the feedwater node.

$W_{sep,l}$, Equation 5.14 becomes

$$EM(1,1)\Delta\overline{h}_1 + EM(1,2)\Delta XE(2) + EM(1,NT+1)\Delta P + EM(1,NT+2)\Delta W_{su}$$

$$= EB(1) ,$$

where

$$EM(1,NT+1) = -\frac{V_1}{\Delta t},$$
$$EM(1,NT+2) = -\left(h_{su} - \overline{h}_1\right), \text{ and}$$

$$EB(1) = W_{FW}^{n+1}\left[(h'_{FW})^{n+1} - \overline{h}_1^n\right] + W_{su}^n\left[h_{su}^n - \overline{h}_1^n\right]$$
$$+ W_{sep,l}^n\left[\left(h'_{sep,l}\right)^n - \overline{h}_1^n\right] - W_1^n\left[(h'_1)^n - \overline{h}_1^n\right] .$$

$EM(1,1)$ and $EM(1,2)$ depend on the flow pattern:

Case 1 and Case 4

$$EM(1,1) = \frac{V_1 m_1}{\Delta t} + W_1\left(\frac{\partial h'}{\partial h}\right)_1 ;$$

$$EM(1,2) = 0.$$

Case 2 and Case 3

$$EM(1,1) = \frac{V_1 m_1}{\Delta t} ;$$

$$EM(1,2) = W_1\left(\frac{\partial h'}{\partial h}\right)_1 .$$

Upper and lower plena The possible flow patterns of the plenum nodes depend on the number of core channels being modeled. The plenum nodes are mixing nodes. So the state variables are $XE(5) = \overline{h}_5$ and $XE(6) = \overline{h}_6$. The possible flow patterns with one core channel is shown in Figure B-2.

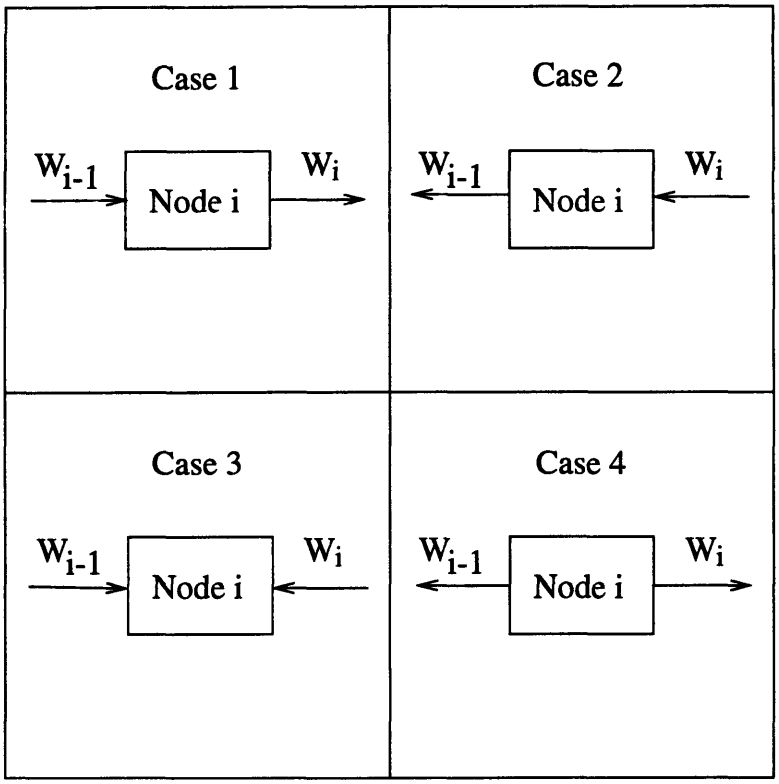

Figure B-2: Possible flow patterns of a single-inlet, single-outlet node.

For lower plenum, Equation 5.11 becomes

$$EM(5,3)\Delta XE(3)+EM(5,5)\Delta\overline{h}_5+EM(5,7)\Delta XE(7)+EM(5,NT+1)\Delta P = EB(5)\ ,$$

where

$$EM(5,NT+1) = -\frac{V_5}{\Delta t}\ \text{, and}$$
$$EB(5) = W_3\left(h'_3 - \overline{h}_5\right) - W_5\left(h'_5 - \overline{h}_5\right).$$

Case 1

$$EM(5,3) = -W_3\left(\frac{\partial h'}{\partial h}\right)_3;$$

$$EM(5,5) = \frac{V_5 m_5}{\Delta t} + W_5\left(\frac{\partial h'}{\partial h}\right)_5;$$

$$EM(5,7) = 0.$$

Case 2

$$EM(5,3) = 0;$$

$$EM(5,5) = \frac{V_5 m_5}{\Delta t} - W_3\left(\frac{\partial h'}{\partial h}\right)_3;$$

$$EM(5,7) = W_5\left(\frac{\partial h'}{\partial h}\right)_5.$$

Case 3

$$EM(5,3) = -W_3\left(\frac{\partial h'}{\partial h}\right)_3;$$

$$EM(5,5) = \frac{V_5 m_5}{\Delta t};$$

$$EM(5,7) = W_5\left(\frac{\partial h'}{\partial h}\right)_5.$$

Case 4

$$EM(5,3) = 0;$$

$$EM(5,5) = \frac{V_5 m_5}{\Delta t} - W_3 \left(\frac{\partial h'}{\partial h}\right)_3 + W_5 \left(\frac{\partial h'}{\partial h}\right)_5 ;$$

$$EM(5,7) = 0.$$

Equation 5.11 when applying to the upper plenum with one core channel is

$$\begin{aligned} & EM(6,4)\Delta XE(4) + EM(6,6)\Delta \overline{h}_6 \\ + \; & EM(6,NT)\Delta XE(NT) + EM(6,NT+1)\Delta P \\ = \; & EB(6) \, , \end{aligned}$$

where

$$EM(6,NT+1) = -\frac{V_6}{\Delta t} \text{ , and}$$
$$EB(5) = W_{NT}\left(h'_{NT} - \overline{h}_6\right) - W_6\left(h'_6 - \overline{h}_6\right).$$

Case 1

$$EM(6,4) = 0;$$

$$EM(6,6) = \frac{V_6 m_6}{\Delta t} + W_6 \left(\frac{\partial h'}{\partial h}\right)_6 ;$$

$$EM(6,NT) = -W_{NT} \left(\frac{\partial h'}{\partial h}\right)_{NT}.$$

Case 2

$$EM(6,4) = W_6 \left(\frac{\partial h'}{\partial h}\right)_6 ;$$

$$EM(6,6) = \frac{V_6\, m_6}{\Delta t} - W_{NT} \left(\frac{\partial h'}{\partial h} \right)_{NT} ;$$

$$EM(6,NT) = 0.$$

Case 3

$$EM(6,4) = W_6 \left(\frac{\partial h'}{\partial h} \right)_6 ;$$

$$EM(6,6) = \frac{V_6\, m_6}{\Delta t} ;$$

$$EM(6,NT) = -W_{NT} \left(\frac{\partial h'}{\partial h} \right)_{NT} .$$

Case 4

$$EM(6,4) = 0;$$

$$EM(6,6) = \frac{V_6\, m_6}{\Delta t} + W_6 \left(\frac{\partial h'}{\partial h} \right)_6 - W_{NT} \left(\frac{\partial h'}{\partial h} \right)_{NT} ;$$

$$EM(6,NT) = 0.$$

For the case with two core channels, the number of possible flow patterns of the lower and upper plena is doubled. Figure B-3 shows the eight possible flow patterns of the lower plenum. The energy equation of the lower plenum becomes

$$\begin{aligned} & EM(5,3)\Delta XE(3) + EM(5,5)\Delta \overline{h}_5 + EM(5,7)\Delta XE(7) \\ + \;& EM(5,NC1+7)\Delta XE(NC1+7) + EM(5,NT+1)\Delta P \\ = \;& EB(5) \ , \end{aligned}$$

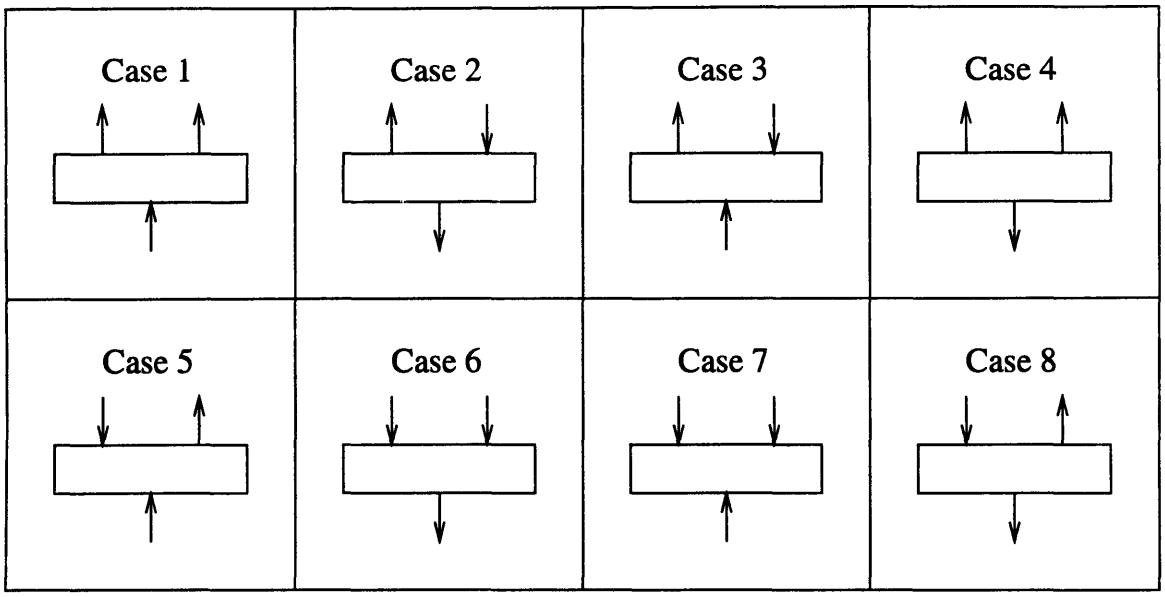

Figure B-3: Possible flow patterns of the lower plenum with two core channels.

where

$$EM(5, NT+1) = -\frac{V_5}{\Delta t} \text{ , and}$$
$$EB(5) = W_3\left(h'_3 - \overline{h}_5\right) - W_5\left(h'_5 - \overline{h}_5\right) - W_{NJ}\left(h'_{NJ} - \overline{h}_5\right).$$

Case 1

$$EM(5,3) = -W_3\left(\frac{\partial h'}{\partial h}\right)_3;$$

$$EM(5,5) = \frac{V_5 m_5}{\Delta t} + W_5\left(\frac{\partial h'}{\partial h}\right)_5 + W_{NJ}\left(\frac{\partial h'}{\partial h}\right)_{NJ};$$

$$EM(5,7) = 0;$$

$$EM(5, NC1+7) = 0.$$

Case 2

$$EM(5,3) = 0;$$

$$EM(5,5) = \frac{V_5\, m_5}{\Delta t} - W_3 \left(\frac{\partial h'}{\partial h}\right)_3 + W_{NJ} \left(\frac{\partial h'}{\partial h}\right)_{NJ};$$

$$EM(5,7) = W_5 \left(\frac{\partial h'}{\partial h}\right)_5;$$

$$EM(5, NC1 + 7) = 0.$$

Case 3

$$EM(5,3) = -W_3 \left(\frac{\partial h'}{\partial h}\right)_3;$$

$$EM(5,5) = \frac{V_5\, m_5}{\Delta t} + W_{NJ} \left(\frac{\partial h'}{\partial h}\right)_{NJ};$$

$$EM(5,7) = W_5 \left(\frac{\partial h'}{\partial h}\right)_5;$$

$$EM(5, NC1 + 7) = 0.$$

Case 4

$$EM(5,3) = 0;$$

$$EM(5,5) = \frac{V_5\, m_5}{\Delta t} - W_3 \left(\frac{\partial h'}{\partial h}\right)_3 + W_5 \left(\frac{\partial h'}{\partial h}\right)_5 + W_{NJ} \left(\frac{\partial h'}{\partial h}\right)_{NJ};$$

$$EM(5,7) = 0;$$

$$EM(5, NC1 + 7) = 0.$$

Case 5

$$EM(5,3) = -W_3 \left(\frac{\partial h'}{\partial h}\right)_3;$$

$$EM(5,5) = \frac{V_5\, m_5}{\Delta t} + W_5 \left(\frac{\partial h'}{\partial h}\right)_5 ;$$

$$EM(5,7) = 0;$$

$$EM(5, NC1+7) = W_{NJ} \left(\frac{\partial h'}{\partial h}\right)_{NJ}.$$

Case 6

$$EM(5,3) = 0;$$

$$EM(5,5) = \frac{V_5\, m_5}{\Delta t} - W_3 \left(\frac{\partial h'}{\partial h}\right)_3 ;$$

$$EM(5,7) = W_5 \left(\frac{\partial h'}{\partial h}\right)_5 ;$$

$$EM(5, NC1+7) = W_{NJ} \left(\frac{\partial h'}{\partial h}\right)_{NJ}.$$

Case 7

$$EM(5,3) = -W_3 \left(\frac{\partial h'}{\partial h}\right)_3 ;$$

$$EM(5,5) = \frac{V_5\, m_5}{\Delta t} ;$$

$$EM(5,7) = W_5 \left(\frac{\partial h'}{\partial h}\right)_5 ;$$

$$EM(5, NC1+7) = W_{NJ} \left(\frac{\partial h'}{\partial h}\right)_{NJ}.$$

Case 8

$$EM(5,3) = 0;$$

$$EM(5,5) = \frac{V_5 m_5}{\Delta t} - W_3 \left(\frac{\partial h'}{\partial h}\right)_3 + W_5 \left(\frac{\partial h'}{\partial h}\right)_5 \ ;$$

$$EM(5,7) = 0:$$

$$EM(5, NC1+7) = W_{NJ} \left(\frac{\partial h'}{\partial h}\right)_{NJ} .$$

The possible flow patterns of the upper plenum with two core channels are shown in Figure B-4. The discretized energy equation of the upper plenum becomes

$$\begin{aligned} & EM(6,4)\Delta XE(4) + EM(6,6)\Delta \overline{h}_6 + EM(6, NC1+6)\Delta XE(NC1+6) \\ + \ & EM(6,NT)\Delta XE(NT) + EM(6,NT+1)\Delta P \\ = \ & EB(6) \ , \end{aligned}$$

where

$$EM(6,NT+1) = -\frac{V_6}{\Delta t} \ , \text{ and}$$
$$EB(5) = W_{NC1+6}\left(h'_{NC1+6} - \overline{h}_6\right) + W_{NT}\left(h'_{NT} - \overline{h}_6\right) - W_6\left(h'_6 - \overline{h}_6\right).$$

Case 1

$$EM(6,4) = 0;$$

$$EM(6,6) = \frac{V_6 m_6}{\Delta t} + W_6 \left(\frac{\partial h'}{\partial h}\right)_6 \ ;$$

$$EM(6, NC1+6) = -W_{NC1+6} \left(\frac{\partial h'}{\partial h}\right)_{NC1+6} ;$$

$$EM(6, NT) = -W_{NT} \left(\frac{\partial h'}{\partial h}\right)_{NT} .$$

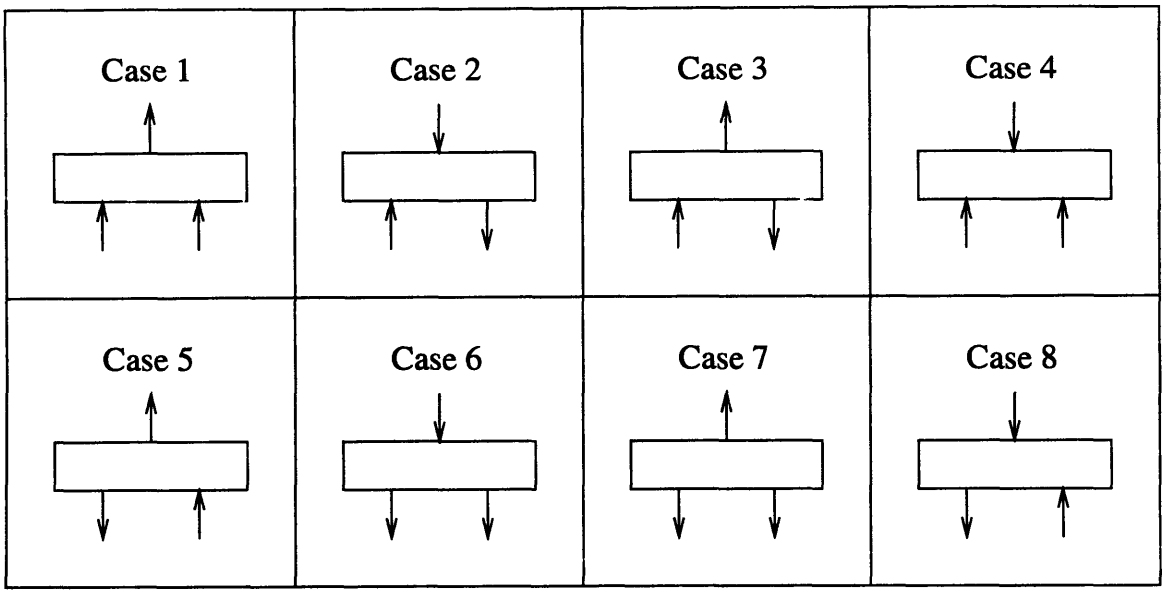

Figure B-4: Possible flow patterns of the upper plenum with two core channels.

Case 2

$$EM(6,4) = W_6 \left(\frac{\partial h'}{\partial h}\right)_6 ;$$

$$EM(6,6) = \frac{V_6 m_6}{\Delta t} - W_{NC1+6} \left(\frac{\partial h'}{\partial h}\right)_{NC1+6} ;$$

$$EM(6, NC1+6) = 0;$$

$$EM(6, NT) = -W_{NT} \left(\frac{\partial h'}{\partial h}\right)_{NT} .$$

Case 3

$$EM(6,4) = W_6 \left(\frac{\partial h'}{\partial h}\right)_6 ;$$

$$EM(6,6) = \frac{V_6 m_6}{\Delta t} ;$$

$$EM(6, NC1+6) = -W_{NC1+6}\left(\frac{\partial h'}{\partial h}\right)_{NC1+6};$$

$$EM(6, NT) = -W_{NT}\left(\frac{\partial h'}{\partial h}\right)_{NT}.$$

Case 4

$$EM(6,4) = 0;$$

$$EM(6,6) = \frac{V_6 m_6}{\Delta t} + W_6\left(\frac{\partial h'}{\partial h}\right)_6 - W_{NC1+6}\left(\frac{\partial h'}{\partial h}\right)_{NC1+6};$$

$$EM(6, NC1+6) = 0;$$

$$EM(6, NT) = -W_{NT}\left(\frac{\partial h'}{\partial h}\right)_{NT}.$$

Case 5

$$EM(6,4) = 0;$$

$$EM(6,6) = \frac{V_6 m_6}{\Delta t} + W_6\left(\frac{\partial h'}{\partial h}\right)_6 - W_{NT}\left(\frac{\partial h'}{\partial h}\right)_{NT};$$

$$EM(6, NC1+6) = -W_{NC1+6}\left(\frac{\partial h'}{\partial h}\right)_{NC1+6};$$

$$EM(6, NT) = 0.$$

Case 6

$$EM(6,4) = W_6\left(\frac{\partial h'}{\partial h}\right)_6;$$

$$EM(6,6) = \frac{V_6 m_6}{\Delta t} - W_{NC1+6}\left(\frac{\partial h'}{\partial h}\right)_{NC1+6} - W_{NT}\left(\frac{\partial h'}{\partial h}\right)_{NT};$$

$$EM(6, NC1+6) = 0;$$

$$EM(6, NT) = 0.$$

Case 7

$$EM(6,4) = W_6 \left(\frac{\partial h'}{\partial h}\right)_6;$$

$$EM(6,6) = \frac{V_6 m_6}{\Delta t} - W_{NT} \left(\frac{\partial h'}{\partial h}\right)_{NT};$$

$$EM(6, NC1+6) = -W_{NC1+6} \left(\frac{\partial h'}{\partial h}\right)_{NC1+6};$$

$$EM(6, NT) = 0.$$

Case 8

$$EM(6,4) = 0;$$

$$EM(6,6) = \frac{V_6 m_6}{\Delta t} + W_6 \left(\frac{\partial h'}{\partial h}\right)_6 - W_{NC1+6} \left(\frac{\partial h'}{\partial h}\right)_{NC1+6} - W_{NT} \left(\frac{\partial h'}{\partial h}\right)_{NT};$$

$$EM(6, NC1+6) = 0;$$

$$EM(6, NT) = 0.$$

Other nodes All the other nodes are single-inlet, single-outlet nodes. The possible flow patterns of these nodes are illustrated in Figure B-2. The energy equation of

node i is

$$\begin{aligned} & EM(i,i-1)\Delta XE(i-1) + EM(i,i)\Delta XE(i) \\ + \; & EM(i,i+1)\Delta XE(i+1) + EM(i,NT+1)\Delta P \\ = \; & EB(i) \ , \end{aligned}$$

where

$$EB(i) = q_i + W_{i-1}\left(h'_{i-1} - \overline{h}_i\right) - W_i\left(h'_i - \overline{h}_i\right),$$

$i-1$ denotes the index of the upstream node, and

$i+1$ denotes the index of the downstream node.

The state variables $\Delta XE(i)$ and the coefficients are flow pattern-dependent.

Case 1 In this case, the node is a normal node, and the state variable is $\Delta XE(i) = h_i$.

$$EM(i,i-1) = -W_{i-1}\left(\frac{\partial h'}{\partial h}\right)_{i-1};$$

$$EM(i,i) = \frac{(f0)_i + (f1)_i}{\Delta t} + W_i\left(\frac{\partial h'}{\partial h}\right)_i;$$

$$EM(i,i+1) = 0;$$

$$EM(i,NT+1) = \frac{g_i}{\Delta t}.$$

$(f0)_i$, $(f1)_i$, and g_i are defined in Equation 5.10.

Case 2 In this case, the node is still a normal node, but the state variable is $\Delta XE(i) = h_{i-1}$.

$$EM(i,i-1) = 0;$$

$$EM(i,i) = \frac{(f0)_i + (f1)_i}{\Delta t} - W_{i-1}\left(\frac{\partial h'}{\partial h}\right)_{i-1};$$

$$EM(i,i+1) = W_i\left(\frac{\partial h'}{\partial h}\right)_i;$$

$$EM(i,NT+1) = \frac{g_i}{\Delta t}.$$

Case 3 In this case, the node is a mixing node, and the state variable is $\Delta XE(i) = \overline{h}_i$.

$$EM(i,i-1) = -W_{i-1}\left(\frac{\partial h'}{\partial h}\right)_{i-1};$$

$$EM(i,i) = \frac{V_i m_i}{\Delta t};$$

$$EM(i,i+1) = W_i\left(\frac{\partial h'}{\partial h}\right)_i;$$

$$EM(i,NT+1) = -\frac{V_i}{\Delta t}.$$

Case 4 In this case, the node is again a mixing node (actually, a "splitting" node), and the state variable is $\Delta XE(i) = \overline{h}_i$.

$$EM(i,i-1) = 0;$$

$$EM(i,i) = \frac{V_i m_i}{\Delta t} - W_{i-1}\left(\frac{\partial h'}{\partial h}\right)_{i-1} + W_i\left(\frac{\partial h'}{\partial h}\right)_i;$$

$$EM(i,i+1) = 0;$$

$$EM(i, NT+1) = -\frac{V_i}{\Delta t}.$$

B.2 Steam Dome Equation System

The steam dome equation system (Equation 5.17) is

$$[A_{SD}]^n \Delta [X_{SD}] = [R_{SD}]^n ,$$

where

$[A_{SD}]$ is a 4×6 matrix,

$\Delta[X_{SD}]$ is a 6×1 column vector, and

$[R_{SD}]$ is a 4×1 column vector.

The state variables and the elements in the steam dome equation system depend on the condition of the steam dome as listed in Table 4.1.

Case 1

In case 1 conditions, W_{ro}^{n+1} and W_{fl}^{n+1} are both zero. The state variables are

$$\Delta [X_{SD}] = [\Delta h_v, \Delta h_l, \Delta V_v, \Delta P, \Delta W_{su}, \Delta W_s]^T .$$

Tables B.1 and B.2 list the elements of $[A_{SD}]$ and $[R_{SD}]$ for this case.

Case 2

For case 2 conditions, $W_{fl}^{n+1} = 0$, and $h_v^{n+1} = h_g^{n+1}$. So

$$\Delta h_v = h_g^n + \left(\frac{\partial h_g}{\partial P}\right)^n \Delta P - h_v^n.$$

Table B.1: The elements of $[A_{SD}]$ for case 1 conditions

$A_{SD}(1,1)$	$\frac{V_v}{\Delta t}\left(\frac{\partial \rho_v}{\partial h_v}\right)$	$A_{SD}(3,1)$	$\frac{V_v}{\Delta t}\left[\rho_v + \left(h_v - \overline{h}_{SD}\right)\left(\frac{\partial \rho_v}{\partial h_v}\right)\right] + W_s$
$A_{SD}(1,2)$	0	$A_{SD}(3,2)$	0
$A_{SD}(1,3)$	$\frac{\rho_v}{\Delta t}$	$A_{SD}(3,3)$	$\frac{\rho_v}{\Delta t}\left(h_v - \overline{h}_{SD}\right)$
$A_{SD}(1,4)$	$\frac{V_v}{\Delta t}\left(\frac{\partial \rho_v}{\partial P}\right)$	$A_{SD}(3,4)$	$\frac{V_v}{\Delta t}\left[\left(h_v - \overline{h}_{SD}\right)\left(\frac{\partial \rho_v}{\partial P}\right) - 1\right]$
$A_{SD}(1,5)$	0	$A_{SD}(3,5)$	0
$A_{SD}(1,6)$	1	$A_{SD}(3,6)$	$\left(h_v - \overline{h}_{SD}\right)$
$A_{SD}(2,1)$	0	$A_{SD}(4,1)$	0
$A_{SD}(2,2)$	$\frac{V_l}{\Delta t}\left(\frac{\partial \rho_l}{\partial h_l}\right)$	$A_{SD}(4,2)$	$\frac{V_l}{\Delta t}\left[\rho_l + \left(h_l - \overline{h}_{SD}\right)\left(\frac{\partial \rho_l}{\partial h_l}\right)\right]$
$A_{SD}(2,3)$	$-\frac{\rho_l}{\Delta t}$	$A_{SD}(4,3)$	$-\frac{\rho_l}{\Delta t}\left(h_l - \overline{h}_{SD}\right)$
$A_{SD}(2,4)$	$\frac{V_l}{\Delta t}\left(\frac{\partial \rho_l}{\partial P}\right)$	$A_{SD}(4,4)$	$\frac{V_l}{\Delta t}\left[\left(h_l - \overline{h}_{SD}\right)\left(\frac{\partial \rho_l}{\partial P}\right) - 1\right]$
$A_{SD}(2,5)$	1	$A_{SD}(4,5)$	$\left(h_{su} - \overline{h}_{SD}\right)$
$A_{SD}(2,6)$	0	$A_{SD}(4,6)$	0

Table B.2: The elements of $[R_{SD}]$ for case 1 conditions

$R_{SD}(1)$	$W_{sep,v} - W_s - W_{wc}$
$R_{SD}(2)$	$W_{wc} - W_{su}$
$R_{SD}(3)$	$W_{sep,v}\left(h_g - \overline{h}_{SD}\right) - \left(W_s + W_{wc}\right)\left(h_v - \overline{h}_{SD}\right)$
$R_{SD}(4)$	$W_{wc}\left(h_f - \overline{h}_{SD}\right) - W_{su}\left(h_{su} - \overline{h}_{SD}\right)$

Table B.3: The elements of $[A_{SD}]$ for case 2 conditions

$A_{SD}(1,1)$	1	$A_{SD}(3,1)$	$\left(h_f - \overline{h}_{SD}\right)$
$A_{SD}(1,2)$	0	$A_{SD}(3,2)$	0
$A_{SD}(1,3)$	$A_{SD,1}(1,3)$	$A_{SD}(3,3)$	$A_{SD,1}(3,3)$
$A_{SD}(1,4)$	$A_{SD,1}(1,4)$ $+A_{SD,1}(1,1)\left(\frac{\partial h_g}{\partial P}\right)$	$A_{SD}(3,4)$	$A_{SD,1}(3,4)$ $+A_{SD,1}(3,1)\left(\frac{\partial h_g}{\partial P}\right)$
$A_{SD}(1,5)$	0	$A_{SD}(3,5)$	0
$A_{SD}(1,6)$	$A_{SD,1}(1,6)$	$A_{SD}(3,6)$	$A_{SD,1}(3,6)$
$A_{SD}(2,1)$	-1	$A_{SD}(4,1)$	$-\left(h_f - \overline{h}_{SD}\right)$
$A_{SD}(2,2)$	$A_{SD,1}(2,2)$	$A_{SD}(4,2)$	$A_{SD,1}(4,2)$
$A_{SD}(2,3)$	$A_{SD,1}(2,3)$	$A_{SD}(4,3)$	$A_{SD,1}(4,3)$
$A_{SD}(2,4)$	$A_{SD,1}(2,4)$	$A_{SD}(4,4)$	$A_{SD,1}(4,4)$
$A_{SD}(2,5)$	$A_{SD,1}(2,5)$	$A_{SD}(4,5)$	$A_{SD,1}(4,5)$
$A_{SD}(2,6)$	0	$A_{SD}(4,6)$	0

The state variables are

$$\Delta\left[X_{SD}\right] = \left[W_{ro}^{n+1},\, \Delta h_l,\, \Delta V_v,\, \Delta P,\, \Delta W_{su},\, \Delta W_s\right]^T.$$

Tables B.3 and B.4 list the elements of $[A_{SD}]$ and $[R_{SD}]$ for this case. In these tables, $A_{SD,1}(i,j)$ and $R_{SD,1}(i)$ represent the elements of $[A_{SD}]$ and $[R_{SD}]$ for case 1 conditions.

Table B.4: The elements of $[R_{SD}]$ for case 2 conditions

$R_{SD}(1)$	$R_{SD,1}(1) - A_{SD,1}(1,1)(h_g - h_v)$
$R_{SD}(2)$	$R_{SD,1}(2)$
$R_{SD}(3)$	$R_{SD,1}(3) - A_{SD,1}(3,1)(h_g - h_v)$
$R_{SD}(4)$	$R_{SD,1}(4)$

Case 3

For case 3 conditions, $W_{ro}^{n+1} = 0$, and $h_l^{n+1} = h_f^{n+1}$. So

$$\Delta h_l = h_f^n + \left(\frac{\partial h_f}{\partial P}\right)^n \Delta P - h_l^n.$$

The state variables are

$$\Delta\left[X_{SD}\right] = \left[\Delta h_v,\, W_{fl}^{n+1},\, \Delta V_v,\, \Delta P,\, \Delta W_{su},\, \Delta W_s\right]^T.$$

Tables B.5 and B.6 list the elements of $[A_{SD}]$ and $[R_{SD}]$ for this case.

Case 4

For case 4 conditions, $h_v^{n+1} = h_g^{n+1}$, and $h_l^{n+1} = h_f^{n+1}$. So

$$\Delta h_v = h_g^n + \left(\frac{\partial h_g}{\partial P}\right)^n \Delta P - h_v^n,$$

and

$$\Delta h_l = h_f^n + \left(\frac{\partial h_f}{\partial P}\right)^n \Delta P - h_l^n.$$

The state variables are

$$\Delta\left[X_{SD}\right] = \left[W_{ro}^{n+1},\, W_{fl}^{n+1},\, \Delta V_v,\, \Delta P,\, \Delta W_{su},\, \Delta W_s\right]^T.$$

Table B.5: The elements of $[A_{SD}]$ for case 3 conditions

$A_{SD}(1,1)$	$A_{SD,1}(1,1)$	$A_{SD}(3,1)$	$A_{SD,1}(3,1)$
$A_{SD}(1,2)$	-1	$A_{SD}(3,2)$	$-\left(h_g - \overline{h}_{SD}\right)$
$A_{SD}(1,3)$	$A_{SD,1}(1,3)$	$A_{SD}(3,3)$	$A_{SD,1}(3,3)$
$A_{SD}(1,4)$	$A_{SD,1}(1,4)$	$A_{SD}(3,4)$	$A_{SD,1}(3,4)$
$A_{SD}(1,5)$	0	$A_{SD}(3,5)$	0
$A_{SD}(1,6)$	$A_{SD,1}(1,6)$	$A_{SD}(3,6)$	$A_{SD,1}(3,6)$
$A_{SD}(2,1)$	0	$A_{SD}(4,1)$	0
$A_{SD}(2,2)$	1	$A_{SD}(4,2)$	$\left(h_g - \overline{h}_{SD}\right)$
$A_{SD}(2,3)$	$A_{SD,1}(2,3)$	$A_{SD}(4,3)$	$A_{SD,1}(4,3)$
$A_{SD}(2,4)$	$A_{SD,1}(2,4)$ $+A_{SD,1}(2,2)\left(\frac{\partial h_f}{\partial P}\right)$	$A_{SD}(4,4)$	$A_{SD,1}(4,4)$ $+A_{SD,1}(4,2)\left(\frac{\partial h_f}{\partial P}\right)$
$A_{SD}(2,5)$	$A_{SD,1}(2,5)$	$A_{SD}(4,5)$	$A_{SD,1}(4,5)$
$A_{SD}(2,6)$	0	$A_{SD}(4,6)$	0

Table B.6: The elements of $[R_{SD}]$ for case 3 conditions

$R_{SD}(1)$	$R_{SD,1}(1)$
$R_{SD}(2)$	$R_{SD,1}(2) - A_{SD,1}(2,2)(h_f - h_l)$
$R_{SD}(3)$	$R_{SD,1}(3)$
$R_{SD}(4)$	$R_{SD,1}(4) - A_{SD,1}(4,2)(h_f - h_l)$

Table B.7: The elements of $[A_{SD}]$ for case 4 conditions

$A_{SD}(1,1)$	1	$A_{SD}(3,1)$	$\left(h_f - \overline{h}_{SD}\right)$
$A_{SD}(1,2)$	-1	$A_{SD}(3,2)$	$-\left(h_g - \overline{h}_{SD}\right)$
$A_{SD}(1,3)$	$A_{SD,1}(1,3)$	$A_{SD}(3,3)$	$A_{SD,1}(3,3)$
$A_{SD}(1,4)$	$A_{SD,1}(1,4) + A_{SD,1}(1,1)\left(\frac{\partial h_g}{\partial P}\right)$	$A_{SD}(3,4)$	$A_{SD,1}(3,4) + A_{SD,1}(3,1)\left(\frac{\partial h_g}{\partial P}\right)$
$A_{SD}(1,5)$	0	$A_{SD}(3,5)$	0
$A_{SD}(1,6)$	$A_{SD,1}(1,6)$	$A_{SD}(3,6)$	$A_{SD,1}(3,6)$
$A_{SD}(2,1)$	-1	$A_{SD}(4,1)$	$-\left(h_f - \overline{h}_{SD}\right)$
$A_{SD}(2,2)$	1	$A_{SD}(4,2)$	$\left(h_g - \overline{h}_{SD}\right)$
$A_{SD}(2,3)$	$A_{SD,1}(2,3)$	$A_{SD}(4,3)$	$A_{SD,1}(4,3)$
$A_{SD}(2,4)$	$A_{SD,1}(2,4) + A_{SD,1}(2,2)\left(\frac{\partial h_f}{\partial P}\right)$	$A_{SD}(4,4)$	$A_{SD,1}(4,4) + A_{SD,1}(4,2)\left(\frac{\partial h_f}{\partial P}\right)$
$A_{SD}(2,5)$	$A_{SD,1}(2,5)$	$A_{SD}(4,5)$	$A_{SD,1}(4,5)$
$A_{SD}(2,6)$	0	$A_{SD}(4,6)$	0

Tables B.7 and B.8 list the elements of $[A_{SD}]$ and $[R_{SD}]$ for case 4 conditions.

Table B.8: The elements of $[R_{SD}]$ for case 4 conditions

$R_{SD}(1)$	$R_{SD,1}(1) - A_{SD,1}(1,1)(h_g - h_v)$
$R_{SD}(2)$	$R_{SD,1}(2) - A_{SD,1}(2,2)(h_f - h_l)$
$R_{SD}(3)$	$R_{SD,1}(3) - A_{SD,1}(3,1)(h_g - h_v)$
$R_{SD}(4)$	$R_{SD,1}(4) - A_{SD,1}(4,2)(h_f - h_l)$

B.3 Steam Line Equation System

The steam line equation system (Equation 5.18) is

$$[STMA]^n \, \Delta [XS] = [STMR]^n ,$$

where

$\Delta [XS] = [\Delta P_1, \cdots, \Delta P_7, \Delta W_1, \cdots, \Delta W_6, \Delta W_{TCV}, \Delta W_s, \Delta P]^T$, the indices of the state variables are indicated in Figure 4-16,

$[STMA]$ is a 15×16 matrix, and

$[STMR]$ is a 15×1 column vector.

Figure B-5 shows the structure of $[STMA]$. The diagonal elements of $[STMA]$ are:

for $1 \leq i \leq 7$,

$$STMA(i,i) = \frac{V_i}{\gamma} \left(\frac{\rho_0}{P_0}\right) \left(\frac{P_0}{P_i^n}\right)^{\left(\frac{\gamma-1}{\gamma}\right)} ;$$

for $8 \leq i \leq 13$,

$$\begin{aligned} STMA(i,i) &= \frac{1}{2}\left[\left(\frac{\ell}{A}\right)_j + \left(\frac{\ell}{A}\right)_{j+1}\right] \\ &+ \frac{\Delta t \, |W_j|}{2 \, \rho_{j+\frac{1}{2}}} \left\{ \frac{1}{2}\left[\left(\frac{f\,\ell}{D\,A^2}\right)_j + \left(\frac{f\,\ell}{D\,A^2}\right)_{j+1}\right] + \frac{K_j}{A^2_{j+\frac{1}{2}}} + \frac{c_{v,j}}{A^2_{v,j}} \right\} , \end{aligned}$$

where $j = i - 7$;

for $i = 14$,

$$STMA(14,14) = \frac{1}{2}\left(\frac{\ell}{A}\right)_6 + \frac{\Delta t \, |W_{TCV}|}{2 \, \rho_{TCV}} \left[\frac{1}{2}\left(\frac{f\,\ell}{D\,A^2}\right)_6 + \frac{c_{TCV}}{A^2_{TCV}}\right] ;$$

for $i = 15$,

$$STMA(15,15) = \frac{1}{2}\left(\frac{\ell}{A}\right)_1 + \frac{\Delta t \, |W_s|}{2 \, \rho_s} \left[\frac{1}{2}\left(\frac{f\,\ell}{D\,A^2}\right)_1 + \frac{K_{vent}}{A^2_{vent}}\right] ,$$

	1	2	3	4	5	6	7	8	9	10	11	12	13	14	15	16
1	X							Δt							-Δt	
2		X						-Δt	Δt							
3			X						-Δt	Δt						
4				X						-Δt	Δt					
5					X						-Δt	Δt				
6						X						-Δt	Δt	Δt		
7							X							-Δt		
8	-Δt	Δt						X								
9		-Δt	Δt						X							
10			-Δt	Δt						X						
11				-Δt	Δt						X					
12					-Δt	Δt						X				
13						-Δt	Δt						X			
14						-Δt								X		
15	Δt														X	-Δt

Figure B-5: The structure of $[STMA]$.

where A_{vent} and K_{vent} are the flow area and loss coefficient of the Venturi tubes at the exit of the steam dome.

The elements of $[STMR]$ are:

$$STMR(1) = \Delta t\,(W_s - W_1 - W_{SRV});$$

$$STMR(i) = \Delta t\,(W_{i-1} - W_i), \text{ for } 2 \le i \le 5;$$

$$STMR(6) = \Delta t\,(W_5 - W_6 - W_{TCV});$$

$$STMR(7) = \Delta t\,(W_6 - W_{TBV});$$

$$\begin{aligned} STMR(i) &= \Delta t\,(P_j - P_{j+1}) \\ &- \Delta t \left\{ \frac{|W_j|\,W_j}{2\,\rho_{j+\frac{1}{2}}} \left\{ \frac{1}{2} \left[\left(\frac{f\,\ell}{D\,A^2} \right)_j + \left(\frac{f\,\ell}{D\,A^2} \right)_{j+1} \right] + \frac{K_j}{A^2_{j+\frac{1}{2}}} + \frac{c_{v,j}}{A^2_{v,j}} \right\} \right\}, \end{aligned}$$

for $8 \le i \le 13$, and $j = i - 7$;

$STMR(14) = \Delta t \left\{ P_6 - P_{TB} - \dfrac{|W_{TCV}|\,W_{TCV}}{2\,\rho_{TCV}} \left[\dfrac{1}{2} \left(\dfrac{f\,\ell}{D\,A^2} \right)_6 + \dfrac{c_{TCV}}{A^2_{TCV}} \right] \right\}$, where P_{TB} is the user-specified turbine inlet pressure;

Table B.9: The elements of $[AM]$

$AM(NT,i)$, $i=1,2$	$\frac{I_i}{\Delta t}+(F_{fr}+F_{loss}+F_{acc})_i$
$AM(NT,i)$, $i=3,5$	$\frac{I_{i+1}}{\Delta t}+(F_{fr}+F_{loss}+F_{acc})_{i+1}$
$AM(NT,NJ+2)$	$\frac{I_3}{\Delta t}+(F_{fr}+F_{loss}+F_{acc})_3$
$AM(NT+1,i)$, $i=4,6\text{–}(NC1+5)$	$\frac{I_{i+1}}{\Delta t}+(F_{fr}+F_{loss}+F_{acc})_{i+1}$
$AM(NT+2,i)$, $i=(NC1+6)\text{–}NT$	$\frac{I_{i+1}}{\Delta t}+(F_{fr}+F_{loss}+F_{acc})_{i+1}$

$$STMR(15)=\Delta t\left\{P-P_1-\frac{|W_s|\,W_s}{2\,\rho_s}\left[\frac{1}{2}\left(\frac{f\,\ell}{D\,A^2}\right)_1+\frac{K_{vent}}{A_{vent}^2}\right]\right\}.$$

B.4 Reactor Vessel Mass and Momentum Equation System

The reactor vessel mass and momentum equation system (Equation 5.19) is

$$[AM]^n\,\Delta\,[XM]=[AB]^n,$$

where

$\Delta\,[XM]=[\Delta W_1,\,\Delta W_2,\,\Delta W_4,\cdots,\,\Delta W_{NJ},\,\Delta P_{core},\,\Delta P_{jet},\,\Delta W_3]^T$,

$[AM]$ is a $(NJ+1)\times(NJ+2)$ matrix, and

$[AB]$ is a $(NJ+1)\times 1$ column vector.

Figure B-6 shows the structure of $[AM]$. The part enclosed by the dashed lines exists only when $NCH=2$. The non-zero elements in rows NT, $NT+1$, and $NT+2$ (for $NCH=2$ only) are listed in Table B.9. Table B.10 lists the elements of $[AB]$.

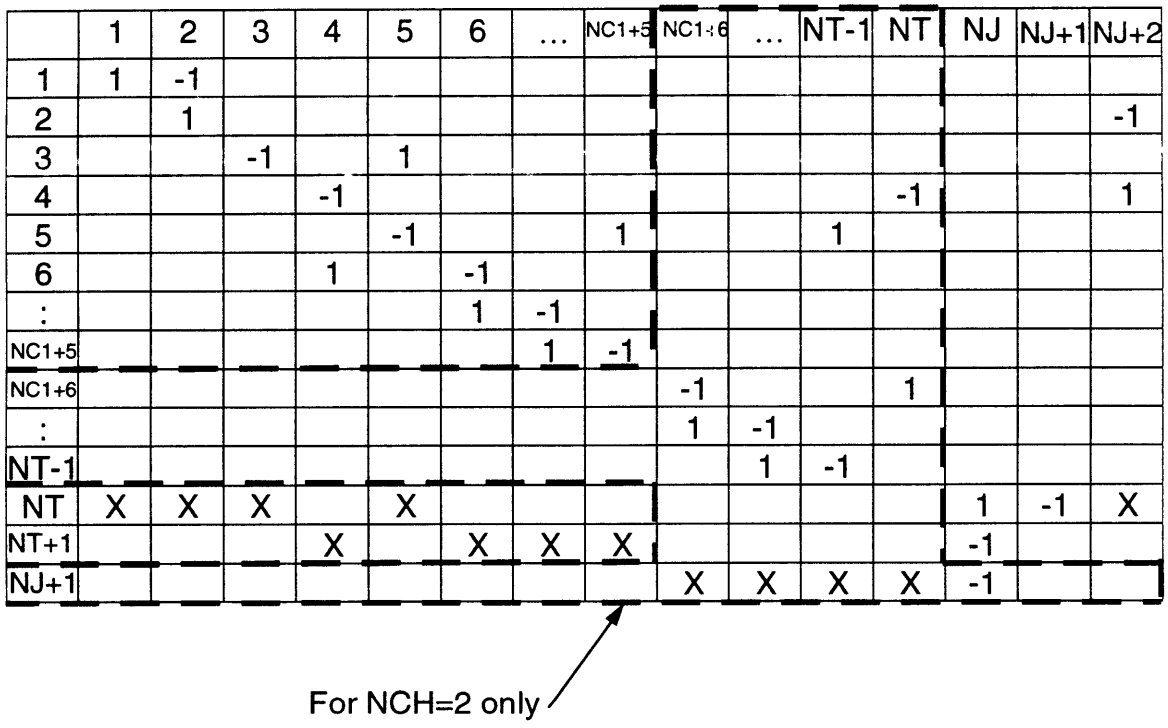

Figure B-6: The structure of $[AM]$.

Table B.10: The elements of $[AB]$

$AB(i)$, $i = 1, 2$	$\frac{\Delta M_i}{\Delta t} - (W_i - W_{i+1})$
$AB(3)$	$\frac{\Delta M_4}{\Delta t} - (W_6 - W_4)$
$AB(4)$	$\frac{\Delta M_5}{\Delta t} - (W_3 - W_5)$ for $NCH = 1$, $\frac{\Delta M_5}{\Delta t} - (W_3 - W_5 - W_{NJ})$ for $NCH = 2$.
$AB(5)$	$\frac{\Delta M_6}{\Delta t} - (W_{NC1+6} - W_6)$ for $NCH = 1$, $\frac{\Delta M_6}{\Delta t} - (W_{NC1+6} + W_{NT} - W_6)$ for $NCH = 2$.
$AB(i)$, $i =$ 6–$(NC1 + 5)$, and $(NC1 + 7)$–$(NT - 1)$	$\frac{\Delta M_i}{\Delta t} - (W_i - W_{i+1})$
$AB(NC1 + 6)$	$\frac{\Delta M_{NC1+7}}{\Delta t} - (W_{NJ} - W_{NC1+7})$ (for $NCH = 2$ only)
$AB(NT)$	$-P_{core} + P_{jet} - \sum_{i=1-4,6} (F_{fr} + F_{loss} + F_{acc}) W_i$ $- \sum_{i=1}^{6} m_i g \Delta z_i + \rho_l g L_{SD}$
$AB(NT + 1)$	$P_{core} - \sum_{i=5,7-(NC1+6)} (F_{fr} + F_{loss} + F_{acc}) W_i$ $- \sum_{i=7}^{NC1+6} m_i g \Delta z_i$
$AB(NT + 2)$ (for $NCH = 2$ only)	$P_{core} - \sum_{i=NC1+7}^{NJ} (F_{fr} + F_{loss} + F_{acc}) W_i$ $- \sum_{i=NC1+7}^{NT} m_i g \Delta z_i$

	1	2	3	4	5	6	7	8
1	-1	-1						1
2		X		X			1	X
3	X		X		X			
4		X		X		X		
5			X		X			
6				X		X		
7	X		X				1	X

Figure B-7: The structure of $[AR]$.

B.5 Recirculation System

The recirculation equation system (Equation 5.20) is

$$[AR]^n \Delta [XR]^n = [BR]^n \ ,$$

where

$\Delta [XR] = [\Delta W_{jet,1}, \Delta W_{jet,2}, \Delta W_{rc,1}, \Delta W_{rc,2}, \Delta\omega_1, \Delta\omega_2, \Delta P_{jet}, \Delta W_3]^T$,

$[AR]$ is a 7×8 matrix, and

$[BR]$ is a 7×1 column vector.

The structure of $[AR]$ is shown in Figure B-7, and the non-zero elements of $[AR]$ are listed in Table B.11. Table B.12 lists the elements of $[BR]$. The r's are defined in Section 5.1.7.

Table B.11: Non-zero elements of $[AR]$

$AR(2,2)$	$\frac{I_{jet}}{\Delta t} - (r_{1,2} + r_{2,2})$	$AR(4,6)$	$-\left(\frac{\partial P_{rcp}}{\partial \omega}\right)_2$
$AR(2,4)$	$(r_{2,2} - r_{3,2})$	$AR(5,3)$	$\left(\frac{\partial T_{rcp}}{\partial W_{rc}}\right)_1$
$AR(2,8)$	r_4	$AR(5,5)$	$\frac{I_{rcp}}{\Delta t} + r_{pump} + \left(\frac{\partial T_{rcp}}{\partial \omega}\right)_1$
$AR(3,1)$	$-r_{6,1}$	$AR(6,4)$	$\left(\frac{\partial T_{rcp}}{\partial W_{rc}}\right)_2$
$AR(3,3)$	$\frac{I_{rc}}{\Delta t} + r_{5,1} + r_{6,1} - \left(\frac{\partial P_{rcp}}{\partial W_{rc}}\right)_1$	$AR(6,6)$	$\frac{I_{rcp}}{\Delta t} + r_{pump} + \left(\frac{\partial T_{rcp}}{\partial \omega}\right)_2$
$AR(3,5)$	$-\left(\frac{\partial P_{rcp}}{\partial \omega}\right)_1$	$AR(7,1)$	$\frac{I_{jet}}{\Delta t} - (r_{1,1} + r_{2,1})$
$AR(4,2)$	$-r_{6,2}$	$AR(7,3)$	$(r_{2,1} - r_{3,1})$
$AR(4,4)$	$\frac{I_{rc}}{\Delta t} + r_{5,2} + r_{6,2} - \left(\frac{\partial P_{rcp}}{\partial W_{rc}}\right)_2$	$AR(7,8)$	r_4

Table B.12: The elements of $[BR]$

$BR(1)$	0
$BR(2)$	$r_{1,2}W_{jet,2} + r_{2,2}W_{s,2} + r_{3,2}W_{rc,2} - r_4W_3 - P_{jet}$
$BR(3)$	$P_{rcp,1} + r_{6,1}W_{s,1} - r_{5,1}W_{rc,1}$
$BR(4)$	$P_{rcp,2} + r_{6,2}W_{s,2} - r_{5,2}W_{rc,2}$
$BR(5)$	$T_{m,1} - r_{pump}\omega_1 - T_{rcp,1}$
$BR(6)$	$T_{m,2} - r_{pump}\omega_2 - T_{rcp,2}$
$BR(7)$	$r_{1,1}W_{jet,1} + r_{2,1}W_{s,1} + r_{3,1}W_{rc,1} - r_4W_3 - P_{jet}$

Appendix C

Constitutive Relations

C.1 Frictional Pressure Drop

The frictional pressure drop of a node is calculated by using a Darcy friction factor. For a node containing a single-phase fluid, the frictional pressure drop is given by

$$\Delta P_{fr} = \left[\frac{f\,\ell}{2D_h} \frac{\left|\overline{W}\right|}{\overline{\rho} A^2} \right] \overline{W},$$

where $\overline{W} = \frac{1}{2}(W_{in} + W_{out})$, and $\overline{\rho} = \frac{1}{2}(\rho_{in} + \rho_{out})$.

The single-phase friction factor f is calculated from the formula for laminar flow in a round tube or the McAdams relation [37]:

$$f = \begin{cases} \dfrac{64}{\mathrm{Re}} & \text{for } \mathrm{Re} \leq 1502, \\ 0.184\mathrm{Re}^{-0.2} & \text{for } \mathrm{Re} > 1502, \end{cases}$$

where

Re is the Reynolds number, $Re = \dfrac{D_h \left|\overline{W}\right|}{\mu A}$, and

μ is the dynamic viscosity.

For a node containing a two-phase fluid, a two-phase friction multiplier is used:

$$\Delta P_{fr} = \left[\phi_{lo}^2 \frac{f_{lo}\,\ell}{2D_h} \frac{\left|\overline{W}\right|}{\rho_f\, A^2} \right] \overline{W},$$

where f_{lo} is the single-phase friction factor calculated by using $\overline{W}$ and saturated water properties. The two-phase friction multiplier ϕ_{lo}^2 is given by the Martinelli-Nelson-Jones correlation [36, 37]:

$$\phi_{lo}^2 = \Omega \left\{ 1.2 \left[\left(\frac{\rho_f}{\rho_g} \right) - 1 \right] \overline{x}^{0.824} \right\} + 1;$$

$$\Omega = \begin{cases} 1.36 + 0.005P + 0.1G - 0.000714PG & \text{for } G \leq 0.7, \\ 1.26 - 0.0004P + \dfrac{0.119}{G} - 0.00028\dfrac{P}{G} & \text{for } G > 0.7; \end{cases}$$

where

$\overline{x} = \dfrac{1}{2}\left(x_{in} + x_{out}\right)$,

P is the system pressure in psia, and

G is the average mass flux in 10^6 lb/hr-ft^2.

For the node in which onset of significant voiding (OSV) occurs, assuming the inlet is at single-phase conditions,

$$\Delta P_{fr} = \left[\left(\frac{f\,\ell_{1\phi}}{\overline{\rho}_{1\phi}} + \phi_{lo}^2 \frac{f_{lo}\,\ell_{2\phi}}{\rho_f} \right) \frac{\left|\overline{W}\right|}{2D_h\, A^2} \right] \overline{W},$$

where

$\ell_{1\phi}$ is the distance from inlet to the point of OSV,

$\ell_{2\phi}$ is the distance from the point of OSV to outlet,

$\overline{\rho}_{1\phi} = \dfrac{1}{2}\left(\rho_{in} + \rho_f\right)$, and

ϕ_{lo}^2 is calculated using $\overline{x} = \dfrac{x_{out}}{2}$.

C.2 Void-Quality Correlation

The drift-flux model used to describe the two-phase flow separation is [37]

$$\alpha = \frac{1}{C_0 \left[1 + \left(\frac{1-x}{x}\right)\frac{\rho_g}{\rho_f}\right] + u_{gj}\left(\frac{\rho_g A}{x W}\right)},$$

where C_0 is the distribution parameter, and u_{gj} is the drift velocity. The EPRI void fraction correlation (the Chexal-Lellouche correlation) is used to calculate C_0 and u_{gj} [71]. This correlation is empirically based and has the following features:

- It is implicit in both void fraction and quality. An iterative scheme is required to calculate C_0 and u_{gj}.
- It is continuous and does not depend on flow regimes.

In this study, only cocurrent flow is considered. The distribution parameter is given by

$$C_0 = F_r\, C_{0v} + (1 - F_r)\, C_{0h},$$

where C_{0v} and C_{0h} are the distribution parameters evaluated for vertical and horizontal flows, and F_r is a flow orientation parameter. Let θ be the angle from the horizontal direction to the flow direction in degree ($-90° \le \theta \le 90°$). Then,

$$F_r = \begin{cases} \dfrac{\theta}{90} & \text{for } \theta \ge 0, \\ \min\left(1, \dfrac{|\theta|}{10}\right) & \text{for } \theta < 0; \end{cases}$$

$$C_{0h} = \left[1 + \alpha^{0.05}\left(1 - \alpha^2\right)\right] C_{0v};$$

$$C_{ov} = \begin{cases} \dfrac{L}{[K_0 + (1 - K_0)\,\alpha^r]} & \text{for } \theta \geq 0, \\ \max \left\{ \begin{array}{c} \dfrac{L}{[K_0 + (1 - K_0)\,\alpha^r]} \\ \dfrac{u^0_{gj}\,(1-\alpha)^{0.2}}{\dfrac{W}{A}\left(\dfrac{x}{\rho_g} + \dfrac{1-x}{\rho_f}\right)} \end{array} \right\} & \text{for } \theta < 0; \end{cases}$$

where

$$L = \frac{1 - \exp(-C_1 \alpha)}{1 - \exp(-C_1)},$$

$$C_1 = \frac{4\,P^2_{crit}}{P\,(P_{crit} - P)},$$

P is the system pressure,

P_{crit} is the critical pressure of water,

$$K_0 = B_1 + (1 - B_1)\left(\frac{\rho_g}{\rho_f}\right)^{0.25},$$

$$r = \frac{1 + 1.57\left(\dfrac{\rho_g}{\rho_f}\right)}{1 - B_1},$$

$$B_1 = \min(0.8,\, A_1),$$

$$A_1 = \left[1 + \exp\left(-\frac{\mathrm{Re}}{60,000}\right)\right]^{-1},$$

$$\mathrm{Re} = \begin{cases} \mathrm{Re}_g & \text{if } \mathrm{Re}_g > \mathrm{Re}_f \text{ or } \theta < 0, \\ \mathrm{Re}_f & \text{if } \mathrm{Re}_g \leq \mathrm{Re}_f, \end{cases}$$

$$\mathrm{Re}_g = \frac{x\,W\,D_h}{\mu_g\,A},$$

$$\mathrm{Re}_f = \frac{(1 - x)\,W\,D_h}{\mu_f\,A},$$

$$u^0_{gj} = 1.41\left[\frac{(\rho_f - \rho_g)\,\sigma\,g}{\rho^2_f}\right]^{0.25} C_2\,C_3\,C_4,$$

$$C_2 = \begin{cases} 0.4757\left[\ln\left(\dfrac{\rho_f}{\rho_g}\right)\right]^{0.7} & \text{for } \dfrac{\rho_f}{\rho_g} \le 18, \\ \begin{cases} 1 & \text{if } C_5 \ge 1, \\ \left\{1 - \exp\left[-\left(\dfrac{C_5}{1-C_5}\right)\right]\right\}^{-1} & \text{if } C_5 < 1, \end{cases} & \text{for } \dfrac{\rho_f}{\rho_g} > 18, \end{cases}$$

$$C_3 = \begin{cases} \max\left[0.5,\ 2\exp\left(-\dfrac{\mathrm{Re}_f}{60,000}\right)\right] & \text{for } \theta \ge 0, \\ 2\left(\dfrac{C_{10}}{2}\right)^{B_2} & \text{for } \theta < 0, \end{cases}$$

$$C_4 = \begin{cases} 1 & \text{if } C_7 \ge 1, \\ [1 - \exp\ (-C_8)]^{-1} & \text{if } C_7 < 1, \end{cases}$$

$$C_5 = \sqrt{150\left(\frac{\rho_g}{\rho_f}\right)},$$

$$C_7 = \left(\frac{D_2}{D_h}\right)^{0.6},$$

$$C_8 = \frac{C_7}{1 - C_7},$$

$$C_{10} = 2\exp\left(\frac{\mathrm{Re}_f}{350,000}\right)^{0.4} - 1.75\,(\mathrm{Re}_f)^{0.03}\exp\left[-\frac{\mathrm{Re}_f}{50,000}\left(\frac{D_1}{D_h}\right)^2\right] + (\mathrm{Re}_f)^{0.001}\left(\frac{D_1}{D_h}\right)^{0.25},$$

$$B_2 = \left[1 + 0.05\left(\frac{\mathrm{Re}_f}{350,000}\right)\right]^{-0.4},$$

$D_1 = 0.0381$ m, and

$D_2 = 0.09144$ m.

The drift velocity is given by

$$u_{gj} = \begin{cases} F_r\, u_{gjv} + (1 - F_r)\, u_{gjh} & \text{for } \theta \ge 0 \\ F_r\, u_{gjv} + (F_r - 1)\, u_{gjh} & \text{for } \theta < 0. \end{cases}$$

where

u_{gjv} and u_{gjh} are the drift velocities for vertical and horizontal flows,

$$u_{gjh} = u_{gj}^{0} \left(1 - \alpha\right)^{B_1},$$

$$u_{gjv} = u_{gj}^{0} C_9,$$

$$C_9 = \begin{cases} \left(1 - \alpha\right)^{B_1} & \text{for } \theta \geq 0, \\ \min\left[0.7,\ \left(1 - \alpha\right)^{0.65}\right] & \text{for } \theta < 0. \end{cases}$$

C.3 Steam Separator Vapor Carryunder Mass Fraction

The amount of vapor carried-under from the steam separator to the downcomer depends on the flow rate and inlet quality of the separator, and the water level outside the separator [57]. In this study, only the effect of the water level is considered. The mass fraction of vapor in the flow from the separator to the feedwater node is given by

$$cu = cu_0 \left(A_{cu,0} + A_{cu,1}\, r + A_{cu,2}\, r^2 + A_{cu,3}\, r^3\right),$$

where

$$r = \frac{L}{L_0},$$

L is the steam dome water level,

L_0 is a reference water level.

L_0, cu_0, $A_{cu,0}$, $A_{cu,1}$, $A_{cu,2}$, and $A_{cu,3}$ are constants supplied by the user. Because specific steam separator performance data are not available, cu is set to zero in the calculations in this study.

C.4 Steam Separator Flow Inertia

The flow inertia of the steam separator is given by [47]

$$I_{sep} = \left(1 - x_{sep}\right)\left(sepi_0 + sepi_1\, x_{sep} + sepi_2\, x_{sep}^2\right),$$

where

x_{sep} is the flow quality of the separator outlet,

$sepi_0 = 120\ \mathrm{m}^{-1}$,

$sepi_1 = 1.357\ \mathrm{m}^{-1}$, and

$sepi_2 = 6.516\ \mathrm{m}^{-1}$.

In the calculation of Kuosheng recirculation pump trip test, $sepi_0$ is set to $70\ \mathrm{m}^{-1}$ for better match of the core flow rate.

C.5 Convective Heat Transfer Correlations

For single-phase conditions, the heat transfer rate from a section of a fuel rod to the coolant is calculated by Equation 4.41. The single-phase heat transfer coefficient is given by the Dittus-Boelter equation [37]:

$$h = 0.023\,\mathrm{Re}^{0.8}\ \mathrm{Pr}^{0.4}\ \frac{k}{D_h},$$

where

Re is the Reynolds number, $\mathrm{Re}= \dfrac{W\,D_h}{\mu\,A}$,

Pr is the Prandtl number, $\mathrm{Pr}= \dfrac{\mu\,c_p}{k}$,

k is the thermal conductivity of water,

μ is the dynamic viscosity of water, and

c_p is the constant pressure specific heat of water.

For two-phase conditions, the Chen correlation with temperature difference weighting is used (see Equation 4.42) [37]. The heat transfer coefficient for the forced convection part is

$$h_{FC} = 0.023\,\mathrm{Re}_l^{0.8}\ \mathrm{Pr}_f^{0.4}\ \frac{k_f}{D_h}F,$$

where

$$\mathrm{Re}_l = \frac{W\,(1-x)\,D_h}{\mu_f\,A},$$

subscript f stands for saturated water,

$$F = \begin{cases} 1 & \text{for } \dfrac{1}{X_{tt}} < 0.1, \\ 2.35\left(0.213 + \dfrac{1}{X_{tt}}\right)^{0.736} & \text{for } \dfrac{1}{X_{tt}} \geq 0.1, \text{ and} \end{cases}$$

$$\frac{1}{X_{tt}} = \left(\frac{x}{1-x}\right)^{0.9}\left(\frac{\rho_f}{\rho_g}\right)^{0.5}\left(\frac{\mu_g}{\mu_f}\right)^{0.1}.$$

The heat transfer coefficient for the nucleate boiling part is

$$h_{NB} = 0.00122\,S\left[\frac{\left(k^{0.79}c_p^{0.45}\rho^{0.49}\right)_f}{\sigma^{0.5}\mu_f^{0.29}h_{fg}^{0.24}\rho_g^{0.24}}\right]\Delta T_{sat}^{0.24}\Delta P^{0.75},$$

where

$$S = \left[1 + 2.53\times 10^{-6}\,\mathrm{Re}_l^{1.17}\,F^{1.4625}\right]^{-1},$$

$$\Delta T_{sat} = T_w - T_{sat},$$

T_w is the wall temperature,

$$\Delta P = P_{sat}(T_w) - P,$$

P is the system pressure, and

$P_{sat}(T_w)$ is the saturation pressure at T_w.

The partial derivative $\dfrac{\partial h_{NB}}{\partial T_w}$ is needed in fuel conduction and convection calculations:

$$\frac{\partial h_{NB}}{\partial T_w} = h_{NB}\left(\frac{0.24}{\Delta T_{sat}} + \frac{0.75}{\Delta P}\left.\frac{\partial P_{sat}}{\partial T}\right|_{T_w}\right).$$

C.6 Material Properties

C.6.1 Fuel rod properties

UO_2 thermal conductivity:

$$k_f = \frac{3825.02}{T_f + 129.41 + 6.0801 \times 10^{-11} T_f^3},$$

where k_f is in W/m-K, and T_f is in K [47].

UO_2 volumetric heat capacity:

$$(\rho c_p)_f = 8.5103 \times 10^{11} \frac{\exp\left(\frac{535.2850}{T_f}\right)}{\left\{T_f \left[\exp\left(\frac{535.2850}{T_f}\right) - 1\right]\right\}^2}.$$

where $(\rho c_p)_f$ is in J/m^3-K, and T_f is in K [47].

Zr-4 thermal conductivity:

$$k_c = 7.51 + 0.0209\,T_c - 1.45 \times 10^{-5}\,T_c^2 + 7.67 \times 10^{-9}\,T_c^3,$$

where k_c is in W/m-K, and T_c is in K [47].

Zr-4 volumetric heat capacity:

$$\begin{aligned}(\rho c_p)_c &= 1.8205 \times 10^6 + 3.0386 \times 10^5\,\xi - 1.0637 \times 10^5\,\xi^2 \\ &+ 2.8103 \times 10^4\,\xi^3 - 2.7236 \times 10^3\,\xi^4,\end{aligned}$$

where

$(\rho c_p)_c$ is in J/m^3-K,

$\xi = \dfrac{T_c - 300}{200}$, and

T_c is in K [47].

Helium thermal conductivity:

$$k_g = 3.36 \times 10^{-3} T_g^{0.668},$$

where k_g is in W/m-K, and T_g is in K [50].

C.6.2 Water properties

The correlations for the following water properties are from reference [41]: $h_f(P)$, $h_g(P)$, $T_l(P)$, $h_l(T_l, P)$, $\rho_l(h_l, P)$, $\rho_v(h_v, P)$, $c_{p,l}(h_l, P)$, $c_{p,v}(h_v, P)$, $\mu_l(h_l, P)$, $\mu_v(T_v, \rho_v)$, $k_l(h_l)$, $k_v(T_v, \rho_v)$, and $\sigma(T_l)$. These correlations are not repeated here. The saturation pressure of water is given by [43]

$$P_{sat} = 10^5 \left(\frac{T - 255.2}{117.8}\right)^{4.484},$$

where P_{sat} is in Pa, and T is in K.

Appendix D

Description of BWR Simulator

The BWR simulator developed in this thesis has been named SIMBA (**SIM**ulator for **B**wr stability **A**nalysis). The SIMBA code is written in ANSI FORTRAN 77, so it is generally portable. SIMBA has been successfully compiled and run on IBM PCs using Microsoft FORTRAN compiler (MSFORT 5.0), and on SUN SPARC and IBM RS/6000 workstations. The source program of SIMBA is filed with the department.

D.1 Program Description

PROGRAM SIMBA: Main driver. It reads in the input data, writes the input data to the output file, and calls the steady-state initialization and transient subroutines.

SUBROUTINE OUT1: Print out calculations results to the files for plotting.

SUBROUTINE OUT: Print out calculation results to the output file.

SUBROUTINE STEADY: Perform steady-state initialization.

SUBROUTINE SSCOL: Calculate steady-state reactor coolant condition.

SUBROUTINE SSPD: Calculate steady-state core channel pressure drop and jet pump pressure rise.

SUBROUTINE BOILB: Calculate boiling boundaries and fluid transport times of the core channels. The boiling boundary is assumed to be at the point of OSV. The fluid transport time through the upper plenum and the separator node is also calculated.

FUNCTION CARRYU: Calculate the separator vapor carryunder mass fraction.

SUBROUTINE RCSS: Calculate steady-state recirculation system parameters.

SUBROUTINE RCTRAN: Construct the equation system of the recirculation system.

SUBROUTINE PUMPHT: Calculate recirculation pump head, torque and their partial derivatives.

FUNCTION CRL: Calculate the interpolating factor for transition between force and natural circulation used in recirculation system calculations.

SUBROUTINE SSCON: Calculate steady-state fuel rod parameters.

SUBROUTINE TRACON: Transient fuel conduction/convection calculations.

FUNCTION DITTUS: Calculate the single-phase force convection heat transfer coefficient by the Dittus-Boelter equation.

FUNCTION FCHEN: Calculate the F factor in the Chen correlation.

FUNCTION GAPK: Calculate helium thermal conductivity.

FUNCTION FUELK: Calculate UO_2 thermal conductivity (assuming 95% TD).

FUNCTION CLADK: Calculate Zr-4 thermal conductivity.

FUNCTION FUELHC: Calculate UO_2 volumetric heat capacity (reference density = 10,011.54 kg/r

FUNCTION CLADHC: Calculate Zr-4 volumetric heat capacity (reference density = 6,487.48 kg/m

FUNCTION PSAT: Calculate the saturated water pressure.

SUBROUTINE STMLNS: Steam line model steady-state initialization.

FUNCTION CVALVE: Calculate the valve coefficient of SRV or TBV.

SUBROUTINE TRANSL: Construct the steam line equation system.

FUNCTION WBC: Calculate the flow rate through SRV or TBV.

SUBROUTINE REACFB: Calculate the thermal feedback reactivity.

SUBROUTINE POINTK: Solve point kinetics equations by adaptive theta method.

SUBROUTINE DECAYS: Calculate initial decay heat precursor concentration.

SUBROUTINE DECAYP: Calculate normalized total power.

SUBROUTINE TRANS: Perform transient calculations. This is the main routine for BWR transient simulations.

SUBROUTINE TABLE: Perform tabular look-up.

SUBROUTINE PIDCON: Simulate a PID controller.

SUBROUTINE SECORD: Simulate a second order system $\frac{Y}{X} = \frac{frq}{(s^2 + damp\, s + frq)}$.

SUBROUTINE LEDLAG: Simulate a lead/lag compensator $\frac{Y}{X} = Gain\left(\frac{1 + tau_1\, s}{1 + tau_2\, s}\right)$.

SUBROUTINE RCPCON: Determine the statuses of the recirculation pumps.

SUBROUTINE STEP: Perform tabular lookup of integer step functions.

SUBROUTINE ENERGY: Setup the reactor vessel energy equation system and the equation system for mass balance.

SUBROUTINE DMDT: Calculate time rate of change of mass of reactor vessel nodes.

SUBROUTINE UPDATE: Update state variables of the reactor vessel energy equation system.

SUBROUTINE HCASE: Update reactor vessel flow path static enthalpies according to the flow pattern.

SUBROUTINE FLOWUD: Update reactor vessel flow path properties.

SUBROUTINE MOMENT: Setup the reactor vessel mass and momentum equation system.

FUNCTION ECELL: Calculate the average volumetric enthalpy of a node.

SUBROUTINE ME1: Calculate the average density and volumetric enthalpy of a node (two-phase condition).

SUBROUTINE ME2: Calculate the average density and volumetric enthalpy of a node (single-phase liquid to two-phase condition).

FUNCTION DPF: Calculate node average pressure drop factor. $DPF = \left(\frac{f\,\ell}{D_h}\right)\frac{|W|}{2\,\rho}$.

SUBROUTINE CASE: Setup flow pattern indices.

SUBROUTINE STATE: Given pressure, calculate saturated water properties.

SUBROUTINE DRIFT3: Chexal-Lellouche Drift flux correlation for transient calculations. Solve for new distribution parameter and drift velocity using new void fraction. The input x is calculated from new void fraction and old C_0, u_{gj}. Then new x calculated from new C_0 and u_{gj} is returned.

SUBROUTINE DRIFT2: Chexal-Lellouche Drift flux correlation for steady-state initialization. Giving flow quality x, solve for void fraction, distribution parameter and drift velocity by Newton's method. The flow quality is used as the first guess for the static quality.

SUBROUTINE PARAM: Calculate B1, K0, r used in the Chexal-Lellouche correlation.

FUNCTION FFACT: Calculate single-phase Darcy-Weisbach friction factor.

FUNCTION PHILO2: Calculate the Martinelli-Nelson-Jones two phase multiplier.

FUNCTION HFF: Calculate the enthalpy of saturated liquid.

FUNCTION HGG: Calculate the enthalpy of saturated vapor.

FUNCTION TL: Calculate the temperature of compressed liquid.

FUNCTION HL: Calculate liquid enthalpy given liquid temperature, pressure, and initial guess using Newton iteration.

FUNCTION ROL: Calculate density of compressed liquid.

FUNCTION ROV: Calculate density of superheated vapor.

FUNCTION CPL: Calculate specific heat of compressed liquid.

FUNCTION CPV: Calculate specific heat of superheated vapor.

FUNCTION VISL: Calculate viscosity of compressed liquid.

FUNCTION VISV: Calculate viscosity of superheated vapor.

FUNCTION CNDL: Calculate conductivity of compressed liquid.

FUNCTION CNDV: Calculate conductivity of superheated vapor.

FUNCTION SURTEN: Calculate surface tension of water.

FUNCTION TEMPS: Calculate water saturation temperature.

SUBROUTINE GAUSS: Perform Gaussian elimination with implicit partial pivoting [72] to a linear system with n unknowns and m equations.

SUBROUTINE BKSB: Perform backward substitution.

D.2 Input Description

Appendix F shows the input files for validation calculations. The input data are supplied by the input file SIMBA.DAT. In this input file, each line of input data is preceded by a comment line describing the names of input parameters. The title is read by the format A80. All other data are read by free format. All input parameters are in SI unit, except for the parameters related to angular speed or reactivity. The angular speed is in rpm, and the reactivity is in dollar. The input parameters are described below.

nch	no. of core channels (1 or 2)
nc1	no. of nodes in channel 1
nc2	no.of nodes in channel 2 (nc1+nc2 $<$ 40)
ttol	total simulation time,
dtmax	max. time step size,
dtstm	max. time step size for steam line model,
dtout	time interval of printing output file,
dtplt	time interval of printing plot files,
idtsw	switch of time step size calculation,
	= 0, fixed dt (dt=dtmax),
	$>$ 0, dt is calculated as min. coolant transport time in the core nodes.
pini	initial pressure
fq	initial reactor power as fraction of rated power
fwcore	initial core flow as fraction of rated flow
alev	initial water level

hpfw	initial feedwater enthalpy
ncirc	natural circulation switch,
	= 0, initial state is forced circulation;
	= 1, initial state is natural circulation, fwcore is an initial guess.
nlow	low speed switch. if nlow = 1 and iptype = 1, then pumps are at low speed for initialization.
prate	rated pressure
qrate	rated reactor power
wrate	rated core flow
alevr	water level at rated condition,
hpfwr	feedwater enthalpy at rated condition,
vol(i)	reactor node flow volume
area(i)	reactor node flow area
dh(i)	reactor node hydraulic diameter
xl(i)	reactor node length
dz(i)	reactor node elevation difference (out - in)
xk(i)	reactor flow path form loss coefficient
theta(i)	reactor flow path direction (with respect to horizontal dir.)
sepi0, sepi1, sepi2	Coefficients of separator inertia correlation. SEP inertia = (1-xa(4))*(sepi0+xa(4)*(sepi1+sepi2*xa(4)))
cu0	reference separator vapor carry under fraction,
acu0, acu1, acu2, acu3	coefficients of third order polynomial for SEP caryunder fraction
alevcu	reference water level for SEP carry under fraction.
	$cu = cu0 * (acu0 + acu1 * R + acu2 * R^2 + acu3 * R^3)$, R=alev/alevcu.
uawsd	steam dome wall condensation heat transfer coefficient ($W/_oC$)

ilevel	number of points in water level–steam volume table (max. 20)
alevel(i)	array of water level
volstm(i)	array of correspoding steam volume
adc	downcomer area of one recirc. loop,
alp	area of lower plenum,
afcv	flow area of flow control valve,
aldc	lower downcomer area of one recirc. loop,
dldc	lower downcomer hydraulic diameter,
xlldc	lower downcomer length,
ajet	total jet pump area in one loop,
djet	jet pump hydraulic diameter,
xljet	jet pump length,
xijet	jet pump inertia,
arc	recirc. pipe area,
drc	recirc. pipe hydraulic diameter,
xlrc	recirc. pipe length,
xirc	recirc. loop inertia,
xkrc	recirc. loop loss coefficient,
as	total jet pump suction area in one loop,
xksf	jet pump suction forward loss coefficient,
xksr	jet pump suction reverse loss coefficient,
an	total jet pump nozzle area in one loop,
xknf	jet pump nozzle forward loss coefficient,
xknr	jet pump nozzle loss coefficient for reverse suction flow,
ad	total jet pump diffuser area in one loop,
xkdf	jet pump diffuser forward loss coefficient,
xkdr	jet pump diffuser reverse loss coefficient,
iptype	type of recirc. pump,(=0 variable speed, =1 constant speed)

tmh, omgh	rated torque and speed at high speed operation,
tml, omgl	rated torque and speed at low speed operation, (for iptype=0, tml=tmh, omgl=omgh) [omgh, omgl:(rpm)]
hr	rated pump head (m),
omgr	rated pump speed (rpm),
tr	rated pump torque (N-m),
qr	rated pump volumetric flow rate (m^3/sec),
xircp	recirc. pump inertia ($kg - m^2$),
rpump	recirc. pump frictional loss factor (N-m/rpm),
a0 - a3	coefficients of dimensionless head curve: $h/a^2 = a0 + a1 * (v/a) + a2 * (v/a)^2 + a3 * (v/a)^3$,
b0 - b3	coefficients of dimensionless torque curve: $b/a^2 = b0 + b1 * (v/a) + b2 * (v/a)^2 + b3 * (v/a)^3$, where h=pump head/rated head, b=pump torque/rated torque, a=pump speed/rated speed, v=pump flow/rated flow (volumetric flow rate).
psp	suppression pool pressure,
pcd	condenser pressure,
ptb	turbine inlet pressure,
vstmln(i)	volume of the ith steamline node,
lstmln(i)	length of the ith steamline node,
astmln	flow area of the steamline,
dstmln	hydraulic diameter of the steamline,
abpln	flow area of the turbine bypass line,
dbpln	hydraulic diameter of the turbine bypass line,
aventu	flow area of venturi tube at steam dome exit,
formsd	form loss coefficient from steam dome to steamline,
form(i)	form loss coefficient at the outlet of the ith steamline node,

asrv	flow area of safety refief valve when fully opened,
amsiv	flow area of MSIV when fully opened,
cvmsiv	valve coefficient of MSIV,
atbv	flow area of turbine bypass valve when fully opened,
atcv	flow area of turbine control valve when fully opened,
cpsrv	capacity of safety relief valve as fraction of rated steam flow rate,
cptbv	capacity of turbine bypass valve as fraction of rated steam flow rate,
qr1, qr2	fractions of power generated in channel 1 and 2,
qa1(1),..., qa1(nc1)	channel 1 normalized axial power shape,
qa2(1),..., qa2(nc2)	channel 2 normalized axial power shape,
beta(i)	delay neutron fraction of ith precursor group,
decay(i)	decay constant of ith precursor group,
prompt	prompt neutron life time.
tfcoe0 – tfcoe3	coefficients of the third order polynomial of fuel temp. feedback reactivity,
vcoe0 – vcoe3	coefficients of the third order polynomial of coolant void feedback reactivity,
tmcoe0 – tmcoe3	coefficients of the third order polynomial of coolant temp. feedback reactivity.
nrod1	No. of fuel rod in channel 1,
rw1	rod outside radius in channel 1,
thicc1	cladding thickness in channel 1,
thicg1	gap thickness in channel 1,
nrod2	No. of fuel rod in channel 2,
rw2	rod outside radius in channel 2,
thicc2	cladding thickness in channel 2,
thicg2	gap thickness in channel 2.
Parameters of pressure controller	
biasl	load demand bias
biasbp	bypass bias

Transient pressure setpoint adjuster	
gpsadj	gain
tau1ps	lead time constant
tau2ps	lag time constant
psadjm	max. pressure setpoint adjustment
Pressure signal compansator	
gpr	gain
tau1pr	lead time constant
tau2pr	lag time constant
Pressure controller	
gpc	gain
tau1pc	lead time constant
tau2pc	lag time constant
Parameters of level controller	
Level signal compansator	
gl	gain
tau1l	lead time constant
tau2l	lag time constant
Flow mismatch signal compansator	
gfm	gain
tau1fm	lead time constant
tau2fm	lag time constant
total level error signal compansator	
gle	gain
tau1le	lead time constant
tau2le	lag time constant
Level controller	
gplc	proportional gain
gdlc	differential gain
gilc	integral gain

Recirc. flow controller parameters	
Load demand error signal compansator	
gld	gain
tau1ld	lead time constant
tau2ld	lag time constant
Master controller	
gpmc	proportional gain
gdmc	differential gain
gimc	integral gain
Neutronic power signal compansator	
gnp	gain
tau1np	lead time constant
tau2np	lag time constant
Recirc. flow controller	
gpfc	proportional gain
gdfc	differential gain
gifc	integral gain
Constants of 2nd order acutators $Y/X = frq/(s^2 + damp * s + frq)$	
Feedwater system	
frqfw	natural frequency constant
dampfw	damping constant
urfw	max. speed (1/sec)
Control valve	
frqcv	natural frequency constant
dampcv	damping constant
urcv	max. speed (1/sec)
Bypass valve	
frqbv	natural frequency constant
dampbv	damping constant
urbv	max. speed (1/sec)

Recirc.flow actuator	
frqfc	natural frequency constant
dampfc	damping constant
urfc	max. speed (1/sec)
Tables convert controller output to actuator demand	
feedwater system	
ilcfw	No. of data pair [< 10]
ulct(i)	array of level controller output
ufwt(i)	array of correspoding feedwater demand
Control valve	
icv	No. of data pair [< 10]
ucvt(i)	array of CV flow demand
dcvt(i)	array of correspoding CV position demand
Bypass valve	
ibv	No. of data pair [< 10]
ubvt(i)	array of BV flow demand
dbvt(i)	array of correspoding BV position demand
Recirc. flow sytem	
ifc	No. of data pair [< 10]
ufct(i)	array of recirc. flow controller output
dfct(i)	array of correspoding recirc. flow demand
SRV parameters	
isrv	No. of SRV bank [< 10]
fsrv(i)	cummulative fraction of ith SRV
pso(i)	open setpoint of ith SRV
psc(i)	close setpoint of ith SRV
ursrv	max. speed of SRV (1/sec)

Forcing function sets: value array, time array, array size (max. 500)	
ftm, tftm, nftm	recirc. motor torque as fraction of rated torque (enter 1.,0.,1 when iptype=1),
fcv, tfcv, nfcv	flow control valve openning (0 - 1.), (enter 1.,0.,1 when iptype=0)
ips1, tips1, nips1	pump 1 status, (ips1=0 trip, 1 hi speed, 2 lo speed)
ips2, tips2, nips2	pump 2 status.
rt, trt, irt	external reactivity,
hfwt, thfw, ihfw	feedwater inlet enthalpy,
alsett, tlset, ilset	water level set point,
psett, tpset, ipset	pressure set point.
dload, tdload, idload	load demand,
MSIV and TCV fast closure settings	
tmsiv	time at which MSIV closes,
rmsiv	MSIV closing rate (1/sec).
tcvtp	time at which TCV trips,
rcvtp	TCV fast closing rate (1/sec).

D.3 Output Description

The results of SIMBA calculations are printed to files SIMBA.OUT and SIMBA.PL1 to SIMBA.PL7. All output parameters are in SI unit, except for the pump speed (rpm) and reactivity (dollar). SIMBA.OUT contains a copy of input values and a page of summary of system condition at the end of each output interval. Table D.1 shows an example of the output page.

SIMBA.PL1 to SIMBA.PL7 contain system parameters in columns. These files can be used by a plotting software for visualizing data trends. SIMBA.PL1 contains reactor pressure, steam dome water level, thermal power, normalized thermal power, normalized fission power, feedwater flow, steam flow, and external, Doppler, void, and moderator temperature reactivities. SIMBA.PL2 contains upper and lower

Table D.1: Example of SIMBA output file

```
1-------------------------------------------------------------
 -------------------------------------------------------------
0        Time:          2.0000
0        Pressure:    .6805E+07
0        Power:       .1766E+10
0        Level:       .7527E+00
0      Norm. Th. P    .6253E+00     Norm. Neutron P .6250E+00
0      FW flow rate   .9102E+03     Steam flow rate .9135E+03
0       JET1 Flow     .2132E+04      JET2 Flow      .2132E+04
0       RC 1 Flow     .4165E+03      RC 2 Flow      .4165E+03
0       RCP 1 Speed   .1691E+04      RCP 2 Speed    .1691E+04
0       FCV 1 Pos.    .1093E+00      FCV 2 Pos.     .1093E+00
0         LP Flow     .4265E+04        UP Flow      .4259E+04
0      Ch 1 IN Flow   .4265E+04      CH 1 OUT Flow  .4250E+04
0      Turbine Flow   .9136E+03      TCV Position   .4114E+00
0      Turb.BP Flow   .0000E+00      TBV Position   .0000E+00
0      SRV Flow       .0000E+00      SRV Position   .0000E+00
0      CH 1 Boil B.   .7620E+00      CH 1 Transp.T. .5116E+01
0      CH 2 Boil B.   .0000E+00      CH 2 Transp.T. .0000E+00
0 UP/SS Transp.Time   .4396E+01
0      CH 1 Inlet H   .1166E+07     CH 1 Subcool H  .9256E+05
 -------------------------------------------------------------
```

plenum flow rates, and the inlet and outlet flow rates of core channels. SIMBA.PL3 and SIMBA.PL4 list the node average void fractions of core channels. SIMBA.PL5 gives the flow rate of jet pumps and recirculation lines, recirculation pump speeds, and flow control valve positions. SIMBA.PL6 contains the flow rates and valve positions of TCV, TBV, and SRV. SIMBA.PL7 contains the boiling boundaries and fluid transport times of core channels.

Appendix E

Post-Processor

A post-processor is used to calculate decay ratio, real part of eigenvalue , and oscillation period from the response of system parameters. This post-processor is the FORTRAN program POST. POST reads in data pairs of time (independent variable) and system parameter (dependent variable). The peaks and valleys of the system parameter are identified. The time separation between two adjacent peaks is the estimated oscillation period. The decay ratio and real part of eigenvalue are given by

$$DR = \left(\frac{Y_2 - Y_{\min}}{Y_1 - Y_{\min}}\right)^2,$$

and

$$\lambda_{real} = \frac{2}{T} \ln\left(\frac{Y_2 - Y_{\min}}{Y_1 - Y_{\min}}\right) = \frac{\ln(DR)}{T},$$

where Y_1, Y_2, and $Y_{\min}$ are adjacent peak and valley values, and T is the oscillation periods. The mean value of the system parameter between the two peaks is estimated as

$$Y_{mean} = \frac{Y_2 - DR \cdot Y_1}{1 - DR} \text{ for } DR \neq 1.$$

The values calculated above are instantaneous values. Average values are calculated using a moving window of five data points. The source program of POST is filed with the department. The input file of the POST program is POST.DAT. POST.DAT specifies the data file containing system response in columns, the lines

Table E.1: Example of POST.DAT

```
*  datfil
simba.pl1
*  nskip,ncolx,ncoly
      2     1     6
```

to be skipped before reading data, and the column numbers of the independent and dependent variables. POST.OUT is the output file of the POST program, and is self-explanatory. Table E.1 shows an example of POST.DAT.

Appendix F

Input Files for Validation Calculations

F.1 Kuosheng Recirculation Pump Trip Transient

```
c  Title(A80)
Kuosheng BWR/6 , 2 channels, 5 cells, dt=0.1 sec.
c  nch,nc1,nc2
2     5     5
c  ttol,dtmax,dtstm,dtout,dtplt,idtsw
30.         0.1          0.1          2.           0.1          0
c  pini,fq,fwcore,alev,hpfw,ncirc,nlow
6.80455e6    0.68     0.9916    0.75        0.827e6       0      1
c  prate,qrate,wrate,alevr,hpfwr
6.89e6       2.8235294e9 10647.0      0.75        0.827e6
c  vol(i),area(i),xl(i),dh(i),dz(i),xk(i),theta(i)
c      ...    ...    ...    ...    ...    ...    ...          [i=1,nc1+nc2+6]
37.1218      19.8515      1.9691       0.6175      -1.9691       0.     -90.
28.2050      8.2805       3.4062       1.0244      -3.4062       0.     -90.
59.1534      8.2805       4.4592       1.0244      -4.4592       0.     -90.
32.2832      8.4319       4.5997       0.1524       4.5997      60.0    90.
93.7286      9.2030       5.2974       0.2594       1.9065      20.9    90.
38.3846     16.7077      2.1488       4.5458       2.1488       1.37    90.
2.58674      3.1877       0.3810       0.0136       0.3810       0.2     90.
2.58674      3.1877       0.3810       0.0136       0.3810       0.2     90.
2.58674      3.1877       0.3810       0.0136       0.3810       0.2     90.
```

```
2.58674     3.1877      0.3810      0.0136      0.3810      0.2    90.
2.58674     3.1877      0.3810      0.0136      0.3810      1.2    90.
2.58674     3.1877      0.3810      0.0136      0.3810      0.2    90.
2.58674     3.1877      0.3810      0.0136      0.3810      0.2    90.
2.58674     3.1877      0.3810      0.0136      0.3810      0.2    90.
2.58674     3.1877      0.3810      0.0136      0.3810      0.2    90.
2.58674     3.1877      0.3810      0.0136      0.3810      1.2    90.
c                                   xk(nj),theta(nj)  [only when nch=2]
                                                        20.9   90.
c  sepi0,sepi1,sepi2
70.         1.357       6.516
c  cu0,acu0,acu1,acu2,acu3,alevcu,uawsd
0.    0.    0.    0.    0.    0.75  2e7
c  ilevel
4
c  alevel(i),i=1,ilevel
0.          2.6306      4.8912          7.9011
c  volstm(i),i=1,ilevel
142.0145    102.5739    50.4676         0.0
c  adc,alp,afcv
2.0702      9.2030      0.0535
c  aldc,dldc,xlldc
1.1321      1.0244      4.4592
c  ajet,djet,xljet,xijet
0.9381      0.0690      4.4592      4.7534
c  arc,drc,xlrc,xirc,xkrc
0.1669      0.0980      23.4788     140.6760    0.0
c  as,xksf,xkfr
0.2042      0.000        25.0
c  an,xknf,xknr
0.0411      0.0         0.0
c  ad,xkdf,xkdr
0.9318      0.          1.0
c  iptype,tmh,omgh,tml,omgl
1           24811.14    1691        4822.29     445
c  hr,omgr,tr,qr,xircp,rpump
268.224     1780        24811.14    2.0668      671.9351    2.67e-3
c  a0,a1,a2,a3
1.3623      -0.2563     0.2218      -0.3203
c  b0,b1,b2,b3
0.003       0.25043     2.1948      -1.4347
c  psp,pcd,ptb
1.013e5     6.76e3      6.4e6
c  vstmln(i),i=1,7
10.23       10.23       32.04       25.83       22.12       25.17  16.19
```

```
c  lstmln(i),i=1,7
7.39        7.39        3.50        2.02        8.69        8.81    6.71
c  astmln,dstmln,abpln,dbpln,aventu,formsd
0.9423      0.5477      0.4366      0.5182      0.9423      0.81
c  form(6),i=1,6
0.4         0.4         0.334       0.167       0.167       2.6
c  asrv,cvsrv,amsiv,cvmsiv,atbv,cvtbv
0.4209      28.5        0.9423      1.725       0.065       3.0
c  atcv,cvtcv,cpsrv,cptbv,frtcvr
0.5767      0.          1.13        0.35
c  qr1,qr2
0.5   0.5
c  qa1(1),qa1(2),...,qa1(nc1)
0.125 0.275 0.3   0.225 0.075
c  qa2(1),qa2(2),...,qa2(nc2)       [only when nch=2]
0.125 0.275 0.3   0.225 0.075
c  beta(1),beta(2),beta(3),beta(4),beta(5),beta(6)
.247e-3     1.3845e-3   1.2222e-3   2.6455e-3   .832e-3     .169e-3
c  decay(1),decay(2),decay(3),decay(4),decay(5),decay(6),prompt
0.0127      0.0317      0.115       0.311       1.4      3.87  2.e-5
c  tfcoe0,tfcoe1,tfcoe2,tfcoe3
3.5538      -7.0105e-3  8.5388e-7   0.
c  vcoe0,vcoe1,vcoe2,vcoe3
0.          -18.777     0.          0.
c  tmcoe0,tmcoe1,tmcoe2,tmcoe3
0.          0.          0.          0.
c  nrod1,rw1,thicc1,thicg1
19344       6.15e-3     0.813e-3    0.137e-3
c  nrod2,rw2,thicc2,thicg2          [only when nch=2]
19344       6.15e-3     0.813e-3    0.137e-3
c  gpsadj,tau1ps,tau2ps,psadjm
2.0e4       0.          25.         2.75e5
c  gpr,tau1pr,tau2pr
1.          2.0         5.0
c  gpc,tau1pc,tau2pc,biasl,biasbp
9.0000e-7   2.          5.0         0.09        0.018
c  gl,tau1l,tau2l,gfm,tau1fm,tau2fm
0.5         0.0         0.1         0.36        0.          0.01
c  gle,tau1le,tau2le,gplc,gdlc,gilc
1.          1.          0.25        4.2         0.          0.07
c  gld,tau1ld,tau2ld,gpmc,gdmc,gimc
1.          0.          0.0         0.5882      0.          0.147
c  gnp,tau1np,tau2np,gpfc,gdfc,gifc
1           0.          4.0         0.0         0.          0.0
c  frqfw,dampfw,urfw,frqcv,dampcv,urcv
```

```
1.0         1.4         0.5         2.0         2.6         0.14
c  frqbv,dampbv,urbv,frqfc,dampfc,urfc,ursrv
7.564       5.498       1.75        2.0         1.2         0.2   1.0
c  ilcfw,icv,ibv,ifc,isrv
2           2           3           2           3
c  ulct(1),...,ulct(ilcfw)
0.          1.1
c  ufwt(1),...,ufwt(ilcfw)
0.          1.0
c  ucvt(1),...,ucvt(icv)
0.          1.5
c  dcvt(1),...,dcvt(icv)
0.          1.0
c  ubvt(1),...,ubvt(ibv)
0.          0.35        1.0
c  dbvt(1),...,dcbt(ibv)
0.          0.99        1.0
c  ufct(1),...,ufct(ifc)
0.          1.75
c  dfct(1),...,dfct(ifc)
0.          1.0
c  fsrv(1),...,fsrv(isrv)
0.2537      0.5669      1.0
c  pso(1),...,pso(isrv)
7.6049e6    7.6738e6    7.7427e6
c  psc(1),...,psc(isrv)
7.4672e6    7.5361e6    7.6050e6
c  nftm,nfcv,nips1,nips2
0           0           2           2
c  ftm(1),...,ftm(nftm)             [if nftm > 0]
c  tftm(1),...,tftm(nftm)           [if nftm > 0]
c  fcv(1),...,fcv(nfcv)             [if nfcv > 0]
c  tfcv(1),...,tfcv(nfcv)           [if nfcv > 0]
c  ips1(1),...,ips1(nips1)          [if nips1 > 0]
c  tips1(1),...,tips1(nips1)        [if nips1 > 0]
1           0
0           5.8
c  ips2(1),...,ips2(nips2)          [if nips2 > 0]
c  tips2(1),...,tips2(nips2)        [if nips2 > 0]
1           0
0           5.8
c  irt,ihfw,ilset,ipset,idload
0           0           0           0           0
c  rt(1),...,rt(irt)                [if irt > 0]
c  trt(1),...,trt(iqt)              [if irt > 0]
```

```
c  hfwt(1),...,hfwt(ihfw)          [if ihfw > 0]
c  thfw(1),...,thfw(ihfw)          [if ihfw > 0]
c  alsett(1),...,alsett(ilset)     [if ilset > 0]
c  tlset(1),...,tlset(ilset)       [if ilset > 0]
c  psett(1),...,psett(ipset)       [if ipset > 0]
c  tpset(1),...,tpset(ipset)       [if ipset > 0]
c  dload(1),...,dload(idload)      [if idload > 0]
c  tdload(1),...,tdload(idload)    [if idload > 0]
c  tmsiv,rmsiv,tcvtp,rcvtp
1.0e7       0.25        1.0e7       10.0
```

F.2 Peach Bottom-2 Turbine Trip Test TT1

```
c  Title(A80)
Peach Bottom-2 tt1, 1 channel x 12 cells + 1 bypass x 1 cell, dt=0.001 s.
c  nch,nc1,nc2
2     12     1
c  ttol,dtmax,dtstm,dtout,dtplt,idtsw
50.         0.001          0.1          2.           0.1          0
c  pini,fq,fwcore,alev,hpfw,ncirc,nlow
6.835e6       0.474         0.988       1.5         0.75e6       0       0
c  prate,qrate,wrate,alevr,hpfwr
7.033e6       3293e6    12915.0      1.5         0.8185e6
c  vol(i),area(i),xl(i),dh(i),dz(i),xk(i),theta(i)
c      ...    ...    ...    ...    ...    ...    ...          [i=1,nc1+nc2+6]
30.285       12.31        2.4360       0.3675      -2.4360       0.0    -90.
30.285       12.31        2.4360       0.3675      -2.4360       0.0    -90.
101.65       12.31        4.9220       0.3675      -4.9220       0.     -90.
35.93        3.93         4.5720       0.1541       4.572        0.648   90.
59.87        10.76        5.4943       0.0502       2.3470       28.9    90.
32.77        19.20        1.7075       0.0099       1.7075       1.      90.
2.33         7.66         0.3048       0.01473      0.3048       0.478   90.
2.33         7.66         0.3048       0.01473      0.3048       0.478   90.
2.33         7.66         0.3048       0.01473      0.3048       0.478   90.
2.33         7.66         0.3048       0.01473      0.3048       0.478   90.
2.33         7.66         0.3048       0.01473      0.3048       0.478   90.
2.33         7.66         0.3048       0.01473      0.3048       0.478   90.
2.33         7.66         0.3048       0.01473      0.3048       0.478   90.
2.33         7.66         0.3048       0.01473      0.3048       0.478   90.
2.33         7.66         0.3048       0.01473      0.3048       0.478   90.
```

```
2.33        7.66        0.3048      0.01473     0.3048      0.478  90.
2.33        7.66        0.3048      0.01473     0.3048      0.478  90.
2.33        7.66        0.3048      0.01473     0.3048      2.038  90.
11.92      3.26        3.6576      0.03204     3.6576      412.3  90.
c                                  xk(nj),theta(nj)  [only when nch=2]
                                                       400.0  90.
c  sepi0,sepi1,sepi2
120.  1.357 6.516
c  cu0,acu0,acu1,acu2,acu3,alevcu,uawsd
0.    0.    0.    0.    0.    1.5   2e7
c  ilevel
3
c  alevel(i),i=1,ilevel
0.          2.4892      8.2652
c  volstm(i),i=1,ilevel
230.66      178.34      0.
c  adc,alp,afcv
6.155       5.38        0.375
c  aldc,dldc,xlldc
4.325       0.3675      4.922
c  ajet,djet,xljet,xijet
1.83        0.01183     4.922       2.69
c  arc,drc,xlrc,xirc,xkrc
0.37        0.6795      28.3234     63.9        0.0
c  as,xksf,xkfr
0.20823     0.485       25.0
c  an,xknf,xknr
0.03934     0.1         1.0
c  ad,xkdf,xkdr
1.83        0.875       1.0
c  iptype,tmh,omgh,tml,omgl
0           30512.8     1668        30512.8     1668
c  hr,omgr,tr,qr,xircp,rpump
218.4       1668        30512.8     2.852        2028.66     2.67e-3
c  a0,a1,a2,a3
1.4356      -0.28       9.8505e-2   -0.2541
c  b0,b1,b2,b3
0.44487     0.84826     -0.26157    -3.1554e-2
c  psp,pcd,ptb
1.013e5     6.76e3      6.2e6
c  vstmln(i),i=1,7
29.91   11.28       26.77       36.65       27.74       34.11       6.0
c  lstmln(i),i=1,7
14.79   6.24        5.45        0.7         0.69        0.84        1.5
c  astmln,dstmln,abpln,dbpln,aventu,formsd
```

```
1.18        0.618       0.28          0.37075     1.18         0.73
c  form(6),i=1,6
1.5375      1.725       0.334         0.167       0.167        2.072
c  asrv,cvsrv,amsiv,cvmsiv,atbv,cvtbv
  0.2371      1.0          1.18          1.725       0.06274      2.28
c  atcv,cvtcv,cpsrv,cptbv,frtcvr
1.18        1.688       1.13          0.262
c  qr1,qr2
1.0       0.
c  qa1(1),qa1(2),...,qa1(nc1)
0.0395 0.0580 0.0681 0.0765 0.0866 0.1008
0.1008 0.1176 0.1168 0.1076 0.0840 0.0437
c  qa2(1),qa2(2),...,qa2(nc2)        [only when nch=2]
0.0
c  beta(1),beta(2),beta(3),beta(4),beta(5),beta(6)
.2075e-3    1.1629e-3   1.0266e-3   2.2222e-3   0.6988e-3   0.1420e-3
c  decay(1),decay(2),decay(3),decay(4),decay(5),decay(6),prompt
0.0127      0.0317      0.115       0.311       1.4      3.87  4.015e-5
c  tfcoe0,tfcoe1,tfcoe2,tfcoe3
0.          -4.03e-3    0.          0.
c  vcoe0,vcoe1,vcoe2,vcoe3
0.          -8.6        0.          0.
c  tmcoe0,tmcoe1,tmcoe2,tmcoe3
0.          -4.94e-2    0.          0.
c  nrod1,rw1,thicc1,thicg1
  40064       7.15e-3     0.94e-3     0.1524e-3
c  nrod2,rw2,thicc2,thicg2           [only when nch=2]
  0           7.15e-3     0.94e-3     0.1524e-3
c  gpsadj,tau1ps,tau2ps,psadjm
2.0e4       0.          25.         2.75e5
c  gpr,tau1pr,tau2pr
1.          2.0         5.0
c  gpc,tau1pc,tau2pc,biasl,biasbp
3.0000e-6   2.          5.0         0.09        0.018
c  gl,tau1l,tau2l,gfm,tau1fm,tau2fm
0.5         0.0         0.1         0.36        0.          0.01
c  gle,tau1le,tau2le,gplc,gdlc,gilc
1.          1.          0.25        4.2         0.          0.07
c  gld,tau1ld,tau2ld,gpmc,gdmc,gimc
1.          0.          0.0        0.5882      0.          0.147
c  gnp,tau1np,tau2np,gpfc,gdfc,gifc
1.           0.          0.0        0.4         0.          0.2
c  frqfw,dampfw,urfw,frqcv,dampcv,urcv
1.0         1.4         1.0         2.0         2.6         0.14
c  frqbv,dampbv,urbv,frqfc,dampfc,urfc,ursrv
```

```
37.564       0.498       1.3     2.0          1.2          0.2          5.0
c  ilcfw,icv,ibv,ifc,isrv
2           2           3           2           4
c  ulct(1),...,ulct(ilcfw)
0.          1.15
c  ufwt(1),...,ufwt(ilcfw)
0.          1.0
c  ucvt(1),...,ucvt(icv)
0.          1.5
c  dcvt(1),...,dcvt(icv)
0.          1.0
c  ubvt(1),...,ubvt(ibv)
0.          0.262       1.0
c  dbvt(1),...,dcbt(ibv)
0.          0.99        1.0
c  ufct(1),...,ufct(ifc)
0.          1.25
c  dfct(1),...,dfct(ifc)
0.          1.0
c  fsrv(1),...,fsrv(isrv)
0.3077      0.6154      0.8462      1.0
c  pso(1),...,pso(isrv)
7.622e6     7.6917e6    7.7614e6    8.6666e6
c  psc(1),...,psc(isrv)
7.5476e6    7.6166e6    7.6855e6    8.5818e6
c  nftm,nfcv,nips1,nips2
0           0           0           0
c  ftm(1),...,ftm(nftm)             [if nftm > 0]
c  tftm(1),...,tftm(nftm)           [if nftm > 0]
c  fcv(1),...,fcv(nfcv)             [if nfcv > 0]
c  tfcv(1),...,tfcv(nfcv)           [if nfcv > 0]
c  ips1(1),...,ips1(nips1)          [if nips1 > 0]
c  tips1(1),...,tips1(nips1)        [if nips1 > 0]
c  ips2(1),...,ips2(nips2)          [if nips2 > 0]
c  tips2(1),...,tips2(nips2)        [if nips2 > 0]
c  irt,ihfw,ilset,ipset,idload
7           0           0           2           2
c  rt(1),...,rt(irt)                [if irt > 0]
c  trt(1),...,trt(iqt)              [if irt > 0]
0.   0.   -0.024    -0.29     -1.66     -14.325   -54.
0.82    0.99    1.028   1.207   1.764   2.51    3.94
c  hfwt(1),...,hfwt(ihfw)           [if ihfw > 0]
c  thfw(1),...,thfw(ihfw)           [if ihfw > 0]
c  alsett(1),...,alsett(ilset)      [if ilset > 0]
c  tlset(1),...,tlset(ilset)        [if ilset > 0]
```

```
c  psett(1),...,psett(ipset)          [if ipset > 0]
c  tpset(1),...,tpset(ipset)          [if ipset > 0]
6.835e6      6.25e6
15.0         50.0
c  dload(1),...,dload(idload)         [if idload > 0]
c  tdload(1),...,tdload(idload)       [if idload > 0]
0.474      -0.09
0.72        0.72
c  tmsiv,rmsiv,tcvtp,rcvtp
1.0e7        0.25         0.41        10.0
```

References

[1] J. A. Thie, "Boiling Water Reactor Stability." *Nucleonics*, 16(3):102–110, March 1958.

[2] T. J. Rausch and H. C. Pfefferlen, "Overview of Current BWR Owners' Group Stability Programs." In *Proceedings: International Workshop on Boiling Water Reactor Stability*, pages 30–44, Holtsville, New York, March 17–19, 1990. OECD, NEA. CSNI-R-178.

[3] USNRC, "Power Oscillations in Boiling Water Reactors (BWRs)." NRC Bulletin No. 88-07, Supplement 1, December 1988.

[4] USNRC, "Power Oscillations at Washington Nuclear Power Unit 2." NRC Information Notice 92-74, November 1992.

[5] USNRC, "Long-Term Solutions and Upgrade of Interim Operating Recommendations for Thermal-Hydraulic Instabilities in Boiling Water Reactors." NRC Generic Letter 94-02, July 1994.

[6] W. Wulff et al., "BWR Stability Analysis at Brookhaven National Laboratory." In *Proceedings of the USNRC Ninth Water Reactor Safety Information Meeting*, volume 3, Addition, pages 1–20, June 1992. NUREG/CP-0119-Vol.3-Add.

[7] USNRC, "Code of Federal Regulations." Title 10, Part 50, Appendix A, General Design Criterion 12.

[8] E. Gialdi et al., "Core Stability in Operating BWR: Operational Experience." *Progress in Nuclear Energy*, 15:447–459, 1985.

[9] B-G Bergdahl and R. Oguma, "BWR Stability Investigation in Ringhals 1 Measurement Data From October 26, 1989." In *Proceedings: International Workshop on Boiling Water Reactor Stability*, pages 142–160, Holtsville, New York, March 17–19, 1990. OECD, NEA. CSNI-R-178.

[10] P. Mata, P. G. Sedano, and J Serra, "Analysis of Confrentes Abnormal Plant transients with RETRAN-02 and RETRAN-03." *Nuclear Technology*, 100:203–215, November 1992.

[11] H. C. Pfefferlen, G. A. Watford, and T. J. Rausch, "BWR Core Thermal-Hydraulic Stability Experience and Safety Significance." In *Proceedings: International Workshop on Boiling Water Reactor Stability*, pages 45–57, Holtsville, New York, March 17–19, 1990. OECD, NEA. CSNI-R-178.

[12] J. March-Leuba, "Average Power Increase During Limit-Cycle Oscillations." *Transactions of the American Nuclear Society*, 60:481–482, 1989.

[13] J. March-Leuba and J. M. Rey, "Coupled Thermohydraulic-Neutronic Instabilities in Boiling Water Nuclear Reactors: A Review of the State-of-the-Art." *Nuclear Engineering and Design*, 145:97–111, 1993.

[14] M. Ishii, "Wave Phenomena and Two-Phase Flow Instabilities." In G. Hetsroni, editor, *Handbook of Multiphase Systems*, section 2.4, pages 2–95 to 2–122. Hemisphere, Washington, 1982.

[15] J. A. Bouré, A. E. Bergles, and L. S. Tong, "Review of Two-Phase Flow Instability." *Nuclear Engineering and Design*, 25:165–192, 1973.

[16] S. Kakaç and T. N. Veziroglu, "A Review of Two-Phase Flow Instabilities." In S. Kakaç and M. Ishii, editors, *Advances in Two-Phase Flow and Heat Transfer -Fundamental and Applications*, volume II, pages 577–667. Martinus Nijhoff Publishers, Boston, 1983.

[17] A. H. Stenning, "Density-Wave Oscillations." MIT Course 22.36 Class Notes HH-B, 1980.

[18] M. Z. Podowski, "Instabilities in Two-Phase Systems." In R. T. Lahey, Jr., editor, *Boiling Heat Transfer–Modern Development and Advances*, pages 271–315. Elsevier Science Publishers, Amsterdam, 1992.

[19] J. March-Leuba, "Density-Wave Instabilities in Boiling Water Reactors." NUREG/CR-6003, ORNL/TM-12130, September 1992.

[20] J. E. Meyer and R. P. Rose, "Application of a Momentum Integral Model to the Study of Parallel Channel Boiling Flow Oscillations." *Journal of Heat Transfer, Trans. ASME, Series C*, 85(1):1–9, 1963.

[21] J. M. Sorensen, A. F. V. Dias, and L. D. Eisenhart, "BWR Stability Analysis: A Comparison of Point, One-Dimensional, and Three-Dimensional Neutronic Model Methodologies." In L. J. Agee, editor, *Proceedings: Sixth International RETRAN Conference*, pages 21–1—21–19, August 1990. EPRI NP-6949.

[22] J. March-Leuba and E. D. Blakeman, "A Mechanism for Out-of-Phase Power Instabilities in Boiling Water Reactors." *Nuclear Science and Engineering*, 107:173–179, 1991.

[23] E. D. Blakeman and J. March-Leuba, "A Parametric Analysis of Decay Ratio Calculations in a Boiling Water Reactor Model." Paper published in the Seventh Power Plant Dynamics, Control and Testing Symposium, Knoxville, Tennessee, May 1989. CONF-890555–4.

[24] S. Langenbuch and K. D. Schmidt, "A Sensitivity Analysis for the BWR Stability Behaviour." In *Proceedings: International Workshop on Boiling Water Reactor Stability*, pages 241–256, Holtsville, New York, March 17–19, 1990. OECD, NEA. CSNI-R-178.

[25] G. C. Park et al., "The Development of a Closed-Form Analytical Model for the Stability Analysis of Nuclear Coupled Density-Wave Oscillations in Boiling Water Nuclear Reactors." *Nuclear Engineering and Design*, 92:253–281, 1986.

[26] P. Saha and N. Zuber, "An Analytical Study of the Thermally Induced Two-Phase Flow Instabilities Including the Effect of Thermal Non-Equilibrium." *International Journal of Heat and Mass Transfer*, 21:415–426, 1978.

[27] O. Yokomizo et al., "Examination of Nuclear Thermal Hydraulic Oscillation Modes in BWR Core." In *Proceedings: International Workshop on Boiling Water Reactor Stability*, pages 175–189, Holtsville, New York, March 17–19, 1990. OECD, NEA. CSNI-R-178.

[28] A. F. Henry, *Nuclear-Reactor Analysis.* The MIT Press, Cambridge, MA, 1975.

[29] L. G. Neal and S. M. Zivi, "The Stability of Boiling-Water Reactors and Loops." *Nuclear Science and Engineering*, 30:25–38, 1967.

[30] J. March-Leuba and C. M. Smith, "Development of An Automated Diagnostic System for Boiling Water Reactor Stability Measurements." *Progress in Nuclear Energy*, 15:27–35, 1985.

[31] J. Balaram et al., "An Analysis of Boiling Water Nuclear Reactor Stability Margin." NUREG/CR-3291, May 1983.

[32] L. A. Carmichael and R. O. Niemi, "Transient and Stability Tests at Peach Bottom Atomic Power Station Unit 2 at End of Cycle 2." EPRI NP-564, June 1978.

[33] J. March-Leuba, "LAPUR Benchmark Against In-Phase and Out-of-Phase Stability Tests." NUREG/CR-5605, ORNL/TM-11621, October 1990.

[34] S. W. Jones and M. C. Humphreys, "Stability Monitoring System Demonstration Program at WNP-2." *Transactions of the American Nuclear Society*, 60:483–484, 1989.

[35] C. M. Mowry, I. Nir, and D. W. Newkirk, "Operational Control of Boiling Water Reactor Stability." *Nuclear Technology*, 109:412–428, March 1995.

[36] R. T. Lahey, Jr. and F. J. Moody, *The Thermal-Hydraulics of a Boiling Water Nuclear Reactor.* American Nuclear Society, La Grange Park, Illinois, second edition, 1993.

[37] N. E. Todreas and M. S. Kazimi, *Nuclear System I–Thermal Hydraulic Fundamentals.* Hemisphere, New York, 1990.

[38] General Electric Company, "BWR/6: General Description of a Boiling Water Reactor," September 1980.

[39] J. E. Meyer, "Conservation Laws in One-Dimensional Hydrodynamics." WAPD-BT-20, September 1960.

[40] A. K. Agrawal et al., "An Advanced Thermohydraulic Simulation Code for Transients in LMFBRs (SSC-L CODE)." BNL-NUREG-50773, February 1978.

[41] S. P. Kao, *A Multiple-Loop Primary System Model for Pressurized Water Reactor Plant Sensor Validation.* PhD thesis, MIT, Department of Nuclear Engineering, July 1984.

[42] J. E. Meyer and E. A. Reinhard, "Numerical Techniques for Boiling Flow Stability Analysis." *Journal of Heat Transfer, Trans. ASME, Series C*, 87:311–312, 1965.

[43] W. H. Strohmayer, *Dynamic Modeling of Vertical U-Tube Steam Generators for Operational Safety Systems.* PhD thesis, MIT, Department of Nuclear Engineering, August 1982.

[44] W. L. Weaver, III, J. E. Meyer, and A. K. Agrawal, "A Few-Pressure Model for Transient Two-Phase Flows in Networks." *Transactions of the American Nuclear Society*, 28:273–274, 1978.

[45] E. L. L. Cabral, *Real-Time Three Dimensional Thermal-Hydraulic Model and Non-Linear Controller for Large PWR Cores.* PhD thesis, MIT, Department of Nuclear Engineering, February 1989.

[46] J. E. Meyer and J. S. Williams, Jr., "A Momentum Integral Model for the Treatment of Transient Fluid Flow." WAPD-BT-25, 1962.

[47] W. Wulff et al., "The BWR Plant Analyzer–Final Report." NUREG/CR-3943, BNL-NUREG-51812, August 1984.

[48] M. A. Pulick and S. G. Margolis, "CRIB 1 – A Steam Generator Stability Analysis Program for the PHILCO-2000 Computer." WAPD-TM-530, December 1965.

[49] J. A. Borkowski et al., "Time Domain Model Sensitivity in Boiling Water Reactor Stability Analysis Using TRAC/BF1." *Nuclear Technology*, 103:34–47, July 1993.

[50] M. M. Giles et al., "TRAC-BF1/MOD1–An Advanced Best-Estimate Computer Program for BWR Accident Analysis, Volume 1: Model Description." NUREG/CR-4356-Vol.1, August 1992.

[51] J. E. Kelly, S. P. Kao, and M. S. Kazimi, "THERMIT-2: A Two-Fluid Model for Light Water Reactor Subchannel Transient Analysis." MIT-EL-81-014, April 1981.

[52] Y. K. Cheung, V. Parameswaran, and J. C. Shang, "BWR Refill-Reflood Program Task 4.7 Model Development–TRAC-BWR Component Models." NUREG/CR-2574, EPRI NP-2376, GEAP-22052, September 1983.

[53] N. E. Todreas and M. S. Kazimi, *Nuclear System II–Elements of Thermal Hydraulic Design.* Hemisphere, New York, 1990.

[54] K. Wong, *Computer Model of a Nuclear Reactor Primary Coolant Pump.* Master thesis, MIT, Department of Nuclear Engineering, August 1982.

[55] L. Y. Liao, "A Study on the Jet Pump Characteristic Curve in Boiling Water Reactors." In R. R. Schultz, editor, *Power Plant Transients - 1990*, pages 81–87. the American Society of Mechanical Engineers, New York, 1990. FED-Vol. 104.

[56] W. Wulff, "Steam Line Dynamics–A Computer Program." NUREG/CR-1438, BNL-NUREG-51186, April 1980.

[57] J. H. McFadden et al., "RETRAN-02–A Program for Transient Thermal-Hydraulic Analysis of Complex Fluid Systems, Volume 1: Theory and Numerics (Revision 2)." EPRI NP-1850-CCMa, Volume 1, Revision 2, November 1984.

[58] J. C. Gehin, *A Quasi-Static Polynomial Nodal Method for Nuclear Reactor Analysis.* PhD thesis, MIT, Department of Nuclear Engineering, September 1992.

[59] J. R. Wang, *The Setup and Application of Time Domain Analysis for the Two-Phase Flow Stability.* PhD thesis, National Tsing-Hua University, Hsing-Chu, Taiwan, May 1993. (In Chinese).

[60] S. J. Wang et al., "Development of the Kuosheng Plant Analyzer and Its Assessment with Plant Data." *Nuclear Technology*, 106:125–134, April 1994.

[61] Weng-Ching Tsai, personal communication, September 1994.

[62] N. H. Larsen, "Core Design and Operating Data for Cycle 1 and 2 of Peach Bottom 2." EPRI NP-563, June 1978.

[63] K. Hornyik and J. A. Naser, "RETRAN Analysis of the Turbine Trip Tests at Peach Bottom Atomic Power Station Unit 2 at the End of Cycle 2." EPRI NP-1076-SR, April 1979.

[64] D. A. Dube, *Development of a Fully Implicit Two-Fluid, Thermal-Hydraulic Model for Boiling Water Reactor Transient Analysis.* PhD thesis, MIT, Department of Nuclear Engineering, August 1980.

[65] J. March-Leuba and P. J. Otaduy, "A Comparison of BWR Stability Measurements with Calculations Using the Code LAPUR-IV." NUREG/CR-2998, ORNL/TM-8546, January 1983.

[66] F. B. Woffindon and R. O. Niemi, "Low-Flow Stability Tests at Peach Bottom Atomic Power Station Unit 2 During Cycle 3." EPRI NP-972, April 1981.

[67] R. K. Otnes and L. Enochson, *Digital Time Series Analysis.* John Wiley & Sons, New York, 1972.

[68] U. S. Rohatgi, L. Y. Neymotin, and W. Wulff, "Assessment of RAMONA-3B Methodology with Oscillatory Flow Tests." *Nuclear Engineering and Design*, 143:69–82, 1993.

[69] The MathWork, Inc., *MATLAB Version 4 User's Guide.* Prentice-Hall, Inc., Englewood Cliffs, NJ, 1995.

[70] T. H. J. J. van der Hagen, I. Pázsit, and O. Thomson, "Methods for the Determination of the In-Phase and Out-of-Phase Stability Characteristics of a Boiling Water Reactor." *Nuclear Technology*, 107:193–214, August 1994.

[71] B. Chexal et al., "A Void Fraction Correlation for Generalized Applications." *Progress in Nuclear Energy*, 27(4):255–295, 1992.

[72] W. H. Press et al., *Numerical Recipes in FORTRAN: the Art of Scientific Computing.* Cambridge University Press, Cambridge, U.K., second edition, 1992.